Title
Study of Nano-treating Effects on High Strength Aluminum Alloys

Author
Yuan, Jie

Publication Date
2021

Peer reviewed|Thesis/dissertation

UNIVERSITY OF CALIFORNIA

Los Angeles

Study of Nano-treating Effects on High Strength Aluminum Alloys

A dissertation submitted in partial satisfaction of the

requirements for the degree Doctor of Philosophy

in Materials Science and Engineering

by

Jie Yuan

2021

`

ABSTRACT OF THE DISSERTATION

Study of Nano-treating Effects on High Strength Aluminum Alloys

by

Jie Yuan

Doctor of Philosophy in Materials Science and Engineering

University of California, Los Angeles, 2021

Professor Xiaochun Li, Chair

High strength aluminum alloys have been used widely in the aerospace and automobile industries because of their high specific strength and good corrosion resistance. The rapid development of electric vehicles promotes the demand for these alloys for energy saving. High-strength aluminum alloys, including heat-treatable 7xxx and 2xxx series, have been studied for decades. Their strength mainly comes from uniformly distributed precipitates inside the grains. High alloying is often required to provide a high-volume fraction of the precipitates to improve their mechanical properties. However, this alloying strategy brings along drawbacks. First of all, a higher strength usually compromises other properties such as ductility, electrical conductivity, and stress corrosion resistance, etc. Secondly, a higher alloying often deteriorates the

`

manufacturing capability of the alloys. For example, AA7034 aluminum alloy containing 11.0-12.0% Zn and 2.5% Mg offers the highest strength among all commercial aluminum alloys. Rapid cooling is required for manufacturing AA7034 because of the need to suppress solidification cracking, porosity, and inhomogeneity induced by the high alloying. Moreover, high alloying often results in bulky secondary phases after common solidification, such as casting, thus making solutionization more difficult. Lastly, thermodynamics imposes inherent limits for alloy element/s solubility, thus unable to bring out more precipitates. In the 2xxx series, an extra amount of Mg cannot be dissolved during solutionization because of this solubility limit. The metallurgical barriers (e.g., manufacturing capability and thermodynamic limits) pose a grand challenge to further design and improve the overall properties of the high-strength aluminum alloys for widespread applications.

A new nanotechnology-enabled metallurgy method, Nano-Treating (NT), has been proposed in recent years. By adding a low volume fraction of nano-reinforcements into an alloy melt (i.e., nano-treating), it can tune the solidification/manufacturing process, microstructure, and properties of the alloy. Researchers have found that nano-reinforcements, especially nanoparticles, can induce heterogeneous nucleation and effectively restrict grain growth during solidification, thus significantly reducing grain size and inhibiting dendritic arm development. When nanoparticles are added to multi-phase alloys, the secondary phase can be altered, refining secondary phases and modifying phase morphology. Moreover, nanoparticles can influence the precipitation behaviors of heat-treatable aluminum alloys. The precipitate free zone was found to be much reduced by nanoparticles. Improved mechanical properties were achieved by nano-treating too. Nano-Treating has emerged as a powerful new metallurgical method in addition to

`

the traditional ones like alloying, grain refining, heat treatment, and plastic deformation. However, the nano-treating effects have never been systematically studied despite their great potential.

To empower this new nanotechnology to improve high-strength aluminum alloys' manufacturing capability and properties, this thesis focuses on the nano-treating effects on solidification behavior and heat-treatment of high-strength aluminum alloys, and a systematic study was conducted.

There are two methods to incorporate and disperse ceramic nanoparticles into the metal matrix. The first method is ex-situ incorporation that requires the addition of existing ceramic nanoparticles into the metal melt from outside. This method is more limited for manufacturing due to the cost of ex-situ ceramic nanoparticles. More often, the interfacial bonding between nanoparticles and matrix is not ideal. The second, more economical method is the in-situ synthesis of nanoparticles inside the molten metals. However, effective control of nanoparticle sizes during in-situ synthesis is challenging. Available controlling processes like rapid solidification, ultrasonication-assist fabrication, and high-energy ball milling are expensive and difficult to scale up for mass production. To enable nano-treating for mass production of metals, a new cost-effective production method must be developed.

The diffusion-controlled growth of a particle is related to the supersaturation of the reactants, diffusivity of reactants, and growth time. As the reaction is typically at high temperatures in molten metal, no surfactants can survive the temperature, thus unable to be utilized for diffusion and growth time control. Therefore, diluting the reactants would be effective in reducing supersaturation for size control of synthesized nanoparticles. A new controlling mechanism on growth time is also needed to achieve a more uniform size distribution. This study discovered an

`

interface-controlled mechanism to successfully fabricate in-situ TiB_2, TiC, WC/W, ZrB_2 nanoparticles with small size and narrow size distribution. The new nanoparticle synthesis method builds a solid foundation for the industry-scale application of nano-treating.

A systematic study of nano-treating effects on solidification and heat treatment was then conducted on high strength aluminum alloys. Examination of the microstructures of the nano-treated alloys and solidification curves suggest a promoted nucleation and effective restriction of grain growth. During the last stage of solidification, the grain coherent point (GCP) is effectively postponed by nanoparticles, thus allowing sufficient time for liquid feeding to prevent solidification shrinkage and hot tearing. These nanoparticles-induced effects can significantly improve the casting capability and mechanical integrity as well as properties of alloys. The volume fraction of the secondary phases is also altered by nano-treating, possibly due to a higher permeability of the coherent solid network and a higher viscosity of the liquid.

Furthermore, the study suggests that a promoted diffusion is achieved by interface and dislocation mediated diffusion. It is believed that nano-treating can effectively promote the solution treatment due to a reduced volume fraction and refined size of secondary phases, which facilitate the dissolution of the secondary phases during solutionization. This promotion effect enables the successful manufacturing of high alloying alloys like AA7034 at slow cooling by traditional casting. Improved dissolution of the secondary phases results in a higher level of supersaturation of the solute atoms within a specific time limit. Dislocations can also serve as heterogeneous nucleation sites to facilitate precipitates. A promoted aging also allows natural aging to yield adequate strength at a relatively short time. In general, nano-treating has two effects: “antibody effect” to improve the manufacturing capability and “vitamin effect,” to tune the

`

microstructure and properties of the alloy. To demonstrate the nano-treating effects, three application case studies are conducted.

The first application case study is to enable the manufacturing of high-strength Al-Zn-Mg-Cu alloy by casting. While the highly alloyed AA7034 alloy offers the highest tensile strength among commercial aluminum alloys, its manufacturing typically requires a rapid solidification process, such as spray casting. Under any regular cooling rate, its high alloying content makes the secondary phase large and difficult to be dissolved. By nano-treating, AA7034 is successfully cast at a slow cooling rate with significantly modified microstructure, including the volume and size of the secondary phases. These refined phases were then more easily dissolved during solutionization to offer a higher mechanical property.

The second application case study demonstrates a solution to eliminating the need for post-welding heat treatment in arc welding of AA7075 alloy, as the post-welding heat treatment is never ideal for large parts and field welding. Unfortunately, it would take years for the natural aging of AA7075 alloy to reach its peak strength. When this alloy was butt welded by a nano-treated 7075 filler wire with a reduced Cu content, the natural aging is promoted, and the weld recovered 77% of the base metal strength after 40 days, which is 50.2% stronger than the control sample welded by pure 7075 filler wire.

The third application case study is to develop and cast high-strength Al-Cu-Mg alloy. AA2024 alloy, a typical high-strength wrought alloy, contains 4.5% Cu and a max 1.8% Mg. Its high alloying makes it prone to solidification defects. Thus, plastic deformation is required to close shrinkage porosity, making this alloy for wrought products only. Moreover, this alloy has a limit of maximum Mg content at 1.8% as a high Mg content would form bulky Al_2CuMg phase in the

`

matrix, which has a limited solubility during solutionizing. Nanoparticles successfully reduced the solidification defects and greatly recovered the ductility of the cast alloy.

In summary, this dissertation first discussed a new interface-controlled mechanism for in-situ synthesis of ceramic nanoparticles to build a solid foundation for economical nano-treating of molten metals. Then the nano-treating effects on solidification and heat treatment were systematically studied. Finally, two critical effects from nano-treating were summarized: “antibody effect” to enable scalable manufacturing of various high-strength aluminum alloys without cracking and shrinkage porosities and “vitamin effect” to improve microstructure and properties of alloys. The effects were successfully demonstrated to develop and manufacture high-performance aluminum alloys: manufacturing high-strength Al-Zn-Mg-Cu alloy, natural aging to AA7075 welds with nano-treated welding wires, and casting of high-strength Al-Cu-Mg alloys.

`

The dissertation of Jie Yuan is approved.

Jenn-Ming Yang

Ajit Mal

Ximin He

Xiaochun Li, Committee Chair

University of California, Los Angeles

2021

`

TABLE OF CONTENTS

`

`

`

`

`

NOMENCLATURE

Al	Aluminum
Al_2O_3	Alumina
Al_3Ti	Titanium Aluminide
B_4C	Boron Carbide
CATA	Computer-Aided Thermal Analysis
CCD	Charge Coupled Device
Cu	Copper
DSC	Differential Scanning Calorimetry
EBSD	Electron Backscatter Diffraction
EDM	Electrical Discharge Machining
EDS	Energy Dispersive X-ray Spectroscopy
EL	Elongation
GTAW	Gas Tungsten Arc Welding
HAADF	High Angle Aunular Dark Field
HRTEM	High Resolution Transmission Electron Microscopy
$KAlF_4$	Potassium Aluminum Fluoride
KBF_4	Potassium Fluoroborate

`

K_2TiF_6	Potassium Hexafluorotitanate
KCl	Potassium Chloride
Mg	Magnesium
MIEA	Modified Indirect Electric Arc
MMNC	Metal Matrix Nanocomposites
Mn	Manganese
NaCl	Sodium Chloride
PWHT	Post-weld heat treatment
SAED	Selected Area Electron Diffraction
SEM	Scanning Electron Microscopy
Si	Silicon
SiC	Silicon Carbide
STEM	Scanning Transimission Electron Microscopy
TEM	Transmission Electron Microscopy
TiB_2	Titanium Diboride
TiC	Titanium Carbide
UTS	Ultimate Tensile Strength
WC	Tungsten Carbide

`

XRD	X-ray Diffraction
YS	Yield Strength
Zn	Zinc
ZrB_2	Zirconium Diboride
ZrC	Zirconium Carbide

`

ACKNOWLEDGEMENTS

I want to express my gratitude to Professor Xiaochun Li for his support of my Ph.D. study, especially during the COVID 19 pandemic. His knowledge, experience, and guidance helped my research and life. Furthermore, I want to thank him for the opportunity to work in this group. He encouraged me to have a scientific understanding and study the physical mechanism behind the experimental results, which is priceless to my Ph.D. study and future career.

I would also like to acknowledge Professors Jenn-Ming Yang, Ajit Mal, and Ximin He to serve in my doctoral committee. I sincerely appreciate their valuable inputs for my research.

I am also very grateful to all my colleagues in the research group for the four years of collaboration, lifetime friendships, and long-standing inspirations.

I also appreciate the help from other collaborators from MetaLi LLC and Southern University of Science and Technology. They offered great help to my research work.

I would like to thank my parents and wife for their unconditional support throughout this journey.

`

VITA

2014, B.S., Materials Science and Engineering, Tsinghua University, China

2017, M.S., Materials Science and Engineering, Tsinghua University, China

JOURNAL PAPERS

Yuan, J., Pan, S., Zheng, T., Li, X. Nanoparticle promoted solution treatment by reducing segregation in AA7034, *Materials Science & Engineering A* 822 (2021) 141691

Yuan, J., Yao, G., Pan, S., Murali, N., Li, X. Size Control of In Situ Synthesized TiB_2 Particles in Molten Aluminum. *Metall Mater Trans A* 52, 2657–2666 (2021)

Yuan, J.; Zuo, M.; Sokoluk, M.; Yao, G.; Pan, S.; Li, X. Nanotreating High-Zinc Al–Zn–Mg–Cu Alloy by TiC Nanoparticles. *In Light Metals* 2020; Tomsett, A., Ed.; The Minerals, Metals & Materials Series; Springer International Publishing: Cham, 2020; pp 318–323.

Yuan, J.; Liu, J.; Song, Q.; Wang, D.; Xie, W.; Yan, H.; Zhou, J.; Wei, Y.; Sun, X.; Zhao, L. Photoinduced Mild Hyperthermia and Synergistic Chemotherapy by One-Pot-Synthesized Docetaxel-Loaded Poly(Lactic-Co-Glycolic Acid)/Polypyrrole Nanocomposites. *ACS Appl. Mater. Interfaces* 2016, 8 (37), 24445–24454.

Sokoluk, M., **Yuan, J.,** Pan, S. Li, X. Nanoparticles Enabled Mechanism for Hot Cracking Elimination in Aluminum Alloys. *Metall Mater Trans A* 52, 3083–3096 (2021).

Pan, S., **Yuan, J.,** Zheng, T., She, Z., Li, X., Interfacial thermal conductance of in situ aluminum-matrix nanocomposites. *J Mater Sci.* 56, 13646–13658 (2021).

Pan, S.; **Yuan, J**.; Zhang, P.; Sokoluk, M.; Yao, G.; Li, X. Effect of Electron Concentration on Electrical Conductivity in in Situ Al-TiB2 Nanocomposites. *Appl. Phys. Lett*. 2020, 116 (1), 014102.

Yao, G.; **Yuan, J**.; Pan, S.; Guan, Z.; Cao, C.; Li, X. Casting In-Situ Cu/CrBx Composites via Aluminum-Assisted Reduction. *Procedia Manuf.* 2020, 48, 320–324.

Liu, R.; **Yuan, J**.; Wang, C. A Novel Way to Fabricate Tubular Porous Mullite Membrane Supports by TBA-Based Freezing Casting Method. *J. Eur. Ceram. Soc*. 2013, 33 (15–16), 3249–3256.

Pan, S.; Zheng, T., **Yuan, J**.; Jin, K., Li, X. TiB2 nanoparticles-regulated oxidation behavior in aluminum alloy 7075. *Corrosion Science.* 2021, 191, 109749.

Pan, S.; Yao, G.; **Yuan, J**.; Sokoluk, M.; Li, X. Manufacturing of Bulk Al-12Zn-3.7Mg-1Cu Alloy with TiC Nanoparticles. *Procedia Manuf.* 2020, 48, 325–331.

`

Yao, G.; Pan, S.; **Yuan, J**.; Guan, Z., Li, X. A novel process for manufacturing copper with size-controlled in-situ tungsten nanoparticles by casting. *Journal of Materials Processing Technology.* 296 (2021) 117187

Zuo, M.; Sokoluk, M.; Cao, C.; **Yuan, J**.; Zheng, S.; Li, X. Microstructure Control and Performance Evolution of Aluminum Alloy 7075 by Nano-Treating. *Sci. Rep*. 2019, 9 (1), 1–11.

Pan, S.; Guan, Z.; Yao, G.; **Yuan, J**.; Li, X. Mo-Enhanced Chemical Stability of TiC Nanoparticles in Molten Al. *J. Alloys Compd*. 2021, 856, 158169.

Yao, G.; Cao, C.; Pan, S.; **Yuan, J**.; De Rosa, I.; Li, X. Thermally Stable Ultrafine Grained Copper Induced by CrB/CrB2 Microparticles with Surface Nanofeatures via Regular Casting. *J. Mater. Sci. Technol.* 2020, 58, 55–62.

Yan, H.; Shang, W.; Sun, X.; Zhao, L.; Wang, J.; Xiong, Z.; **Yuan, J**.; Zhang, R.; Huang, Q.; Wang, K.; Li, B.; Tian, J.; Kang, F.; Feng, S.-S. "All-in-One" Nanoparticles for Trimodality Imaging-Guided Intracellular Photo-Magnetic Hyperthermia Therapy under Intravenous Administration. *Adv. Funct. Mater*. 2018, 28 (9), 1705710.

Zhong, Y.; Ma, Z.; Zhu, S.; Yue, J.; Zhang, M.; Antaris, A. L.; **Yuan, J**.; Cui, R.; Wan, H.; Zhou, Y.; Wang, W.; Huang, N. F.; Luo, J.; Hu, Z.; Dai, H. Boosting the Down-Shifting Luminescence of Rare-Earth Nanocrystals for Biological Imaging beyond 1500 Nm. *Nat. Commun*. 2017, 8 (1), 737.

Yan, H.; Chen, Y.; Sun, X.-D.; Zhao, L.-Y.; Zhang, C.-X.; Bian, L.; Yang, Y.-H.; Liu, Y.-Z.; **Yuan, J**.; Yao, Y.; Wu, Q. Controlled Synthesis of Fe3O4 Single Crystalline Spheres in One Solvothermal System and Their Application in MRI. *J. Nanosci. Nanotechnol*. 2017, 17 (3), 1983–1991.

Xie, W.; Gao, Q.; Wang, D.; Wang, W.; **Yuan, J**.; Guo, Z.; Yan, H.; Wang, X.; Sun, X.; Zhao, L. Melatonin Potentiates "inside-out" Nano-Thermotherapy in Human Breast Cancer Cells: A Potential Cancer Target Multimodality Treatment Based on Melatonin-Loaded Nanocomposite Particles. *Int. J. Nanomedicine* 2017, 12, 7351–7363.

PATENTS

Li, X.; **Yuan, J**.; Yao, G.; Zheng, S. Interface-Controlled in-Situ Synthesis of Nanostructures in Molten Metals for Mass Manufacturing, PCT/US2020/027775, October 15, 2020.

`

Chapter 1 Introduction

1.1 Background and motivation

Aluminum alloys have been intensively used in every aspect of human life in the past decades. They have high specific strengths, high corrosion resistance, and excellent damage tolerance. High strength 2xxx and 7xxx series aluminum alloys are heat treatable Al-Cu alloys and Al-Zn-Mg alloys and are widely used in the automobile and aerospace industries. Since 1991, the aluminum content in light vehicles has improved by more than 50% for a significant reduction in fuel consumption[1]. As a result, more efforts have been devoted to developing new aluminum alloys to achieve better mechanical properties while maintaining reliability. Engineers acquired impetus high toughness by reducing impurity levels, such as iron and silicon. Also, the resistance to exfoliation and stress corrosion cracking can be improved by utilizing special tempers or adding extra microalloying elements like zirconium and scandium[2]. However, alloying has a certain limitation due to manufacturing difficulty. For example, as typical precipitation strengthening alloy, the strength of Al-Zn-Mg-Cu alloy fundamentally depends on the volume fraction and distribution of fine precipitates. Though higher zinc content could theoretically provide better strength, it might also introduce coarser secondary phases formed during solidification, which is hard to dissolve during heat treatment[3]. Moreover, high-strength Al-Zn-Mg-Cu alloys and Al-Cu-Mg alloys become more sensitive to strain rate during post-processing, such as extrusion, and more susceptible to stress corrosion cracking. The cast-ability also suffers from the high alloy content. Higher alloying content makes the alloy more susceptible to porosity, hot tearing, and inhomogeneity during casting[4]. This dilemma of achieving extra high strength by high alloying content and poor processing capability makes the task difficult. Fortunately, adding a small volume

`

fraction of inert nanoparticles into original alloys might create a new path to obtaining the next level of overall performance.

It is well established that incorporating a small volume fraction of nanoparticles into metals can achieve effective grain refinements and secondary phase modification. Nanoparticles change the solidification behavior of a melt. Chen et al. found that for Al-20Bi alloy, the size of the secondary phase, with the help of TiCN nanoparticles, could be smaller than the sample without nanoparticles by orders of magnitudes[5]. Choi et al. also discovered that the formation of dendritic arms of the primary phases during casting would be suppressed. Adding alumina (Al_2O_3) nanoparticles into the melt significantly reduced the hot tearing of A206 cast alloy comparing to conventional grain refinement[6]. Sokoluk et al. discovered that AA7075 alloys could be safely arc welded without hot cracks by utilizing AA7075 welding wires that contain titanium carbide (TiC) nanoparticles[7]. In addition, Li et al. discovered the potential of a more uniform distribution of precipitates and less precipitate free zone (PFZ) along the grain boundary in Al-Zn-Mg-Cu alloy incorporated with TiN nanoparticles[8]. With the help of nanoparticles, it is thus highly possible to modify the precipitates, the grain size, and secondary phases. The nanoparticles have the potential to break the limits of convention metallurgy. Since it influences different aspects of metal processing, a new term, “nano-treating,” is invented to denote the overall modification of nanoparticles. However, the underlying mechanism of nano-treating is not systematically studied.

Nano-treating of molten metals could be achieved in two ways: The ex-situ approach incorporates the nanoparticles from outside, whereas the in-situ method synthesizes nanoparticles inside the melt. The in-situ route is believed to be more economical and provide more stable, cleaner nanoparticles with stronger interfacial bonds with matrices[9]. Therefore, if an in-situ alloy master with a high volume of nanoparticles could be economically made, it would enable the mass

`

production of nano-treated alloys in industries. In-situ methods have been studied to fabricate ceramic particle enhanced composites for decades. However, there is no effective mechanism to achieve small size and narrow size distribution of nanoparticles synthesized in molten metals at elevated temperatures.

Nano-treating can improve the overall performance of high-strength aluminum alloys and eliminate traditional manufacturing difficulties. As microstructures determine materials' properties, it is important to understand how nanoparticles would influence the microstructure of the alloys, including solute atoms, primary phases, secondary phases, and precipitates, etc. As nano-treating would modify the microstructures at different materials processing stages, it is necessary to study its effect on solidification, heat treatment, and plastic deformation. Nano-treating methods can then be successfully applied to manufacture high-strength aluminum alloys beyond conventional limits.

1.2 Research objectives

The objectives of this study include (1) Study size-control mechanism and develop an effective in-situ synthesis method of nanoparticles with narrow size distribution; (2) Study how nano-treating influences solidification, heat treatment, and plastic deformation of aluminum alloys; (3) Apply nano-treating for development, manufacturing, and application of high-strength Al-Zn-Mg-Cu and Al-Cu-Mg alloys.

:

1.3 Work summary

The dissertation will be organized as follows.

`

- Chapter 2 reviews the metal matrix nanocomposites, current fabrication methods, and existing research of nanoparticles' influence on alloy systems.
- Chapter 3 describes a new interface controlled in-situ fabrication method of different ceramic nanoparticles in different metals
- Chapter 4 studies how nanoparticles modified the microstructures of the alloys during solidification, heat treatment, and plastic deformation.
- Chapter 5 presents the nano-treating effects on high-strength Al-Zn-Mg-Cu alloys.
- Chapter 6 discusses nanoparticle influence on natural aging and its application for welded AA7075 alloy
- Chapter 7 studies nano-treating enabled design and casting of unprecedented high-performance Al-Cu-Mg alloys
- Chapter 8 draws conclusions for this study.
- Chapter 9 provides recommendations for future work.

`

Chapter 2 Literature Review

2.1 Nano-treating

2.1.1 Nano-treated alloy and metal matrix nanocomposites

Nano-treating is to modify the alloy by adding a small number of ceramic nanoparticles[10]. Metal matrix nanocomposite (MMNC) is a multiphase metallic material where the reinforcements have one dimension less than 100 nm[11]. Therefore, by definition, a nano-treated alloy is a specific type of MMNCs whose volume fraction of nano-reinforcements is low. Nano-treating is more focused on how nano-particulates modify the manufacturing process, structure, and properties of the alloy. MMNCs are often known as a certain type of composite materials that combines the properties of both base materials and reinforcements: metal bases have good ductility and high toughness, while ceramic reinforcements can add more strength and modulus to MMNCs[11]. The strengthening mechanisms have been a key focus for MMNCs, especially when a high-volume fraction of nano-reinforcements is incorporated. The extra strength comes from the load transfer effect, Orowan strengthening, coefficient of thermal expansion (CTE) mismatch, and elastic modulus (EM) mismatch[12]. On the other side, Nano-treating intends to influence the solidification behavior, heat treatment, and plastic deformation of the alloy.

2.1.2 Nanoparticle-enabled grain refinement

Nanoparticles are effective grain refiners[13]. The main mechanisms of nanoparticle-enabled grain refinement include nanoparticle-enabled heterogeneous nucleation[14] and growth restriction[15] of the primary phase. Optical images of Al-10Si alloys refined by TiCN nanoparticles were presented in Figure 2-1[15].

`

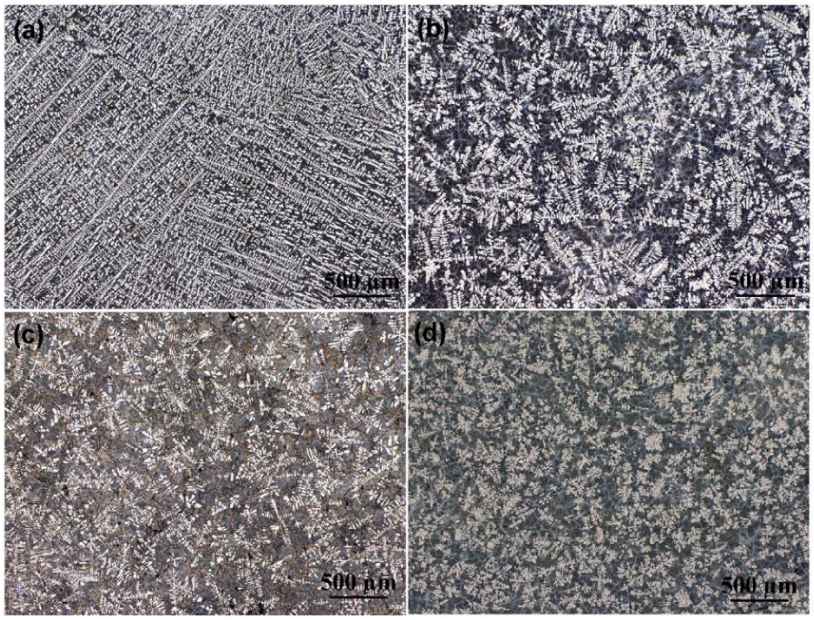

Figure 2-1. Typical micrographs of as-cast Al–10Si alloys with increasing the NP addition levels. (a) Matrix alloy; (b) 0.5 vol.%; (c) 1 vol.%; (d) 2 vol.% [15]

During solidification or phase transformation, heterogeneous sites, e.g., inclusions and mold walls, can decrease the nucleation energy barrier, thereby increasing the nucleation rate. An illustration of heterogeneous nucleation on a flat facet of a nanoparticle is shown in Figure 2-2.

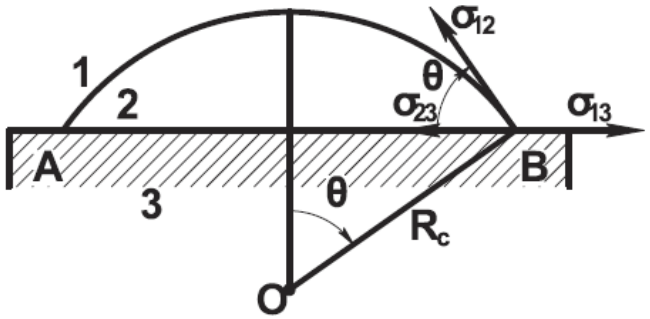

Figure 2-2. Diagram of a solid-phase nucleus on a flat facet of a nanoparticle. 1 – melt, 2 – nucleus, 3 – nanoparticle[16]

`

The volume rate of heterogeneous nucleation can be calculated as Equation. 2-1.

$$N_{het} = fC\exp\left(-\frac{\Delta G^*_{NP}}{kT}\right) \tag{2-1}$$

where f denotes the rate that each nucleus can be made supercritical, C is the number of atoms in contact with heterogeneous nucleation sites per unit volume, ΔG^*_{hom} is the activation energy barrier against homogeneous nucleation, k is Boltzmann's constant, T is absolute temperature, ΔG^*_{NP} is work of formation of the nucleus on the nanoparticle, and it is shown in Equation 2-2[16].

$$\Delta G^*_{NP} = \frac{1}{3}\pi\sigma^{\infty}_{12}R_0^2\left(1-\frac{6\delta}{R_0}\right)(1-cos\theta)^2(2+cos\theta) + E \tag{2-2}$$

Here, R_0 is related to a critical value of nucleus radius(R_c and $R_c = R_0(1-\delta/R_0)$), σ^{∞}_{12} is the free energy of a flat surface, δ is the Tolman parameter and equal in the order of magnitude to the diameter of melt atom[17], θ is the wetting angle between nanoparticle and the melt, E is the activation of diffusion. Comparing to the homogeneous critical formation energy of nucleus,$\Delta G^*_{NP} = 4\pi\sigma^{\infty}_{12}R_c^2 + E$, The activation energy of nucleation is greatly reduced Therefore, nanoparticles will promote nucleation of the metals.

During solidification, the solid front is covered by nanoparticles and the gain growth velocity will be reduced as indicated by Equation2-3[15].

$$\frac{dR}{dt} = \lambda_C(1-p\Theta) \tag{2-3}$$

Here, *R* is the grain size, *t* is time, λ_C is variable indicate the growth velocity when no nanoparticles are added, p is a diffusion-hindrance efficiency, Θ is the coverage of nanoparticles on dendrite surface, and it is a function of particle volume fraction and time. It is obvious that the growth velocity largely depends on the diffusion-hindrance efficiency *p.* Its value is measured as 0.933 in

`

an Al-Si alloy with 2 vol.% of TiCN nanoparticles at low cooling rates[15], which indicates a strong inhibition of the grain growth.

By promotion of nucleation and growth restriction, nanoparticles serve as promising grain refinement agents. On the other hand, alloys containing nanoparticles could retain the grain size at higher temperatures, such as heat treatment, because of Zinner pining effect[18]. The maximum mean grain size can be theoretically estimated by Equation 2-4,

$$R_{max} = \frac{4r}{3f_v} \tag{2-4}$$

where r is the nanoparticle radius and f_v is the volume fraction of the nanoparticles.

2.1.3 Nanoparticle-enabled second phase modification

The incorporation of nanoparticles can also modify the secondary phases in alloys. Nanoparticles could modify the eutectic structure because nanoparticles can induce nucleation of the eutectic structure. This phenomenon in hypo-eutectic Al-Si alloy was investigated by Wang et al. [19]. $TiC_{0.5}N_{0.5}$ ceramic nanoparticles are good heterogeneous nucleation sites for Si because of lattice matching between Si and this nanoparticle. As shown in Figure 2-13, the cellular substructure of the eutectic grains was reduced from 28 μm to 8.5 μm when 1.5 vol.% of the nanoparticles were added. The interspacing between Si particles was also reduced.

`

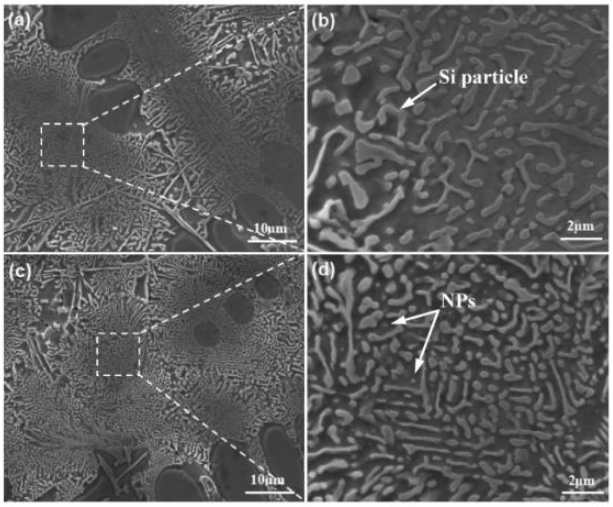

Figure 2-3 SEM picture of eutectic phase in (a-b) Al- Si matrix alloy; (c-d) modified with 1.5vol% nanoparticles

Nanoparticles may self-assemble onto the secondary phase surfaces to significantly refine the structure of the secondary phases. One example is the Zn-Bi immiscible alloy could be modified by tungsten (W) nanoparticles, as shown in Figure 2-4[20]. Bi would subside at the bottom of the ingot because of its higher density, but it turned to be spherical droplets with the help of W nanoparticles.

`

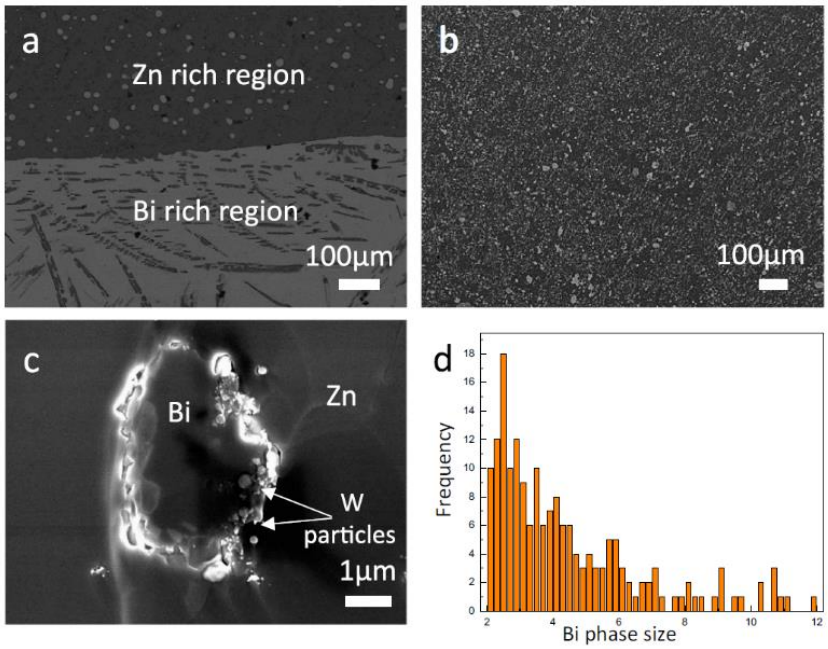

Figure 2-4 SEM images and size distribution of the Bi phase in Zn-Bi alloys: (a) Pure Zn-8Bi; (b-c) Zn-8Bi-2 vol.% W nanocomposites; (d) Histogram of Bi phase size distribution in Zn-8Bi-2 vol.% W nanocomposites[20]

2.1.4 Nanoparticle influence on precipitates

Nanoparticles can influence the precipitation behavior of an alloy system. When the nanoparticles are incorporated into the matrix, it usually will not alter the precipitation sequence[21]. However, the influence could vary in different systems.

Saboori et al. studied the Elektron21 (Mg-RE-Zr-Zn) alloy reinforced by AlN nanoparticles[22]. It was discovered that AlN nanoparticles might stabilize the precipitates during solution treatment, as shown in Figure 2-5. This is due to the reaction between the AlN nanoparticle and Nd in the matrix to form Al_2Nd. It also hurts aging so that the hardness of the nanoparticle incorporated alloy did not increase as much as a pure alloy. The aging is markedly faster than unreinforced alloy as well. The reason is that the coefficient of thermal expansion of the ceramic nanoparticles and the host alloy is largely different that after quenching, a mismatch between nanoparticles and matrix

`

would induce a high density of dislocations around the nanoparticles. These dislocations increase the heterogeneous nucleation rate of precipitates and increase the diffusion coefficient of solute atoms along the dislocations.

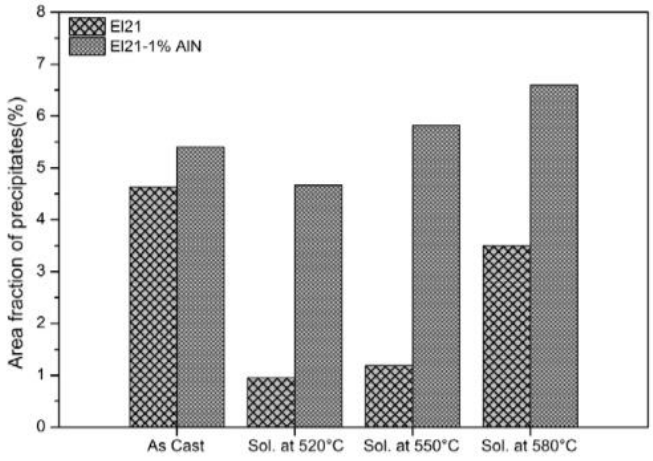

Figure 2-5 The area fraction of precipitates in El21 and El21–1.0 wt.%AlN after casting and solution treatment at different temperatures[22]

The influence is quite different in Al-Cu system reinforced by TiC nanoparticles[23]. Adding nanoparticles results in finer θ′ precipitates so that both the tensile strength and ductility increased, as shown in Figure 2-6. The authors discovered that the addition of the nano-sized TiC particles would increase the density of dislocations in the composites. Then, more θ′ precipitates were obtained in the composites. Furthermore, as the α-Al grains in the composites are finer than those in the pure Al–Cu alloy, the diffusion distance of the Cu atoms becomes shorter during the solution process. Therefore, the finer and more uniformly distributed θ′ precipitates were formed in the α-Al grains during the aging process.

`

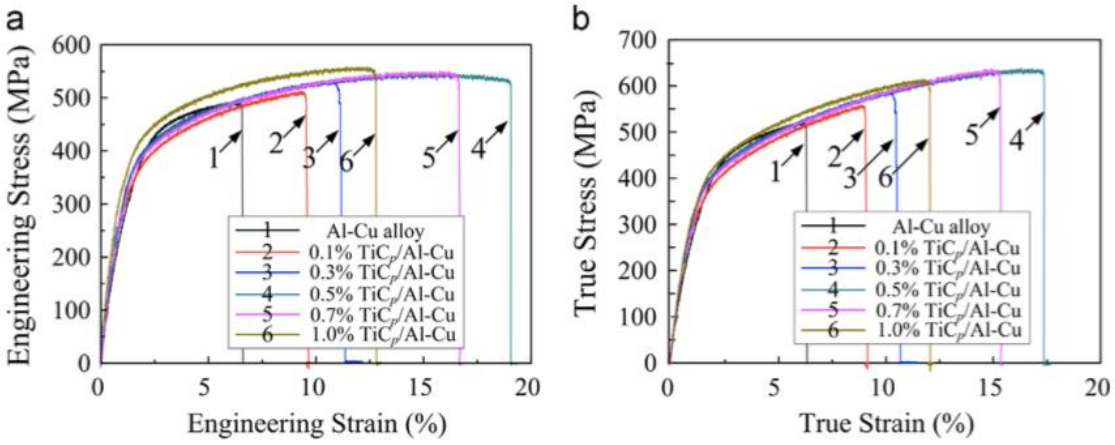

Figure 2-6 Engineering stress-strain curve for Al-Cu alloy with or without TiC nanoparticles[23]

In the Al-Zn-Mg-Cu system, the overall performance of TiN nanoparticle reinforced alloy also exceeds the one without nanoparticles[8]. Compared with the alloy with only Ti or without any refiner, the TiN nanoparticle addition improves the solution of the alloying elements, retains the fine grains of the Al-Zn-Mg-Cu alloy during the solid solution process, and enhances the Vickers hardness of the solution treated alloy. During the aging process, the TiN nanoparticles accelerate the evolution of the GP zones from the supersaturated solid solution but inhibit the precipitations of the η' phase and η phase. The DSC results show that the stability of GP zones was increased by TiN nanoparticles, which inhibits the further evolution of GP zones to the η' phase. Furthermore, the PFZ is narrowed by adding TiN nanoparticles, as shown in Figure 2-7. The PFZ zone was reduced from 70nm to 30nm because more GP zones were formed near the grain boundary when TiN existed.

`

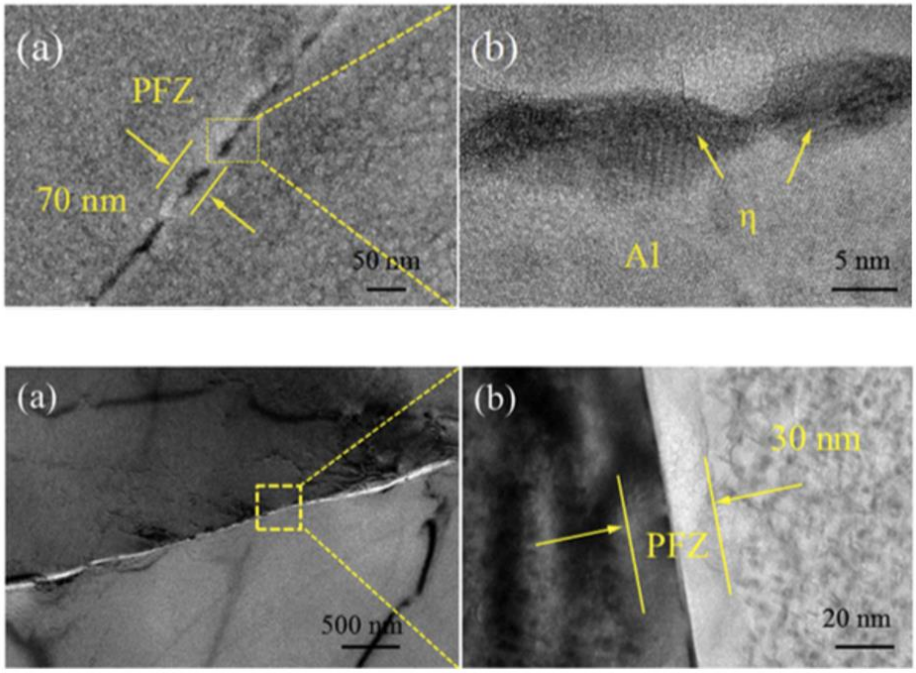

Figure 2-7 HRTEM pictures of PFZ zones in Al-Zn-Mg-Cu alloy (top)without or (bottom)with TiN nanoparticles[8]

2.1.5 Nanoparticles modified solidification behavior

Nano-treated alloys show a modified solidification behavior. Cao et al. discovered the nanoparticles could effectively control nucleation and grain growth due to a continuous nucleation mechanism shown in Figure 2-8[24]. Ultra-fine grained/nanocrystalline Cu-WC, Al-TiB_2, and Zn-WC nanocomposites were cast at a slow cooling rate. They suggest that the conventional growth restriction factor Q in Equation 2-5[25] can be increased to infinite and refine grains down to the interparticle spacing limit under slow cooling.

$$d = a + \frac{b}{Q} \tag{2-5}$$

Here d is the grain size; a is a constant indicating the interparticle spacing, and b is a constant related to nucleation. The restriction factor was improved due to continuous heterogeneous

`

nucleation and growth restriction in the nano-treated metal. The nucleation event was stopped in pure metal by increased temperature due to latent heat released during solidification.

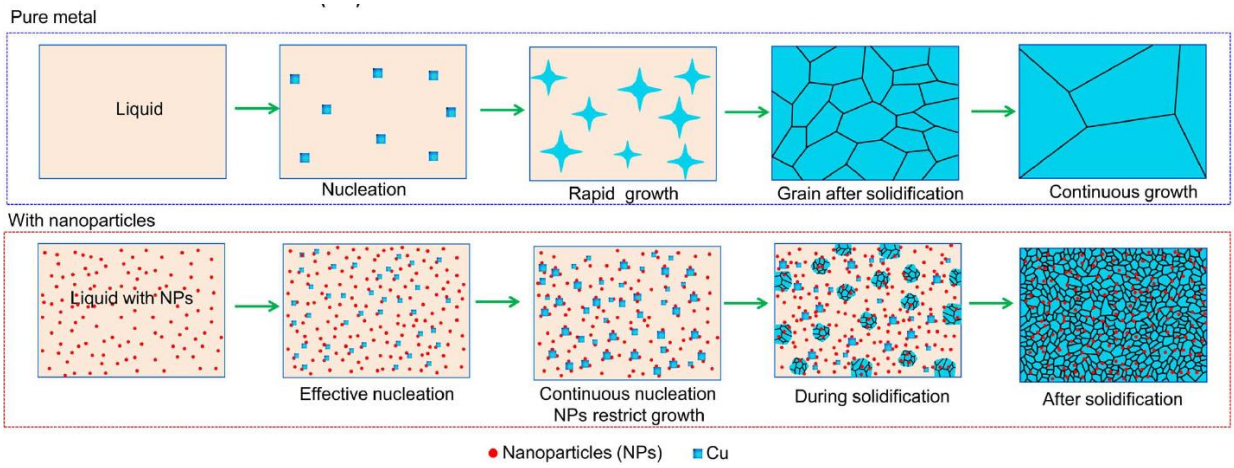

Figure 2-8. Schematic illustrations of phase evolution during solidification of pure metal and metal with nanoparticles [24]

2.1.6 Strengthening effect of nanoparticles

The strengthening effect by nanoparticles in the matrix is similar to precipitates and inclusions in the matrix, but ceramic nanoparticles have higher hardness and stiffness. Meanwhile, nano-treating induced grain refinements also strengthen the alloy. The strengthening effects are summarized below.

(1) Orowan strengthening

Orowan strengthening is effective for nano-treated alloys. This is because hard non-shearable ceramic nanoparticles would impede the movement of the dislocations in the grain, and during plastic deformation, the dislocations will be bowed around the particles called Orowan loops[26]. The Orowan strengthening can be determined by the Orowan-Ashby equation:

$$\Delta\sigma_{Orowan} = \frac{0.13G_m b}{d_p[\left(\frac{1}{2V_p}\right)^{\frac{1}{3}}-1]} ln\frac{d_p}{2b} \quad (2\text{-}6)$$

where G_m, b, V_p and d_p are the shear modulus of the matrix, the Burger vector, the volume fraction, and the diameter of the nanoparticles, respectively. However, this strengthening effect highly depends on the distribution of the nanoparticles. For nanoparticles distribute uniformly inside grains, the Orowan strengthening is significant with only a small volume fraction of nanoparticles, but the strengthening would be weaker if nanoparticles locate at grain boundaries.

(2) Hall-Petch strengthening

Because nanoparticles significantly reduce grain size, strengthening from grain boundaries is significant. Because of an orientation difference in two grains, dislocation movement from one grain to another can be impeded by grain boundaries. Therefore, grain boundaries are practical strengthening elements. The Hall-Petch equation is used to describe the extra stress induced by grain refinement[26].

$$\Delta\sigma_{H-P} = k_y(d_m^{-\frac{1}{2}} - d_c^{-\frac{1}{2}}) \quad (2\text{-}6)$$

Here, $\Delta\sigma_{H-P}$ is the extra strength, k_y is the strengthening coefficient, d_m is average grain size in the monolithic sample, d_c is average grain size in the nanocomposite sample.

(3) Load bearing strengthening

When hard reinforcements are added into the matrix, the load-bearing transfer from the soft matrix to stiff and hard reinforcements under external force will strengthen the base material[27]. The strengthening from particulate reinforcements can be expressed as the following equation

`

$$\Delta\sigma_{Load} = 1.5V_p\sigma_i \quad (2\text{-}7)$$

Here $\Delta\sigma_{Load}$ is the increased yield strength, V_p is the volume fraction of particulate reinforcements, σ_i is the interfacial strength of the matrix material. The load-transfer effect depends on the interfacial bonding strength. Therefore, a stronger interface bonding will be more effective in transferring load from the matrix to hard reinforcements.

(4) CTE mismatch

The mismatch in coefficient of thermal expansion (CTE) between the reinforcements and the metal matrix will result in geometrically necessary dislocations (GNDs)[28]. The extra dislocations density due to CTE mismatch will strengthen the metal by

$$\Delta\sigma_{CTE} = \sqrt{3}\beta Gb\sqrt{\frac{12\Delta\alpha\Delta T V_p}{\boldsymbol{b}d_p}} \quad (2\text{-}8)$$

where $\Delta\sigma_{CTE}$ is the extra strength, G is the shear modulus, β is a constant, $\Delta\alpha$ is the CTE difference between hard particles and matrix, ΔT is the temperature difference between test and processing. However, the number of dislocations generated by nanoparticles is less than macroparticles, making the CTE mismatch strengthening less significant.

2.1.7 Other effects.

Nanoparticles induced solute segregation

Solute segregation at the particle/matrix interface was observed. When the solute atom has high binding energy with the ceramic particle or reacts with the ceramic particle, the solute atoms tend to segregate at the particle/matrix interface. For example, Mg segregates at the Al/B_4C interfaces as presented in Figure 2-9[29].

`

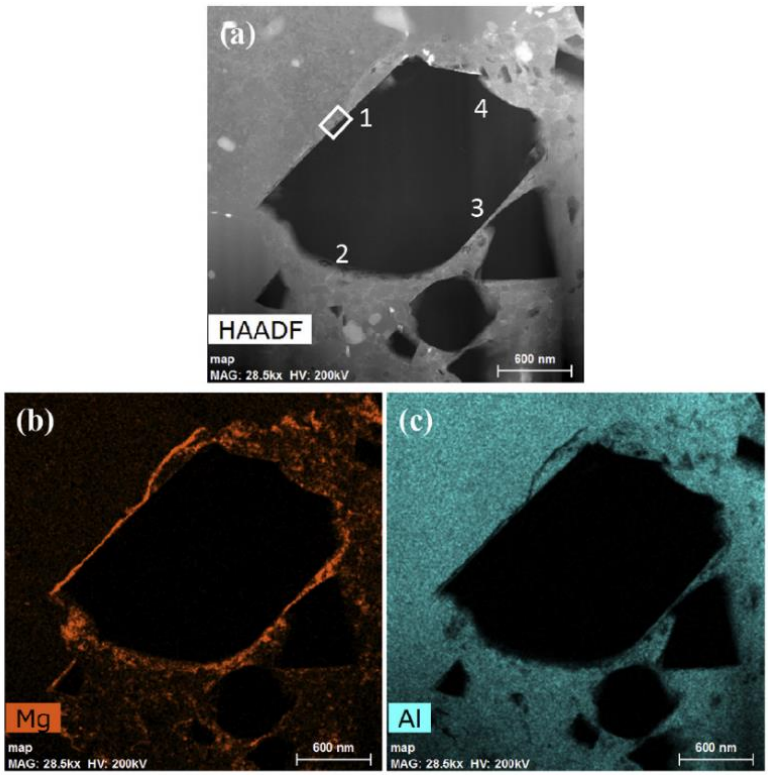

Figure 2-9 (a) High-angle annular dark-field STEM image showing a B4C particle; EDXS maps illustrate the distribution of (b) Mg, (c) Al, within the composite[29]

Nanoparticle influence on phase transformation

Usually, nanoparticles do not change the thermodynamics of the alloy system. For example, the precipitation sequence of an Al-Zn-Mg-Cu alloy will not be altered by nanoparticles[30]. However, there are certain cases nanoparticles can change the phase transformation behavior. One specific example is presented in Figure 2-10[31]. Grain boundaries perovskite materials will induce phase transformation because grain boundaries are at a high-energy state. Nanoparticles at grain boundaries can inhibit heterogeneous nucleation of $Ba_{0.5}Sr_{0.5}Co_{0.8}Fe_{0.2}O_{3-\delta}$. in a fuel cell cathode by blocking the metal ion diffusion along grain boundaries.

`

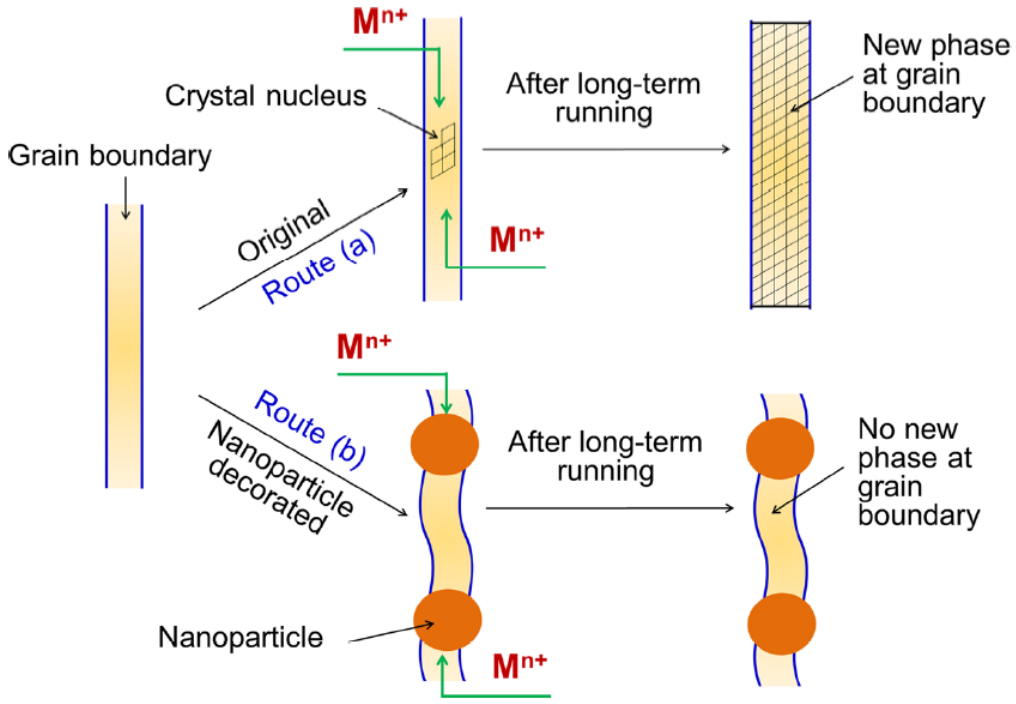

Figure 2-10. Schematic of the nanoparticles' inhibition of phase transformation at grain boundaries. (Route a) Metal ions diffuse easily along the grain boundary and form a nucleus, and then the nucleus grows to the trigonal phase at the grain boundary after long-term operation at low temperature. (Route b) Nanoparticles located at the grain boundary, leading to a zigzag structure; the nanoparticles block the diffusion of metal ions along the grain boundary and inhibit the nucleation and growth of the trigonal phase at the grain boundary even after long-term operation at low temperature[31]

`

2.2 Incorporation of nanoparticles into molten metals

Nanoparticles can be added to the metal by ex-situ methods or in situ exothermal reactions. Conventionally, it is believed that after incorporation, due to the large surface-to-volume ratio, nanoparticles tend to agglomerate to reduce the overall surface energy in the metal. Their surface dominant characteristics make them more reactive inside the matrix. Fortunately, in 2015, the self-stabilization mechanism was discovered by Chen et al. and the foundation for nanocomposites application was then built[32]. Inert ceramic nanoparticles are usually chosen to prevent chemical reaction with metal matrix.

2.2.1 Ex-situ incorporation

Typically powder metallurgy, deformation processing, vapor phase processing, and solidification processing are used to process nanoparticle enforced metal/alloy. Among these processing methods, the least expensive production method is solidification processing. There are various avenues by which researchers have created nanostructures and nanocomposites materials using solidification. The solidification methods can be divided into three categories: rapid solidification, mixing of nano-size reinforcements in the liquid followed by solidification, and infiltration of liquid into a preform of reinforcement followed by solidification. A typical salt-assisted incorporation schematic illustration is shown in Figure 2-11[33]. In this experiment, Mg is melt first and then the mixture of magnesium chloride flux and TiC nanoparticles was laid on the top of the molten metal. The flux could help to dissolve the oxide layer at the nanoparticle surface and facilitate the incorporation of nanoparticles.

`

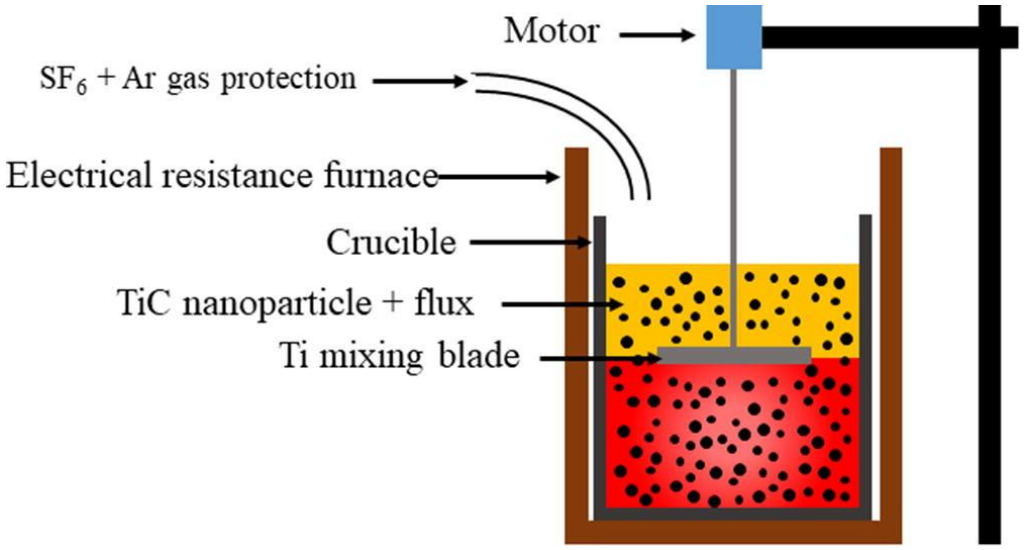

Figure 2-11. Salt assist incorporation of TiC nanoparticles into Mg[33]

2.2.2 In-situ incorporation

In situ incorporation is to synthesize and incorporate nanoparticles in molten metals simultaneously. The in situ method is relatively inexpensive as nanoparticles are expansive reinforcement material. On the other hand, the conventional ex-situ method normally needs to overcome poor wettability between the reinforcements and the matrix due to surface contamination of the reinforcements. The in situ nanoparticles exhibit the following advantages: (a) the in situ nanoparticles are thermodynamically more stable at the matrix; (b) the interfaces between nanoparticles and matrix are clean, resulting in a strong interfacial bonding; (c) the in situ formed nanoparticles can be finer in size and their distribution in the matrix more uniform, yielding better mechanical properties[34]. The commonly used reaction process can be classified into four categories. (a) solid-liquid reaction; (b) vapor-liquid-solid reaction; (c) solid-solid reaction, and (d) liquid-liquid reaction. Direct reaction synthesis (DRS)[35–44,44–48], flux assisted synthesis (FAS)[21,49–69], self-propagating high-temperature synthesis (SHS)[70–72], exothermic dispersion (XD)[73,74], reactive hot

`

pressing (RHP)[74,75], reactive spontaneous infiltration (RSI)[76], mechanical alloying (MA)[77–80], vapor-liquid-solid reaction processing (VLS)[81–84], selective laser melting (SLM)[85], hot isostatic pressing (HIP)[86], laser-induced reaction (LIR)[87], spark plasma sintering (SPS)[88], laser cladding (LC)[89], and plasma transferred arc (PTA)[90,91], etc. have been applied for in-situ fabrication. Here we will focus on flux-assisted synthesis (FAS) as it is one of the popular liquid-liquid reactions.

The flux-assisted synthesis is first developed by the London Scandinavian Metallurgical Company to produce aluminum matrix composites, as shown in Figure 2-18[34]. The mixture of salts provides the source of titanium and boron for the synthesis of TiB_2. Aluminum could reduce the Ti and B from the salt, and the following exothermal reaction would take place.

$$3K_2TiF_6 + 13Al = 3TiAl_3 + 3KAlF_4 + K_3AlF_6 \quad (2\text{-}9)$$

$$2KBF_4 + 3Al = AlB_2 + 2KAlF_4 \quad (2\text{-}10)$$

$$AlB_2 + TiAl_3 = TiB_2 + 4Al \quad (2\text{-}11)$$

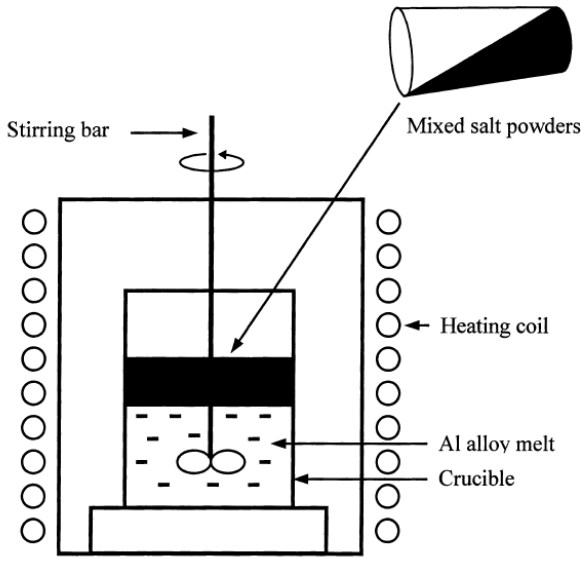

Figure 2-12 Schematic diagram of an apparatus for fabricating in situ metal matrix composites by means of FAS[34]

`

A disadvantage of this method is the poor control of the particle size distribution. Most in situ methods would only be able to produce microparticles[57]. When the particles are synthesized in low-temperature systems, templates or surfactants could be used to control the growth of the particle. However, in high-temperature systems, nanoparticle growth control becomes difficult. It is also challenging to produce a high loading ratio (e.g.,>5vol%) using the mixed salt system due to high viscosity. Tang et al. synthesized in situ nano-sized TiB_2 in Al by an improved method. The fabricated nanocomposite is shown in Figure 2-13[51]. The size control is done by slowly adding the salt mixture on top of the Al melt so that the growth rate of the nanoparticles is controlled by the concentration of Ti and B in the salt. However, from the SEM and TEM pictures, there are still lots of particles larger than 100nm, and a high loading ratio is not achieved.

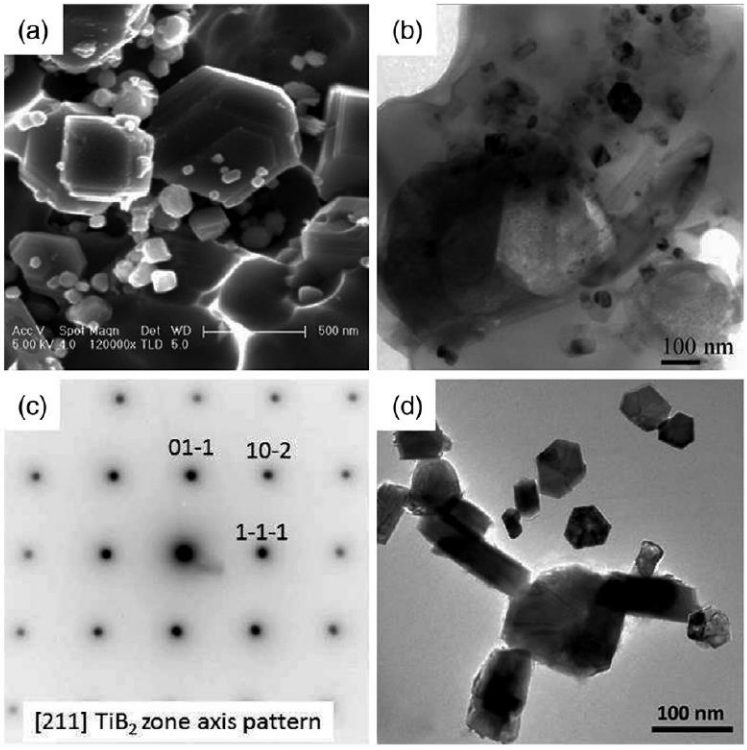

Figure 2-13 (a) SEM secondary-electron and (b) TEM bright-field images of the as-cast Al–TiB_2 composite (c) [211] ZAP from a nanosized particle corresponding to the TiB_2 phase and (d) TEM bright-field image of the free-standing TiB_2 particles [51]

`

2.2.3 Size control of in-situ synthesized nanoparticles

With a constant volume fraction, smaller particles will result in smaller interparticle spacing to achieve higher strength, better ductility, and improved fatigue resistance[92,93]. The size of the ex-situ nanoparticles depends on the original size of the nanoparticles before being added to the metal matrix. However, during in situ synthesis, as nanoparticles nucleate and grow in the melt, it is difficult to control the particle size and size distribution in the molten metal since these reactions usually take place at temperatures above the melting point of the base metal, and there is a lack of effective measures, such as templates[94,95]. Therefore, in-situ particles grow rapidly after nucleation if there are sufficient reactants, forming relatively large particles. Ostwald ripening also induces a continuous growth of particles after the reaction to minimize the overall surface energy[96]. Therefore, particles synthesized in molten metal are rarely nano-sized.

Theoretically, the size of the particles can be controlled by either restricting growth speed or growth time. There are some methods to fabricate nano-sized particles in molten metal. Rapid solidification processing (RSP) provides one costly solution to reduce growth time by rapidly solidifying the reaction liquid. For example, TiB_2 nanoparticles of 40-80 nm were obtained by RSP[97]. Figure 2-14 shows that Cu-B and Cu-Ti melts were injected into a faster-cooled copper mold to fabricated nano TiB_2 nanoparticles. In addition, flux-assisted synthesis (FAS) has the capability of producing nano-sized TiB_2. Very fine TiB_2 nanoparticles were synthesized by the exothermic reaction between molten aluminum, KBF_4, and K_2TiF_6[18,51,58]. The fluoride salts will be reduced by aluminum and releasing boron and titanium into the aluminum melt. TiB_2 particles will nucleate and grow in the molten aluminum. Ju et al. have achieved an average size below 100nm[18]. However, there is still a significant amount of micro/submicron-particles synthesized

`

together with nano-sized particles due to a lack of growth control. Ultrasonication could further reduce the average size by increasing nucleation through acoustic cavitation[98], but, as stated before, the ultrasonic-assisted reaction is limited to a lab scale. Growth control of particles at high temperatures is still difficult.

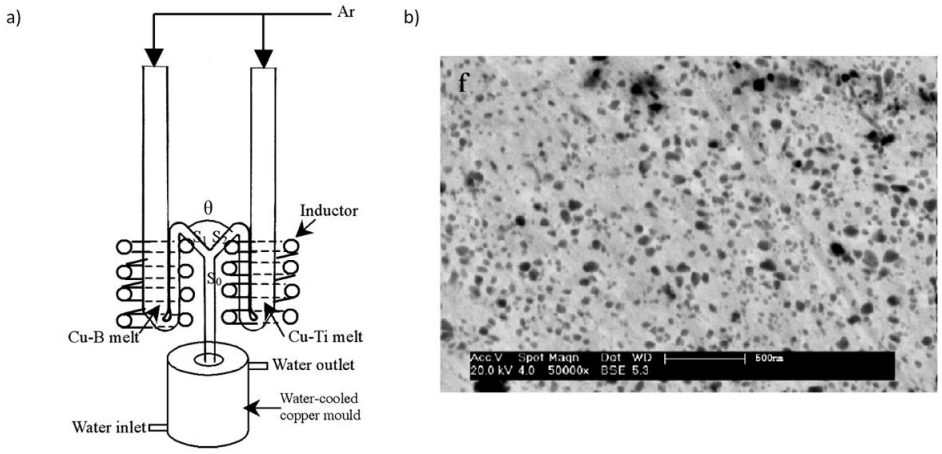

Figure 2-14. a) Schematic diagram of in situ reaction for double-beam melts. B) SEM of in-situ TiB_2 particles in copper fabricated by double-beam melts[97]

2.2.4 Dispersion of nanoparticles in molten metal

The nanoparticles in the metal matrix tend to form clusters due to their high surface energy. A thermally-activated nanoparticle self-dispersion and stabilization mechanism in molten metals was published in Nature[32]. In molten metal, three types of energies influence the dispersion of the nanoparticles. They are interfacial energy (short-range), van der Waals potential (long-range), Brownian motion energy (thermal energy). The interfacial energy creates an energy barrier between nanoparticles and stops nanoparticles from sintering. The van der waals force between the same substance is attractive and brings nanoparticles close to each other. The thermal energy helps nanoparticles escape the van der waals attraction.

`

As shown in Figure 2-15, The Van der Waals attractions between two nanoparticles can be calculated by Equation (2-12)

$$W_{vdw} = -\frac{\left(\sqrt{A_{NP}}-\sqrt{A_{liquid}}\right)^2}{6}\frac{R}{D} \quad (2\text{-}12)$$

where *D* is the distance between nanoparticles, *A* is the Hamaker constant, *R* is the nanoparticle radius. The equation is only effective when D is larger than two atomic layers of molten metal. As shown in Equation (2-12), W_{vdw} decreases when the difference between the Hamaker constants of the nanoparticle and the molten metal. Smaller particle size also reduces the attraction.

The thermal energy for Brownian motion is shown in Equation (2-13)

$$E_b = kT \quad (2\text{-}13),$$

where *k* is the Boltzmann constant, *T* is the absolute temperature. The thermal energy is proportional to temperature. Therefore high temperatures help nanoparticles escape the energy valley in Figure 2-15.

When two nanoparticles get closer to each other, the liquid metal atoms will be pushed out between them. This effect produces an energy barrier, and this energy can be written in the following equation:

$$W_{barrier} = S\left(\sigma_{NP} - \sigma_{NP-liquid}\right) = S\sigma_{liquid}\cos\theta \quad (2\text{-}14)$$

where *S* is the effective area, σ_{NP} is the surface energy of the nanoparticles, $\sigma_{NP-liquid}$ is the interfacial energy between the nanoparticle and molten metal, θ is the contact angle molten metal on the nanoparticle surface. Because the energy barrier prevents nanoparticles from sintering, a

`

higher energy barrier is preferred. From this equation, a higher energy barrier could be obtained by a smaller wetting angle.

These energies are the theoretical foundation for nanoparticles self dispersion in molten metal.

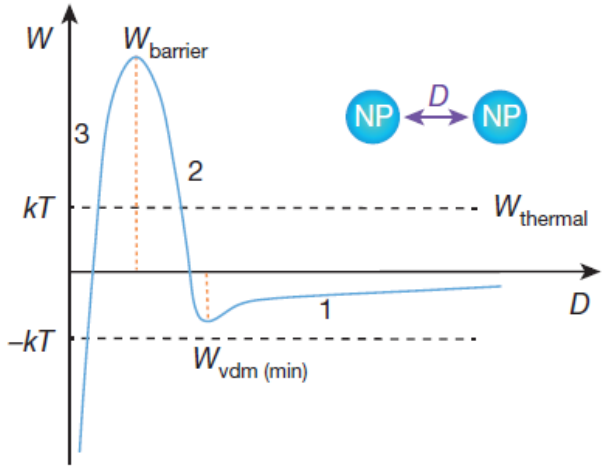

Figure 2-15. The principle of self-dispersion and stabilization of nanoparticles in molten metals [32]

2.3 Al-Zn-Mg-Cu alloys

2.3.1 Basics on Al-Zn-Mg-Cu alloy

Aluminum is one of the most abundant elements on earth, and its alloys have a history of more than 170 years. It is also one of the most widely used non-ferrous alloy. According to Statista, global aluminum consumption is projected to 64.2 million metric tons in 2021[99]. It is a basic structural material for aerospace and automobile applications. For example, the aluminum alloy takes up more than half of the total materials in Boeing 777 and 20% in the most advanced Boeing 787 airplanes shown in Figure 2-16[100]. The alloy and temper systems for aluminum are named and documented in *Aluminum Standards and Data* and *ANSI H35.1*[2]. Among different aluminum

`

alloys, the 7xxx series (Al-Zn-Mg-Cu alloy) exhibit the highest mechanical strength. The 7xxx series alloys are heat treatable alloy containing zinc as the main alloy element, magnesium, and copper. By quenching after solutionizing at elevated temperature, zinc, magnesium, and copper can be in supersaturated solid solutions. Uniformly distributed, nano-sized $MgZn_2$ precipitates will form to strengthen the alloy during aging. These lightweight, strong alloys are relatively inexpensive. Comparing to other structure materials, these alloys are among the most easily fabricated with supreme performance. They are intensively used in conventional aerospace applications. For instance, 7050 alloys are used for internal fuselage structures, while 7150, 7055, and 7055 alloys are used for upper wing covers[101]. The typical microstructure of 7xxx series alloy is shown in Figure 2-17 with refined grain structures by Ti[102]. The black phase is the eutectic phase of $MgZn_2$ and Al.

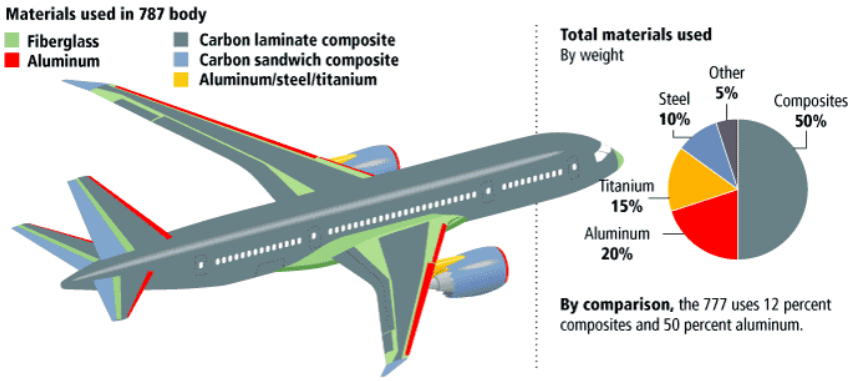

Figure 2-16 Materials used in Boeing 787 body[100]

`

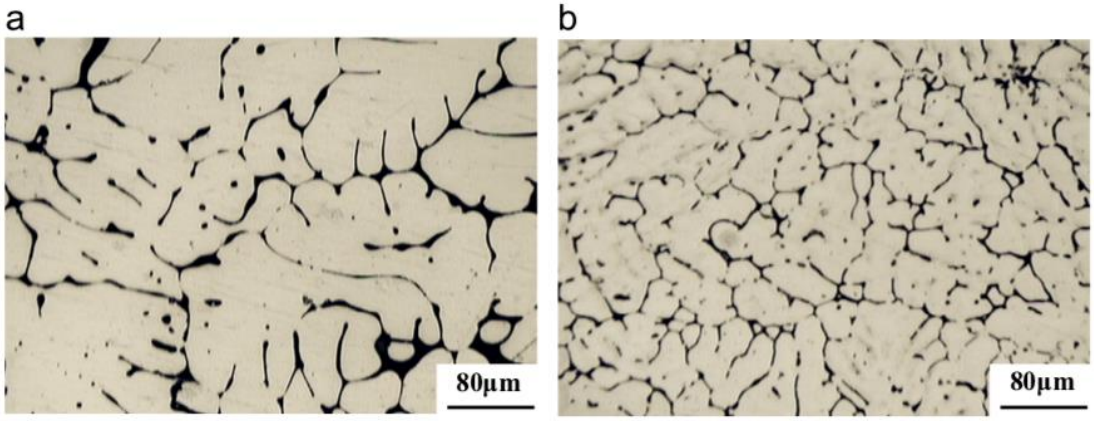

Figure 2-17 Optical image of 7050 alloys. a)no grain refinement, b)refined by Ti [102]

2.3.2 Solution/Aging mechanism

As shown in Figure 2-18, the precipitation sequence of typical Al-Zn-Mg-Cu alloys is well studied in the past decades. The cast ingot is first solutionized at a temperature around 460-470°C. It is directly followed by water quenching to form a supersaturated solid solution (SSSS). During or immediately after quenching, clusters of vacancies will form to facilitate Guinier-Preston (GP) zones formation during aging. In detail, GP zones form at the early stage of precipitation. As the aging time goes longer, GP zones grow into the η' phase which is the precursor for the η phase ($MgZn_2$). The typical temperature vs. time diagram is shown in Figure 2-19.

Figure 2-18 schematic sequence of the precipitation in 7xxx series alloy[103]

`

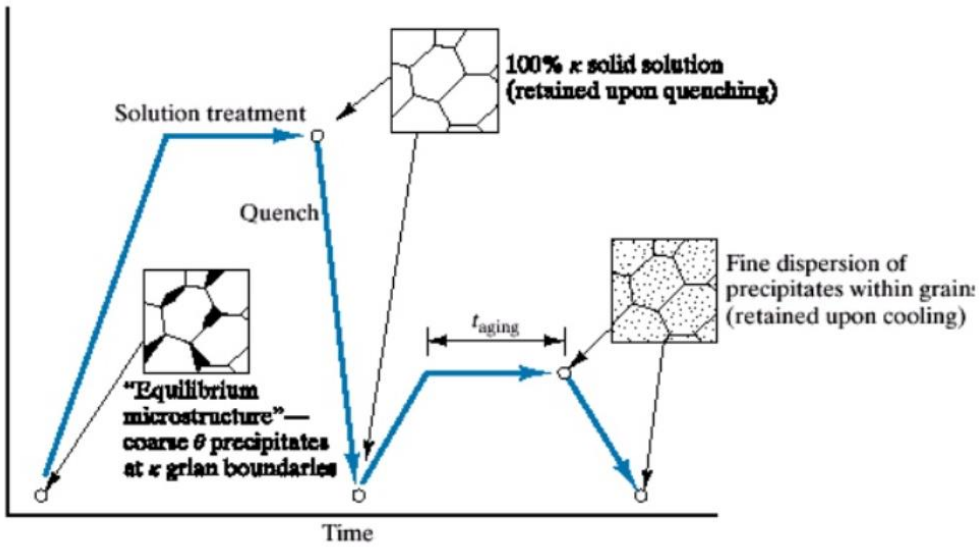

Figure 2-19 Typical precipitation hardening process

The 7xxx series alloys are among those most heavily alloyed. Four major secondary phases possibly exist during solidification, namely η($MgZn_2$), T($Al_2Mg_3Zn_3$), S(Al_2CuMg), and θ(Al_2Cu) phases[104]. A typical SEM picture of the as-cast 7xxx alloy is shown in Figure 2-20. The white phase in A is η($MgZn_2$), whereas the darker one in B is some Fe-rich impurity phase. The light grey in C shows θ(Al_2Cu) and the darker phases of E and F demonstrate S(Al_2CuMg) phase.

`

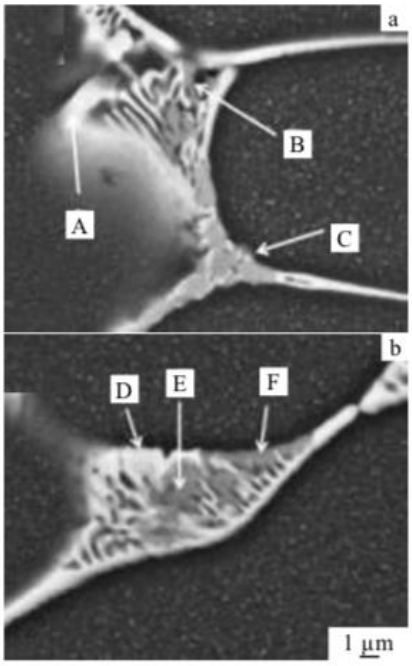

Figure 2-20 SEM picture of as-cast 7xxx alloy[105]

The temperature used for solutionizing is usually around 470°C but no higher than the melting temperature for these constituent phases (475-500°C[106,107]). When the alloy is overheated, voids will be left at the location where these secondary phases locate. They will become crack nucleation and propagation sites, thus deteriorating the mechanical performance[108]. However, except for the η phase, T, S, and other impurity phases dissolve slowly at conventional solution temperatures. Undissolved particles will reduce the performance of the alloy due to fewer fine precipitates and increase crack initiation and propagation[109]. Xu et al. [108,110] tried step solution treatment to dissolve these different phases one by one to avoid overheating. Less fraction of particles was left, as shown in Figure 2-21.

`

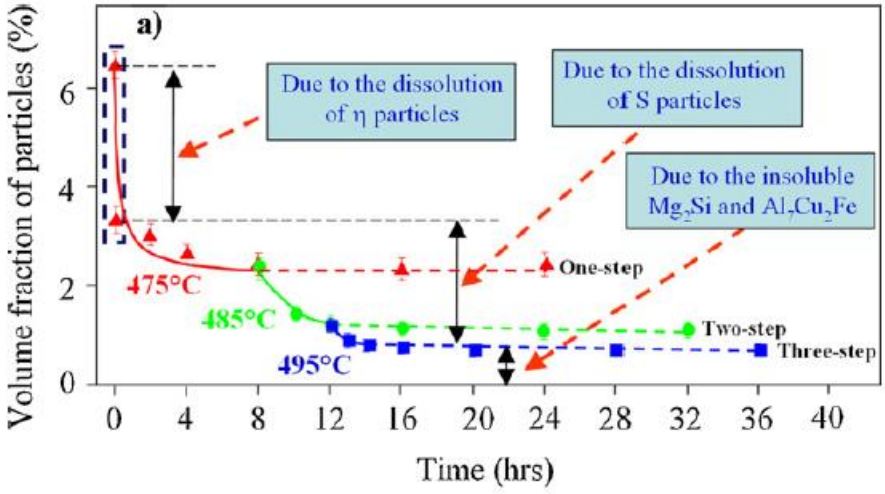

Figure 2-21 Dissolution process of secondary particles in AA7175 alloy

After solution treatment and quenching to obtain the SSSS, aging is utilized to produce fine and uniformly distributed precipitates. When SSSS forms, there will be supersaturated vacancies inside the matrix. These vacancies also agglomerate and form clusters with other alloying elements. When the temperature is raised for aging, these clusters develop into some GPI and GPII zones. The GPI zones are coherent with matrices, and the GPII zone are zinc-rich layers on {111} planes. Both GP zones are precursors of η' phase[18], as shown in Figure 2-22e. Different aging parameters will lead to different microstructures and sizes of the precipitates. Therefore, aging conditions generate alloys with different performances[112]. Generally, higher temperatures will have faster evolution for the precipitates. When aged at 95°C, the Zn vacancy cluster could be retained for quite a long time. However, these vacancy clusters diminish within 30min[113]. GPI and GPII zones will be observed after aging at 100 °C for 1.5-2 hours and, after 7 hours, the η' phase will form. If the alloy remains at 150 °C for 6 hours, η nucleates on η' phase[114]. Grain boundary could serve as a sink of vacancies. Therefore, precipitate free zones (PFZ) will form near the grain boundaries. As shown in Figure 2-22a, a typical PFZ with around 70nm width exists. A higher

`

concentration of solutes at grain boundary would produce larger precipitates[8]. Along grain boundaries, large η can be seen in Figure 2-22b.

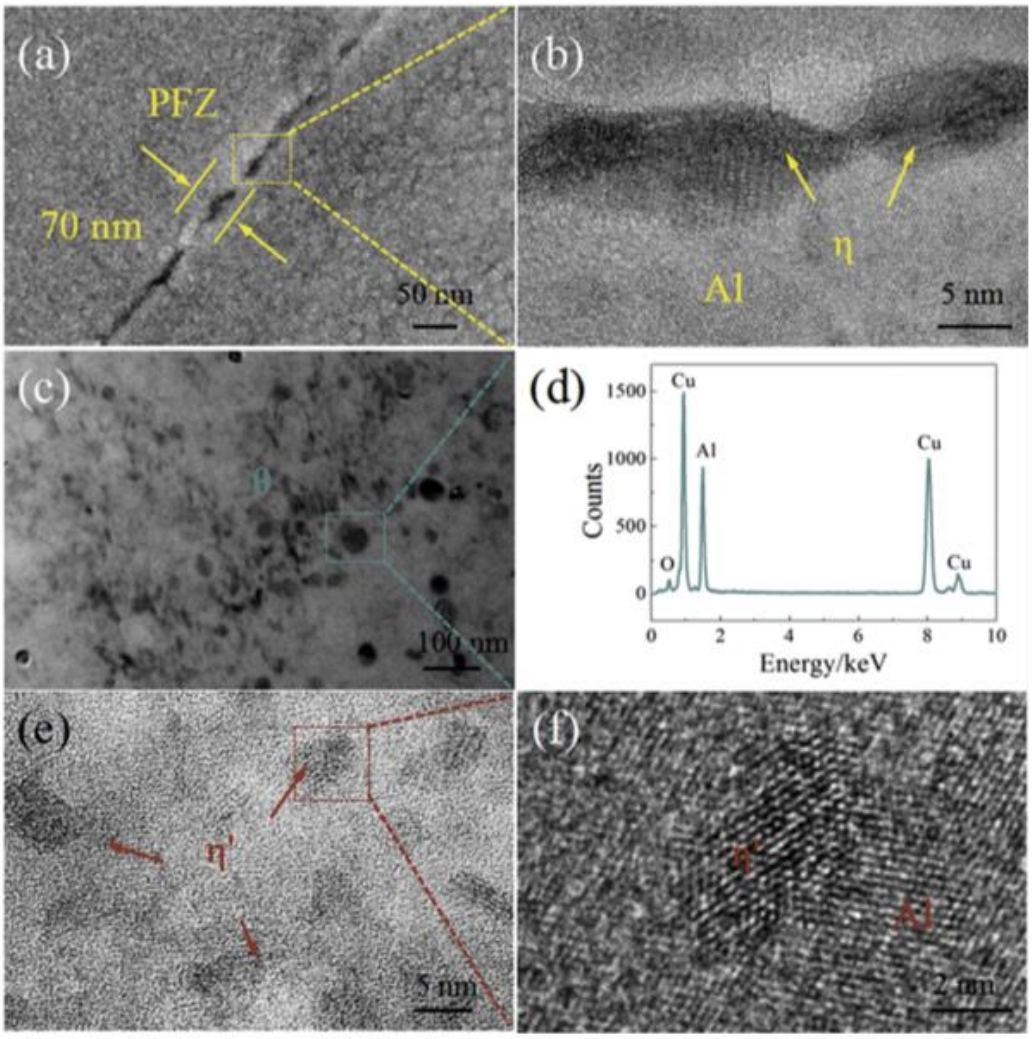

Figure 2-22. TEM images of the structure of (a)PFZ zones, (b) η phase on grain boundary; (c-d) The θ phases and its EDS analysis; (e-f) The HRTEM images of the η' phase [18]

The properties of the alloys are directly related to their microstructures, which could be tuned by different solutions and aging treatments. In Figure 2-23, the hardness of a high zinc 7xxx series alloy changes with aging time at 120 ^{o}C. The hardness increases dramatically at the initial 4h due to the strengthening from GP zones formation. Later on, the hardness dropped a little and increased again until 20h due to η' precipitate formation and growth. The hardness decreased again

`

as the precipitates further grew larger[115]. Different types of aging treatments are invented for the 7xxx series to control the size and distribution of precipitates. For example, T6 heat treatment is single stage aging that results in higher strength but less corrosion resistance as it produces smaller precipitates. T7X is two-stage aging used for higher fracture toughness and stress corrosion resistance[112].

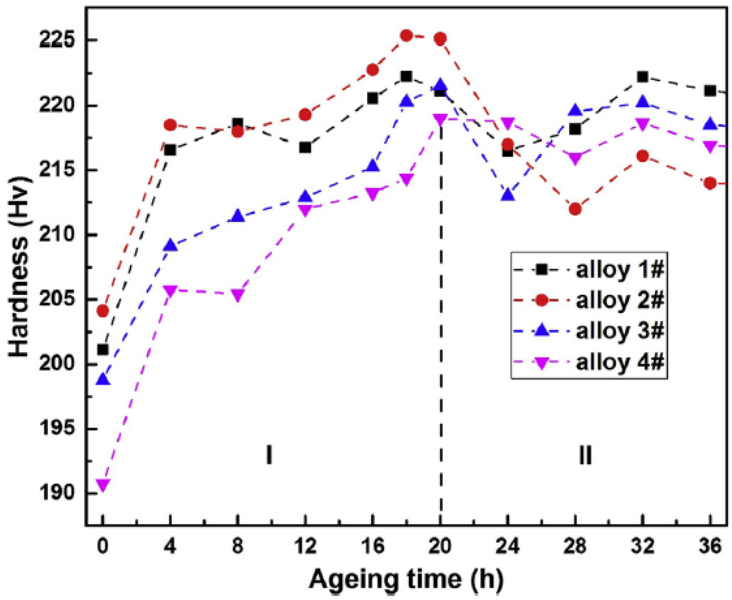

Figure 2-23 Relationship between hardness and aging time of 4 solution-treated high zinc 7xxx alloy [115]

2.3.3 High-zinc Al-Zn-Mg-Cu alloy

In the 7xxx series alloy, Zn and Mg are the main strengthening elements. High-zinc aluminum alloy usually exhibits high strength and high hardness together with higher sensitivity to different types of corrosion (SCC, intergranular corrosion, and exfoliating corrosion) due to residual T phase upon solutionizing. Meanwhile, the elongation and fracture toughness also decrease[116]. The (Zn + Cu) to Mg ratio is believed to strongly affect the residual Mg because the Cu and Al could dissolve in the precipitates to form $Mg(Zn, Al, Cu)_2$[117]. When the (Zn + Cu) to

`

Mg ratio is greater than 2, there will be remaining Mg in the alloy and vice versa. The final properties would be affected by the composition variation, and the heat treatment applied.

In 7055 alloy, the zinc content already exceeds 8 wt.%, and in 7A60 alloy, Zn content approaches 9 wt.%. Other high zinc alloys are 7150, 7050, 7085, 7449, 7136, 7056, etc. The yield strength could increase 100MPa when the Zn content increased from 5.59wt% to 7.84wt%. However, the ductility drops as the Zn content increases since the volume fraction of the coarse eutectic phase increases as well.

The thermodynamic calculation of high zinc alloy was performed by the Calculation of Phase Diagram (CALPHAD) method by Liu et al. Different contents of Zn, Mg, and Cu determine the formation of η, T, S phase. The polythermal section is shown in Figure 2-24[118]. The phase diagram represents three different Zn contents in three different colors. The blue one has 8.8% Zn. The black one contains 9.2% Zn, and the red dot line represents 9.6% of Zn. The important regions are 5(α(Al) + η($MgZn_2$) + θ(Al_2Cu)), 11(α(Al) + η($MgZn_2$) + θ(Al_2Cu) + S(Al_2CuMg)) and 13(α(Al) + η($MgZn_2$) + S(Al_2CuMg)). θ phase forms in region 5 and S phase precipitates in region 13 while both exist in region 11. The mass fraction of the main strengthening phase η can be obtained in the phase diagram. For example, in the alloy of Al-xZn-1.7Mg-2.3Cu, the mass fraction of η phase increases from 8.8% to 9.6% as Zn content increases from 9.2% to 10.0%.

`

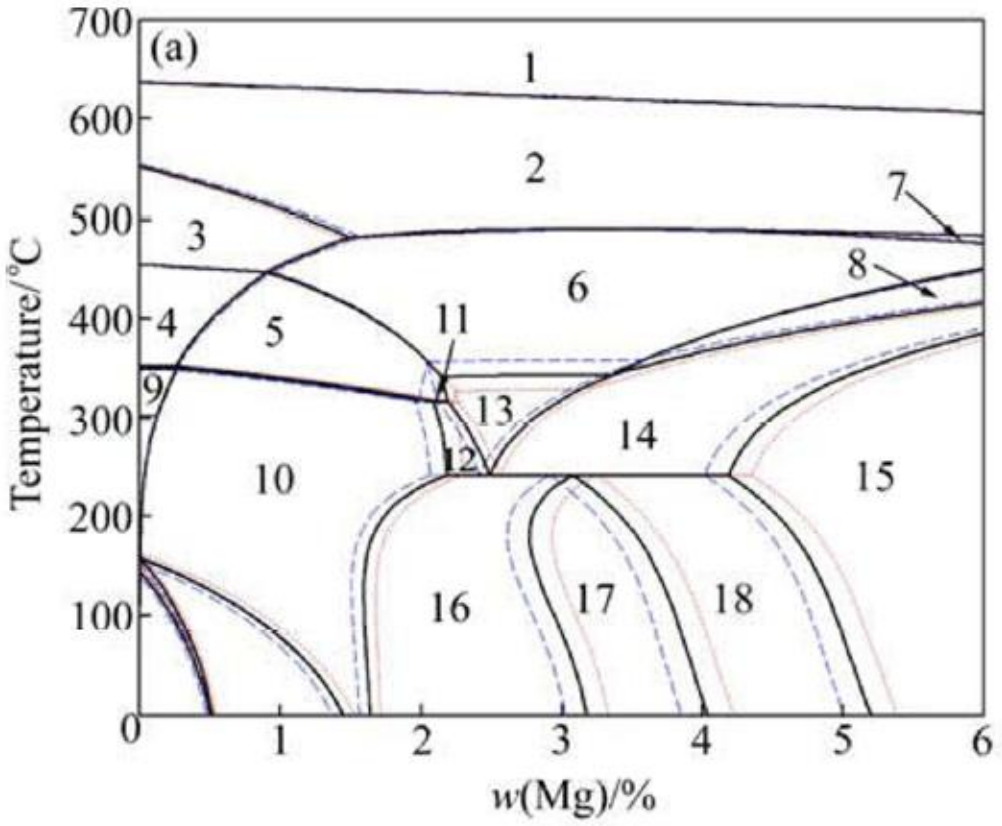

Figure 2-24 Calculation polythermal section of Al−Zn−Mg−Cu phase diagram (blue dash line: 8.8% Zn, 0−6% Mg, 2.3% Cu; black line: 9.2% Zn, 0−6% Mg, 2.3% Cu; red dot line: 9.6% Zn, 0−6% Mg, 2.3% Cu) [118]

Several fundamental studies on the high zinc containing 7xxx alloy have been conducted in very recent years. The aging behavior of the high zinc alloys is one of the focuses. Liu et al. applied a heating aging treatment(HAT) in that the aging is performed with a continuously rising aging temperature[119]. They aged the alloy from 100ºC to 180ºC with different heating rates. The process follows the same precipitation sequence but provides higher tensile, yield, and conductivity than conventional T6 treatment. Wen et al. approved that the tensile strength decreases as the precipitation size distribution increases and the distance between neighbor precipitates increases when the aging deepens, as shown in Figure 2-25[112]. In the figure, T7 tempers are two-step aging with second aging at 160ºC. T79 has the shortest second step aging

`

time, while T73 has the longest. Later they also discovered that, with higher zinc content, the strength would decrease slower after peak aged, and the resistance to fatigue crack propagation is also higher as more large sharable precipitates(<5nm) are formed in the matrix[120]. After conventional heat treatment, the ultimate tensile strength of high zinc 7xxx alloy could reach 700MPa[121]. The higher cooling rate during casting, such as spay-deposition, can further improve the strength to 800MPa[115].

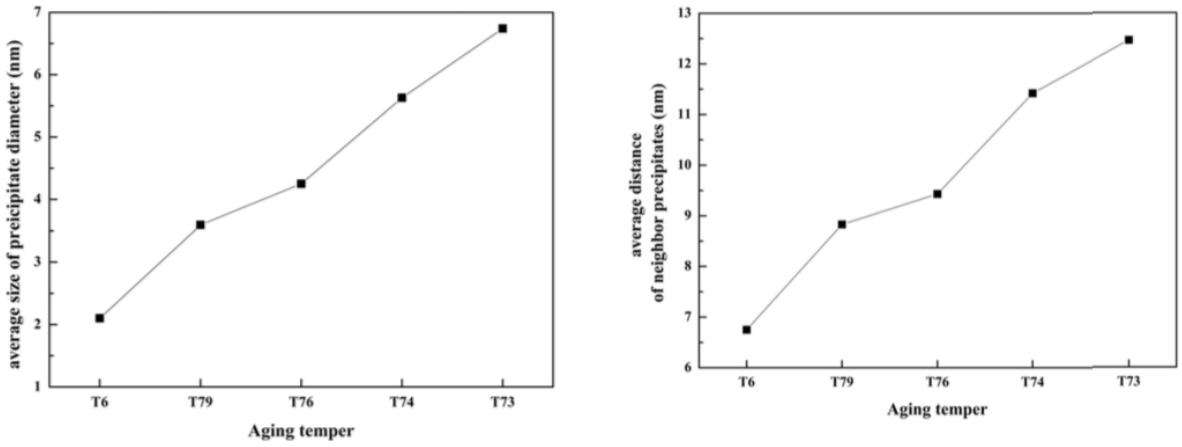

Figure 2-25 average precipitation size and the average distance between precipitates of different tempers [112]

It is possible to achieve better performance of Al-Zn-Mg-Cu alloy by adding a higher alloying content. However, heavy alloying would reach a limit as it is impossible to have infinitely more uniform and small precipitates inside the alloy. Suitable solution treatment becomes more complex and takes more time. They are more sensitive to hot tearing as well. The casted 7xxx alloy is generally considered to be unweldable by arc welding. Either the elements (Zn, Mg, Cu) in the as-casted alloy will cause liquidation cracking and solidification cracking during welding, or the joint of heat-treated alloy loses a large fraction of strength after welding. One example is AA7034 alloy. It offers the highest tensile strength (~750MPa) among all commercially available

`

aluminum alloys. Its super high strength comes from its high alloy contents, about 11-12% zinc and 2.0-3.0% magnesium. However, its castability suffers as the high alloy content makes the alloy more susceptible to porosity, hot tearing, and inhomogeneity[4]. Moreover, a high alloy content results in severe segregation at grain boundaries with large secondary phases[122,123], making solution treatment more difficult. A higher volume fraction of coarser secondary phase at grain boundaries would need extra time and higher temperature for dissolution during solution treatment[118,124] and, in many cases, resulting in a deteriorated mechanical properties[122,123]. Therefore, the conventional casting of aluminum 7034 alloy is not desirable at a slow cooling rate. The commercial AA7034 alloy is produced by rapid solidification, such as spray casting in that a high cooling rate (10^2 - 10^6 K/s) is utilized to reduce cracks, porosity, and solute segregation[115,125,126]

2.3.4 Current Al-Zn-Mg-Cu composites

The nanoparticle-reinforced Al-Zn-Mg-Cu alloys attracted considerable attention as nanoparticles can potentially further improve their performance. Different types of nanoparticles have been added into the Al-Zn-Mg-Cu system, including TiB_2 and TiN. As mentioned earlier, adding TiN nanoparticles into the Al-Zn-Mg-Cu system would increase the strength and ductility together. Chen et al. fabricated some in-situ TiB_2 (5-10wt.%) reinforced AA7075 alloy, and its bending properties are improved due to dislocation strengthening, Orowan strengthening, and grain boundary strengthening[56]. Ma et al. studied the fatigue behavior of in situ TiB_2/7050 composite[127]. The in-situ TiB_2/7050 composite exhibited a smaller grain size, higher elastic modulus, enhanced yield strength, better ultimate tensile strength, and superior fatigue limit over the unreinforced 7050 alloys. TiB_2 particles impeded dislocations from piling up at the inclusions and delayed the crack initiation there. Thus fatigue property effectively improved in the composite.

`

Ju et al. investigated the friction stir processed Al-Zn-Mg-Cu with nano-sized TiB_2[18]. The distribution of nanoparticles could be improved by friction stirring, and fine grain size could be maintained after T6 heat treatment so that both the strength and ductility of the alloy were improved.

The nanoparticles would cause a problem if not dispersed well. Wang et al. studied the stress corrosion cracking behavior of an extruded in-situ TiB_2 reinforced 7050 alloy[128]. The clustered TiB_2 nanoparticles formed bands along the grain boundaries after extrusion, and these bands sped up the propagation of cracks along the recrystallized grains (intergranular fracture), as shown in Figure 2-26. It facilitates the formation of recrystallized structures while dislocations are piled up near nanoparticles. Also, there is a significant potential difference between the particles bands and matrix.

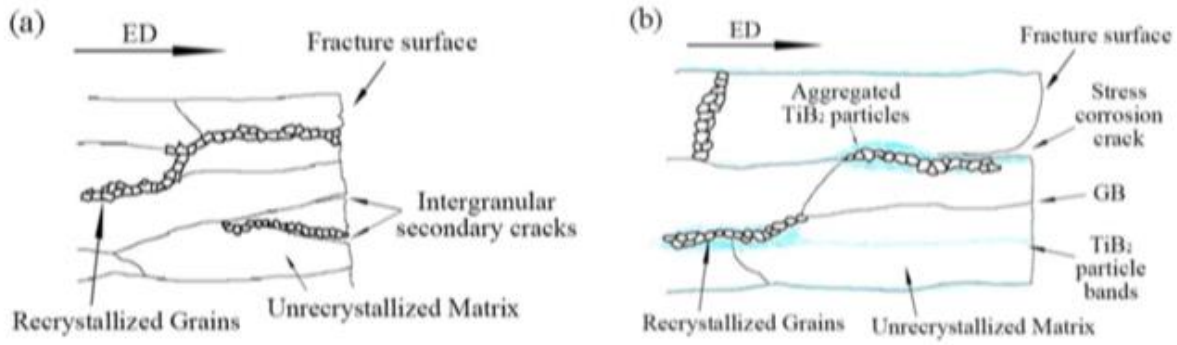

Figure 2-21. Schematic diagrams showing the influence of recrystallized grains on a crack path: (a) 7050 Al alloy, (b) TiB2/7050 composite [128]

`

2.4 Al-Cu-Mg alloys

2.4.1 Basics on Al-Cu-Mg alloy

Al-Cu-Mg alloys belong to 2000 series aluminum alloys, which are frequently used in the aerospace industry. The primary element in the 2000 series is copper. The earliest aerospace aluminum alloy was AA2017, which had a yield strength of 280 MPa. AA2024 was developed with better properties later. Some yield strengths and the year of introduction for aluminum alloys were shown in Figure 2-22[129]. The heat-treatable 2000 series typically contains 2-10 wt.% of copper. The highest strength is reached when 4-6 % of Cu is added along with other elements. Mg is often added to the Al-Cu system to provide extra strength by changing the aging characteristics[101]. The commercial AA2024 alloy has an ultimate tensile strength of 470 Mpa after T4 heat treatment, and SiCp/2024 aluminum alloy composites prepared by Angers et al. reached a UTS above 600 MPa[130].

`

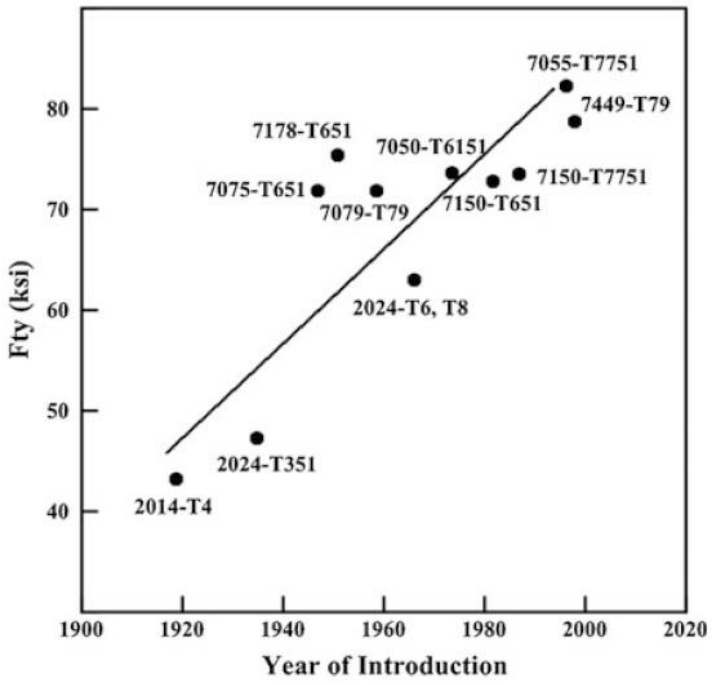

Figure 2-22. Yield strengths versus year of introduction of Al alloys[101]

2.4.2 Solution/Aging mechanism

The aluminum corner of the Al-Cu-Mg phase diagram and the distribution of phases in the solid was shown in Figure 2-23[131]. When the Mg composition is low (Cu/Mg >8), the main strengthening phase is Al_2Cu (θ phase). When Mg content is higher (4 < Cu/Mg < 8), The Al_2CuMg phase (S phase) forms. At this time, both Al_2Cu and Al_2CuMg phases control the property. When the Mg content increases (1.5 < Cu/Mg < 4), the critical strengthening phase becomes Al_2CuMg. The precipitation sequence of 2xxx alloys is considered to be: supersaturated solid solution (SSSS) → solute clusters →Guinier–Preston–Bagaryatsky (GPB) zones → S' → S phase[132] when the Cu/Mg is higher than 2. This sequence may vary when the composition changed.

`

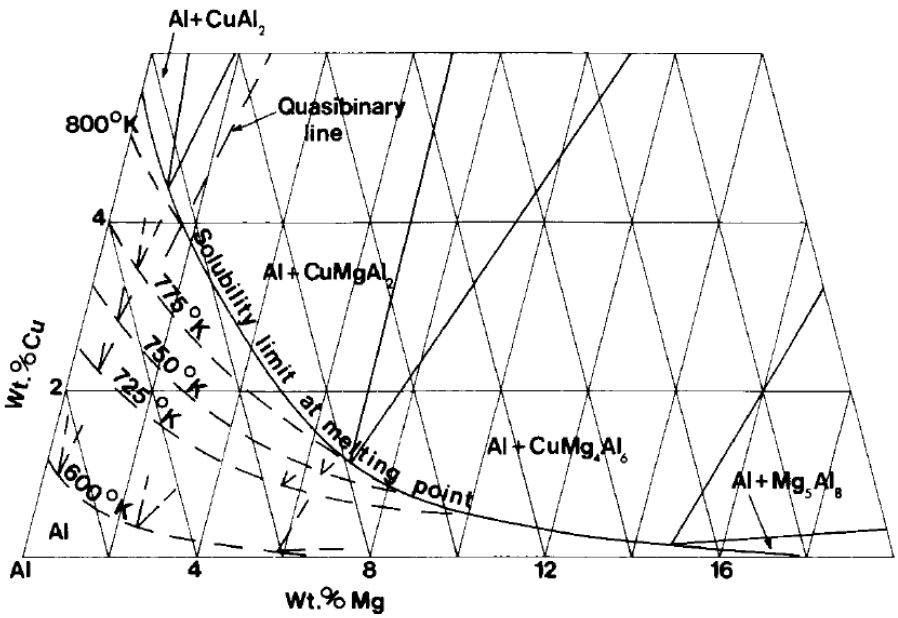

Figure 2-23. Aluminum corner of the aluminum-copper-magnesium diagram. Phase distribution in the solid and solid solubilities at various temperat[131]

`

Chapter 3 Fabrication of Master Nanocomposite Alloy

The cost of nanoparticle incorporation has been a long-standing problem for the industry application of metal matrix nanocomposites. The ex-situ incorporation utilizes expensive ceramic nanoparticles, while traditionally, the in-situ fabrication requires high-cost tools like rapid solidification and high-temperature ultrasonication. Therefore, a novel incorporation method of relatively inexpensive is necessary to enable nano-treating for industrial-scale applications.

This chapter reports a novel molten salt-assisted fabrication method to successfully fabricate in-situ boride nanoparticles (e.g., TiB_2, ZrB_2) and in-situ carbide submicron/nano-particles (TiC, WC). The size distribution of the synthesized particles was narrow, and the average size was smaller than other similar methods. The parameters that control the particle size were studied, and a new interface reaction model was proposed to explain the size controlling mechanism. Salt-assisted incorporation of ex-situ nanoparticles was also fabricated for comparison.

3.1 Ex-situ incorporation of nanoparticles

The flux-assisted ex-situ incorporation is a widely used method to add ceramic nanoparticles. When metal melts, there is an oxide layer on the surface of the molten metal, which prevents nanoparticles from entering the liquid metal. Fluoride flux ($KAlF_4$, Na_3AlF_6, etc.), chloride flux ($MgCl_2$, NaCl, KCl, etc.), and some oxide flux (borax) are used to facilitate the incorporation of nanoparticles by breaking or dissolving the oxide layer. Many nanoparticles, such as TiC nanoparticles, are also sensitive to oxygen in the air. Therefore, their surface will usually be oxidized. These nanoparticles were mixed with flux salt first and then added on top of the molten pool. The flux also dissolves the oxide layer on the surface of the nanoparticles. Nanoparticles will then be transferred into molten metal if the surface energy between

`

nanoparticles and metal is less than the surface energy between nanoparticles and salt. During this process, stirring and ultrasonication can be used to facilitate the incorporation.

This section reports a molten salt-assisted method incorporating TiC nanoparticles into molten aluminum and WC into molten copper. Al-TiC and Cu-WC nanocomposites with various concentrations of nanoparticles were fabricated. The Microhardness of the nanocomposites was tested.

3.1.1 Flux-assisted ex-situ incorporation of TiC into Al

TiC nanoparticles (US Research Nanomaterials, 60-100nm) were first incorporated into molten Al through flux-assisted ex-situ method to fabricate Al-TiC nanocomposite. TiC has good wettability with molten aluminum. The illustration of the experiment is shown in Figure 3-1. In brief, the nanoparticles were first mixed with $KAlF_4$ salt (5 vol.% of nanoparticles in salt) in a shaker (SK-O330-Pro) for 20 mins. Pure aluminum was melted at 820^{o}C in a graphite crucible, and the mixture of salt was added to the top of the melt. A graphite blade was placed close to the salt melt interface for stirring at 60 RPM. The designed volume fraction of TiC in Al is 10 vol.%

`

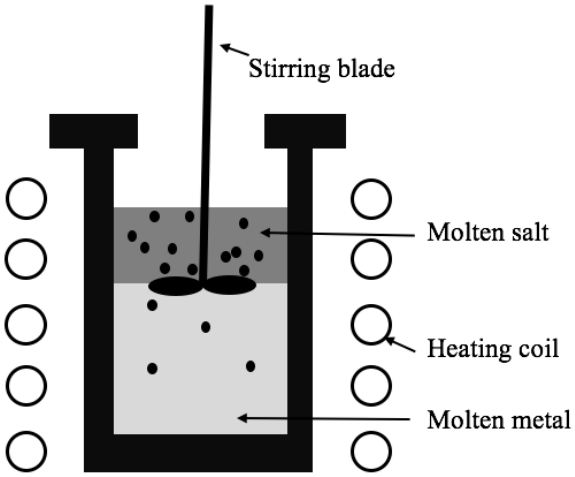

Figure 3-1 Illustration of flux-assisted incorporation of nanoparticles

The microstructure of the Al-TiC nanocomposite was examined by optical images and scanning electron microscopy (SEM, ZEISS Supra 40VP) equipped with energy-dispersive X-ray spectroscopy (EDS). The ground and polished samples for SEM were processed by low-angle ion milling at 4° and 4.5 kV for 40min (Model PIPS 691, Gatan). The volume fractions of TiC in the samples were calculated based on atomic percentages of Ti and Al elements from EDS mapping. The optical image, SEM picture, and EDS scanning of the ex-situ Al-TiC nanocomposite are shown in Figure 3-2. In Figure 3-2a, the brighter phase is the Al_3Ti intermetallic phase, a decomposition product of TiC. The decomposition happens at a temperature below 780^{o}C during cooling. The gray phases in the figure are TiC pseudo-clusters. In Figure 3-2b, the large particles are Al_3Ti. As the solidification front pushes TiC nanoparticles during solidification, they are all at the grain boundaries. Figure 3-2c is the mapping of Ti elements, and EDS results showing the Ti weight percentage are in Figure 3-2d. However, EDS is not able to detect carbon. According to the weight ratio between Ti and Al, it is concluded that TiC takes up 4.4 vol.% in the composite.

`

Therefore, the final volume fraction of TiC is less than the designed 10 vol.%. Considering some of the Ti detected in the EDS as Al_3Ti, the incorporation efficiency is not ideal.

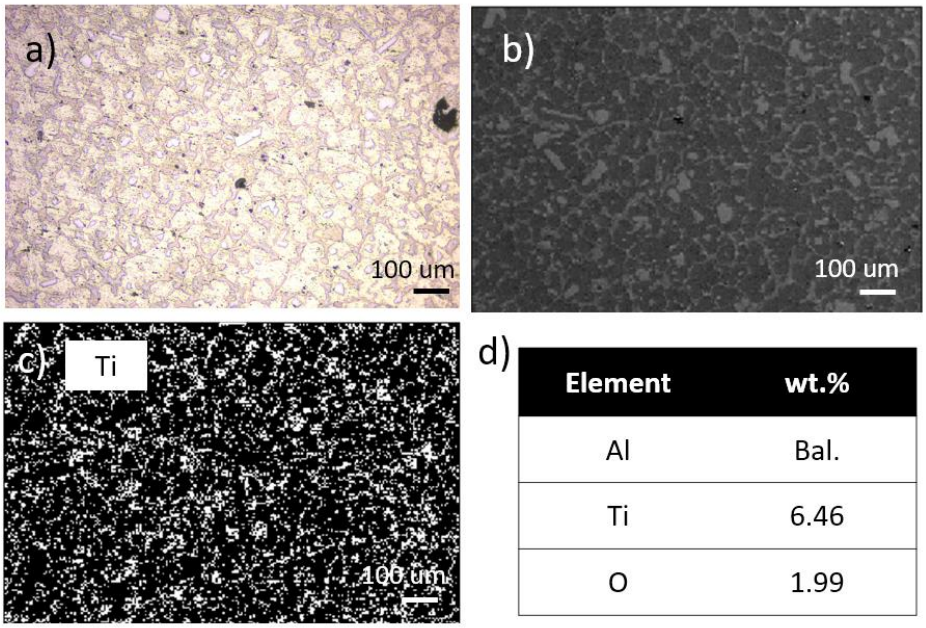

Element	wt.%
Al	Bal.
Ti	6.46
O	1.99

Figure 3-2 a). Optical image of the synthesized Al-TiC nanocomposite, b) SEM image of Al-TiC nanocomposite c) EDS mapping of Ti element in b), d) weight percentage of different elements

3.1.2 Flux-assisted ex-situ incorporation of WC into Cu

WC nanoparticles (US Research Nanomaterials, 80-200nm) were incorporated into molten Cu through a similar flux-assisted ex-situ method. The experiment set-up is the same as Figure 3-1. Briefly, WC nanoparticles were mixed with KAlF4 salt (10 vol.% of nanoparticles in salt) in a shaker (SK-O330-Pro) for 20 min. Pure Cu was melted at 1250^{o}C in a graphite crucible, and the mixture of salt was added on the top of the melt. Mechanical stirring at 60 RPM was applied. The incorporation took 10 min. After incorporation, the molten salt was removed by a steel spoon, and the fabricated composite was cast in a graphite mold. The designed volume fraction of WC nanoparticles in Cu is 5 vol.%. Similar characterization methods were applied to Cu-WC

`

nanocomposites. The optical image, SEM picture, and EDS scanning of the Cu-WC nanocomposite are shown in Figure 3-3. In Figure 3-3a, the gray phase is WC nanoparticle pseudo-clusters, and these pseudo-clusters can also be seen in SEM pictures in Figure 3-3b. Unlike the TiC nanoparticles, WC nanoparticles were not pushed to the grain boundaries but formed island-like clusters. EDS results show the W weight percentage in Figure 3-2d. According to the weight ratio between W and Cu, the final WC volume percentage is 4.2 vol.%. The resulted volume fraction is less than designed 5 vol.%. The Microhardness of the sample is 96.3 ± 52.9 HV.

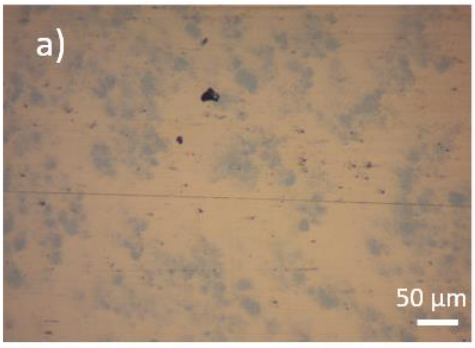

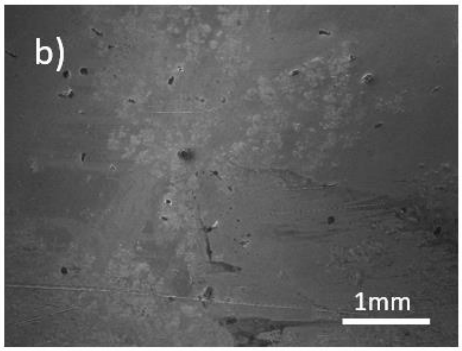

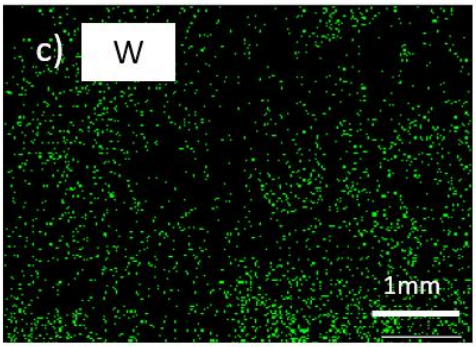

d)

Element	wt.%
Cu	Bal.
W	9.07
O	1.62

Figure 3-3 a). Optical image of the synthesized Cu-WC nanocomposite, b) SEM image of Cu-C nanocomposite c) EDS mapping of W element in b), d) weight percentage of different elements

3.2 In-situ fabrication of borides

This section presents a new flux-assisted method to fabricate boride nanoparticles. TiB_2 and ZrB_2 nanoparticles were fabricated in molten aluminum. Since these reactions take place at

`

temperatures above the melting point of aluminum, no templates are available to control the particle size[94,95]. Therefore, TiB_2 particles grow too large when there are sufficient reactants. Ostwald ripening also induces a continuous growth of particles after reaction to minimize the overall surface energy[96]. Therefore, particles synthesized in molten metal are usually not nano-sized. However, there are some methods to refine the particle size. For example, rapid solidification can generate tiny and uniform TiB_2 nanoparticles by reducing the reaction time[97], but its high cost and low productivity limit its commercialization. Ultrasonic-assisted reaction[133] is another option to fabricate small and uniform nanoparticles, but it suffers similar drawbacks. Therefore, a new dilution method was applied to achieve a smaller size and narrow size distribution of nanoparticles. The method will be described below.

3.2.1 Flux-assisted in-situ synthesis of TiB_2 in Al

The reactions used to fabricate TiB_2 are described in Equations 2-8, 2-9, and 2-10. The starting materials include aluminum (>99.8%) (RotoMetals, USA) and powders of potassium aluminum fluoride (KAlF4) (AMG Aluminum North America, USA), potassium tetrafluoroborate (KBF4, >99.5%), and potassium hexafluorotitanate (K_2TiF_6, >97%) (Alfa Aesar, USA). The illustration for the synthesis setup is shown in Figure 3-4. First, an aluminum ingot (50 g) was melted in the air in a high-purity graphite crucible heated by an induction furnace at a designated temperature of 1023K. The surface oxide layer was then removed by a steel spoon, and a designated amount of $KAlF_4$ cover salt was added on top of the molten metal for dilution. The amount of $KAlF_4$ was determined by the concentration of K_2TiF_6 in salt (0.4 g/cm^3). The reaction salts, KBF_4 and K_2TiF_6, were mixed and added afterward. The quantity of K_2TiF_6 was calculated according to a designed volume percentage of TiB_2 particles. It is set at 2.0 vol.% and 20.0 vol.% here. In this study, the molar ratio between KBF_4 and K_2TiF_6 was fixed at 2.05 to produce TiB_2.

`

The extra KBF_4 was applied to compensate for KBF_4 volatilized during the reaction due to its higher partial pressure. The reaction time was 10 min. After the reaction, the salt pool was removed, and the molten aluminum was cast in a steel rod mold. The reaction temperatures, K_2TiF_6 concentration in the total salt pool, and reaction holding time varied for different samples according to design.

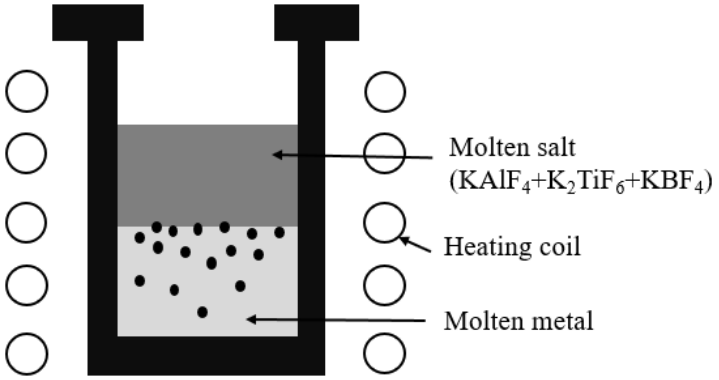

Figure 3-4. Illustration of the synthesis setup

The microstructure of the synthesized Al-TiB_2 nanocomposites was examined by optical imaging and SEM equipped with EDS. The samples were ground, polished, and etched with Poulton's reagent to reveal the grain structure. To reveal TiB_2 particles under SEM, the samples were low-angle ion milled at 4° and 4.5 kV for 30 min after grinding and polishing. Type II secondary electron (SE2) imaging and Type I secondary electron immersion lens (in-lens) imaging were utilized in SEM. More than 200 nanoparticles were measured from the in-lens SEM micrographs to obtain an average size and size distribution. In-lens mode micrographs were chosen for measuring because they provided the best contrast between particles and the aluminum matrix.

`

In situ Al-TiB_2 nanocomposites with approximately 2 vol.% of ceramic phase (thereafter Al-2TiB_2) were fabricated. The optical and SEM micrographs of one sample are presented in Figure 3-5 to show the typical morphology of the new in situ Al-TiB_2 nanocomposites. The average grain size of the Al-2TiB_2 sample is 134 ± 27 μm, as shown in Figure 3-5a. In Figure 3-5b, the islands are nanoparticle pseudo-clusters where nanoparticles are separated by only a few layers of metal atoms. Figure 2-5c is the EDS mapping of Ti in Figure 2-5. The calculated TiB2 volume percentage is 2.0 vol.% in this sample. Figure 3-5d is nanoparticle micrographs at higher magnifications. These small nanoparticles were still separated from each other due to the nanoparticles' self-dispersion in molten metal[32]. The nanoparticles from this sample have an average size of approximately 30 nm and show a narrow size distribution, as shown in Figure 3-5d.

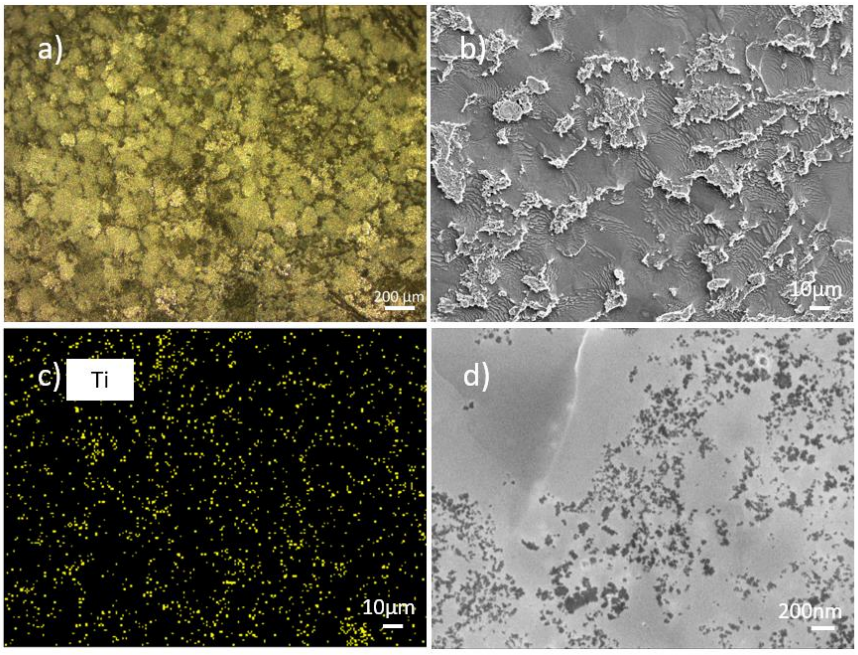

Figure 3-5. Morphology of in-situ Al-TiB_2 nanocomposite. a) optical image of a synthesized Al-TiB_2 nanocomposite with 2 vol.% TiB_2; b) SEM pictures (SE2) of the nanocomposite, c) EDS mapping of Ti element in b). b) SEM pictures (in-lens) of the nanocomposite of higher magnification

`

In situ Al-TiB_2 nanocomposites with approximately 2 vol.% (Al-2TiB_2) and 20 vol.% (Al-20TiB_2) were both fabricated. The later reaction took 30 min. The SEM images were presented in Figure 3-6. For comparison, the Al-20TiB_2 sample in Figure 3-6b is full of nanoparticles. Unlike Al-2TiB_2 where nanoparticles form pseudo-clusters, Al-20TiB_2 is covered by these pseudo-clusters, but they were still separated from each other and did not sinter together.

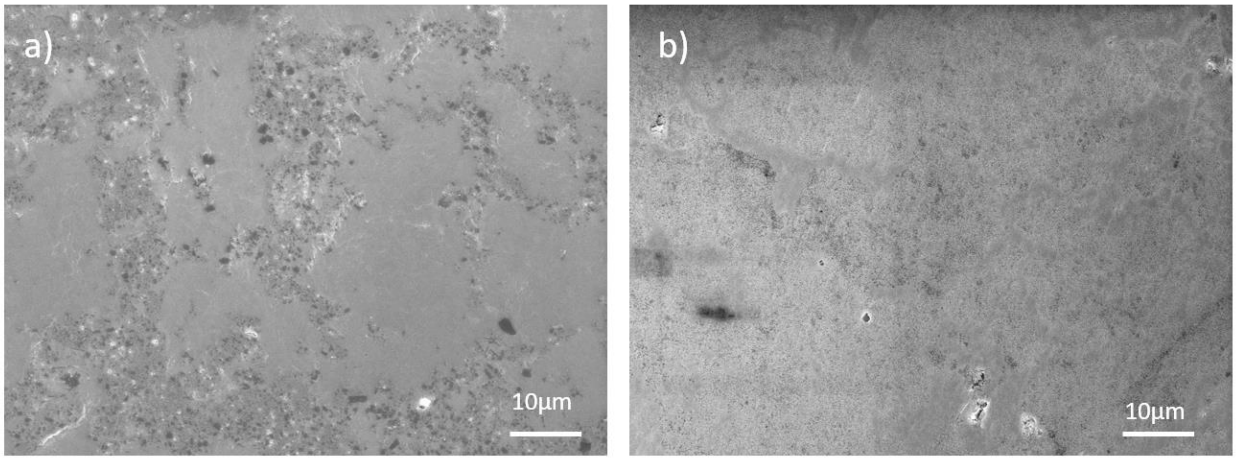

Figure 3-6. SEM pictures (in-lens) of the Al-2TiB_2, b) SEM pictures (in-lens) of the Al-20TiB_2

Transmission electron microscopy (TEM, T12 Quick CryoEM, CryoET) (FEI, 120kV) was used to verify the formation of nanoparticles. Cu Kα (λ=0.1542 nm) radiation was used for bulk nanocomposite XRD analysis. Nanoparticles were separated from the matrix for the TEM study. HCl (5%) solution was used to dissolve the aluminum matrix, and the aqueous suspension of the remaining nanoparticles was separated via centrifuge. These nanoparticles were then characterized by TEM and selected area electron diffraction (SAED). In-lens mode micrographs were chosen for measuring because they provided the best contrast between particles and the aluminum matrix. The XRD patterns of an Al-2TiB_2 sample and an Al-20TiB_2 are shown in Figure 3-7a. Because the TiB_2 peak intensity in Al-2TiB_2 is weak, an Al-20TiB_2 XRD pattern is presented as well. Small

`

TiB_2 peaks were detected in the Al-2TiB_2 sample, while the Al-20TiB_2 sample exhibited strong TiB_2 peaks, confirming the formation of TiB_2. In Figure 3-7b, the TEM picture of the extracted nanoparticles proves the small size of the nanoparticles in narrow size distribution. Furthermore, the SAED pattern of the nanoparticles was in accordance with the facets of TiB_2, as shown in Figure 3-7c. Since a limited number of nanoparticles were selected for SAED, the diffraction circles consist of a limited number of dots.

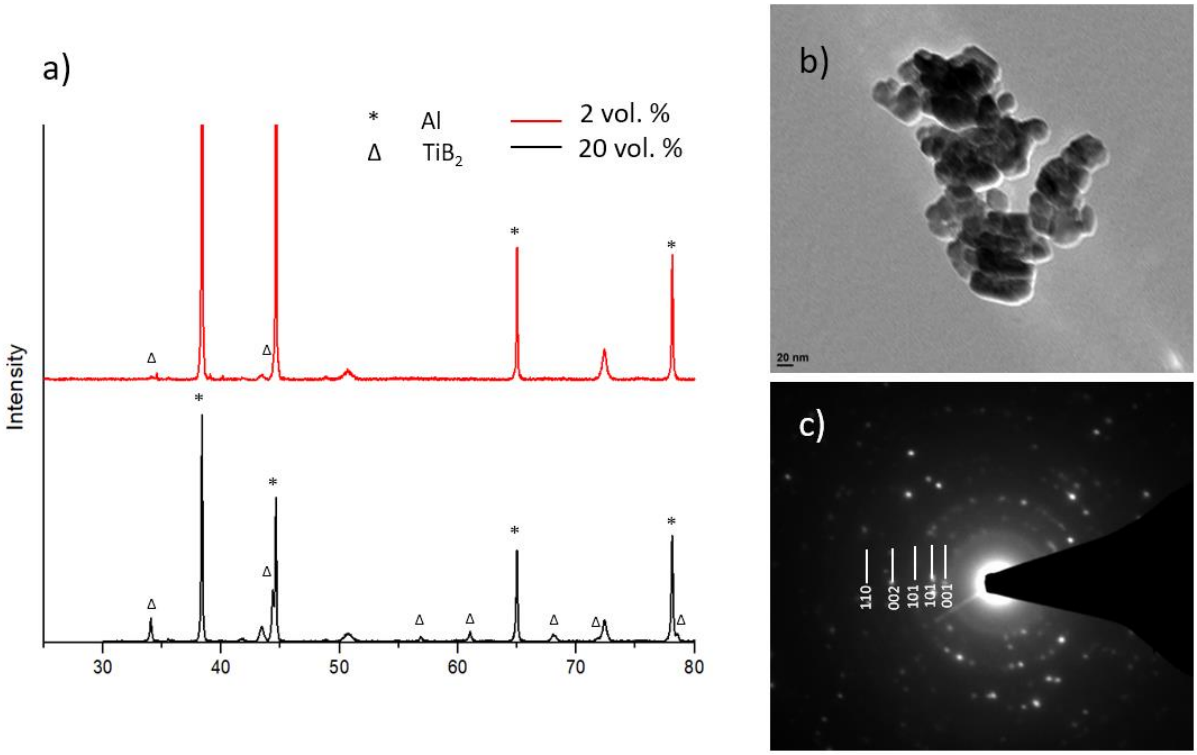

Figure 3-7. a) XRD pattern of Al-TiB2 nanocomposites of different volume percentages; b) TEM image of extracted TiB_2 nanoparticles; c) SAED pattern of the nanoparticles from b)

In-lens mode micrographs were chosen for measuring because they provided the best contrast between particles and the aluminum matrix. The final size distribution of the 2 vol.%

`

sample is presented in Figure 3-8. The largest particles seen are about 50 nm, and the average size is 22.1 ± 8.2 nm.

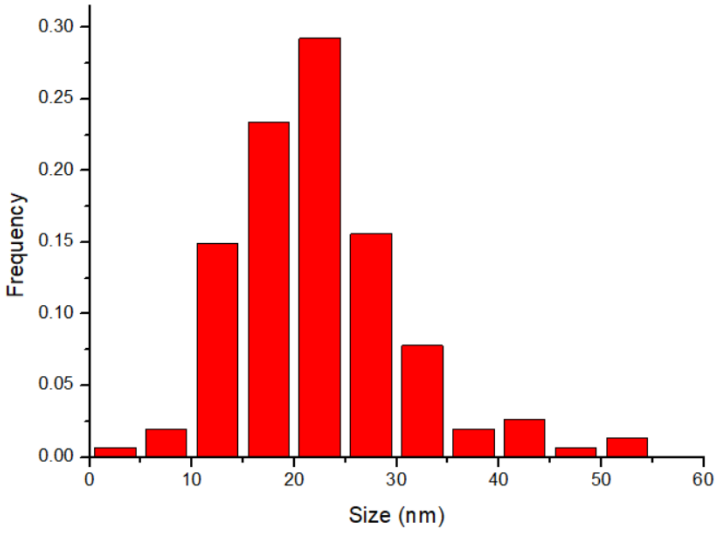

Figure 3-8. TiB_2 nanoparticles size distribution

3.2.3 Flux-assisted in-situ synthesis of ZrB_2 in Al

The fabrication method for in-situ ZrB_2 is quite like the method for TiB_2. The reaction used for ZrB_2 synthesis is shown in Equation 3-1, 3-2, and 3-3[134]. The experiments process is similar to the fabrication of TiB_2 in Al. Briefly, the aluminum was melted at 750°C, and the dilution salt, $KAlF_4$, was added on top of the aluminum melt. Then the mixture of K_2ZrF_6 and KBF_4 was added. The sample was designed to contain 2 vol.% of ZrB_2. The reaction took 10 min. After the reaction, salt was removed, and the fabricated sample (Al-2ZrB_2) was cast in a graphite crucible.

$$K_2ZrF_6 + \frac{13}{3}Al = Al_3Zr + \frac{4}{3}AlF_3 + 2KF \quad (3\text{-}1)$$

$$2KBF_4 + 3Al = AlB_2 + 2AlF_3 + 2KF \quad (3\text{-}2)$$

`

$$Al_3Zr + AlB_2 = ZrB_2 + 4Al \quad (3\text{-}3)$$

The SEM images of the Al-2ZrB_2 are shown in Figure 3-9. SE2 mode was applied because two different particles were observed, showing different contrast in the SE2 mode. In Figure 3-9a, ZrB_2 nanoparticles formed bands, and larger white Al_3Zr precipitates also exist. The experiment was not optimized, and extra KBF_4 should be added to react with the remaining Al_3Zr, or the reaction might take longer than 10 min so that the reaming the Al_3Zr could be reacted. A larger magnified SEM image is shown in Figure 3-9b. Most particles are nano-sized, and these nanoparticles are separated from each other and do not sinter together. The size distribution of the nanoparticles was shown in Figure 3-10. The average size of the ZrB_2 nanoparticles is 75.3 ± 31.5 nm.

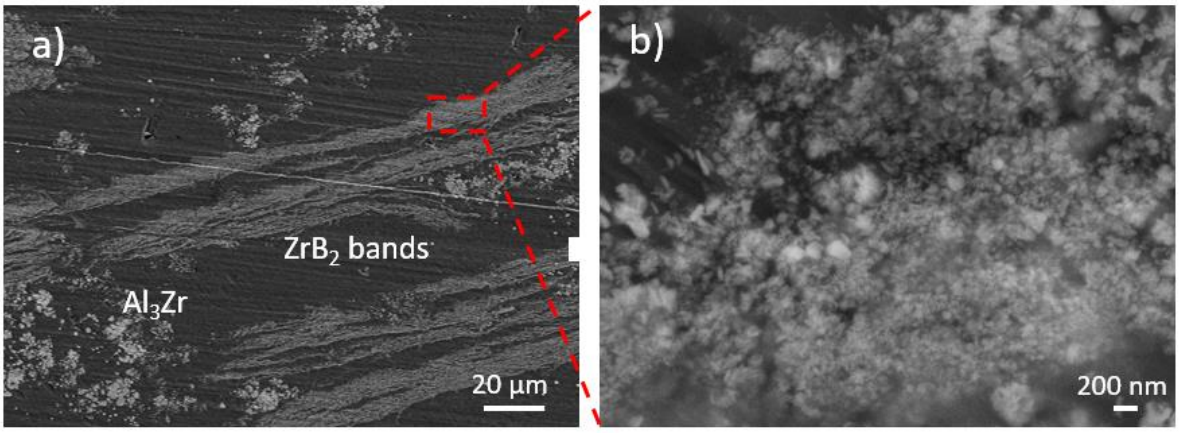

Figure 3-9. a) SEM pictures of the Al-2ZrB_2, b) SEM image of the selected region in the red rectangle

`

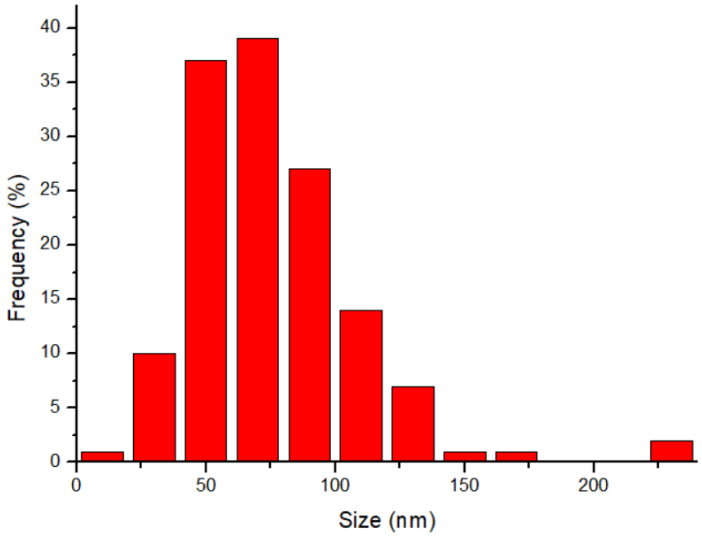

Figure 3-10. ZrB_2 nanoparticles size distribution

3.3 In-situ fabrication of carbides.

Carbides were fabricated using a similar dilution method. Metal salts were used to provide metal ions. Activated carbon, charcoal, and sugar were used as carbon sources. Unlike boron salt, the solubility of carbon in salt is low. Therefore, higher temperatures are required to accelerate these reactions. Different carbon sources were also tried to promote the reaction.

3.3.1 Flux assisted in-situ synthesis of TiC in Al

For TiC nanoparticles fabrication, charcoal particles (> 1mm), activated carbon powder (50 µm), and sugar (>1mm) are selected as carbon sources. The buffer salt is $KAlF_4$. The amount of carbon source used is 150% excess more than K_2TiF_6 because carbon can be oxidized during the reaction. Briefly, Al was melted as 900^{o}C in a graphite crucible heated by an induction furnace, and buffer salt was added on top. The volume ratio between Al and buffer salt was fixed at 1:2. Next, one carbon source (charcoal, activated carbon, or sugar) and K_2TiF_6 were mixed with buffer salt at a ratio of 1 :1 and were added on top of the Al melt. The reaction took two hours, and

`

mechanical stirring (60 RPM) was applied. Because sugar is flammable, the salt mixture containing sugar should be added slowly. It is designed to fabricate 2 vol.% of TiC inside aluminum. After the reaction is done, the salt pool was removed, and the samples were cast in a graphite crucible. The reactions are listed below.

$$3K_2TiF_6 + 13Al = 3Al_3Ti + 3KAlF_4 + K_3AlF_6 \quad (3\text{-}4)$$

$$Al_3Ti + C = TiC + 3Al \quad (3\text{-}5)$$

The samples were ground, polished, and ion milled for SEM images. The synthesized nanoparticles were also extracted from the aluminum matrix and prepared for TEM observation. XRD was applied to confirm the formation of TiC nanoparticles. Furthermore, the size of the nanoparticles was measured. All these procedures are similar to Al-TiB_2 sample characterization therefore not discussed again.

The SEM images are shown in Figure 3-11. The sample fabricated using activated carbon is shown in Figure 3-11a, b. There is almost no Al_3Ti and shows a much higher synthesis efficiency than ex-situ Al-TiC. All nanoparticles were pushed to the grain boundaries during solidification, indicating a good dispersion of TiC nanoparticles in the aluminum melt. At the grain boundaries, the nanoparticles were separated from each other, as shown in Figure 3-11b, and these nanoparticles have a small size distribution. The sample fabricated using charcoal is presented in Figure 3-11c, d. The reaction was incomplete in that not many TiC particles are seen in the sample while large Al_3Ti intermetallic phases are observed. TiC particles form pseudo-clusters in this sample, and the size of the TiC particles is larger. The slower reaction was due to the slower dissolution of carbon from charcoal caused by a smaller surface-to-volume ratio. Figure 3-11e, f are the SEM images of the Al-TiC sample fabricated using sugar. Some carbon with irregular

`

shapes was incorporated into the matrix, but not many Al_3Ti is seen in the sample indicating the reaction was done completely. The nanoparticles shown in Figure 3-11f are denser than particles in Figure 3-11b.

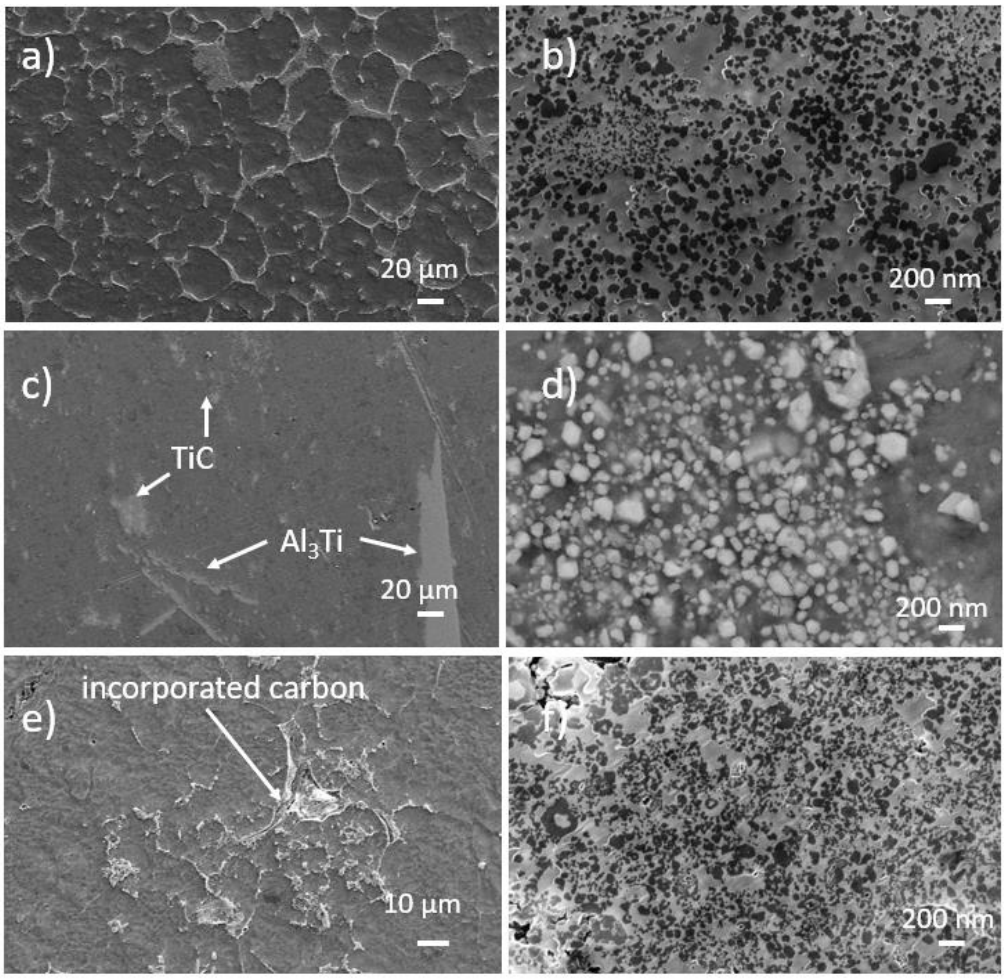

Figure 3-11. SEM pictures of the in-situ Al-TiC sample, a, b) fabricated using activated carbon, c, d) fabricated using charcoal, e, f) fabricated using sugar

XRD confirms the formation of TiC in Figure 3-12. In all three samples, TiC peaks exist, but the peak of the charcoal sample is smaller, indicating fewer TiC particles are fabricated. Moreover, there are more prominent Al_2O_3 peaks in the charcoal sample that a small number of

`

oxides were trapped into the melt during stirring. Figure 3-12b is the TEM image of the TiC particles extracted from the activated carbon sample.

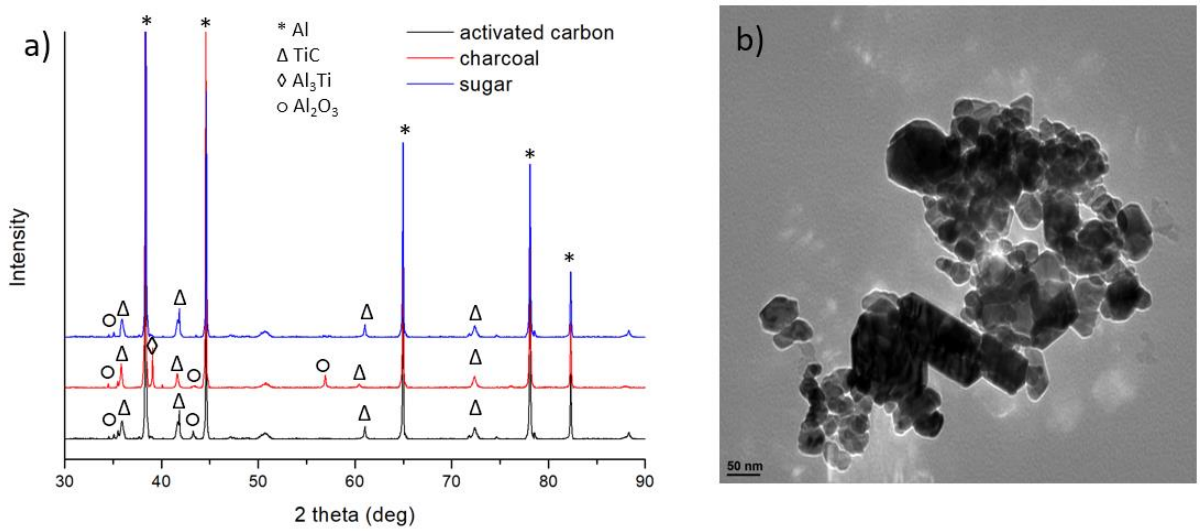

Figure 3-12. a) XRD pattern of Al-TiC nanocomposites fabricated from different carbon sources; b) TEM image of extracted TiC nanoparticles

The TiC nanoparticle size distribution is shown in Figure 3-13. The average sizes of the TiC nanoparticles fabricated are 61.0 ± 22.1 nm (activated carbon), 153.0 ± 89.0 nm (charcoal), and 35.7 ± 21.6 nm (sugar). First, the TiC nanoparticles are much smaller than the size of the carbon source (activated carbon ~ 50 μm, charcoal > l mm, and sugar >1 mm), indicating the dissolution of carbon and nucleation of TiC in the melt. It is also found that the average size of the sugar sample is the smallest while the size of the charcoal sample is the largest and the activated carbon sample in between. The possible reason is that the dissolution of carbon sources is different. Sugar dissolved the fastest because when it was added to molten metal, it decomposed to small carbon-containing molecules/ions and left a high surface area porous carbon[135]. Charcoal dissolved slowest because of its low surface-to-volume ratio. When carbon dissolved in the aluminum melt,

`

concentration was low, nucleation of TiC particles would happen. Faster dissolution caused a faster nucleation rate and a higher number of nanoparticles. If the carbon dissolution was slow, the slowing coming carbon will help the growth of the existing nanoparticles but not the nucleation of new nanoparticles. This might be why the sugar sample has the smallest particle size, but the charcoal sample has the largest nanoparticle.

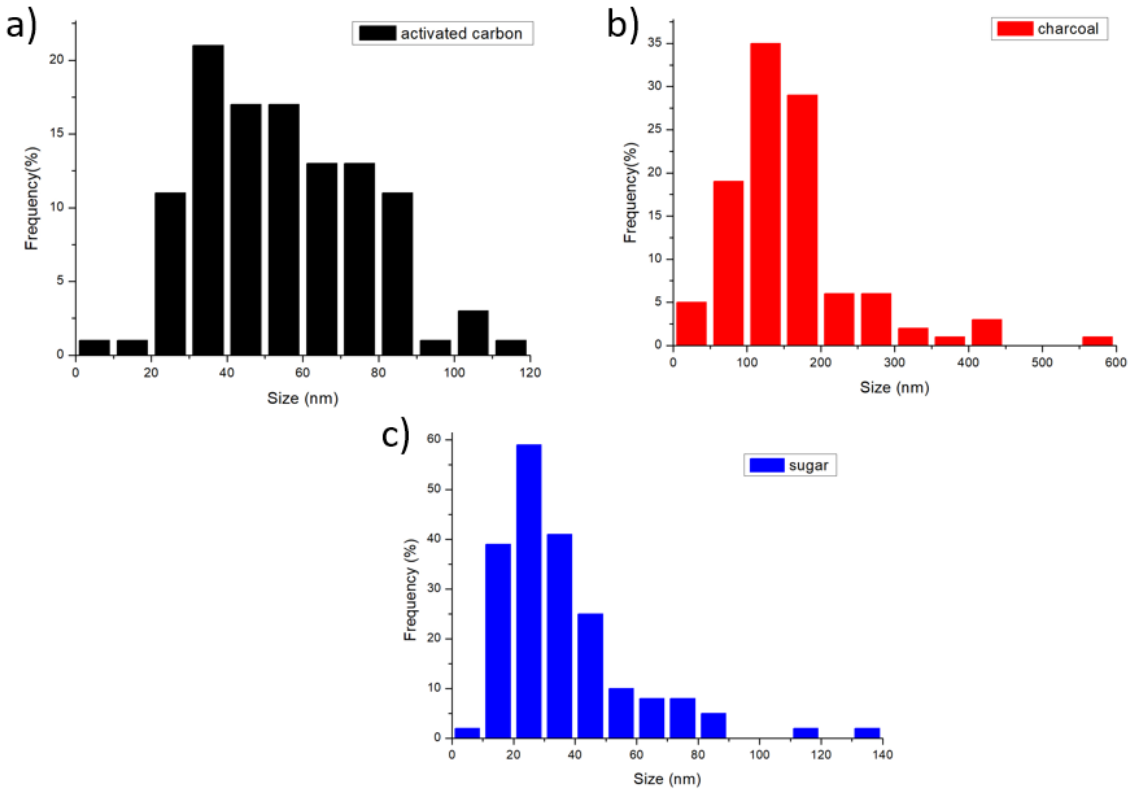

Figure 3-13 Size distribution of in-situ TiC nanoparticles fabricated using a) activated carbon, b) charcoal, c) sugar

3.3.2 Flux assisted in-situ synthesis of W/WC in Cu

W/WC particles were fabricated in molten Cu by a similar method. It is the very first time WC particles were fabricated using flux-assisted reaction. Briefly, Cu was melted at 1100^{o}C first. $KAlF_4$ was the buffer salt. The volume ratio between Cu and buffer salt is 1:1. A certain amount

`

of Al is added to aluminum as a reduction agent. WO_3 powder is the tungsten source, and it was mixed with activated carbon and $KAlF_4$. The mixture was then added to the buffer salt, and the reaction took 30 min. Finally, the salt was removed, and the sample was cast in a graphite mold for further characterization. The in-situ reactions are shown in Equations 3-6 and 3-7 below.

$$2Al + WO_3 = Al_2O_3 + W \tag{3-6}$$

$$W + C = WC \tag{3-7}$$

The SEM images of the Cu-W/WC composite were presented in Figure 3-14. As seen in Figure 3-14a, two types of particles exist in the sample. One type of particle is the sphere with curved surfaces. The other type of particle is the polygon with sharp edges and flat surfaces. The sphere particles are W particles, and the polygons are WC. There are many remaining W particles in the sample because the reaction is slow. Both carbon and tungsten have very low solubilities in molten metal, and thus the reaction was incomplete. The average size of the W particles is 413.5 ± 213.9 nm, and the average size of WC particles is 265.2 ± 122.6 nm. The size distribution of these two particles is shown in Figure 3-15. The synthesized WC particles have an average size above 100 nm due to a higher reaction temperature in molten Cu. Particles are growing fast in high-temperature environments. It is currently unsure why W became particles. One explanation is that tungsten dissolved into the melt first due to the reaction shown by Equation 3-6, and the nucleation of W happened later in the molten Cu. Compared to the ex-situ Cu-WC nanocomposites, the in-situ sample has limited advantages. The in-situ particles are larger, and it might take a much longer reaction time to react to all remaining W particles. The ex-situ Cu-WC is easy to make and carries smaller WC particles.

`

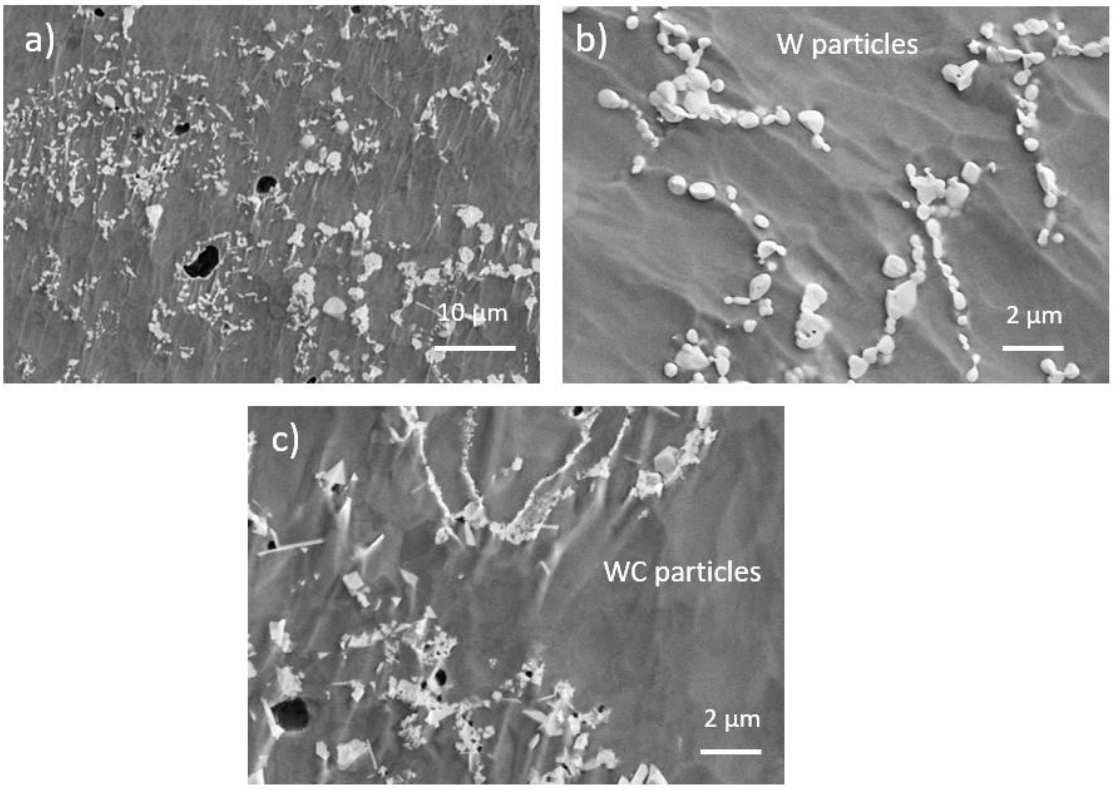

Figure 3-14. SEM pictures of the in-situ Cu-W/WC sample. a) large area consists of both particles, b) region with W particles, c) region with WC particles

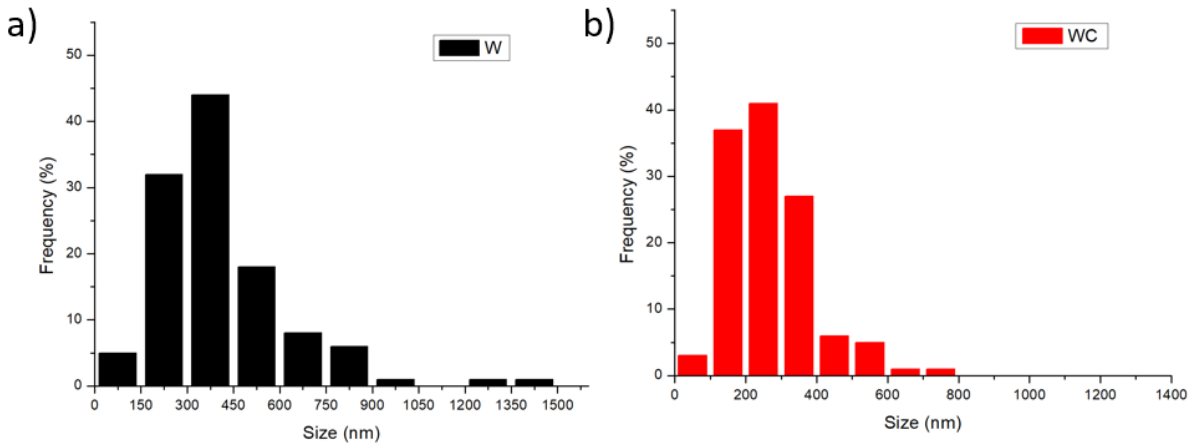

Figure 3-15. Size distribution of in-situ a). W particles and b) WC particles

`

3.4 Size distribution

The average size of in-situ TiB_2, TiC, and WC was collected from the literature. Ashby charts of the in-situ fabricated particles' size distribution by different temperatures were made. The following methods can fabricate the in-situ TiC particles: direct reaction synthesis (DRS)[37–45,136], rapid solidification processing (RSP)[40,137–139], vapor-liquid-solid reaction process (VLS)[81–84], self-propagating high-temperature synthesis (SHS)[70,71,140,141], mechanical alloying (MA)[77,80], hot isostatic pressing (HIP)[86] and flux-assisted synthesis (FAS)[65–67]. The corresponding Ashby chart of in situ TiC particles is presented in Figure 3-16. Here, using nano-diamond in mechanical alloying is marked as MA*. It is shown two methods can fabricate in-situ nanosized TiC particles. One way is by MA, but nano-sized reactants should be used. Another method is rapid solidification which is not suitable for mass production.

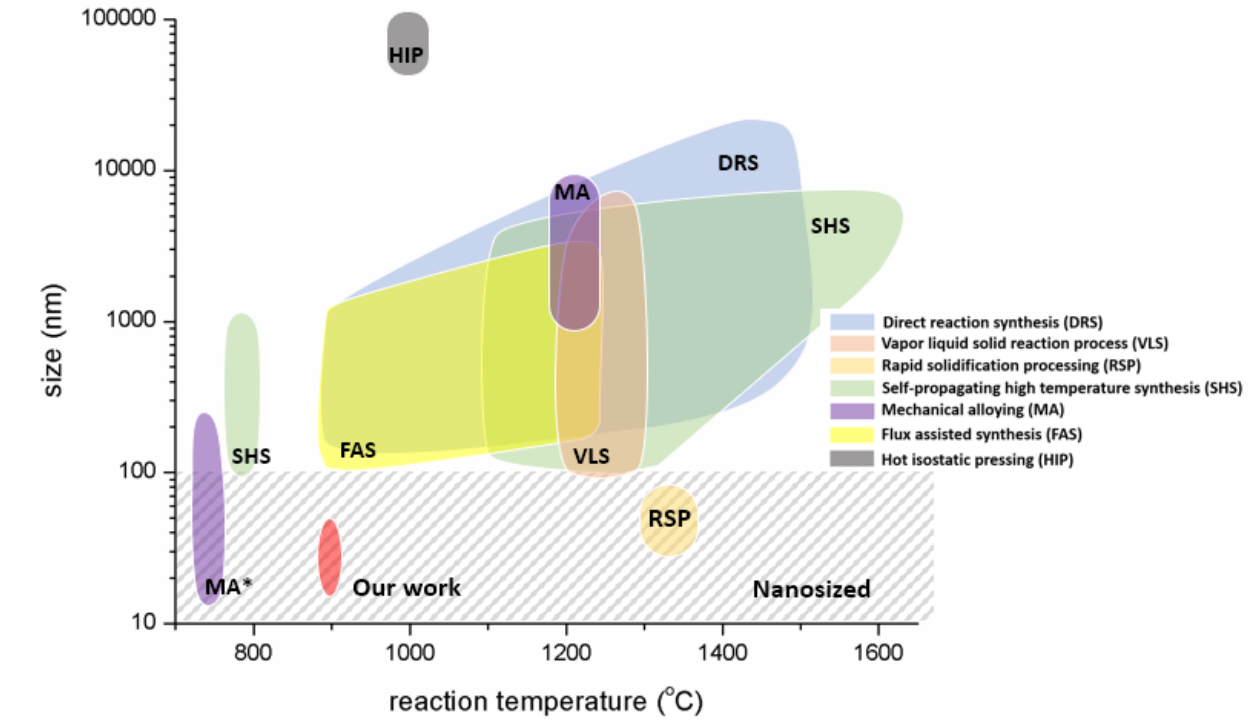

Figure 3-16. Size distribution of the in-situ fabricated TiC particles by different methods and at different temperatures

`

The in-situ TiB_2 particles synthesized by direct reaction synthesis (DRS)[35,36,44], reactive, spontaneous infiltration (RSI)[76], rapid solidification processing (RSP)[97], self-propagating high-temperature synthesis (SHS)[140], mechanical alloying (MA)[78,79], flux-assisted synthesis (FAS)[49,52,54–64,142–144], reactive hot pressing (RHP)[74,75] and exothermic dispersion (XD)[73,74], Ultrasonic-assisted FAS is indicated as FAS*[133], FAS with high-speed stirring is indicated as FAS**[51,53]. Rapid solidification after direct reaction synthesis is indicated as DAS*[145]. The corresponding Ashby chart is shown in Figure 3-17. Similarly, MA and RSP can produce TiB_2 nanoparticles. FAS with high-speed stirring or ultrasonication can also help reduce the size of the particles, but high-speed stirring and ultrasonication are limited in industry applications. Therefore, the dilution method is currently the only economical way of producing nano TiB_2.

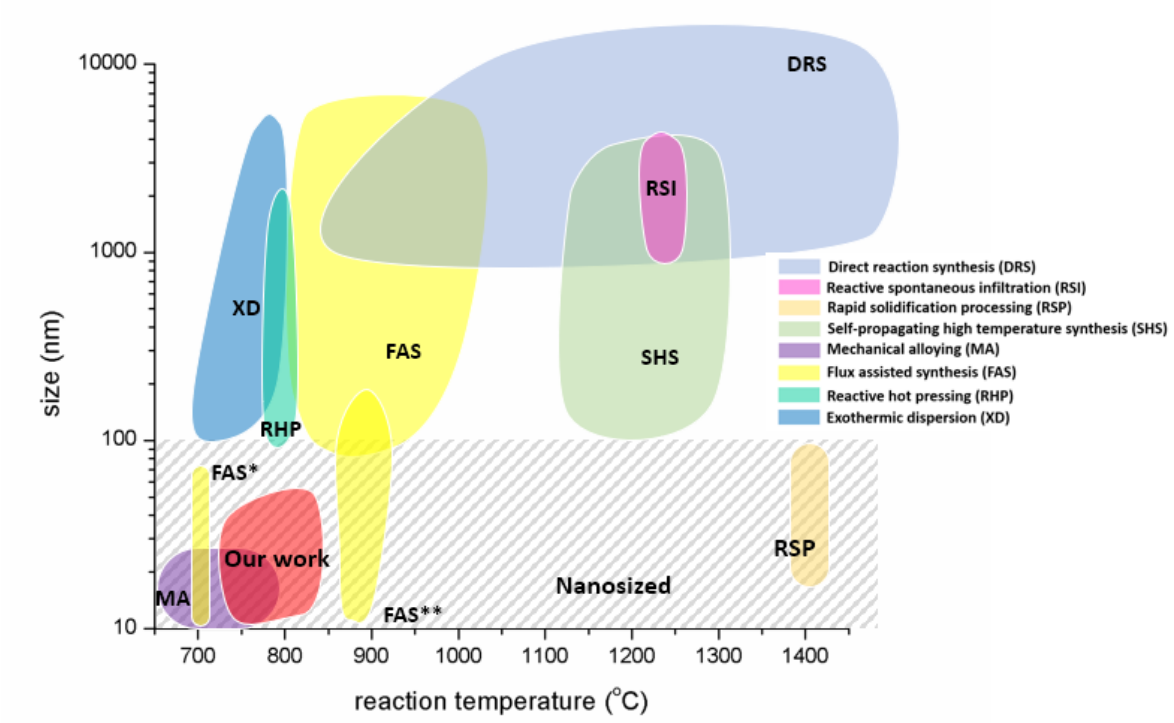

Figure 3-17. Size distribution of the in-situ fabricated TiB_2 particles by different methods and at different temperatures

`

There is limited research on in-situ WC particles. DRS[44,46–48] is the most common method for in situ fabrication of WC. Besides, researchers also tried spark plasma sintering (SPS)[88], laser-induced reaction (LIR)[87], and laser cladding (LC)[89]. All these methods produce macroparticles that have average sizes above 1 µm. Our dilution method produced the smallest particles among all methods.

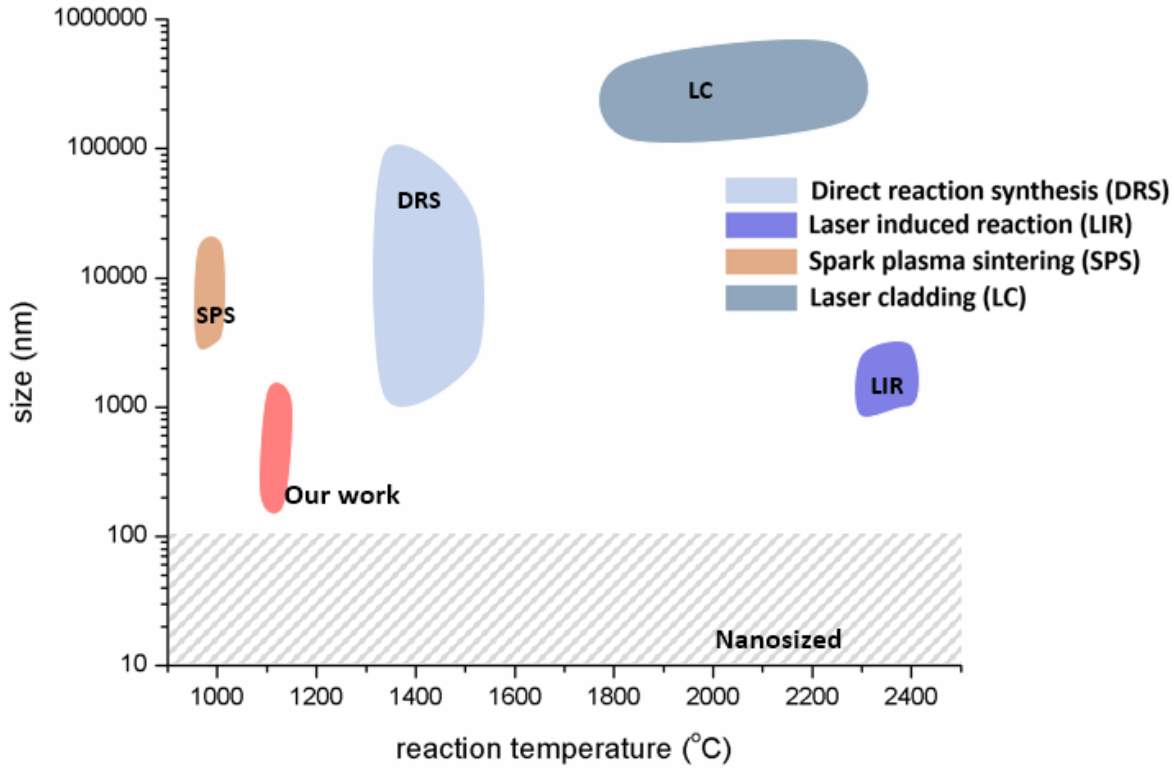

Figure 3-18. Size distribution of the in-situ fabricated WC particles by different methods and at different temperatures

Minor works have been conducted for in situ fabrication of ZrB_2. SHS[72] was applied to fabricate Al-ZrB_2 composite and get particle size of about 2 µm. Zhang et al. produced in situ (Al_3Zr + ZrB_2)/Al composites by FAS to yield particles of 400 nm[68]. Kumar et al. synthesized

`

submicron ZrB_2 particles between 25 nm to 2 μm by FAS. The average size of our ZrB_2 nanoparticles is 75.3 ± 31.5 nm.

3.5 Interface size control mechanism

The dilution method has shown a better capability of size control during in situ fabrication, but the mechanism is not clear. Here we use TiB_2 as a model to study the underlying mechanism for size control. The reaction for TiB_2 synthesis can be divided into several steps. First, Al quickly reduces KBF_4 and K_2TiF_6 at the salt-metal interface. Second, the reduced B and Ti dissolve and diffuse into the Al melt from the interface to form Al_3Ti and AlB_2 when their concentrations exceed certain limits, and Al_3Ti and AlB_2 may not form if the concentration of Ti or B in aluminum is low. The reduction of K_2TiF_6 is much faster than the reduction of KBF_4[146]. Thus Al_3Ti forms first in the aluminum melt and then reacts with incoming B from the salt. Finally, the nucleation and growth of TiB_2 particles occur when B and Al_3Ti react with each other. Since the Gibbs free energy for reaction ($AlB_2 + Al_3Ti = TiB_2 + 4Al$) is = -5189143 - 266.4T J mol[147]. It will be negative below 1373K, and therefore B will react with Al_3Ti to form TiB_2 rather than to form AlB_2.

The classical growth model indicates the growth of a particle is dependent on the surface reaction and diffusion of reactants. The particle's growth is then divided into three categories: surface reaction-controlled growth, diffusion-controlled growth, and mixed-controlled growth, depending on which process is the limiting factor[96]. The growth of TiB_2 is assumed to be diffusion-controlled[148], so the particle size from the diffusion-controlled growth model can be written as $r = (2DSt)^{1/2}$. Here, r is the radius, D is the diffusivity of the reactant, S is the supersaturation as a function of concentration, and t is the growth time[5]. When KBF_4 and K_2TiF_6 salts are used for TiB_2 synthesis, the reactions between Al and fluoride salts are fast; the nucleation and growth of TiB_2

`

will then take place when there are constant titanium and boron fluxes from the salt-aluminum reaction. This provides a supersaturated environment and longer reaction time for TiB_2 that nucleated at the beginning of the process and makes the particle size distribution wider. Another problem is that when K_2TiF_6 and KBF_4 are added directly onto molten salt, a large amount of heat will be released by this reaction to increase the temperature of the melt. This temperature fluctuation makes particle size control more difficult.

3.5.1 The influence of reaction time, temperature, and concentration

K_2TiF_6 concentration in the molten salt solution, reaction temperature, and reaction holding time was selected as variables to study nanoparticle formation and control mechanisms. A nanoparticle fraction of 2 vol.% was chosen because it is commonly used in nanoparticle-reinforced aluminum alloys. In the salt pool, samples utilizing different K_2TiF_6 concentrations between 0.2 g/cm^3 and 1.31 g/cm^3 were fabricated. The highest concentration of K_2TiF_6 was 1.31 g/cm^3 when no $KAlF_4$ was used for dilution, which is the concentration in conventional synthesis methods that used the mixture of KBF_4 and K_2TiF_6. The reaction temperature and holding time were fixed at 1023 K and 10 min in this study. The average size and the size distribution of these samples are shown in Figures 3-19. The particles have the smallest average size (22.1 nm) and narrowest size distribution when the K_2TiF_6 concentration is 0.4 g/cm^3. The area shaded in red in Figure 3-19a is the frequency of the particles larger than 100 nm. The average size and size distribution become larger when the K_2TiF_6 concentration increases above 1.0 g/cm^3. The average size of the particles drops from 32.5 nm to 22.1 nm when the concentration increases from 0.2 g/cm^3 to 0.4 g/cm^3, as the size measurements included both remaining Al_3Ti particles and TiB_2 nanoparticles because both these particles are black polygon in SEM images under the in-lens mode and thus it is difficult to distinguish. When the K_2TiF_6 concentration rises from 0.4 g/cm^3

`

to 0.8 g/cm^3, the average size of TiB_2 particles remained nearly unchanged. Then, it started to increase as the K_2TiF_6 concentration continued to increase. Furthermore, the size fluctuation for the samples produced with a concentration between 0.4 g/cm^3 and 0.8 g/cm^3 is smaller than other samples, which indicates a narrower size distribution. As in Figure 3-19a, the red shaded area is the frequency of particles above 100 nm. The number of these sub-micron particles increases sharply when the K_2TiF_6 concentration is above 1.0 g/cm^3. It suggests that the percentage of large particles was effectively reduced by the dilution of $KAlF_4$ in the salt mixture.

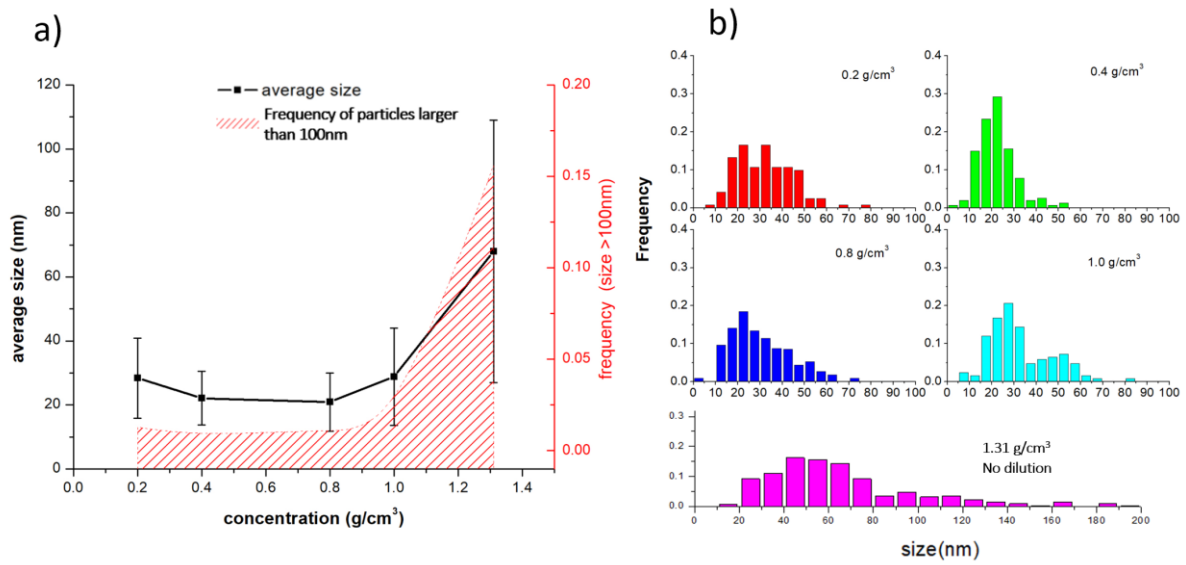

Figure 3-19. a) Average size of synthesized TiB_2 vs. K_2TiF_6 concentration (with a reaction time of 10 min at 1023 K) and the frequency of particles larger than 100nm; b) particle size distribution using different K_2TiF_6 concentrations

Different temperatures between 993 K and 1373 K were selected to study the temperature effects on the particle size. The K_2TiF_6 concentration and reaction holding time for this study are fixed at 0.4 g/cm^3 and 10 min, respectively. The average size and size distribution are shown in Figure 3-20a and Figure 3-20b. As the reaction temperature increases, the average size of the particles first drops a little and then increases again. The initial drop in the average size is due to

`

the unfinished reaction and the inclusion of larger Al_3Ti particles. At 993 K, the average size is larger than that in the sample prepared at 1023 K. Starting from 1023 K, the higher temperature results in a larger average size and broader size distribution. The overall trend is that the size of the formed TiB_2 increases with temperature.

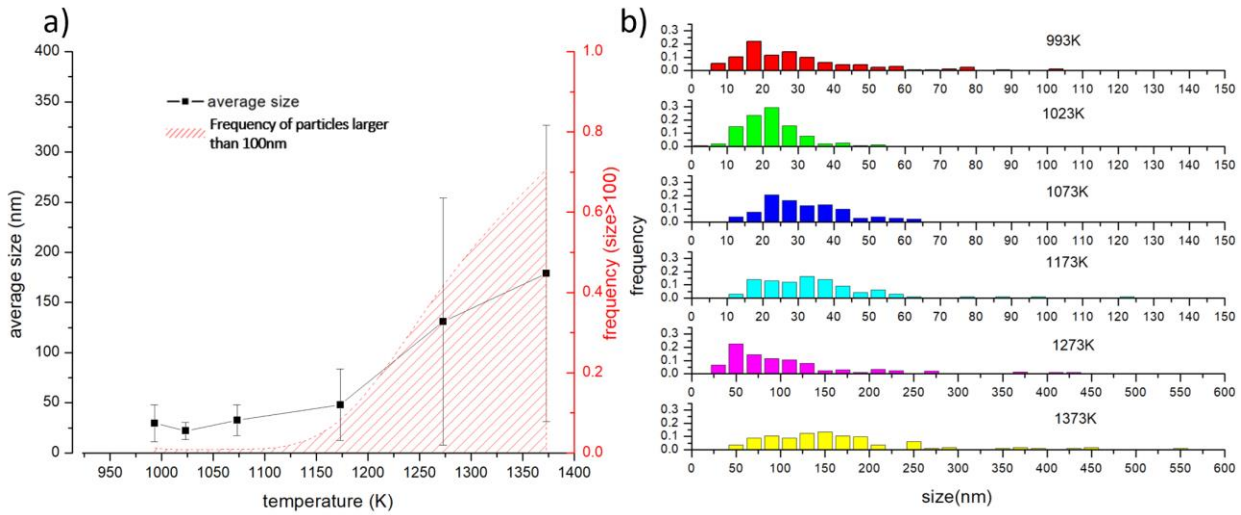

Figure 3-20. a) Average size of synthesized TiB_2 vs. reaction temperature (after a reaction time of 10 min with a K_2TiF_6 concentration of 0.4 g/cm^3) and the frequency of particles larger than 100 nm; b) size distribution of particles under different temperatures

The average sizes of the particles under different holding times are plotted in Figure 3-21a. The concentrations of K_2TiF_6 in these samples were fixed at 0.4 g/cm^3 with the reaction temperature at 1023 K. Like the size-concentration and size-temperature plots, both the average size and distribution range drop at the beginning and rise afterward. Unreacted Al_3Ti causes the initial drop, and further growth of the particles results from Ostwald ripening, where small nanoparticles tend to dissolve, and large particles tend to grow due to a reduction in total surface energy. The nanoparticles' growth velocity at this temperature is slow. From 10 min to 60 min,

`

the average size increased from 22.1 nm to 30.7 nm, and the frequency of particles larger than 100 nm increased slightly but remained low at about 2%.

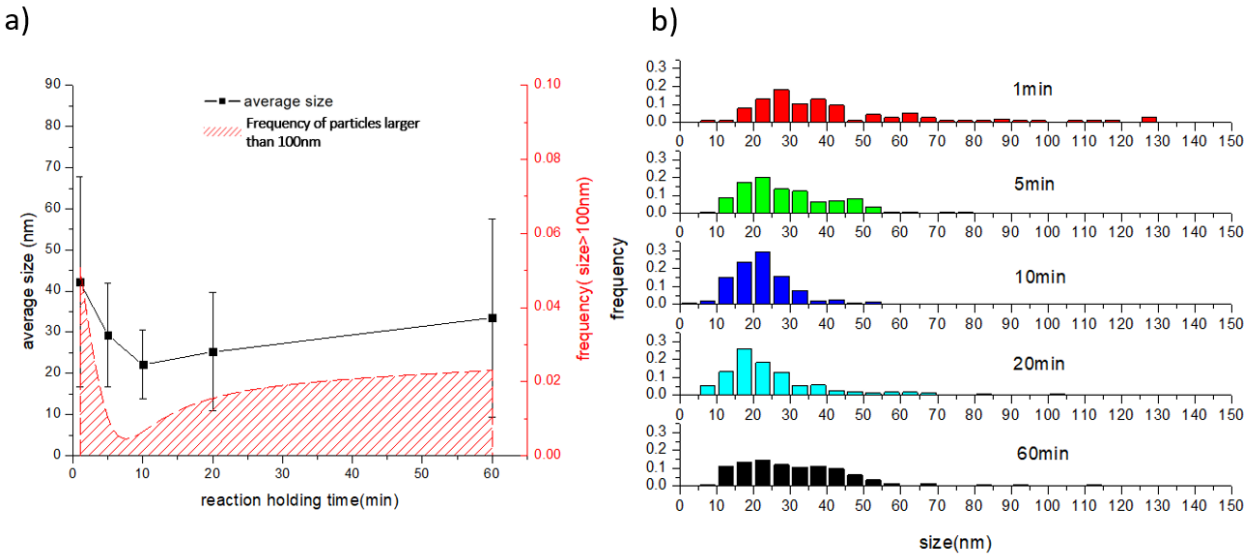

Figure 3-21. a) Average size of synthesized TiB_2 vs. reaction holding time (with a K_2TiF_6 concentration of 0.4 g/cm^3 at 1023 K) and the frequency of particles larger than 100 nm; b) size distribution of particles of different reaction holding time

3.5.2 Interface diffusion-controlled growth model

The formation of TiB_2 nanoparticles from large Al_3Ti intermetallic particles was observed in a sample after only a 1 min reaction. A clear interface between the earlier-formed Al_3Ti and new TiB_2 from this reaction is presented in Figure 3-22a. As mentioned before, Al_3Ti will form first due to the faster reduction of K_2TiF_6, and because no AlB_2 was observed in the 1-min-reaction sample, the reactant B is believed to come from the salt-metal reaction while Ti is from the dissolution of Al_3Ti. Early formed Al_3Ti will continuously be consumed until all boron is into the aluminum melt and react with Ti. It suggests that an interface diffusion-controlled growth model can describe the growth of nanoparticles. The potential growth mechanism is illustrated in Figures 3-22b, where boron flux comes from the matrix to react with titanium released from Al_3Ti.

`

Heterogeneous nucleation of TiB_2 nanoparticles on the Al_3Ti interface can happen, and the particles' growth was limited close to the interface. As the reaction continues, the Al_3Ti is consumed, and the interface is pushed backward. In Figure 3-22c, the concentration profiles of boron and titanium are illustrated. The boron concentration profile is $C_{B,x}$, the concentration far away from the interface is $C_{B,\infty}$, while the concentration at the interface is $C_{B,i}$. Similarly, the concentration of dissolved titanium is $C_{Ti,x}$. At the interface, titanium has the highest concentration, $C_{Ti,i}$ and it drops quickly away from the interface. There is a narrow region where the concentration of these reactants is high enough for the growth of TiB_2. Away from this region, the dissolved Ti and B and solid TiB_2 are at equilibrium, meaning growth will not continue. This is an ideal case when K_2TiF_6 reacts much faster than KBF_4 such that no other Ti would come from the Al/salt liquid interface to promote the growth of particles when the reduction of K_2TiF_6 is complete. The width of the growth region is defined as Δx. Ostwald ripening is not considered in this model since the size of the nanoparticles is not very sensitive to the reaction holding time in this study. We assume that the diffusion of boron and the reaction rate between boron and titanium are fast, so the growth of the particles is only diffusion-controlled, as stated in another paper[148].

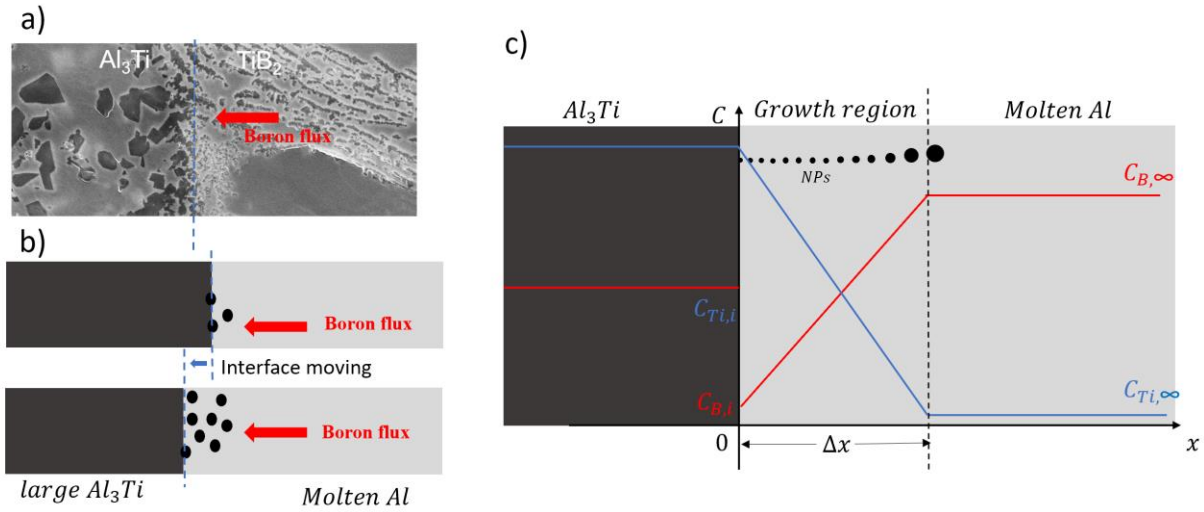

`

Figure 3-22. a) SEM picture of a reaction region where TiB_2 nanoparticles (NPs) form, with the reaction interface drawn; b) illustration of the reaction model where the reaction interface will move when Al_3Ti is consumed; c) concentration profile of Ti and B close to the reaction interface

We can assume the concentration of Ti is constant far away from and at the interface. Therefore, $C_{Ti,\infty}$ and $C_{Ti,i}$ are constant. The diffusion in the growth region is steady so that the concentration profile can be written as:

$$C_{Ti,x} = C_{Ti,i} - \left(\frac{C_{Ti,i} - C_{Ti,\infty}}{\Delta x}\right) \cdot x \tag{3-8}$$

Here, $C_{Ti,\infty} \ll C_{Ti,i}$.

The diffusion-controlled particle growth can be written as:

$$dr = \frac{V_{TiB_2} D_{Ti} \left(C_{Ti,x} - C_{Ti,NP}\right)}{r} dt$$[149] (3-9)

Here, r is the radius of a particle, V is the molar volume of TiB_2, D_{Ti} is the diffusivity of titanium, and $C_{Ti,NP}$ is the concentration of titanium at the nanoparticle interface. Here, we assume the diffusion of boron is fast enough such that the diffusion of titanium from Al_3Ti determines the particle growth. Similarly, $C_{Ti,NP} \ll C_{Ti,x}$. Based on mass conservation, the titanium released from the Al_3Ti should be equal to the titanium reacted to form TiB_2 nanoparticles, as shown in Equation (3-10):

$$J_{Ti} dt = \rho_{Ti,Al_3Ti} dx \tag{3-10}$$

Here, J_{Ti} is the titanium flux released from Al_3Ti, and ρ_{Ti,Al_3Ti} is titanium's molecular density (mol/m^3) in Al_3Ti. According to Fick's law, the flux can be written as:

$$J_{Ti} = D_{Ti} \frac{C_{Ti,i} - C_{Ti,\infty}}{\Delta x} \tag{3-11}$$

`

D_{Ti} is the diffusivity of titanium in liquid aluminum, and $D_{Ti} = D_{Ti}^{0} \exp\left(-\frac{\Delta G_a}{kT}\right)$. D_{Ti}^{0} is the diffusivity under standard conditions, and ΔG_a is the activation energy of diffusion. After plugging Equations (3-8), (3-10), (3-11) into Equation (3-9), we can determine the size of a particle:

$$r = (\frac{1}{2} V_{TiB_2} \rho_{Ti,Al_3Ti})^{\frac{1}{2}} \cdot \Delta x \tag{3-12}$$

When the interface moves a distance Δx, the total amount of titanium in the nanoparticles in the growth region should be equal to the amount of titanium released from Al_3Ti:

$$N \cdot \rho_{Ti,NP} \cdot \frac{4}{3}\pi r^3 = \rho_{Ti,Al_3Ti} \cdot \Delta x \cdot 1\ m^2 \tag{3-13}$$

Here, N is the number of particles in this region, and $1\ m^2$ is the unit area. N can then be calculated from nucleation rate and time:

$$N = \dot{N} \cdot t_{NP} \cdot 1\ m^2 = f_0 N_A\ C_{Ti,i}\ \exp\left(-\frac{\Delta G^*}{kT}\right) \cdot t_{NP} \cdot\ 1\ m^2 \tag{3-14}$$

Here, $\dot{N}$is the nucleation rate, t_{NP} is the time needed for the interface to move a distance Δx where $t_{NP} \cdot \frac{dx}{dt} =$ Δx, f_0 is a coefficient of how fast titanium atoms form stable nuclei, N_A is Avogadro's number, $N_A\ C_{Ti,i}$ is the total number of titanium atoms close to the interface, $\Delta G^*$is the critical nucleation energy, k is the Boltzmann constant, T is absolute temperature, and $1\ m^2$ is the unit area. After plugging Equations (3-10), (3-11), (3-12), (3-14) into Equation. (3-13), the radius of the particles can be written as:

$$r = Cexp(-\frac{P}{T}) \tag{3-15}$$

In Equation (3-15), C and P are constant numbers that can be expressed as:

`

$$C = \left[\frac{3D_{Ti}^{0}}{4\pi\rho_{Ti,NP}f_0 N_A}\left(\frac{1}{2}V_{TiB_2}\rho_{Ti,Al_3Ti}\right)^{\frac{1}{2}}\right]^{\frac{1}{4}} \quad (3\text{-}16)$$

$$P = \frac{\Delta G_a - \Delta G^*}{4k} \quad (3\text{-}17)$$

In this simplified model under a reactant dilution, the radius of synthesized nanoparticles is simply a function of temperature, while neither the concentration nor reaction time influence the average particle size. The irrelevance of concentration may be attributed to the extremely fast reduction of K_2TiF_6 by Al, such that the titanium flux comes solely from Al_3Ti. However, experimental results showed an increase in the average size of the particles when concentration was increased beyond the dilution range. As the model assumes the growth of particles is limited in the growth region, it no longer holds at a higher concentration of K_2TiF_6, which would result in a chaotic reaction at the aluminum/salt interface with the formed particles continuing to grow with incoming Ti from elsewhere in the solution. The temperature-size curve was fitted using Equation (3-15), as shown in Figure 3-23; from fitting, the factors C and P are 74572.9 nm and 8247.3 K, respectively.

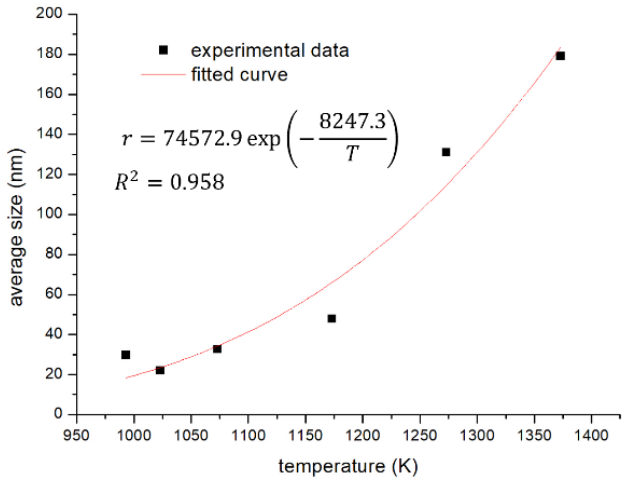

Figure 3-23. The average particle size at various temperatures

`

P indicates how diffusion activation energy, critical nucleation energy, and temperature affect particle size. Generally, faster diffusion will result in a larger particle size. Therefore, either higher temperature or smaller diffusion activation energy will make the particles larger. On the other hand, a faster nucleation rate means more small particles are generated. Thus larger critical nucleation energy promotes the growth of larger particles in a lower quantity. P can also be estimated from currently available data. The activation energy of titanium diffusion in liquid aluminum can be estimated to be roughly 30 kJ/mol[150,151]. Unfortunately, data regarding $\Delta G^*$is not available in the literature. TiB_2 can heterogeneously nucleate on the Al_3Ti surface to form a coherent interface[152]. Furthermore, the energy released by the reaction between boron and Al_3Ti is $(-43.4 \times 10^3 + 15.8T)$ J/mol[36] and thus provides a strong driving force to initiate nucleation. In one example, the value of $\Delta G^*$for heterogeneous calcium carbonate nucleation on quartz is 16 ± 3 kJ/mol[153]. The ΔG^* for TiB_2 nucleation would be of the same order. Therefore, from current available data, P can be calculated to have an order of magnitude of 10^3. This number is comparable with the fitted result from the experimental data. However, the data for pre-exponential factors in the nucleation rate is scarce, especially for systems at such high temperatures. Therefore, it is currently difficult to estimate C.

The interface diffusion-control model provides one possible explanation as to why particles synthesized at high temperatures could remain nano-sized without surfactants. The traditional diffusion-controlled growth model or surface reaction model[96] predicts particles could continue to grow, and the particle's size depends on the reaction time. However, there are still limitations to this diffusion-controlled model. Firstly, the particles must grow in a steady system where reactants come from opposite directions to react in a region near the interface. But normally, Al_3Ti moves in the liquid, and the boron flux might not be constant since KBF4 is consumed continuously

`

during the reaction. Secondly, the movement of the particles is neglected. Some particles can move and enter other growth regions close to Al_3Ti particles due to their Brownian motion. Finally, the reaction is assumed to be determined mainly through titanium diffusion. The diffusion of boron, reaction speed at the nanoparticle interface, and the rate at which titanium leaves Al_3Ti are all assumed to be fast enough such that titanium diffusion is the dominating factor.

3.6 Summary

1. Flux-assisted ex-situ method was applied to fabricated Al-TiC and Cu-WC nanocomposites for comparison.

2. A dilution method is invented to fabricated in-situ Al-TiB_2 nanocomposite, Al-ZrB_2 nanocomposite, Al-TiC nanocomposite, and Cu-W/WC composite. Except for the Cu-W/WC samples, the in-situ fabricated particles offer a much narrower distribution and are smaller than other methods reported in the literature. The finest TiB_2 nanoparticles fabricated were 22.1 ± 8.4 nm. The average size of ZrB_2 is 75.3 ± 31.5 nm. The TiC particles can be fabricated using activated carbon, charcoal, and sugar. The one made from sugar has the smallest size of 35.7 ± 21.6 nm. The Cu-W/WC sample has two different particles left in the Cu matrix, and the formed particles are larger (265.2 ± 122.6 nm) comparing to the ex-situ Cu-WC sample. Comparing to the ex-situ method, the in situ Al-TiC fabricated using activated carbon or sugar has little Al_3Ti left in the sample indicating a complete reaction.

3. A interface-controlled reaction model is built to explain the size controlling mechanism in the dilution method for TiB_2 fabrication. The result indicates that the size of the particles is a function of absolute temperature and is independent of K_2TiF_6 concentration in a diluted reactant solution. However, the model fails at high K_2TiF_6 concentrations because the reaction is no longer

`

steady; the average size increases dramatically with temperature. Furthermore, Ostwald ripening is relatively slow, so the particles did not grow large for a longer holding time at 1023 K, which is suitable for mass processing in the industry.

`

Chapter 4 Nano-Treating Effects

Nano-treating is to modify the manufacturing process, microstructure, and properties of the alloy by adding a small volume percentage of ceramic nanoparticles in metals. Ceramic nanoparticles are effective grain refinement agents, and they alter the solidification behavior during casting, welding, and additive manufacturing. Both primary and secondary phases can be significantly refined. Moreover, it might change the thermodynamics and kinetics of solution treatment and aging. During plastic deformation, nanoparticles can also influence recrystallization and impede grain growth. This chapter conducts experiments to study the nano-treating effects using different aluminum and copper alloy systems. The results show nano-treating has excellent potential in breaking the barriers of traditional metallurgy and achieving unprecedented performance for alloys.

4.1 Nanoparticle influence on solidification

It is known that nanoparticles can refine grain during solidification because they serve as heterogeneous nucleation sites for the primary phases and impede grain growth. Here in this section, TiC nanoparticles were added to aluminum 7075 alloys to study the influence of nanoparticles on solidification.

4.1.1 Solidification curves

A control sample without nanoparticles (pure AA7075) and a sample containing 1 vol.% of TiC nanoparticles (7075-1NP) were fabricated for a solidification study. Briefly, pure aluminum was melted first at 820^{o}C, higher than conventional AA7075 alloy because TiC nanoparticles were not thermally stable below 750^{o}C in aluminum melt[154]. Pure Zn, Mg, Cu, and Al-3TiC were added to the molten aluminum to obtain the designated composition. Here Al-3TiC is an in-situ Al-TiC

`

master nanocomposite containing 3 vol.% of TiC nanoparticles. Mechanical stirring and degassing were applied for 40 mins. The alloys were then cast in a steel mold. The samples were cut, ground, polished, etched for characterization. The composition of the fabricated samples was tested by spark emission spectrometer (Spark CCD 7000, NCS). Each sample was tested three times, and the results are shown in Table 4-1. TiC volume fraction was calculated accordingly. These two samples have a typical AA7075 alloy composition, and the 7075-1NP sample carries approximately 0.86 vol.% of TiC nanoparticles. The optical images of the two samples are shown in Figure 4-2. Dendrite arms are clearly shown in the pure AA7075 sample. AA7075 has a grain size of several hundred micrometers. The nanoparticles refine the grains of 7075-1NP while nanoparticles pseudo-clusters exist along the grain boundaries. Shrinkage porosities could be seen in the optical images of the AA7075 sample and confirmed by SEM images as inserted in Figure 4-1a. No shrinkage porosity was observed in the nano-treated 7075-1NP sample.

Table 4-1. Compositions of the AA7075 and 7075-1NP samples

	Al	Zn(wt.%)	Mg(wt.%)	Cu(wt.%)	Ti (wt.%)	TiC (vol.%)
AA7075	Bal.	5.61 ± 0.02	2.42 ± 0.02	1.33 ± 0.01	0.00 ± 0.00	-
7075-1NP	Bal.	5.53 ± 1.11	2.51 ± 0.09	1.45 ± 0.09	1.17 ± 0.13	0.86 ± 0.01

`

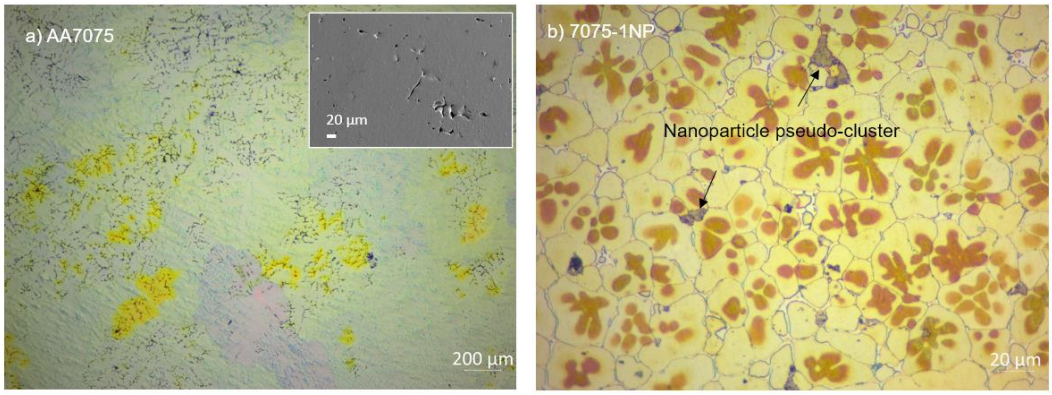

Figure 4-1. Optical images of the a) AA7075 sample and b) 7075-1NP sample. The inserted SEM image shows the shrinkage porosities

A two-thermocouple computer-aided thermal analysis (CATA)[155] system is shown in Figure 4-2. The CATA system is applied to record the temperature change during solidification. Briefly, samples of 400 g were melted at 750^{o}C and cooled in an alumina crucible. Its temperature was recorded by two thermocouples every 0.1 seconds by a data acquisition (DAQ) system. One thermocouple was placed in the center of the melt, and the other was attached to the wall of the alumina crucible. The average cooling rate is determined by the ratio of the total solidification temperature range over the total solidification time. The CATA system is utilized for temperature recording instead of DSC analysis because DSC analysis is usually done at a constant cooling or heating rate. In contrast, the CATA records the temperature of solidification in casting.

`

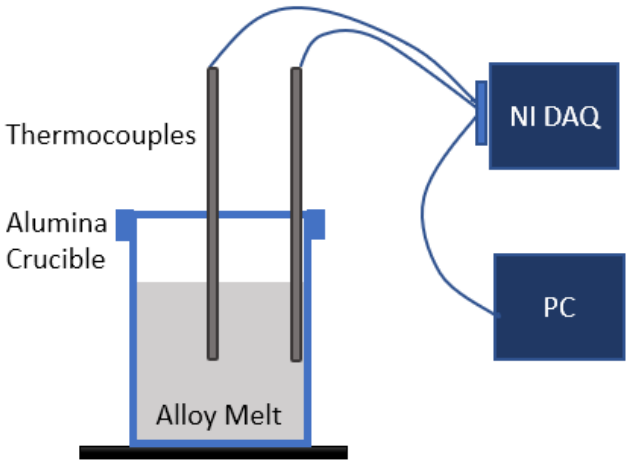

Figure 4-2. Illustration of temperature recording system during solidification

The temperature in the center of the ingot (T_c) and the temperature close to the wall (T_w) were recorded. The solidification curves were presented in Figure 4-3. The first derivative of temperature with respect to time (dT/dt) was calculated to show phase transformation and heat release[156,157]. The corresponding solid volume fraction was calculated based on the Newtonian baseline[158]. The solidification process was divided into three stages. Stage 1 indicates the nucleation event of α-aluminum, which starts from the first turning point of the cooling curve where the 7075-1NP sample has a fast drop of dT/dt, representing rapid heterogeneous nucleation initiated by TiC nanoparticles. In contrast, the initial drop in AA7075 was gentle. Stage 2 is the growth of α-aluminum, which is from 630°C to 480°C. Stage 3 indicates the nucleation and growth of the eutectic phase, where there is a peak in dT/dt. The calculated solid volume fraction at different temperatures is shown in Figure 4-3b. 7075-1NP started nucleation of α-aluminum at a smaller undercooling (higher temperature) due to heterogeneous nucleation, and it had a fast solidification speed at the beginning. At stage 3, the volume fraction of the eutectic phase was

`

different even though these alloys have similar composition and cooling conditions. The 7075-1NP had a lower volume of eutectic phases (4.4 vol.%), and the AA7075 has 6.0 vol.%.

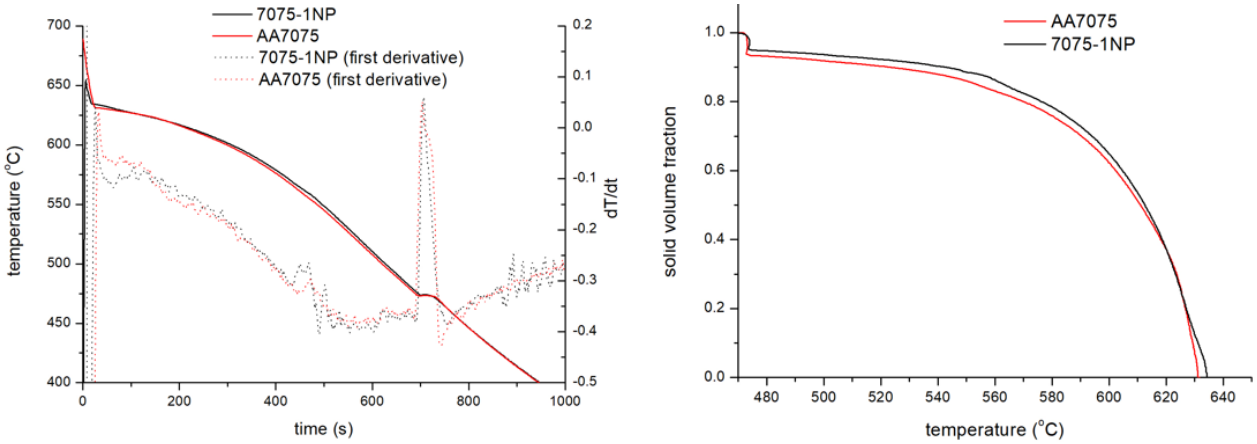

Figure 4-3. a) Cooling curves and dT/dt curve of AA7075 and 7075-1NP samples, b) solid volume fraction vs. temperature

4.1.2 Grain coherency point

The heat was transferred from the melt to the crucible wall. Thus the temperature recorded in the center thermocouple is higher than the temperature close to the wall. Meanwhile, latent heat from liquid-solid transformation will generate heat. If the heat transfer is lower than the heat generated, the overall temperature will rise. When free-floating solids in the liquid form a coherent network, the heat transfer is promoted through the solid, dominating over latent heat generation. Then, the temperature starts to drop. The grain coherency point (GCP) is the point at which the heat transfer through the solid becomes dominant during solidification[155]. The effect of nanoparticles on the GCP was studied by CATA. The temperature difference between T_w and T_c indicates whether heat transfer or heat generation is dominant. Figure 4-4 shows the cooling curves and delta T curves for AA7075 and 7075-1NP. The GCP is where the absolute delta T value reaches a maximum after the first peak, as indicated by blue dash lines. The grain coherency

`

temperatures (in the center) were derived with respect to the time. For the AA7075, GCP was at 633.1ºC while at 623.6 ºC for 7075-1NP. TiC nanoparticles lower the GCP, which means it takes longer to form a solid network in the melt. This is because nanoparticles inhibit grain and dendritic arm growth in the melt. Postponed GCP can reduce the casting defects, including hot cracking and shrinkage porosity, by allowing sufficient time for liquid backfill during solidification[159,160]. Optical images confirmed this elimination of the shrinkage porosity in Figure 4-1.

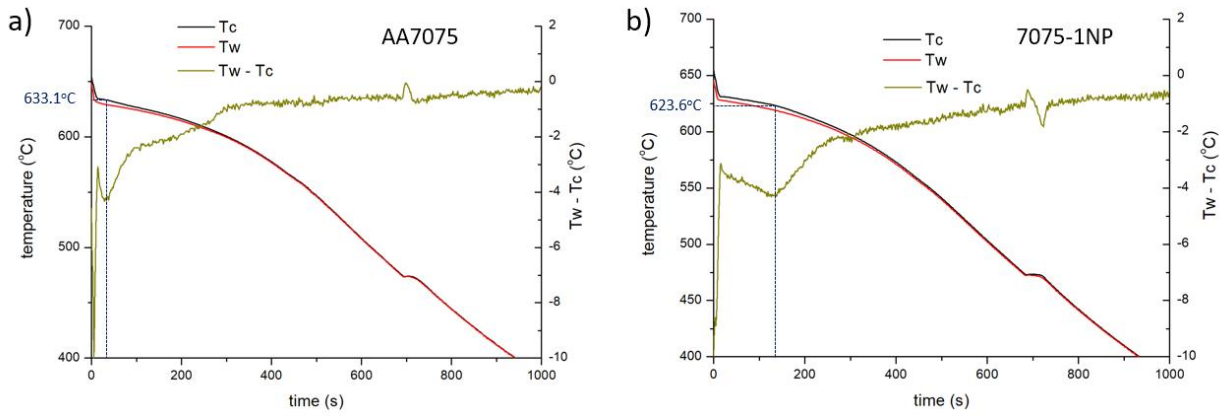

Figure 4-4. Cooling curves and Tw – Tc curves of a) AA7075 sample and b) 7075-1NP sample

4.2 Nanoparticle solute element interaction

When nanoparticles exist, one atom's energy state at the nanoparticle surface would be different from the energy in the matrix. In this section, a Cu-WC sample was prepared. Mg was added to the matrix to study the composition difference.

The first step is to fabricate Cu-20Mg master alloy. Pure Mg was wrapped in copper foil. Pure Cu, wrapped Mg were placed in a graphite crucible. $MgCl_2$ salt was added for oxidation protection. The crucible was slowly heated to 1000ºC and remained there for 20 min. The salt was removed, and the Cu-Mg master was cast in a graphite crucible. The second step is to fabricate

`

Cu-Mg-WC composite. Pure copper was melted at 1250 ^{o}C in a graphite crucible. WC nanoparticles were mixed with $MgCl_2$. A certain amount of Cu-20Mg master with the WC-salt mixture was added on top. It was designed to have 0.4 wt.% of Mg and 5 vol.% of WC. After 10 mins, salt was removed, and the sample was cast in a graphite crucible. The master was then prepared for SEM and EDS observation. As WC nanoparticles form pseudo-clusters in Cu, there are nanoparticle (NP) rich and free regions. EDS mapping was performed in different regions to discover a difference in Mg composition in two regions, as shown in Figure 4-5. The overall Mg content is 0.25 wt.%, and the loss was due to the oxidation of Mg. In the NP-free region, the Mg weight percentage dropped to 0.19%. EDS point scanning was applied to confirm the results. In Figure 4-6, the Mg weight percentage is 0.38 ± 0.13% within the NP-rich zone while 0.16 ± 0.05% in the NP-free region showing that Mg has a higher concentration in the NP-rich region, which could be attributed to more defects (interfaces, voids, dislocations, grain boundaries) existed in the nanoparticle-rich zone where elements stay in these defects to reduce overall energy. Similar effects are grain boundary segregation[161] and solute enrichment at the particle interface[162].

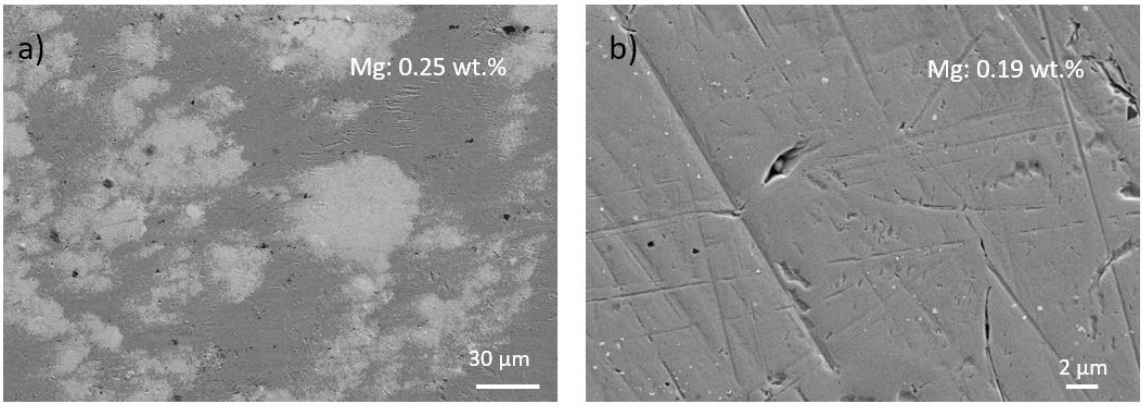

Figure 4-5. a). SEM image of the Cu-0.25Mg-5WC sample, b) larger magnification of NP free region

`

a)

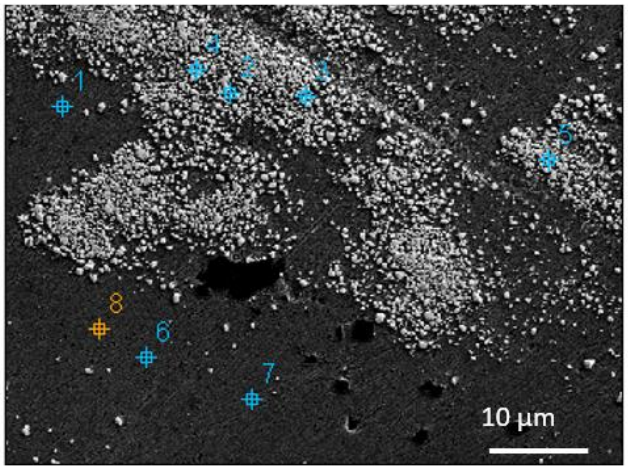

b)

Point No.	NP rich region	NP Free region
1		0.172
2	0.200	
3	0.379	
4	0.500	
5	0.428	
6		0.182
7		0.091
8		0.192
Ave.	0.38	0.16
STD	0.13	0.05

Figure 4-6. a) SEM image of the Cu-0.25Mg-5WC sample, b) Mg composition by point scanning

4.3 Nanoparticle influence solutionization

Heat treatment is often necessary for many alloys to obtain advantageous properties. Solution treatment is to raise a sample to a temperature below liquidus temperature to dissolve secondary phases. If the secondary phases were not entirely dissolved into the metal matrix, they would be detrimental to alloy properties such as ductility, corrosion resistance, and fatigue. Here in this section, a high-zinc Al-8.6Zn-2.8Mg-1.8Cu alloy containing TiC nanoparticles was fabricated to study how nanoparticles influence solution treatment.

The Al-8.6Zn-2.8Mg-1.8Cu sample containing 1.0 vol.% of TiC was fabricated. In-situ Al-TiC master nanocomposite containing 3 vol.% of TiC nanoparticles was used. Pure aluminum was melted at 860^{o}C, and argon protection was applied. Designated amounts of pure zinc, magnesium, copper, and Al-TiC master nanocomposite were added to the melt. Mechanical stirring (30RPM) was applied to help achieve a homogeneous melt. After 10 mins, the surface oxidation layer was skimmed away before casting the alloy in a steel rod mold. A control sample without nanoparticles

`

was fabricated as well. Optical images and SEM were used for microstructure observation. Detailed parameters are similar to previous sections. The actual composition of the alloy was studied by inductively coupled plasma mass spectroscopy (ICP-MS, NexION 2000, PerkinElmer). Differential Scanning Calorimetry (DSC) (TA Instruments, Q600) was used to test the latent heat during heating. The weight of the tested samples was 40 mg, and the heat flow was normalized. The chemical compositions of the samples are shown in Table 4-2. The calculated TiC volume percentage is 1.0 vol.%. The optical images of the two samples were shown in Figure 4-7. The grain size of the control sample is 272.3 ± 69.2 μm while the nano-treated sample has an average grain size of 30.4 ± 10.3 μm.

Table 4-2. Compositions of the Al-8.6Zn-2.8Mg-1.8Cu sample

Sample No.	Zn	Mg	Cu	Fe	Si	Ti	Al
Control	8.84±0.02	2.91±0.17	1.80±0.02	0.08±0.00	0.04±0.00	0.00±0.00	Bal.
Nano-treated	8.67±0.54	2.83±0.07	2.05±0.03	0.17±0.01	0.04±0.00	1.61±0.01	Bal.

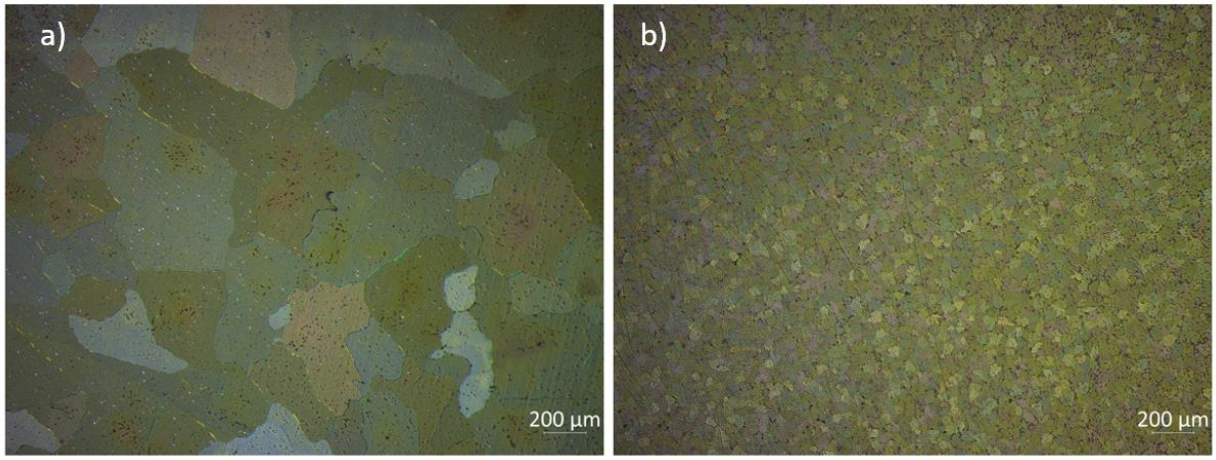

Figure 4-7. Optical images of as-cast a) control sample; b) nano-treated sample

`

4.3.1 Solution temperatures

DSC analysis was done to select a suitable solution treatment temperature for the alloy. The heat flow during heating up was recorded and presented in Figure 4-8. There is a gradual turning point of the curve at around 460^{o}C, where the melting of the eutectic phase starts. Three different solution treatments were experimented with after homogenization at 450^{o}C for 24 hours based on the DSC results. The first one is solution treatment at 460^{o}C for 1.5 hours. The second is 470^{o}C for 1.5 hours, and the last is a step solution treatment at 460^{o}C for 1 hour followed by 480 ^{o}C for 1 hour. The SEM images of the nano-treated sample after solution treatment were presented in Figure 4-9. The remaining secondary phases were calculated using the SEM pictures. The percentage (area percentage in the SEM pictures) was obtained from each sample's three SEM images. The as-cast sample contains 7.50 ± 1.03% of the secondary phase. After solution treatment at 460^{o}C for 1.5 hours, the remaining secondary phase is 2.37 ± 0.35%, and the percentage drops to 1.27 ± 0.02% for the solution temperature at 470^{o}C. The step solution treatment (460^{o}C for 1 hour followed by 480 ^{o}C for 1 hour) further reduces the remaining secondary phase to 1.12 ± 0.09%. Therefore, this step solution treatment was chosen for the following experiments.

`

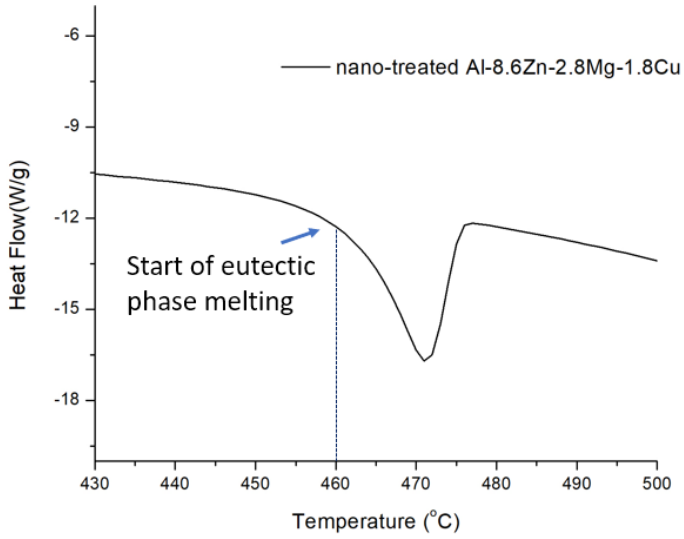

Figure 4-8. DSC analysis. Heat flow during heating up

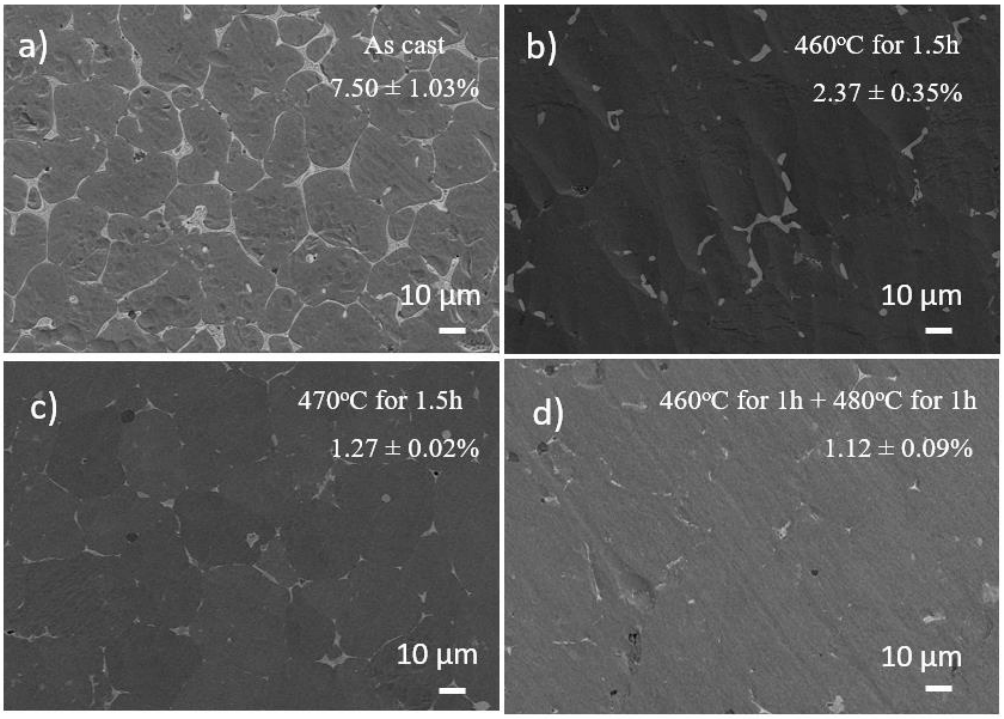

Figure 4-9. SEM images of the nano-treated sample with different heat treatments. a) as cast, b) 460°C for 1.5 hours, c) 470°C for 1.5 hours, d) 460°C for 1 hour and 480°C for 1 hour. The inserted numbers are the area percentages of the undissolved secondary phases

`

4.3.2 Dissolution of secondary phase

The same heat treatment was applied to the control sample. SEM images of the control sample and the nano-treated one were shown in Figure 4-10. After solution treatment, a large secondary η phase ($MgZn_2$) in the control sample, as shown in Figure 4-10a, b, was not completely dissolved. On the contrary, in Figure 4-10c, d, most secondary phases were dissolved in the nano-treated sample. In the control sample, a large sphere-shaped η phase was in the matrix, and long stripe-shaped secondary phases (more than 10 μm) were along the grain boundaries. These large secondary phases could reduce the overall properties of the alloy. Moreover, the undissolved secondary phase means fewer precipitates could be formed during the aging process. With the help of nanoparticles, no large η phase was observed after solution treatment. Some relatively sizeable secondary phase (Al_7Cu_2Fe) was found in the nano-treated sample due to iron contamination. Nanoparticles could be found along the grain boundaries. As shown in Figure 4-10d, the nanoparticles mark a contour of a disappeared secondary phase similar to the one shown in Figure 4-10b, which could be direct evidence of nano-treating facilitated solutionization.

`

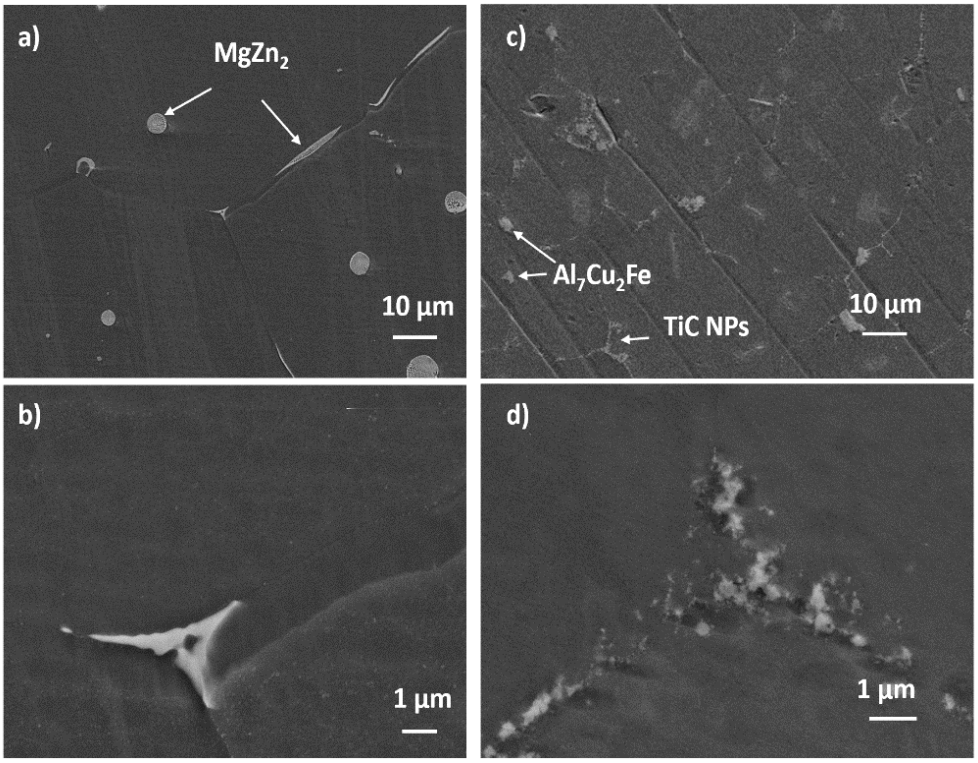

Figure 4-10. SEM pictures of the control sample and the nano-treated alloy after solution treatment, a, b) control sample; c, d) nano-treated sample

The remaining secondary phases of the control sample were also calculated, and the comparison of area fraction was shown in Figure 4-11. In the as-cast samples, about 7% of the area was occupied by secondary phases, while there is no significant difference between the control sample and the nano-treated sample. After two-step solution treatment, 2.95 ± 0.31% of the secondary phase remained in the control sample, while only 1.12 ± 0.22% remained in the nano-treated sample. Most secondary phases were dissolved in the nano-treated sample, considering the nanoparticles added in and the undissolved phases in the secondary phase zones. The faster dissolution is probably caused by a faster diffusion of the alloying elements. The presence of nanoparticles would provide a high area of the nanoparticle-matrix interface. The diffusivity along these interfaces would be higher to facilitate atoms diffuse into the matrix. Moreover, there would

`

be a higher dislocation density in the region close to nanoparticle pseudo-dispersion zones due to a high CTE mismatch[21]. Dislocations could also help alloying elements diffusion. Traditionally these large secondary phases in high-zinc Al-Zn-Mg-Cu alloy will make the alloy more sensitive to hot cracking and stress corrosion cracking during solid-state processing. Nano-treating could provide a new method to eliminate all large secondary phases.

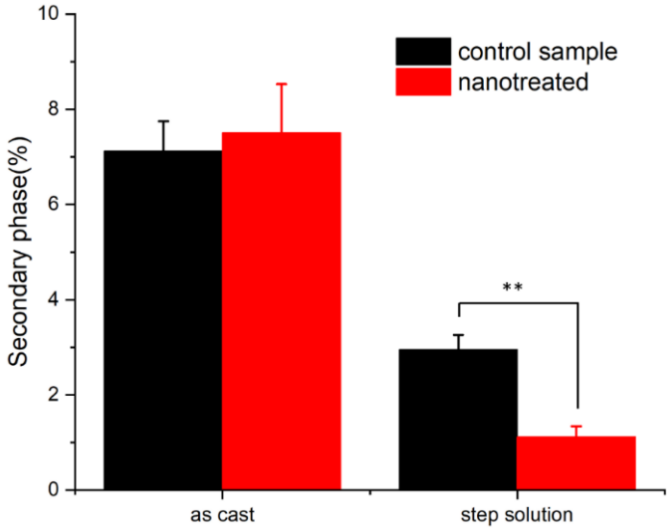

*Figure 4-11. Percentage of remaining secondary phase. (** p<0.01)*

To study the promoted dissolution of the secondary phase, the time required to dissolve a certain amount of solutes is described by Equation 4-1, where t is the time; M is the amount of secondary phase; A is area; $\frac{\partial C}{\partial x}$ is the concentration gradient of solute atoms, and D is the diffusivity of solute. Thus, mathematically, a reduction in M, M/A, and an increase in D can reduce the dissolution time.

$$t = \frac{M}{A \cdot \frac{\partial C}{\partial x} \cdot D} \tag{4-1}$$

`

Figure 4-12 shows that the as-cast nano-treated high-zinc Al-Zn-Mg-Cu alloy has smaller secondary phase domains (~10 μm) while the control sample has significantly larger secondary phases. This indicates that nanoparticles reduce the M/A ratio by modifying the secondary phase, which helps reduce dissolution time. In Chapter 4.1, the reduction of the overall volume fraction of secondary phases was found in the 7075-1NP sample, which is a manifestation of reduced total M. However, Figure 4-11 shows the nano-treated high-zinc Al-Zn-Mg-Cu alloy has a slightly larger volume fraction of secondary phases. This dilemma will be discussed and explained in Chapter 5.4.

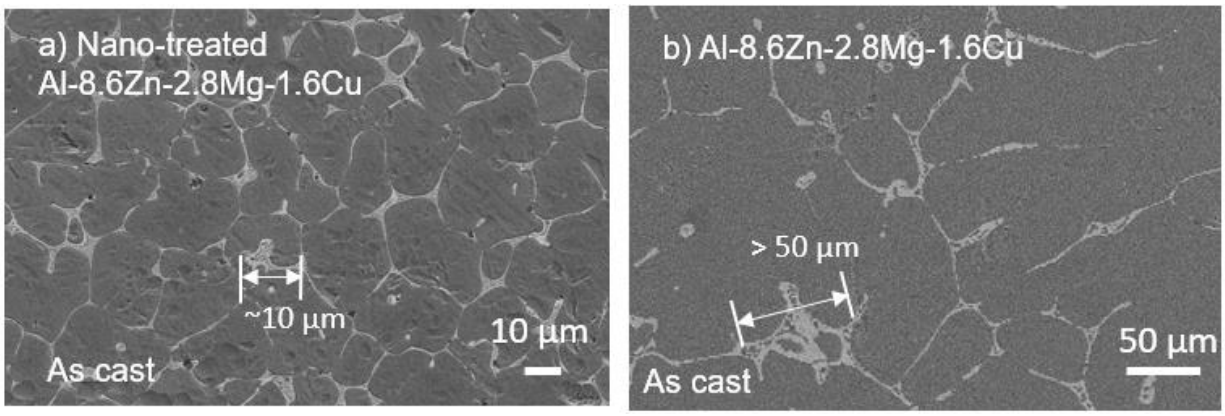

Figure 4-12. SEM images of the as-cast samples. a) nano-treated Al-8.6Zn-2.8Mg-1.6Cu sample and b) the control sample

Another factor related to the dissolution speed is diffusivity. It is well known that the diffusivities of solute atoms through different media are different, and their relationship is $D_{interface} > D_{dislocation} > D_{bulk}$[163]. The diffusion through interfaces or grain boundaries is faster than the diffusion along dislocations, and the diffusion in bulk is the slowest. As nanoparticles are pushed to the grain boundaries to stay with secondary phases, significant nanoparticle-secondary phases interfaces exist to facilitate diffusion.

`

4.4 Nanoparticle influence on aging and precipitation

Nanoparticles influence not only the solution treatment but also the aging process. After solutes are dissolved into the matrix, the alloys are water quenched to obtain supersaturated solid solutions. Precipitates form when the alloys are heated again. Uniform precipitates can significantly enhance the strength of the alloys. The nucleation of the precipitates is usually related to vacancies[162,164]. Stress corrosion cracking (SCC) has been a long-term issue for high-strength Al-Zn-Mg-Cu alloy. The SCC is related to the precipitation free zone (PFZ) close to the grain boundaries[165], where vacancies are depleted. Here in this section, the nanoparticles' influence on the aging process of different Al-Zn-Mg-Cu alloys was studied. The PFZ was determined by TEM as well.

4.4.1 Aging time

The high-zinc Al-8.6Zn-2.8Mg-1.8Cu alloy discussed in Chapter 4.3 was further used for the aging study. After step solution treatment, both the control and nano-treated samples were water quenched to get a supersaturated solid solution. The samples were then placed at 120^{o}C in a heat treatment oven at different times. Microhardness tests were done to observe the different stages of aging. The microhardness vs. aging time curves is presented in Figure 4-13. As discussed before, the nano-treated sample dissolved more alloying elements, and thus more precipitates could form. At the initial half an hour, the strength of both samples increased dramatically due to the formation of GP zones. After that, the hardening became slower and reached a peak at around 4h. After that, the hardness dropped, attributed to the growth of GP zones. For the nano-treated sample, the hardness increased to 233HV in 16 hours when some GP zones transformed into η' phase[166]. The peak hardness is improved by 10HV with 1 vol.% TiC nanoparticles, which is the same as in other Al-TiC nanocomposite experiments[167]. The nano-treated sample would reach peak

`

hardness earlier than the control sample because nanoparticles facilitate the aging process[162]. The higher hardness indicates a higher strength of the nano-treated sample. However, the above-facilitated aging is based on a different solution treatment result since more solute elements dissolve in the solid solution. When the concentration of the alloying elements is higher, the nucleation of GP zones would be easier.

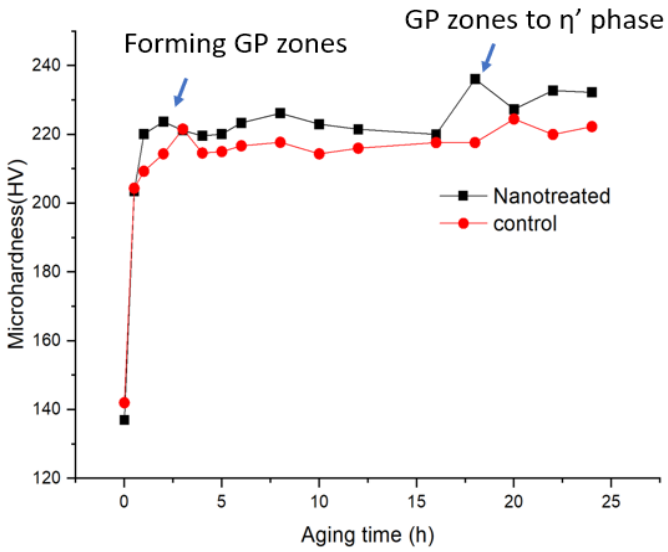

Figure 4-13. Microhardness vs. aging time(Al-8.6Zn-2.8Mg-1.8Cu alloy)

The case mentioned above shows facilitated aging in artificial aging. Natural aging was then studied in aluminum 7005. This alloy has relatively low alloying contents (Al-4.5Zn-1.4Mg), and thus the solute elements can be quickly dissolved during solution treatment. The fabrication method of the control 7005 alloy and nano-treated 7005 alloys was similar to that of the high-zinc Al-8.6Zn-2.8Mg-1.8Cu alloy. The solution treatment was at 450^{o}C for 1 hour. Then the samples were air quenched and left in air for natural aging. The microhardness profile during aging was presented in Figure 4-14. Generally, the nano-treated sample (black line) has a higher

`

microhardness due to its smaller grain sizes. The nano-treated sample reached its highest microhardness after 8 days of natural aging, while the pure AA7005 alloy reached its first peak after 10 days' natural aging. Due to the transformation of GP zones to the η' phase, the hardness drops, and the nano-treated sample also reached the first microhardness valley earlier, as shown in Figure 4-14. Therefore, it is believed that nanoparticles also facilitate natural aging.

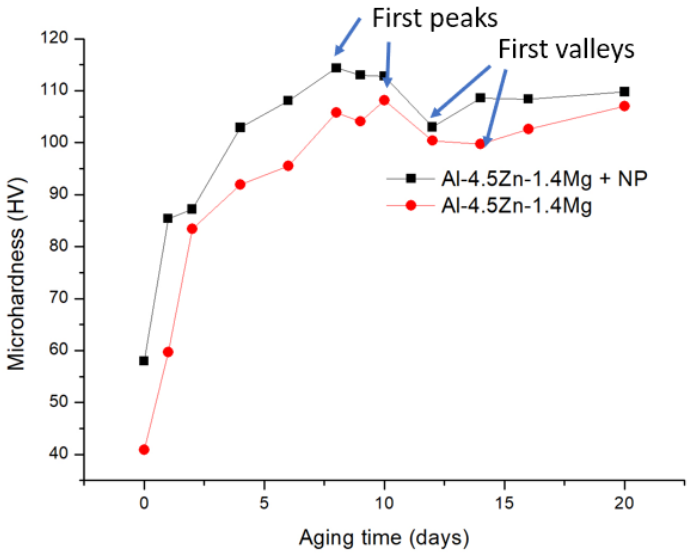

Figure 4-14. Microhardness vs. aging time (Al-4.5Zn-1.4Mg alloy)

There are two potential causes to facilitate aging. One is the higher supersaturation caused by the better dissolution of secondary phases, and the other is by promoted diffusion of solute atoms in the matrix. As shown by the HAADF-STEM images in Figure 4-15, dislocations were found close to nanoparticles. For example, in both the Al-6.0Zn-2.8Mg-0.5Cu sample containing 1.0 vol.% of TiC and the Al-4.6Cu-3.0Mg sample with 1.0 vol.% of TiC, dislocations were observed after solutionization and water quenching. These dislocations not only facilitated the

`

diffusion of solute atoms but also became nucleation sites for GP zones[168]. More details about these two samples are discussed in Chapters 6 and 7.

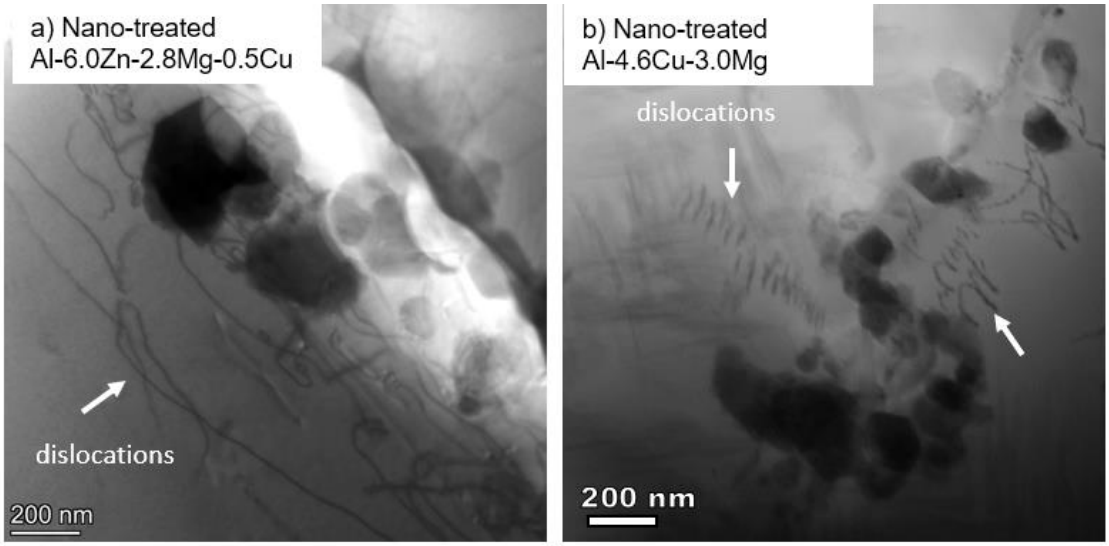

Figure 4-15. HAADF-STEM images of a) Al-6.0Zn-2.8Mg-0.5Cu sample containing 1.0 vol.% of TiC and b) Al-4.6Cu-3.0Mg with 1.0 vol.% of TiC, after solutionization and quenching

4.4.2 Precipitate free zone

The precipitate free zone (PFZ) of AA7034 alloy and a nano-treated 7034 alloy was compared in Figure 4-16. Aluminum alloy 7034 (Al-11.5Zn-3.5Mg-1.5Cu) was fabricated and heat-treated for TEM observation. Both control and nano-treated samples contain 1 vol.% TiC nanoparticles. The fabrication method was similar to other Al-Zn-Mg-Cu alloys described in the previous sections. The PFZ of the nano-treated one is 30 nm wide, while approximately 50 nm wide for the pure AA7034. Since the formation of PFZ is related to the depletion of vacancies or solute atoms, the decreased PFZ indicates nano-treating induced a more uniform distribution of the solute atoms across the grain boundary or less vacancy depletion close to the grain boundary. The density of the precipitates was also different. The nano-treated sample shows much denser

`

precipitates than the control one. The higher density of the precipitate attributes to a higher supersaturation level of the solutes due to a better dissolution of secondary phases.

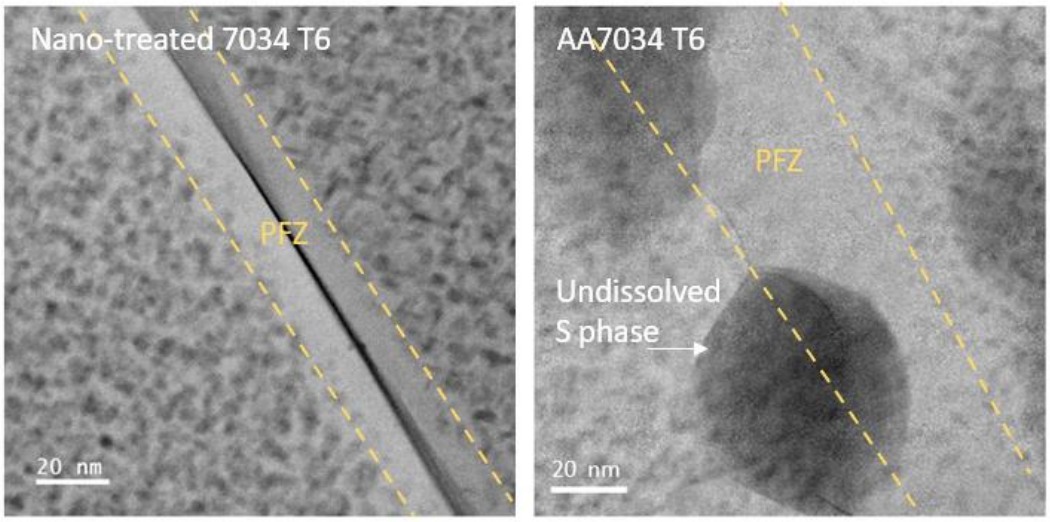

Figure 4-16. TEM images of the PFZ zone and precipitates in nano-treated 7034 alloy(left) and AA7034 alloy (right)

4.5 Nanoparticle influence on texture

Nanoparticles can affect the microstructure during plastic deformation. The orientation of the grains would be influenced. The cast ingot was extruded at 450℃ with an extrusion ratio of 30 and an extrusion rate of 0.1 mm/s. The texture analysis was performed by a Bruker D8 Advance X-ray diffractometer (equipped with Euler ring, Cu Kα (λ=0.1542 nm), 40kV, 40mA). During 2theta scanning, samples were placed perpendicular to the extrusion direction along the radial plane. The Schultz reflection method was applied to get the pole figure. As aluminum alloy structure is FCC, (111), (200), and (220) pole figures are measured and presented in Figure 4-17. Both the 7034-1NP sample and AA7034 sample exhibit typical fiber texture but the nano-treated sample (7034-1NP) has relatively weaker texture, as shown by the texture intensity.

`

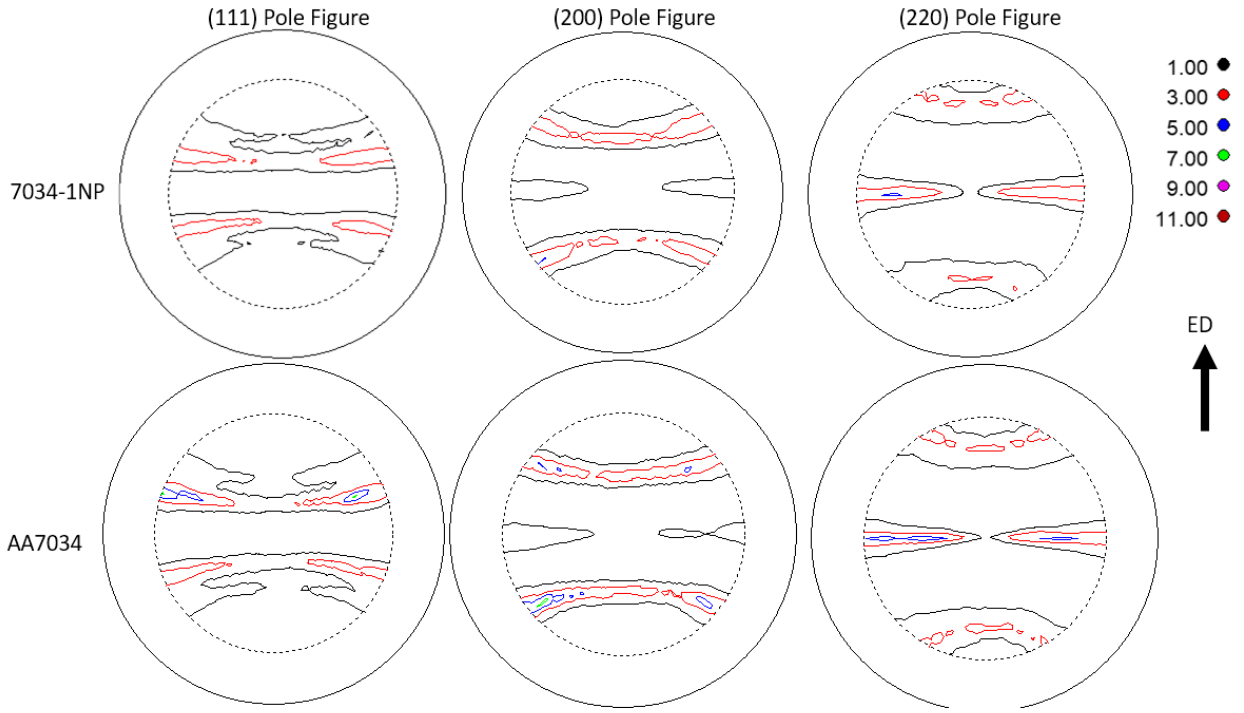

Figure 4-17. Measured pole figures of 7034-1NP and AA7034 sample

4.6 Summary

Nanotreating effects on alloys are studied, and the summary is presented below:

1. Solidification: During solidification, a nano-treated 7075 alloy starts nucleation of the primary phase at a smaller undercooling (higher temperature) due to heterogeneous nucleation. Nanoparticles also reduce the final volume fraction of eutectic phases. The nano-treated sample has a lower grain coherency point, as it takes longer to form a solid network in the melt. It suggests that nanoparticles inhibit both grain growth and dendritic arm growth in the melt. The lower grain coherency point is beneficial for preventing casting defects such as hot cracking and shrinkage porosity.

`

2. Solute elements: In the Cu-Mg-WC nanocomposite, Mg concentration is higher in the nanoparticle-rich regions. This shows that the nanoparticles tend to attract solute atoms from the matrix.

3. Solution treatment: TiC nanoparticles are found to promote the dissolution of secondary phases during solution treatment of Al-8.6Zn-2.8Mg-1.8Cu alloy. After a step solution treatment, the remaining secondary phase in the nano-treated alloy is 1.12 ± 0.22%, while 2.95 ± 0.31% for the control sample. The facilitated solution treatment is due to refined secondary phases and a promoted diffusion caused by diffusion along with the interfaces and dislocations in the nano-treated sample.

4. Aging and precipitation: TiC nanoparticles facilitate the artificial aging process in Al-8.6Zn-2.8Mg-1.8Cu alloy and natural aging in AA7005 alloy. The promoted aging is caused by a higher supersaturation of solute atoms and dislocations. In addition, nanoparticles reduce the width of the precipitate free zone and increase the precipitation density in AA7034. This is attributed to a better supersaturation and a more uniform distribution of solute atoms after quenching.

5. Texture: TiC nanoparticles reduce the texture intensity in aluminum 7034 alloys.

Overall, the nano-treating effects can be summarized in Figure 4-18. Briefly, nano-treating alters the solidification behavior and promotes solution treatment and aging. Two critical effects are summarized according to their functions: “antibody effect” to enable alloys manufacturing by eliminating solidification cracks during casting of these difficult-to-cast alloys, promoting solution treatment of highly-alloyed metals, promoting aging, and “vitamin effect” to tune alloy microstructure and properties.

`

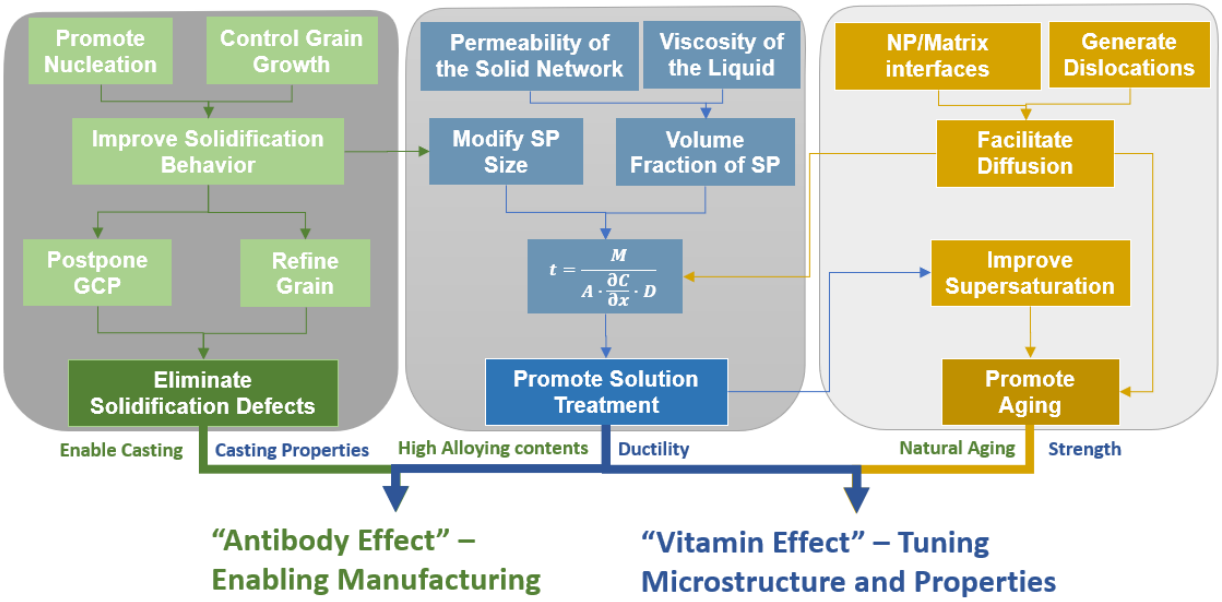

Figure 4-18. Illustration of nano-treating effects

`

Chapter 5 High Strength Al-Zn-Mg-Cu Alloy

New clean-energy vehicles have become popular. Aluminum alloys were used increasingly to reduce the overall weight of vehicles. High-zinc Al-Zn-Mg-Cu alloys provide the highest strength among all aluminum alloys. Zn and Mg are the main strengthening elements, while the total amount of Zn, Mg, and Cu determine the strength as they form the precipitates (η and its precursor η')[131] for strengthening. To achieve super high strength, higher zinc content is preferred. Yang et al. fabricated Al-16Zn-3Mg-1Cu alloy to deliver a strength of 800MPa[169]. AA7034 alloy consists of 11-12% Zn and 2.0-3.0% of Mg is the strongest commercial aluminum alloy with a tensile strength of 750 MPa. However, certain drawbacks come with high alloying. First, the high alloy content will often cause severe segregation at the grain boundary, resulting in coarse secondary phases[122,123,169]. These secondary phases are difficult to be dissolved during solution treatment[118,124]. Secondly, a higher Zn content makes the alloy prone to hot cracking, porosity, and inhomogeneity during solidification[4,131]. A fast cooling rate (10^2 - 10^6 K/s) is often required to suppress these issues. For example, AA7034 is usually produced by spray casting, which makes it expensive to produce.

As discussed in Chapter 4, nano-treating can modify the solidification behavior of the alloy, refine the microstructure, and promote the solution treatment. Nano-treating may enable the casting of high-zinc aluminum alloys. Here in this chapter, the nano-treated high-zinc aluminum alloy was fabricated using the conventional casting method at a slow cooling rate, and high-strength and reasonable ductility were achieved. A similar two-thermocouple computer-aided thermal analysis (CATA) system in Figure 4-2 was applied to record the cooling curve during solidification.

`

5.1 Fabrication of nano-treated high zinc Al-Zn-Mg-Cu alloy

AA7034 alloy containing different volume percentages of TiC nanoparticles were fabricated. The nano-treated samples containing 1.0 vol.% and 2.0 vol.% of nanoparticles are termed 7034-1NP and 7034-2NP, respectively. The control sample is termed AA7034 here. The fabrication of the nano-treated alloys is similar to 7075-1NP samples in Chapter 4.1. Briefly, pure aluminum was melted first at 820^{o}C. Then, a certain amount of master nanocomposites containing 3.2 vol.% of TiC nanoparticles, pure zinc, magnesium, and copper were added to obtain the designated composition. Stirring and degassing were applied for 40 mins before the alloy was downhill cast in an alumina crucible. The final ingot was a rod with a diameter of 45 mm. The temperature of recorded by a CATA system as in Figure 4-2. The temperature recording frequency was 10 Hz, and both center and wall temperatures (T_c and T_w respectively) were recorded. The cast ingot was homogenized at 450^{o}C for 24h and extruded at 450℃. The extrusion ratio is 30, and the extrusion rate is 0.1 mm/s. A control sample of pure AA7034 was also fabricated.

Pieces of the sample were cut from the center of the ingots and prepared for optical, SEM, and TEM characterization. Tensile bars of ASTM standard were cut by wire electrical discharge machining (EDM). These tensile bars were solutionized at 480^{o}C for 2 hours, followed by water quenching. The aging was done at 120℃ for 16 hours. Microhardness was measured as well. The average cooling rate during casting was determined by the ratio of the total solidification temperature range over the total solidification time. The volume fraction of secondary phases was estimated by the area fraction of secondary phases in the SEM images. ImageJ was used to calculate the volume fraction of secondary phases in SEM images. The images were converted to black/white images by adding a brightness threshold, and the area fraction of the secondary phases were then calculated. Finally, the composition of the samples was tested by a spark emission

`

spectrometer (Spark CCD 7000, NCS). All the above property tests including, tensile, microhardness, volume fraction, and composition tests, were done 6 times, and average values are presented later in this chapter.

5.2 Microstructure before and after heat treatment

The composition of the samples was presented in Table 5-1. The fabricated AA7034 and nano-treated 7034-1NP and 7034-2NP samples have similar compositions except for different TiC volume fractions.

Table 5-1. Compositions of the samples

	Al	Zn(wt.%)	Mg(wt.%)	Cu(wt.%)	Ti (wt.%)	TiC (vol.%)
AA7034	Bal.	11.53 ± 0.02	3.31 ± 0.02	1.53 ± 0.01	0.00 ± 0.00	-
7034-1NP	Bal.	11.13 ± 1.11	3.53 ± 0.09	1.45 ± 0.09	1.19 ± 0.13	0.97 ± 0.01
7034-2NP	Bal.	11.35 ± 0.25	3.56 ± 0.05	1.66 ± 0.05	2.41 ± 0.23	2.01 ± 0.02

The optical images were presented in Figure 5-1. TiC nanoparticles act as very effective grain refiners[10,170]. At the slow cooling in this study, the grain size of cast AA7034 is above 500 µm but reduced to 59.1 ± 4.9 µm and 49.1 ± 7.0 µm after adding 1 vol.% and 2 vol.% of TiC nanoparticles, respectively. The large black dots in Figure 5-1c, e are nanoparticle pseudo-clusters and secondary phases after etching. White arrows indicate the extrusion direction of these samples in Figure 5-1 b, d, f. The nanoparticle pseudo-clusters were extended to parallel black bands along the extrusion direction. The bands are wider and denser in the 7034-2NP sample due to a higher volume fraction of nanoparticles. Dendritic arms appeared in the as-cast AA7034 sample before extrusion, but they disappeared after extrusion. TiC nanoparticles suppressed the dendritic arms as they inhibit the grain growth to form equiaxed grains during solidification [6,171]. These dendritic grains were modified to equiaxed grains by nanoparticles.

`

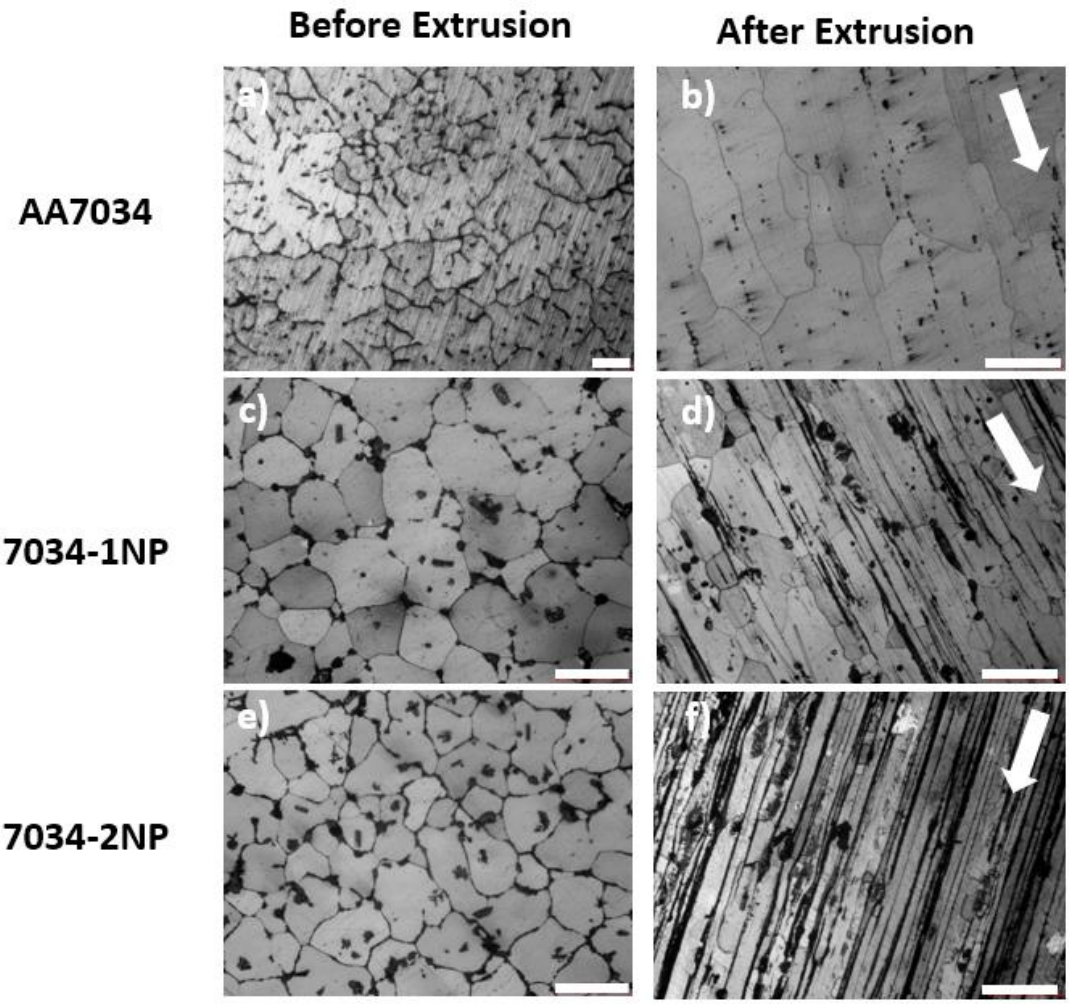

Figure 5-1. Optical images of fabricated nano-treated 7034 of different nanoparticle volume fractions before and after extrusion. Scale bar = 100 µm. Write arrows indicate extrusion direction

SEM images were taken to reveal a more detailed microstructure in the samples before heat treatment. As shown in Figure 5-2, without nano-treating, the AA7034 cast sample has severe segregation at grain boundaries as thicker eutectic lamellas, mainly the T ($Mg(Zn, Cu, Al)_2$) phase was shown in Figure 5-2a, b. The eutectic phases of 7034-1NP and 7034-2NP between the equiaxed grains are shown in Figure 5-2d, g. Nanoparticles usually reside with the eutectic phase as indicated by the arrows in Figure 5-2e, h, as the solid front pushed nanoparticles during

`

solidification [172]. After nano-treating, smooth, connected, and thick secondary phases became rugged and divorced to yield a better hot tearing resistance[155]. After extrusion at 450℃, the secondary phases were partially dissolved during hot extrusion. The connected secondary phases of the AA7034 sample were broken into segments. The nanoparticle pseudo-clusters in 7034-1NP and 7034-2NP samples were elongated as bands as shown in Figure 5-2f, g. The undissolved secondary phases can be seen between nanoparticle bands and within the bands in 7034-1NP and 7034-2NP samples.

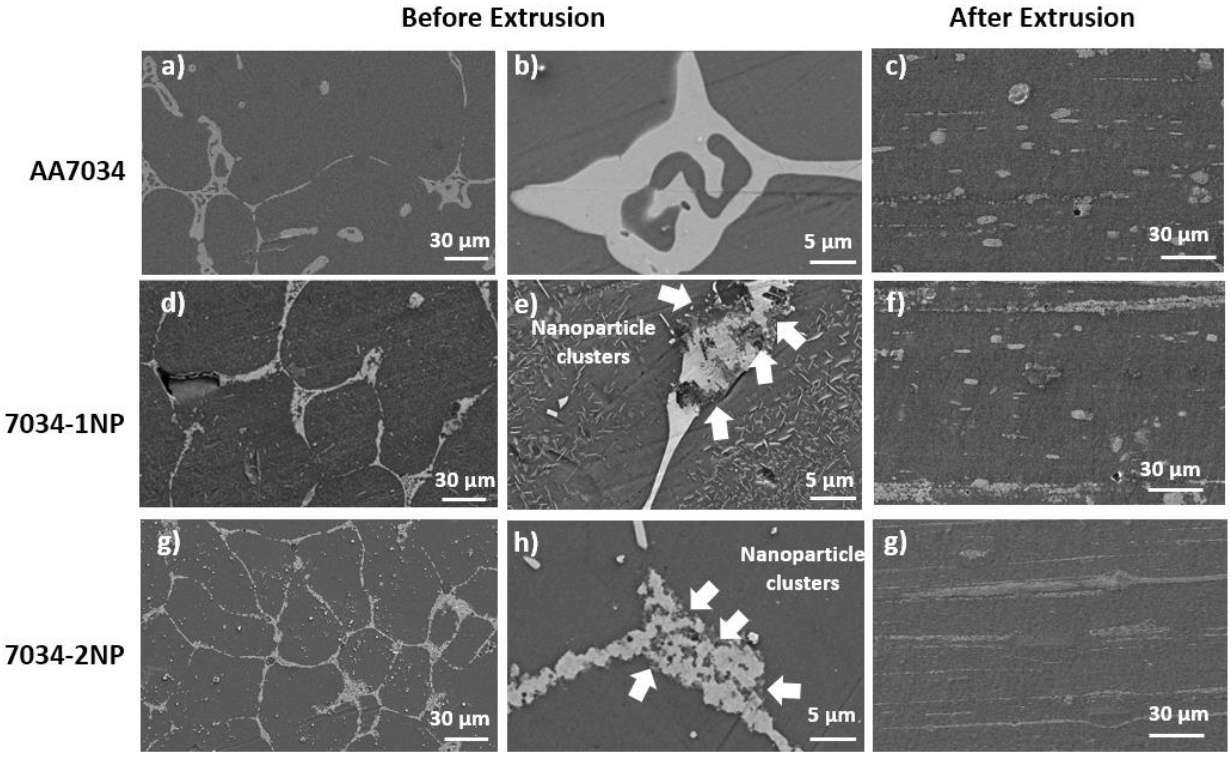

Figure 5-2. SEM images of nano-treated alloys and control samples. a, b)AA7034, d, e)7034-1NP, g, h)7034-2NP before extrusion. c)AA7034, f)7034-1NP, g)7034-2NPafter extrusion. White arrows indicate nanoparticles

SEM images of the samples after heat treatment were presented in Figure 5-3. Since the transformation from T phase to S(Al_2CuMg) is difficult when Zinc content is higher than 8 wt.%[173],

`

here in this work, we mainly focus on T phase dissolution. The dissolution was incomplete in the AA7034 samples (Figure 5-3a, b) and 7034-1NP samples before extrusion (Figure 5-3c). Because of recrystallization, the morphologies of AA7034 samples before and after extrusion are similar. All secondary phases were dissolved in 7034-2NP samples with or without extrusion, while the secondary phases in 7034-1NP dissolved completely only after extrusion. According to Fick's second law, the time needed for a certain amount of solutes (M) to diffuse across a surface area (A) can be expressed as[174]:

$$t = \frac{M}{A \cdot \frac{\partial C}{\partial x} \cdot D}, \tag{5-1}$$

in which t is time, $\partial C/\partial x$ is the composition gradient, and D is the diffusivity of the solute. Therefore, extrusion can help solution treatment because some secondary phases can be dissolved during hot extrusion, and the large eutectic phases were deformed and split into smaller thin segments (smaller M/A). Furthermore, defects, including dislocations, voids, grain boundaries formed during extrusion, would provide highways for solute diffusion (larger D) and promote dissolution during solution treatment. Nanoparticles have a positive effect on dissolution as well. There were no secondary phases in 7034-2NP samples, as shown in Figure 5-3e, while there were some T phases left in the 7034-1NP sample, but the segments were smaller than the remaining ones in the AA7034 sample, indicating a smaller M compared to AA7034. The interface of the secondary phases was rugged to yield a larger surface area for diffusion. The promoted dissolution also benefited from a faster diffusion through boundaries and dislocations as ceramic nanoparticles would generate a higher density of dislocations[21,162].

`

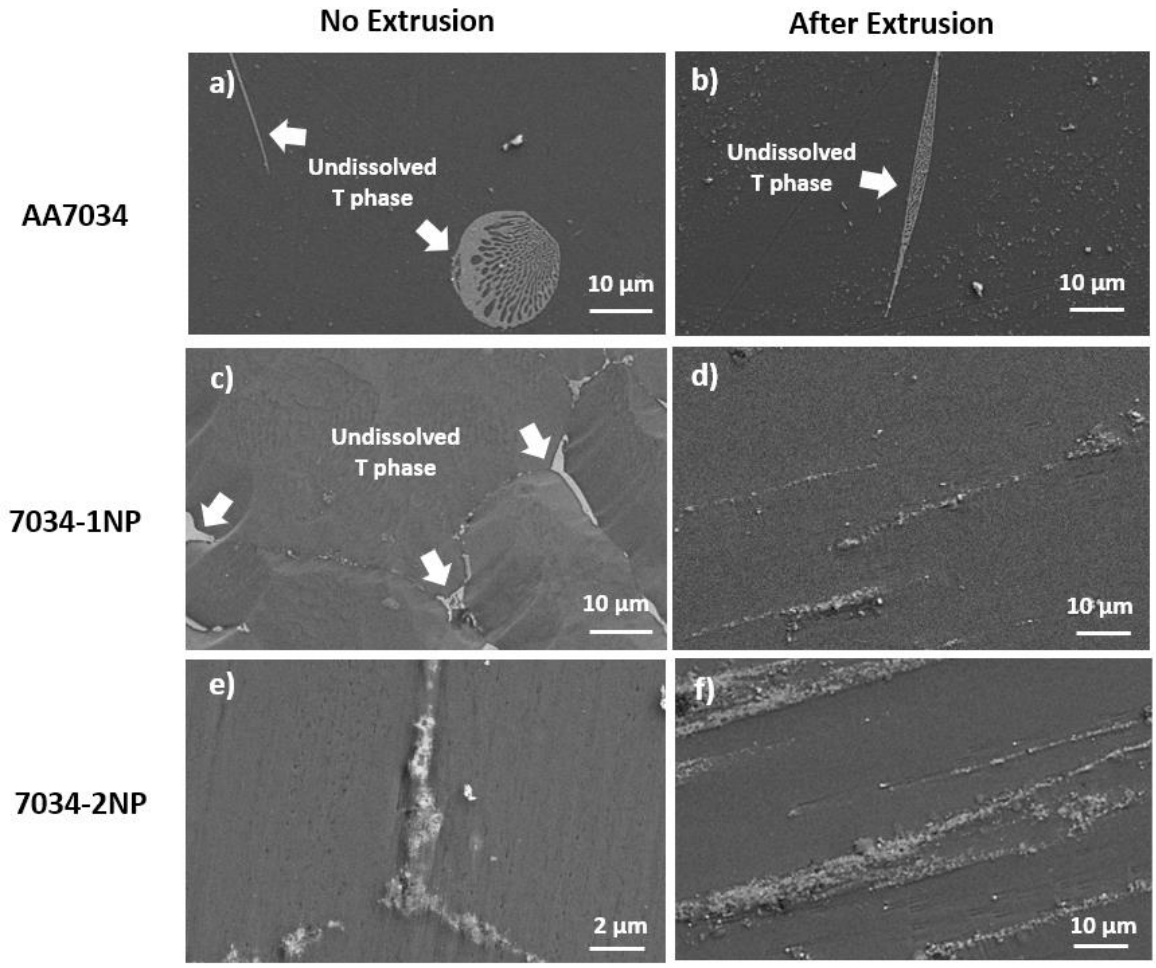

Figure 5-3. SEM images of samples after heat treatment a) AA7034 without extrusion, b) AA 7034 after extrusion, c) 7034-1NP without extrusion, d) 7034-1NP after extrusion, e) 7034-2NP without extrusion, f) 7034-2NP after extrusion

A more detailed observation of the precipitates and precipitate free zone (PFZ) along the grain boundaries is done by TEM. In Figure 5-4a, nanoparticle clusters can be found along the grain boundary, but no secondary phases remained. However, in Figure 5-4c, undissolved secondary phases exist along the grain boundaries. Higher magnification images of 7034-2NP are presented in Figure 5-4b. Grain boundary segregation of Zn, Cu, and Mg is indicated by EDS mapping on the right, and the corresponding PFZ is approximately 15 nm wide. The 15 nm is very narrow comparing to the size of PFZ from other works[8,162]. The PFZ of AA7034 is different, a

`

solute depletion region of Zn is wide between the remaining secondary phases, and the distribution of Mg is uniform in this region. The boundary of the Zn depletion region is not sharp, but the composition change of Zn is more gentle. It is also found that precipitates of the nano-treated sample are larger than AA7034 showing a precipitation promotion by nanoparticles. Overall, A better dissolution of the secondary phases was confirmed in TEM, and a smaller PFZ if found in the 7034-2NP sample.

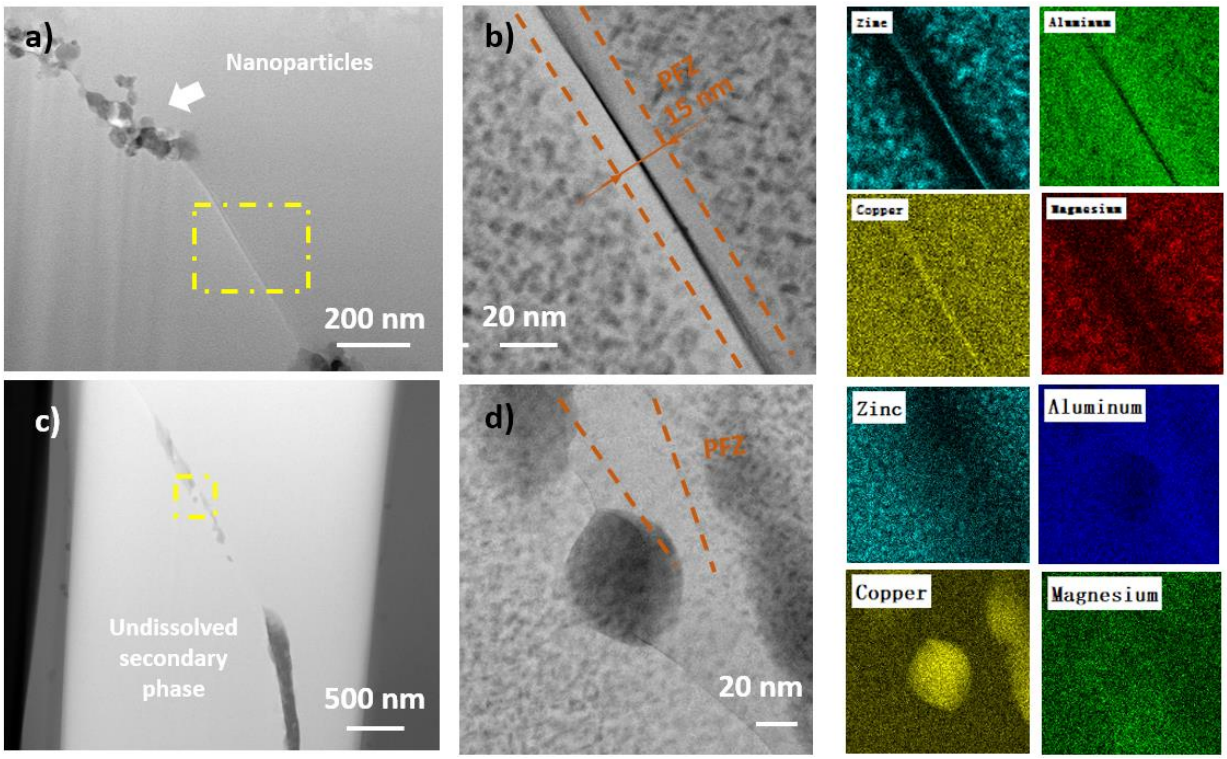

Figure 5-4. TEM images of a) 7034-2NP, b) higher magnification of the grain boundary of the region in a yellow square of 7034-2NP sample, c) AA7034 samples, d) higher magnification of the grain boundary containing undissolved secondary phase. Corresponding EDS mappings of b, d) are on the right

5.3 Mechanical properties

Mechanical properties of the fabricated samples after heat treatment were tested. The microhardness of all samples was about 230HV with or without extrusion, as shown in Figure 5-

`

5a, and there is no significant difference among these samples. The microhardness data indicates a potential high strength of all 7034 alloys. However, in Figure 5-5b, the tensile testing results show that all samples broke at around 300 MPa before the yield except for 7034 alloys modified by nanoparticles after extrusion. This is a piece of direct evidence that AA7034 alloys produced by conventional casting have low ductility and strength. After nano-treating, cast 7034 alloys did not offer good mechanical properties. When both nano-treating and extrusion were applied, the ductility of 7034-1NP and 7034-2NP samples rose to 4.1 ± 1.3% and 2.0 ± 0.92%, respectively. More detailed mechanical properties were presented in Table 5-2.

Table 5-2. Mechanical properties of the samples

Sample	UTS (MPa)		Yield (MPa)		Ductility (%)		Microhardness (HV)	
	No Extrusion	After extrusion	No Extrusion	After extrusion	No Extrusion	After extrusion	No Extrusion	After extrusion
AA7034	154.2 ± 85.2	298.7 ± 107.8	-	-	0.25 ± 0.06	0.53 ± 0.21	234.1 ± 6.0	239.2 ± 2.4
7034-1NP	306.2 ± 89.1	709.7 ± 50.4	-	680.9 ± 51.2	0.44 ± 0.10	4.1 ± 1.3	238.1 ± 7.3	229.5 ± 6.4
7034-2NP	230.9 ± 103.1	769.1 ± 68.3	-	754.4 ± 27.9	0.32 ± 0.09	2.0 ± 0.9	237.8 ± 7.4	231.5 ± 9.9

The low ductility of samples and control samples before extrusion might be attributed to casting inclusions and formed porosity, as shown in Figure 5-6. The ductility of 7034-1NP and 7034-2NP was still limited because of casting inclusions and oxides as the degassing was done at a high temperature (820℃). The SEM images of the fracture surfaces were shown in Figure 5-7. The AA7034 sample (Figure 5-7a) after extrusion and heat treatment showed a brittle fracture and undissolved T phases fractured during tensile testing. Both 7034-1NP and 7034-2NP samples show

`

ductile dimple fracture mode, but the dimples are not uniform, and there are discontinuities across the surfaces. One oxide inclusion is seen in the 7034-1NP sample, and a secondary crack exists. A better casting quality control can potentially improve the ductility of the nano-treated samples.

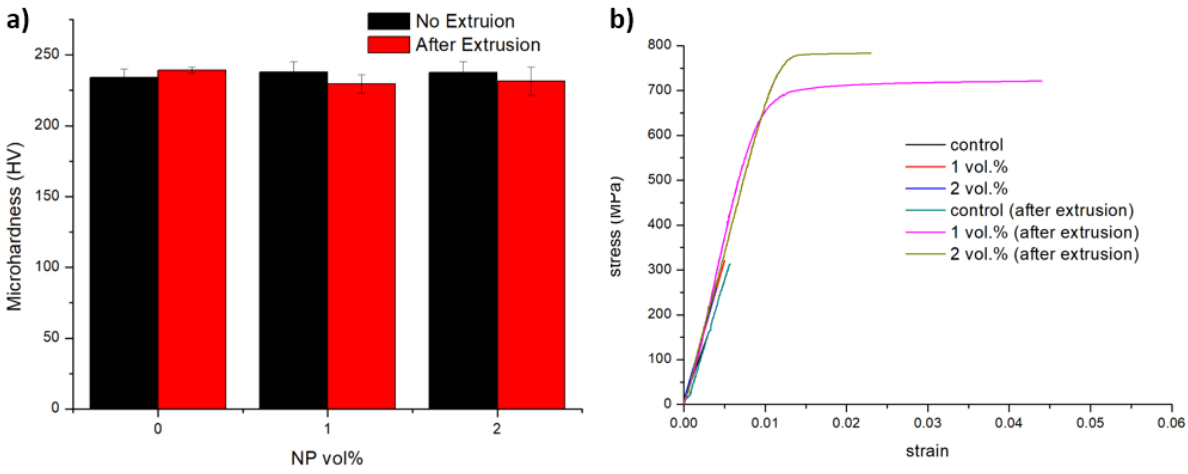

Figure 5-5. a) Microhardness and b)tensile testing results after T6 heat treatment

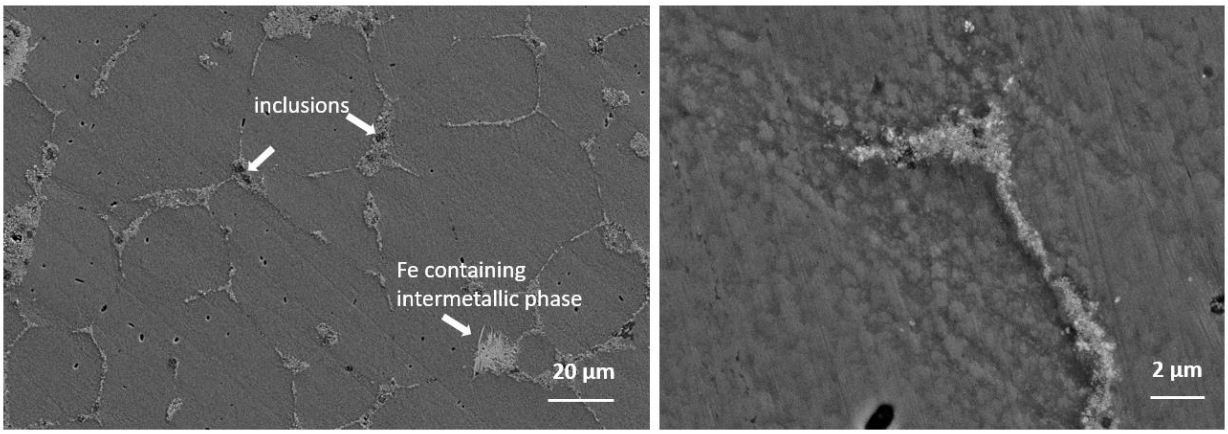

Figure 5-6. SEM pictures of 7034-2NP after heat treatment

`

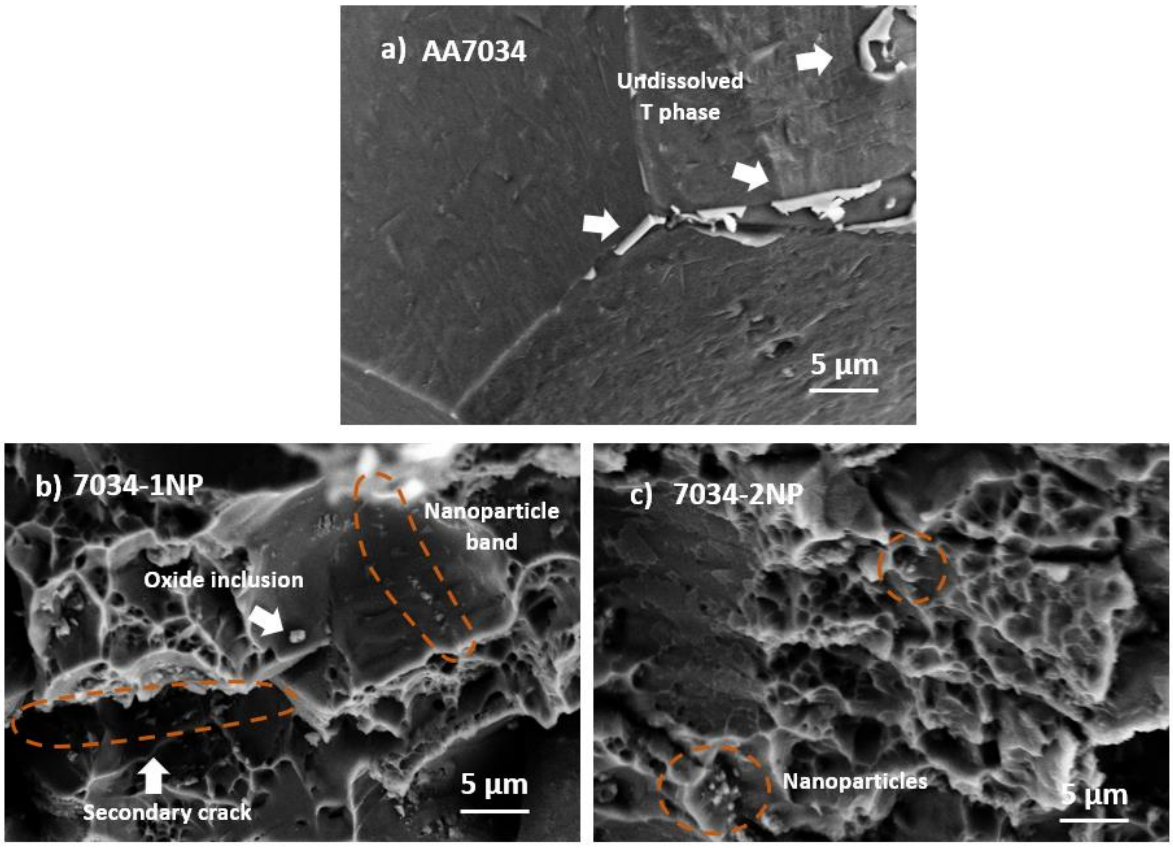

Figure 5-7. SEM images of fracture surfaces of the samples after extrusion and heat treatment. a) AA7034, b) 7034-1NP, c) 7034-2NP

5.4 Promotion of solution treatment

To further investigate the influence of nano-treating on the solidification behavior, the cooling curves of the samples during solidification were recorded, and the illustration of the recording system is shown in Figure 5-8a. The cooling curves of AA7034, 7034-1NP, and 7034-2NP were presented in Figure 5-8b. The first derivative of temperature with respect to time (dT/dt) was calculated to show phase transformation and heat release[156,157]. The corresponding solid volume fraction(Figure 5-8c) was calculated based on the Newtonian baseline[158]. The solidification process was divided into three stages, as shown in Figure 5-8b, c. Stage 1 indicates

`

the nucleation event of α-aluminum where the 7034-2NP sample has the sharpest drop of dT/dt, representing rapid heterogeneous nucleation initiated by TiC nanoparticles. In contrast, the initial drop in AA7034 was gentle. Stage 2 shows the growth of α-aluminum. Stage 3 indicates the nucleation and growth of the eutectic phase.

The calculated solid volume fraction at different temperatures is shown in Figure 5-8c. Nano-treated samples started nucleation of α-aluminum at a smaller undercooling due to heterogeneous nucleation, and the 7034-2NP sample had a fast solidification speed at the beginning. At stage 3, the volume fraction of the eutectic phase was different though these three alloys have similar composition and cooling conditions. The 7034-1NP and 7034-2NP samples had a lower volume of eutectic phases (8.6 vol.% and 7.9 vol.% respectively), while AA7034 has the highest (11.4 vol.%). The 7034-1NP sample had 24.5% less volume fraction of the eutectic phase, while 7034-2NP had 30.8% less than AA7034, showing less segregation in the nano-treated samples after casting. The overall cooling rate is low at 0.25 K/s according to cooling curves. The deduction of the volume of the secondary phase was confirmed by SEM images, as shown in Figure 5-9. These SEM images were converted to black/white images while the white phase indicates secondary phases. Therefore, the area fraction of the white phase can be used to estimate the volume fraction of the secondary phase. Similarly, the AA7034 sample has the highest area fraction of the secondary phase. The 7034-1NP sample has 22.5% less white phase, and the 7034-2NP sample has 25.4% less. Considering the white phase is a combination of nanoparticles and secondary phase, the area fraction of secondary phases was lower than the white area. This result matches well with the volume fraction calculated from the cooling curve.

`

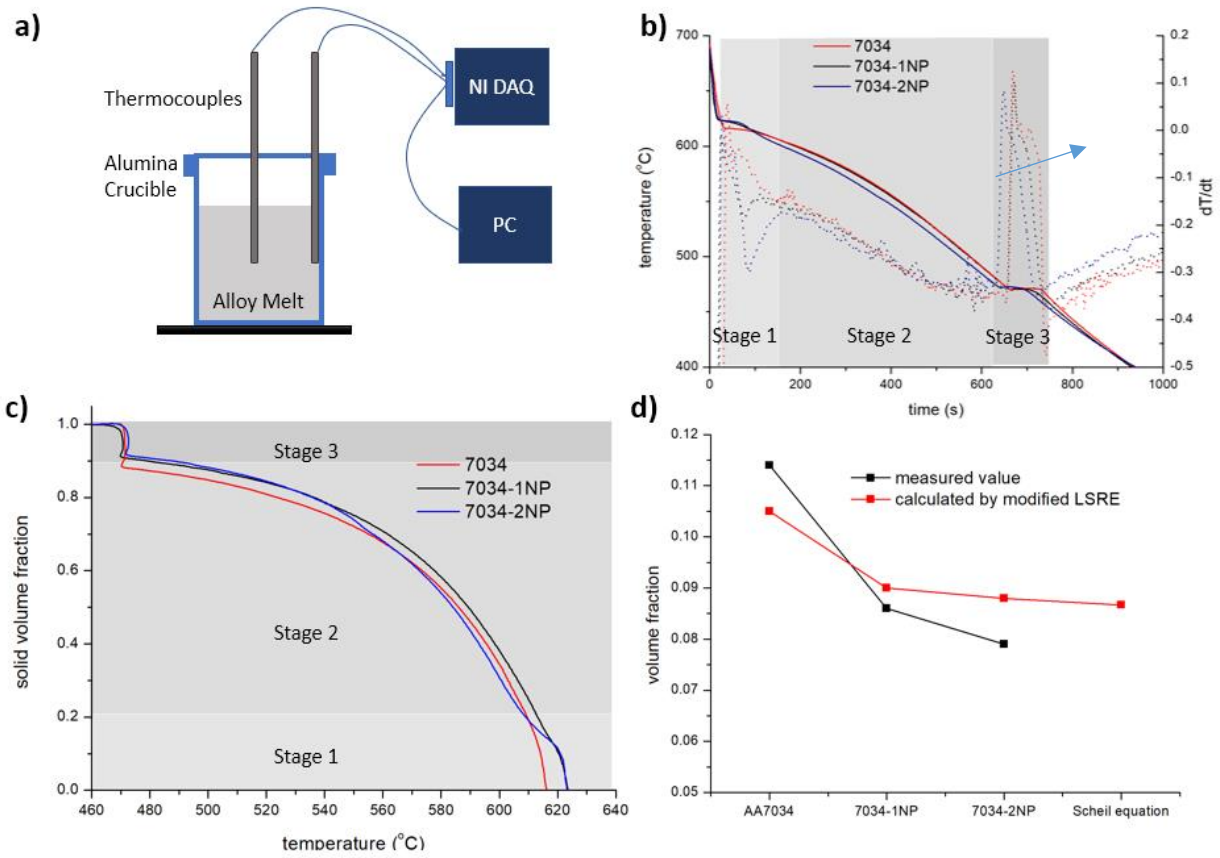

Figure 5-8. a) illustration of temperature recording system during solidification; b) cooling curves and the first derivative of the cooling curve; c) solid volume fraction vs temperature curve; d) Measured volume fraction of eutectic phase and calculated volume of eutectic phase by LSRE

`

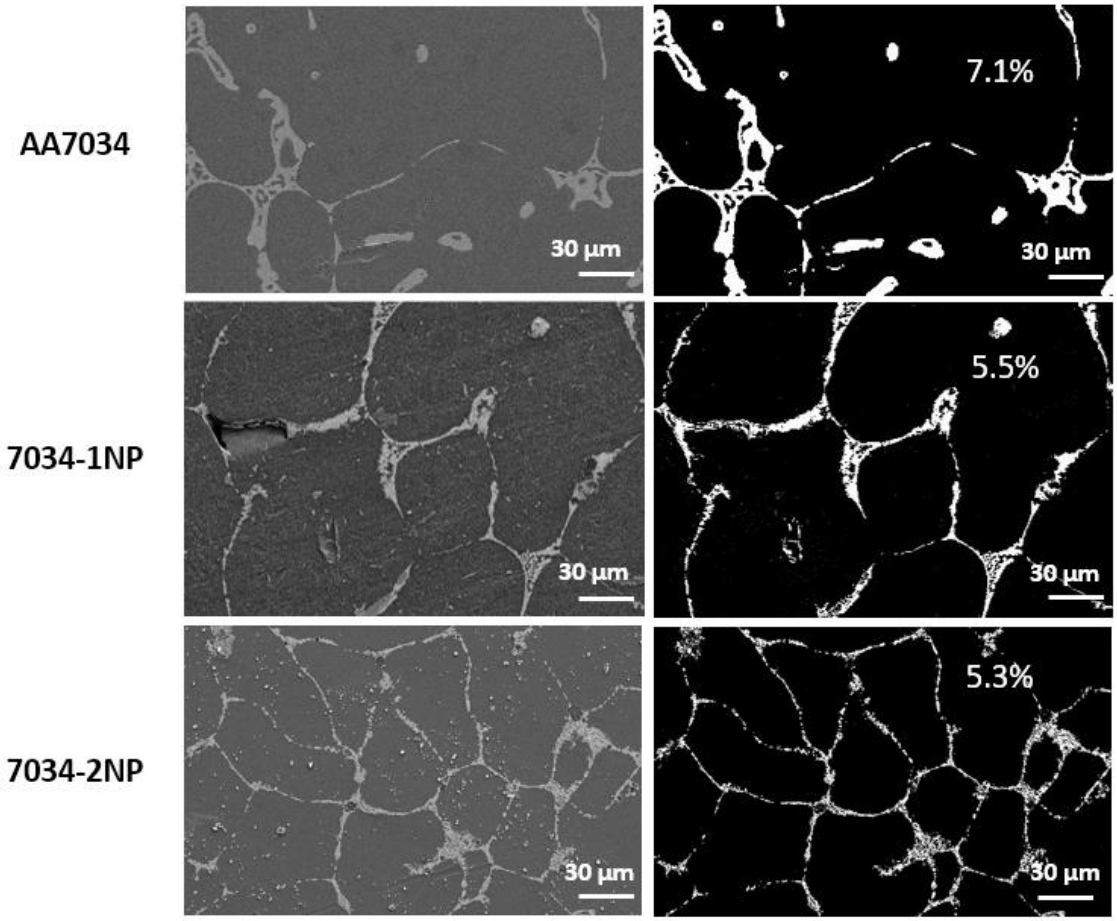

Figure 5-9. SEM images and converted black and white colors. The percentage indicates the area fraction in white color

At the final stage of solidification, when the volume fraction of liquid gets low, a coherent solid network forms[155]. When liquid aluminum solidifies, the volume decreases as solid aluminum has a larger density. Liquid flow should come from an unsolidified region and compensate for the shrinkage. This process will cause macrosegregation along the ingot[175]. The composition of the liquid can be calculated and used to predict the eutectic volume fraction. A modified local solute redistribution equation (LSRE)[176] was used to calculate the volume of the eutectic phase, and the results are presented in Figure 5-8d. The LSRE describes the liquid composition in a small volume in the liquid-solid "mushy" region of a solidifying ingot. It is assumed that the solute enters or

`

leaves the element only by liquid flow. The liquid is well mixed and there is little diffusion in the solid. The LSRE Equation (5-2) is written below:

$$\frac{df_s}{dC_L} = \frac{(1-f_s)}{C_L}\frac{(1-\beta)}{(1-k)}\left(1-\frac{u_n}{v_T}\right) \tag{5-2}$$

Here f_s is solid volume fraction and $f_s + f_L = 1$; C_L is liquid composition; β is solidification shrinkage, and it is written below; k is partition function; u_n is normal liquid velocity; v_T is isotherm velocity. Here β is:

$$\beta = \frac{\rho_S - \rho_L}{\rho_S} \tag{5-3}$$

ρ_S and ρ_L are solid density and liquid density respectively. For liquid aluminum, ρ_S is 2.7 g cm^{-3} and ρ_L is 2.4 g cm^{-3}. k was estimated from an Al-$MgZn_2$ pseudo phase diagram[177], and it is roughly 0.2. v_T is the velocity of isotherm and it is measured from the cooling curves. Both temperature in the center of the ingot and the temperature close to the wall were recorded to estimate v_T and it is approximately 0.002 m s^{-1}. From Darcy's law, u_n is written in Equation (5-4):

$$u_n = -\frac{K}{\mu f_L}(p' + \rho_L g_r) \tag{5-4}$$

Here, K is permeability, μ is the viscosity of the liquid, p is the pressure of the liquid, ρ_L is the density of the liquid and g_r is the acceleration of gravity. At a slow cooling rate, we assume $p' \ll \rho_L g_r$. According to Kozeny–Carman relation[178], K can be written in Equation (5-5).

$$K = \frac{f_L^3}{5S_S^2} \tag{5-5}$$

Here, f_L is the volume fraction of the liquid and S_S is solid-liquid interfacial area per unit volume, and it can be estimated from the 2D optical image as:

`

$$S_s = (4/\pi)L_A \tag{5-6}$$

Here, L_A is the perimeter of the solid-liquid interface per unit image area. According to the optical images, the values of S_s for AA7034, 7034-1NP and 7034-2NP samples are 2.1×10^4 m^{-1}, 3.10×10^4 m^{-1} and 3.8×10^4 m^{-1} respectively. Therefore, the permeability of the nano-treated sample was reduced since they have larger S_S. The effective viscosity[179] of the liquid containing nanoparticles can be given by:

$$\mu_{eff} = \frac{\mu_{Al}}{1-34.87(d_{NP}/d_f)^{-0.3} f_{NP}^{1.03}} \tag{5-7}$$

μ_{Al} is the viscosity of liquid aluminum, and its value is 1.0 mPa·s [180]. d_{NP} is the diameter of nanoparticles. f_{NP} is the volume fraction of nanoparticles in the liquid. Because nanoparticles were all pushed by the solidification front and stay in the liquid, f_{NP} could be written as:

$$f_{NP} = \frac{f_{NP}^0}{f_L} \tag{5-8}$$

where f_{NP}^0 is the initial volume fraction of nanoparticles. In Equation (5-7), d_f is equivalent diameter of a base fluid molecule, and it could be written as:

$$d_f = 0.1\left(\frac{6M}{N\pi\rho_{f0}}\right)^{1/3} \tag{5-9}$$

in which M is the molecular weight of the base fluid, N is the Avogadro number, and ρ_{f0} is the mass density of the base fluid calculated at temperature T_0 = 293 K. The effective viscosity, μ_{eff} will be increased by nanoparticles. However, when the volume fraction of nanoparticles is low, permeability is the key influencing factor.

`

By plugging Equations (5-3, 5-4,5-5, 5-6, 5-7. 5-8. 5-9) into Equation (5-2) with all known physical values, the eutectic liquid volume fraction of AA7034, 7034-1NP and 7034-2NP are 0.105, 0.090, 0.088 respectively. The eutectic volume fraction is 0.0867, calculated by the Scheil equation for reference. The lowered eutectic volume fraction was a direct result of reduced normal liquid velocity u_n. Nanoparticles would affect u_n by changing permeability and viscosity, and particularly, in this case, the permeability is reduced.

As shown in Equation 5-5, the permeability is inversely proportional to S_s, the solid-liquid interfacial area per unit volume, but nanoparticles do not always increase S_s. Nanoparticles can suppress dendrite arms and refine grain size. Even though smaller grains can increase S_s but by eliminating the dendrite arms reduces S_s. Therefore, it is possible that the overall S_s would be reduced, and the final volume fraction of eutectic phases increases, especially when the cooling rate is high so that the dendrite arm spacing in the pure alloy is small. A different case that nanoparticles increase the volume fraction of eutectic phases was also performed to verify the modified model, as shown in Figure 5-10.

A small amount(30g) of the melt alloys was cast in a steel rod mold to achieve a higher cooling rate (4 K/s). The AA7075 sample shows much thin dendritic arms, indicating a much smaller permeability. The nano-treated sample, though significantly refined the structure, has a larger permeability. The area fraction of white phases in the AA7075 sample was 4.2%, and it increased to 5.0% after the addition of nanoparticles.

`

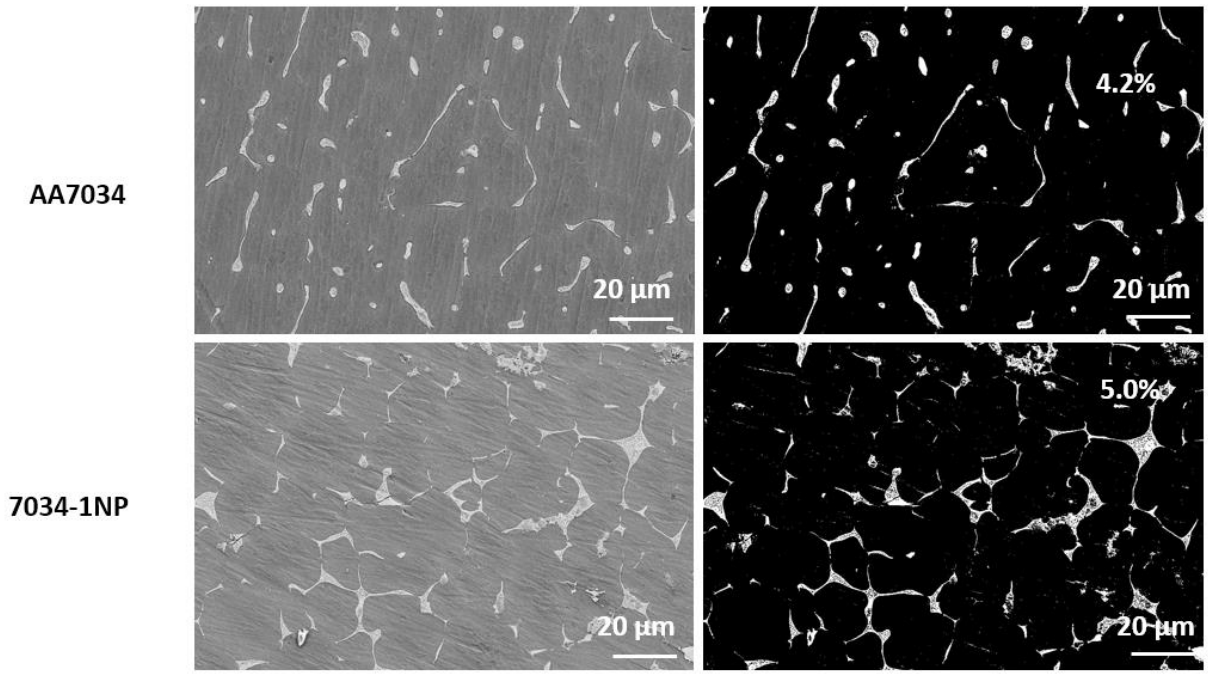

Figure 5-10. SEM images of fast cooled samples and converted black/white images. The percentage in the images is the area fraction of white color

5.5 Summary

The nano-treated AA7034 alloys were successfully cast by down-hill casting at a low cooling rate of 0.25 K/s. After extrusion and heat treatment, it showed reasonable ductility and high strength. The improved mechanical properties were due to the more complete dissolution of secondary phases that were difficult to dissolve for the high alloying AA 7034 alloy. The nano-treated samples show ductile fracture behavior, while the AA7034 sample has brittle fracture mode. The nano-treated cast samples have less segregation and carry fewer, smaller secondary than those in AA7034. A modified local solute redistribution equation (LSRE) was applied to calculate the volume of the eutectic phase. It shows that nanoparticles can change the volume fraction of the eutectic phase by influencing the permeability of the coherent solid network in the final stage of solidification and the viscosity of the molten melt. Furthermore, the dissolution of the secondary

`

phases in 7034-1NP and 7034-2NP samples was promoted due to an accelerated diffusion through interfaces and dislocations.

`

Chapter 6 Nano-Treating Promoted Natural Aging

Many aluminum alloys have been used on aircraft and spaceships due to their high specific strengths. Many of these components are colossal parts that large furnaces and quenching tanks are required for heat treatment. The manufacturing cost is thus very high. In some occasions like arc welding, post heat treatment is not favored as well. For example, it is difficult to conduct heat treatment after field welding outside factory. Natural aging is an aging process at room temperature without the need of heat-treating furnaces, thus saving energy and reducing manufacturing costs. Researchers have demonstrated that alloys after natural aging can achieve comparable properties to those after T6 heat treatment[181]. Despite the benifits of natural aging, natural aging of many alloys was not often used in industrial applications because it takes too long to complete. An example of Al–4.4Zn–2.0Mg–0.54Mn–0.2Zr alloy shows that its tensile strength continuously increased for 10 years during natural aging[181].

It has been demonstrated that both artificial and natural aging can be facilitated by nano-treating in Chapter 4.4. Here in this chapter, typical Al-Zn-Mg-(Cu) alloys were nano-treated with TiC nanoparticles to study the nano-treating effects. Subsequently, the promoted aging was applied to arc welding. Since post-weld heat treatment (PWHT) is hard to accomplish in many cases, such as field welding or welding of colossal parts, solution treatment was also not desired. Therefore, natural aging after casting or welding was applied to these alloys.

Furthermore, since high quench sensitivity makes solution treatment necessary, the quench sensitivity of these alloys with different Cu contents was also studied in this chapter. Cu has a strong interaction with vacancies and increases the quench sensitivity of the alloy. At last, AA7075

`

plates were arc welded by specially designed nano-treated welding wires before natural aged for 40 days to achieve an excellent mechanical property.

6.1 Fabrication of nano-treated Al-6.0Zn-2.6Mg-xCu alloys

The fabrication of the Al-Zn-Mg-Cu alloys is similar to the previous casting experiments. Briefly, pure aluminum was melted at 820^{o}C. Pure Zn, Mg, Cu, and master nanocomposite alloy containing 3.5 vol.% TiC nanoparticles were added to the melt. Fluxing and degassing were applied for 30 mins before the alloys were cast into a rod steel mold. Control samples without nanoparticles were also fabricated by the same method but at 750^{o}C. Casting experiments were conducted to measure the cooling rate during solidification. One thermal couple was placed in the center of the mold to record the cooling curve. The average cooling rate during solidification was 2.73 K/s. Pieces of the sample were cut from the center of the ingots and prepared for optical, SEM, and TEM characterizations. The chemical composition of the samples was determined by a spark CCD (Spark CCD 7000, NCS). Tensile bars, according to ASTM standard, was cut by wire EDM. To test the quench sensitivity of different samples, samples were solutionized at 473^{o}C for 1.5h and quenched in water (40.0 K/s) or cooled in the air (2.21 K/s). The composition and designation of the samples are listed in Table 6-1. Briefly, the samples with "-NP" are nano-treated with 1 vol.% of TiC nanoparticles. The "A-0Cu" alloys have 0 wt.% of Cu, and the "B-0.5Cu" alloys have 0.5 wt.% of copper; the "C-1Cu" alloys have 1 wt.% of copper.

Table 6-1. Sample names and composition (unit. wt.%)

samples	Al	Zn	Mg	Cu	Ti	Si	Fe	TiC vol.%
A-0Cu	Bal.	6.01 ± 0.16	2.48 ± 0.07	0.00 ± 0.00	0.00 ± 0.00	0.04 ± 0.01	0.03 ± 0.01	0.00 ± 0.00
A-0Cu-NP	Bal.	5.97 ± 0.22	2.61 ± 0.10	0.00 ± 0.00	1.17 ± 0.12	0.08 ± 0.01	0.10 ± 0.01	0.86± 0.01
B-0.5Cu	Bal.	6.07 ± 0.16	2.53 ± 0.03	0.52 ± 0.02	0.00 ± 0.00	0.02 ± 0.00	0.04 ± 0.00	0.00 ± 0.00
B-0.5Cu-NP	Bal.	5.93 ± 0.23	2.74 ± 0.09	0.59 ± 0.01	1.24 ± 0.04	0.06 ± 0.00	0.09 ± 0.01	0.91 ± 0.00
C-1Cu	Bal.	6.18 ± 0.15	2.63 ± 0.09	1.11 ± 0.06	0.00 ± 0.00	0.03 ± 0.00	0.03 ± 0.00	0.00 ± 0.00
B-1Cu-NP	Bal.	6.01 ± 0.29	2.49 ± 0.10	1.10 ± 0.05	1.26 ± 0.09	0.07 ± 0.01	0.11 ± 0.01	0.93 ± 0.01

`

The optical images of the fabricated samples are shown in Figure 6-1 with measured average grain sizes. The black dots in the optical images in Figure 6-1 a-c are eutectic phases with nanoparticles at the grain boundaries. They have small equiaxed grains, typically between 30–40 μm, due to the grain refinement effects of the nanoparticles. The difference in Cu composition did not influence the grain size. The control samples in Figure 6-1 e-g have large grain sizes, and dendric arms exist. Extra Cu forms thinner dendritic arms and smaller grain sizes, as shown in Figure 6-1h. Generally, the grain size of the control samples is much larger than the nano-treated ones.

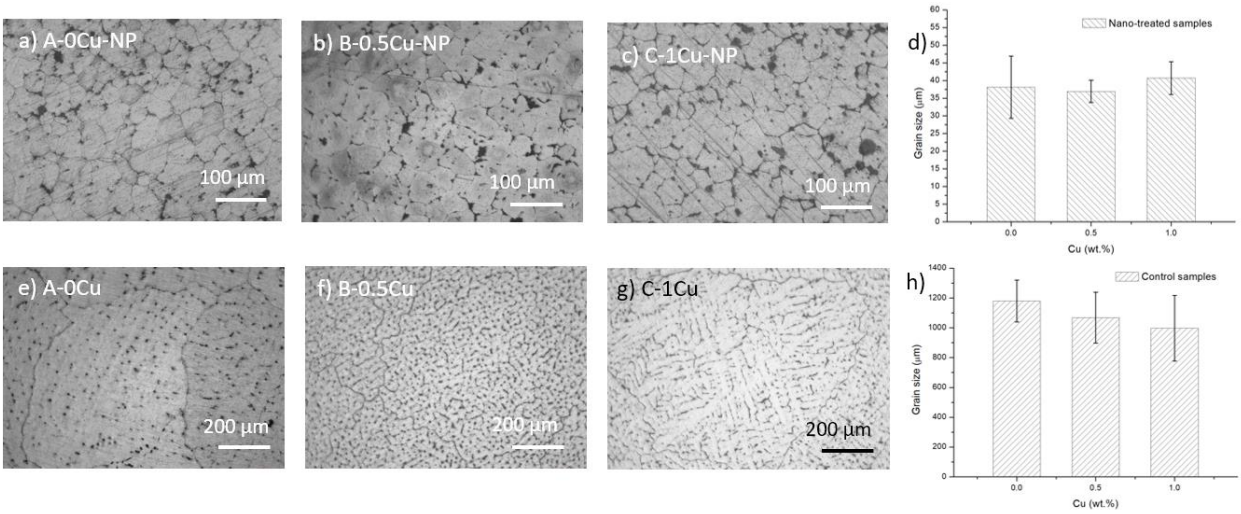

Figure 6-1. Optical images of etched nano-treated samples, a) A-0Cu-NP, b) B-0.5Cu-NP, c) C-1Cu-NP, and d) grain sizes. Optical images of etched control samples, e) A-0Cu, f) B-0.5Cu, g) C-1Cu, and d) their grain sizes

SEM images of the as-cast and solutionized samples were shown in Figure 6-2. More details are revealed by the SEM images. In the as-cast samples, the secondary phases in the nano-treated samples are at the grain boundaries. In contrast, most of the secondary phases in the control samples formed isolated islands where liquid pockets existed between dendritic arms during the last stage of the solidification. A higher Cu content causes a higher volume fraction of secondary

`

phases after casting, as shown in Figure 6-2 a, e, i and Figure 6-2 c, g, k. After solution treatment at 473°C for 1.5h, most secondary phases were dissolved. Nanoparticle pseudo-clusters are shown in Figure 6-2 b, f, g, and some Al_3Ti intermetallic phases were inside the grains. There is little difference among the three nano-treated samples after solution treatment. While no residue secondary phase existed in the control samples of A-0Cu and B-0.5Cu after solutionization, there are still a small number of secondary phases left in the C-1Cu sample. An SEM image with a higher magnification is presented in Figure 6-3a showing the pseudo-cluster of nanoparticles after solution treatment. The measured size distribution of the particles is given in Figure 6-3b. The average size of these particles is 110.5 ± 79.0 nm. The average size of these particles is in-situ synthesized in the industry with a larger average size than our previous in-situ fabricated TiC in the lab.

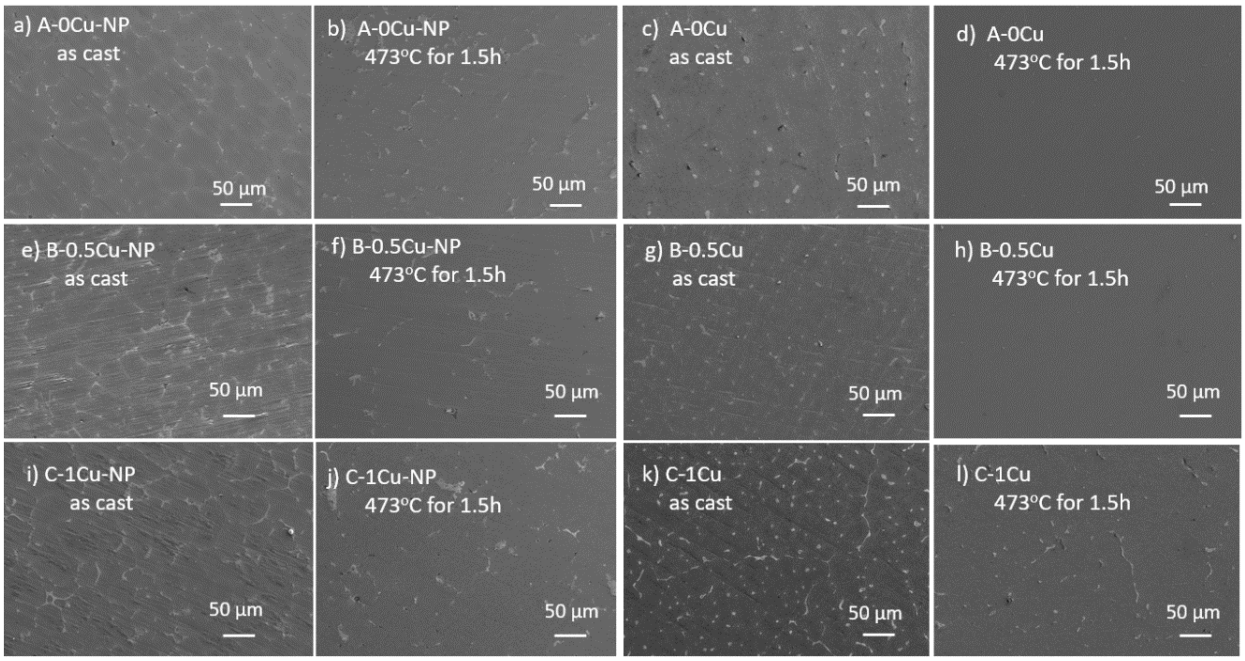

Figure 6-2. SEM images of as-cast samples: a) A-0Cu-NP, c) A-0Cu, e) B-0.5-NP, g) B-0.5Cu, i) C-1Cu-NP, k) C-1Cu. Corresponding SEM images of samples after solution treatment at 473°C for 1.5h: b) A-0Cu-NP, d) A-0Cu, f) B-0.5-NP, h) B-0.5Cu, j) C-1Cu-NP, l) C-1Cu

`

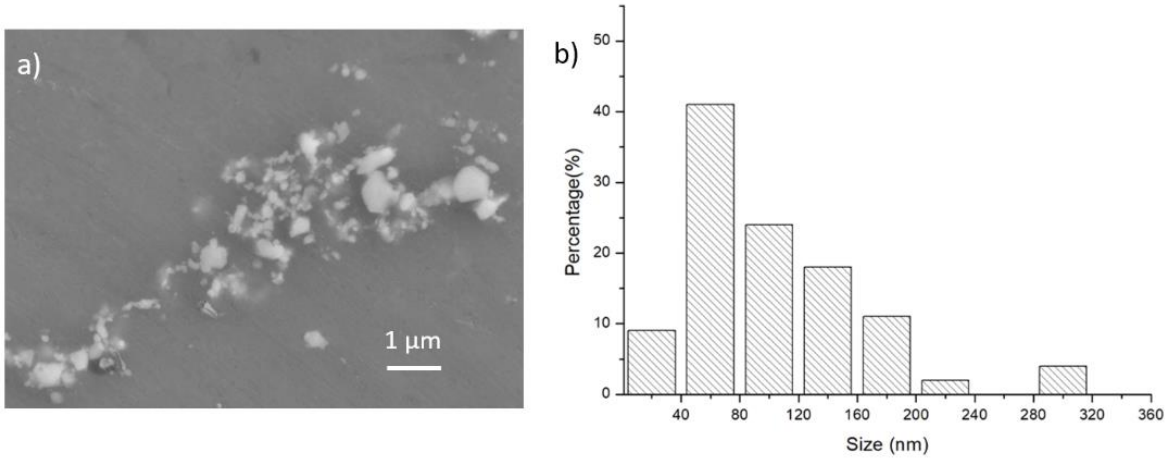

Figure 6-3 a) SEM images of remaining TiC nanoparticles after solution treatment from sample A-0Cu-NP; b) nanoparticle size distribution

6.2 Natural aging and mechanical properties

The samples with different Cu contents were solutionized and either water quenched or air-cooled. Together with the as-cast samples, these samples were placed at room temperature (25 ± 5^{o}C) for 44 days. Microhardness was recorded during the natural aging process, and the hardness evolution curves are presented in Figure 6-4. There are two peaks accompanied by two valleys in each sample. Peak I indicate the clustering of Zn and Mg elements. The formation of GPI zones causes peak II. Valley I is caused by the transition of some clusters to GPI zones, and Valley II is caused by some GPI zones evolving to GPII zones. Figure 6-4a represents the curves of the nano-treated B-0.5Cu-NP sample after different processing conditions. Before natural aging (natural aged for 0 days), the B-0.5Cu-NP sample after water quenching has the lowest microhardness because all secondary phases were dissolved. The sample after air cooling has the highest hardness because precipitation happened during cooling. The precipitation speeds of the B-0.5Cu-NP samples in Figure 6-4a are similar since the positions of the two peaks and two valleys are similar. After 44 days of natural aging, the sample after water quenching and air-cooling show higher

`

microhardness than the cast sample. Similar trends were observed in the B-0.5Cu sample, as shown in Figure 6-4b. Still, valley I is not as sharp as the ones in Figure 6-4a because the formation of solute clusters and transformation of clusters to GPI zones are happening simultaneously. Valley II is at natural aging of 30 days, which is later than valley II (20 days) in the nano-treated sample indicating slower precipitation of the control samples. In Figure 6-4c, d, the cast samples of different Cu% are compared. The positions of the peaks in nano-treated samples are similar and mostly earlier than the same peaks and valleys in the respective control samples, indicating facilitated precipitation by nano-treating.

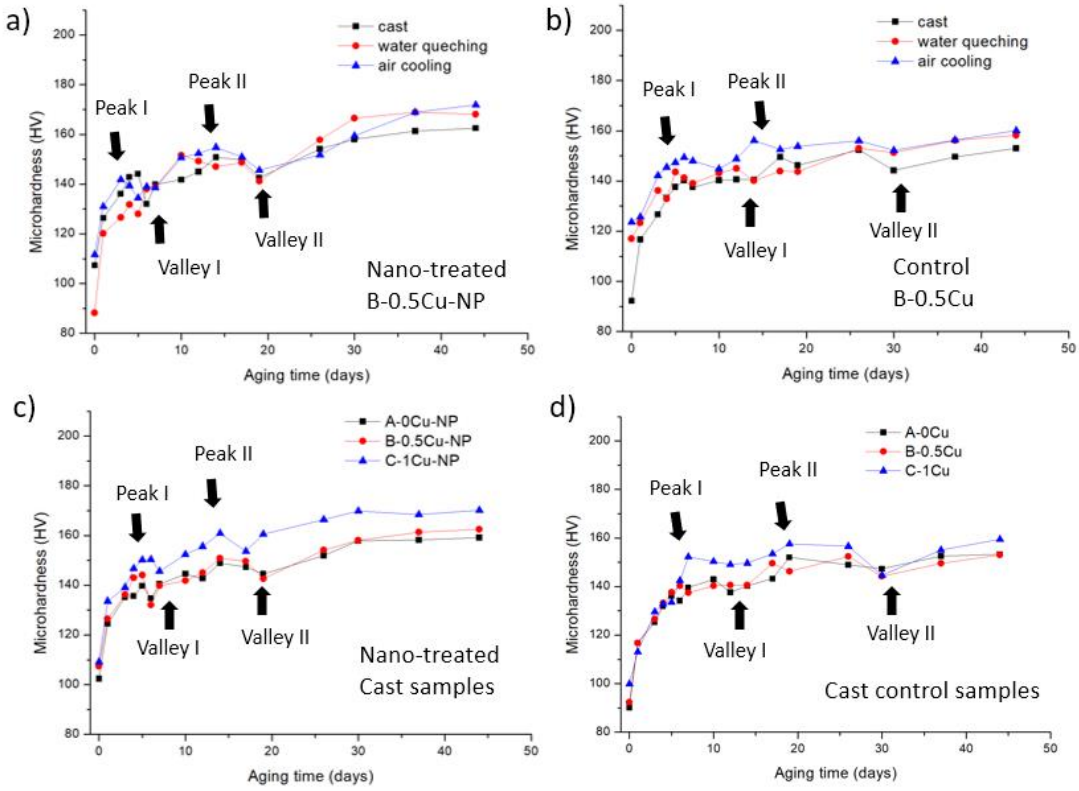

Figure 6-4. a) B-0.5Cu-NP and b) B-0.5Cu sample's hardness during natural aging after casting, water quenching, and air cooling; c) nano-treated samples and d) control samples' hardness during natural aging after cast. Peak I indicates the clustering of solute atoms; Peak II indicate the formation of GPI; Valley I indicate the transition from clustering to GPI zones; Valley II indicates the transition from GPI zones to GPII zones

`

The peak hardness during 44 days of natural aging was summarized in Figure 6-5. The nano-treated samples have higher microhardness than the control samples because nanoparticles promoted precipitation and refined microstructure. The microhardness generally increases with more Cu content. The air-cooled sample offers the highest microhardness in the nano-treated samples, possibly due to extra precipitation during cooling. The cast one has the lowest microhardness since the secondary phases are not fully dissolved. Thus, fewer solutes participate in the matrix. The control samples show a similar trend, but the difference between the air-cooled sample and the water-quenched one is small. When the copper content is below 1%, the quench sensitivity is low[182]. However, the larger difference in the nano-treated samples shows that nanoparticles will increase the quench sensitivity of the alloy.

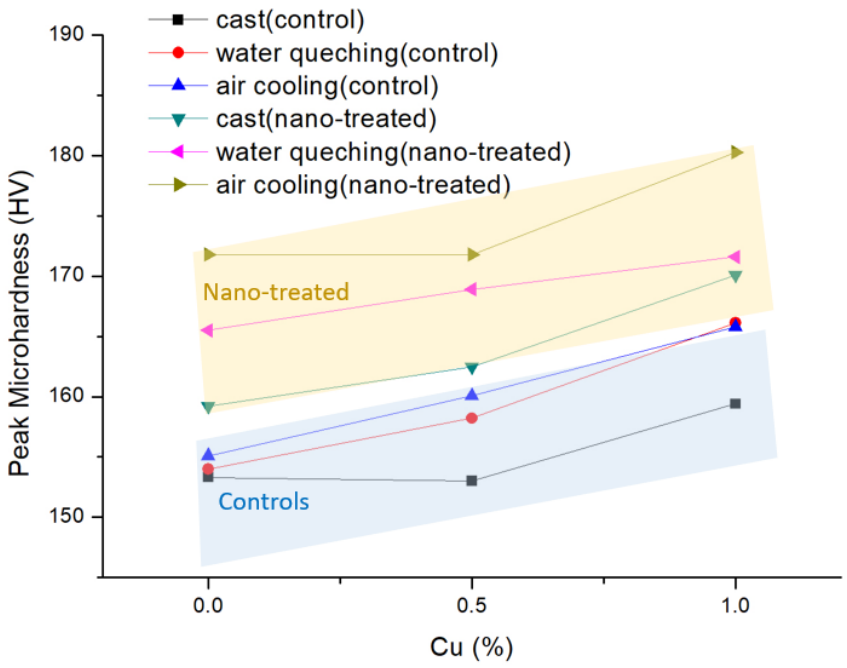

Figure 6-5. Peak microhardness of all samples during natural aging in 44 days

`

Tensile tests were carried out, and the testing results are shown in Figures 6-6, 6-7, and 6-8. The stress-strain curves of B-0.5Cu-NP samples natural aged 40 days are shown in Figure 6-6a and a comparison of the properties in Figure 6-6b. Similar to the microhardness, the sample after air cooling has the highest ultimate tensile strength (UTS). Due to the undissolved secondary phases, the cast sample has the lowest UTS, YS (yield strength), and EL (elongation). The property changes of the B-0.5Cu-NP sample during aging is presented in Figure 6-7. Longer natural aging time results in better UTS and YS. The elongation is similar. The strength improvement from 20 to 30 days is larger than the improvement from 30 to 40 days, indicating that the strengthening from GPI zones is better than solute clusters, but the strengthening from GPI zones and GPII zones are similar. The properties of the samples with different Cu weight percentage is shown in Figure 6-8. Nano-treated samples with higher Cu wt.% have higher UTS, YS, and a slightly lower EL. All the control samples broke before yield due to the existence of casting defects. The yield strengths of these samples are not measured.

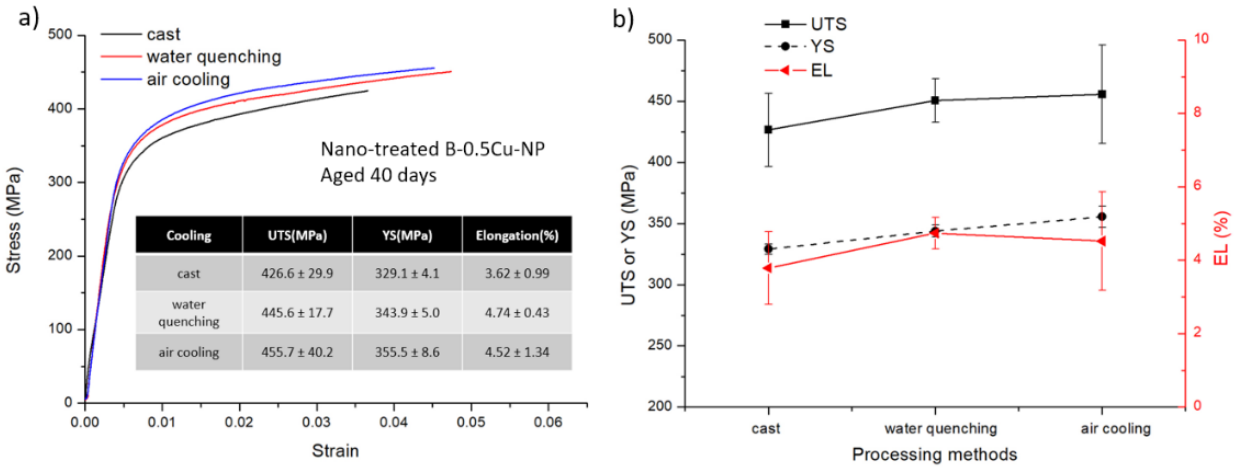

Cooling	UTS(MPa)	YS(MPa)	Elongation(%)
cast	426.6 ± 29.9	329.1 ± 4.1	3.62 ± 0.99
water quenching	445.6 ± 17.7	343.9 ± 5.0	4.74 ± 0.43
air cooling	455.7 ± 40.2	355.5 ± 8.6	4.52 ± 1.34

Figure 6-6. a) Tensile testing of the nano-treated B-0.5Cu-NP samples aging for 40 days after casting, water quenching, and air cooling. The inserted table contains tensile data. b) Comparison of the corresponding UTS, YS, and EL values of each sample

`

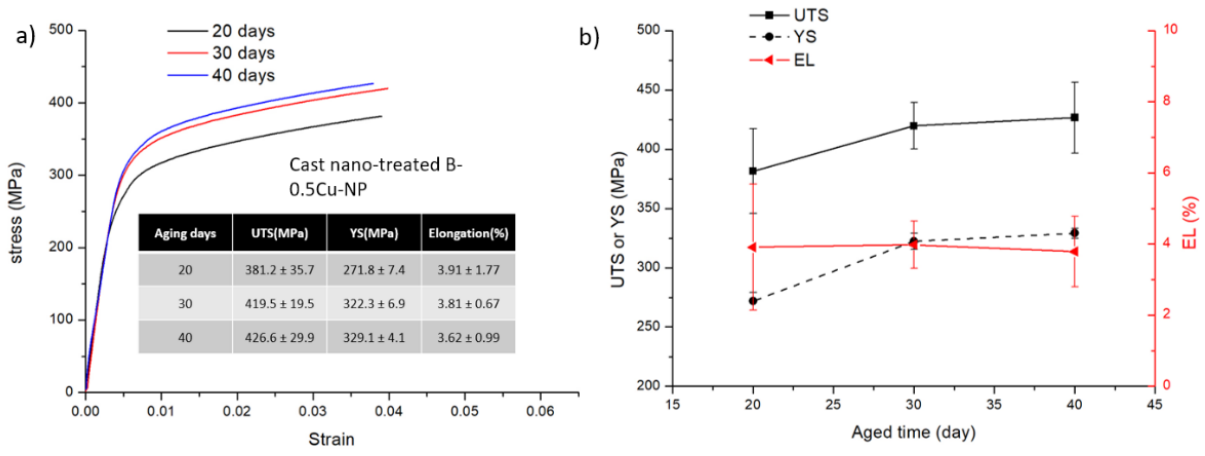

Aging days	UTS(MPa)	YS(MPa)	Elongation(%)
20	381.2 ± 35.7	271.8 ± 7.4	3.91 ± 1.77
30	419.5 ± 19.5	322.3 ± 6.9	3.81 ± 0.67
40	426.6 ± 29.9	329.1 ± 4.1	3.62 ± 0.99

Figure 6-7. a) Tensile testing of the nano-treated B-0.5Cu-NP samples aged 20, 30, and 40 days after casting. The inserted table contains tensile data. b) Comparison of the corresponding UTS, YS, and EL values of each sample

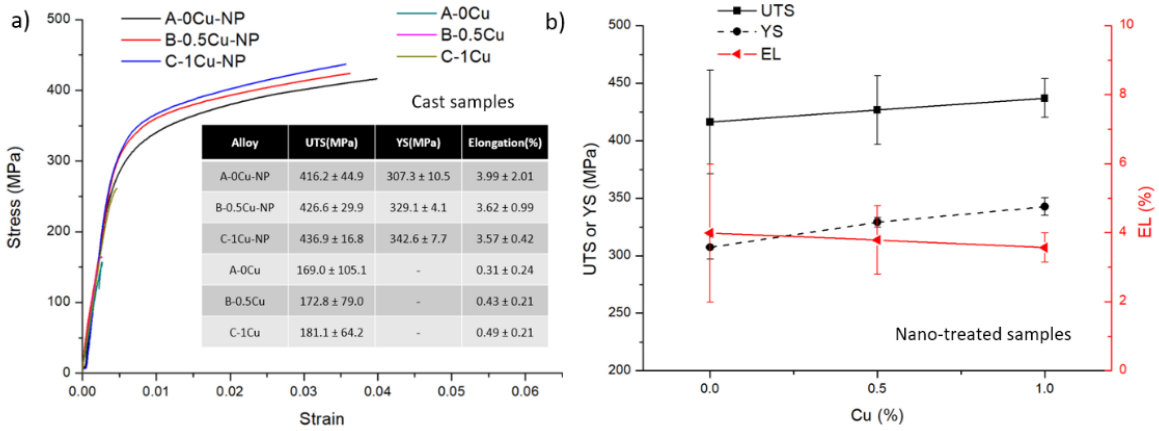

Alloy	UTS(MPa)	YS(MPa)	Elongation(%)
A-0Cu-NP	416.2 ± 44.9	307.3 ± 10.5	3.99 ± 2.01
B-0.5Cu-NP	426.6 ± 29.9	329.1 ± 4.1	3.62 ± 0.99
C-1Cu-NP	436.9 ± 16.8	342.6 ± 7.7	3.57 ± 0.42
A-0Cu	169.0 ± 105.1	-	0.31 ± 0.24
B-0.5Cu	172.8 ± 79.0	-	0.43 ± 0.21
C-1Cu	181.1 ± 64.2	-	0.49 ± 0.21

Figure 6-8. a) Tensile testing of all samples aged for 40 days after casting. The inserted table contains tensile data. b) Comparison of the corresponding UTS, YS, and EL values of the nano-treated samples

6.3 Precipitation evolution during natural aging

The precipitation was studied by DSC analysis. B-0.5Cu-NP and B-0.5Cu cast samples natural aged for different days were heated from 100°C to 300°C at a heating rate of 10K/min. The recorded heat flow curves are presented in Figure 6-9. Two peaks were marked in the samples. The first peak from 120°C to 160°C indicates the dissolution of GPI zones, and a smaller peak

`

from 180°C to 210°C represents the dissolution of GPII zones[183]. The peak area represents the volume of the corresponding GP zone. Because these peaks have overlapped, a tangent line to both ends of Peak II was drawn, and the area between this tangent line and the peak is measured as shown in Figure 6-9a. This value is not the absolute value of the GP II volume but effectively indicates the difference between different samples. The Peak II areas are presented in the inserted tables. The peak II area increases with aging days in both samples, indicating the formation of GPII zones during natural aging. Comparatively, the B-0.5Cu-NP sample has a much larger peak II area comparing to the B-0.5Cu sample. This means the aging speed is facilitated by nano-treating, which is in accordance with the microhardness data.

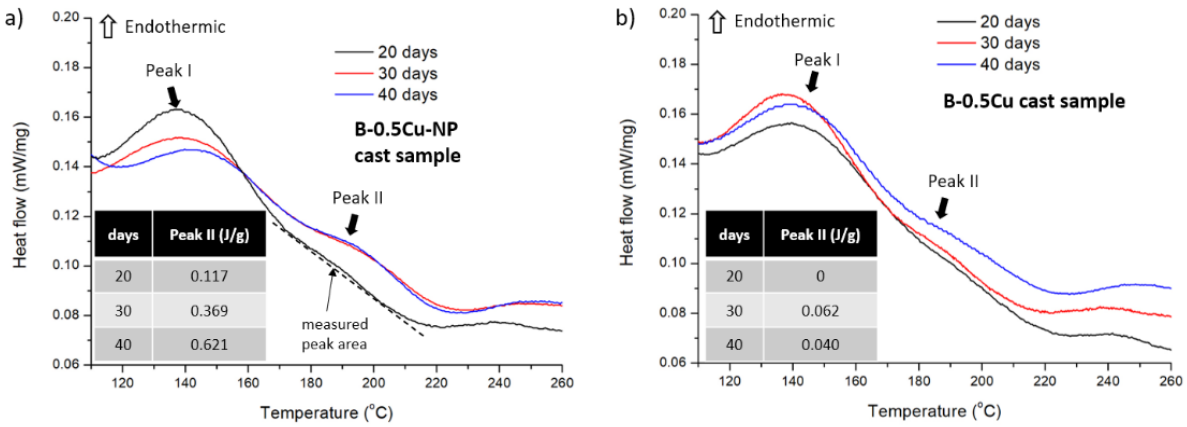

Figure 6-9. a) Heat flow during heating up the a) B-0.5Cu-NP cast sample and b) B-0.5Cu cast sample with different natural aging days. Peak I is an endothermic peak representing GPI zone dissolution. Peak II is an endothermic peak representing GPII zone dissolution. The inserted table is the calculated peak II area indicating the volume of GPII zones

6.4 Welding and natural aging of AA7075 plates

The previous results have confirmed the promoted natural aging by nano-treating. The next step is to study the natural aging of AA7075 after arc welding. The B-0.5Cu-NP was chosen for filler material because plates to be welded were commercial AA7075 alloy that contains 1.6% of Cu. As a higher Cu content resulted in higher strength, 0.5 % of Cu was chosen to obtain the final

`

composition in weld close to 1.0%. Because nanoparticles have been shown to increase the quench sensitivity, Cu percentage above 1.0% was not considered here in this research. The B-0.5Cu was used as a control group. The welding wires were cut from the casting ingots by wire EDM, and the crosssection of these wires was 1.5 mm × 1.5 mm squares. The surface was polished by grinding papers before welding. The welding setup is shown in Figure 6-10a. The welding was conducted by fusing 150 × 75 × 3.00 mm AA7075 plates (T6) with v-groove in butt weld. The AA7075 plates were clamped onto a Cu backing plate. The welding parameters are presented in Table 6-2, and the resulted welds are presented in Figure 6-10b, c. After polishing and etching, base material (BM), heat affected zone (HAZ), and welded metal (WM) were examined.

After natural aging for 40 days, the microhardness across different regions was measured and presented in Figure 6-10d. The WM and HAZ sizes are similar in both nano-treated and control samples, but the nano-treated sample overall has higher microhardness. The width of the WM is about 7 mm, while the width of the HAZ is 16 mm. At the edge of the WM, both samples show microhardness peaks, and an elevated Cu composition might cause these peaks due to the mixture of the filler with the base material. Similar peaks at the edge of the WM were also observed elsewhere[184]. The microhardness of the nano-treated sample in the WM reaches above 150HV, while about 140HV for the control sample. Unfortunately, the lowest strength was in the HAZ in both samples. The lowest microhardness of the nano-treated sample is 125 HV while below 110HV for the control sample. The less degraded HAZ is explained by the nanoparticle's effect on heat flow during welding[7,185]. Nanoparticle allows gradual heat-releasing during solidification due to contineous nucleation and grain growth restriction. Moreover, the nanoparticle can increase the viscosity and reduce the heat conductivity of the melt. The gradual and reduced heat flow dissolved fewer precipitates in the HAZ than the HAZ in the control sample. The chemical composition of

`

the welded metal (WM, in the middle) is tested by a spark CCD and presented in Table 6-3. There are 0.76 vol.% of nanoparticles and 0.72 ± 0.01 wt.% of Cu in WM of the nano-treated sample.

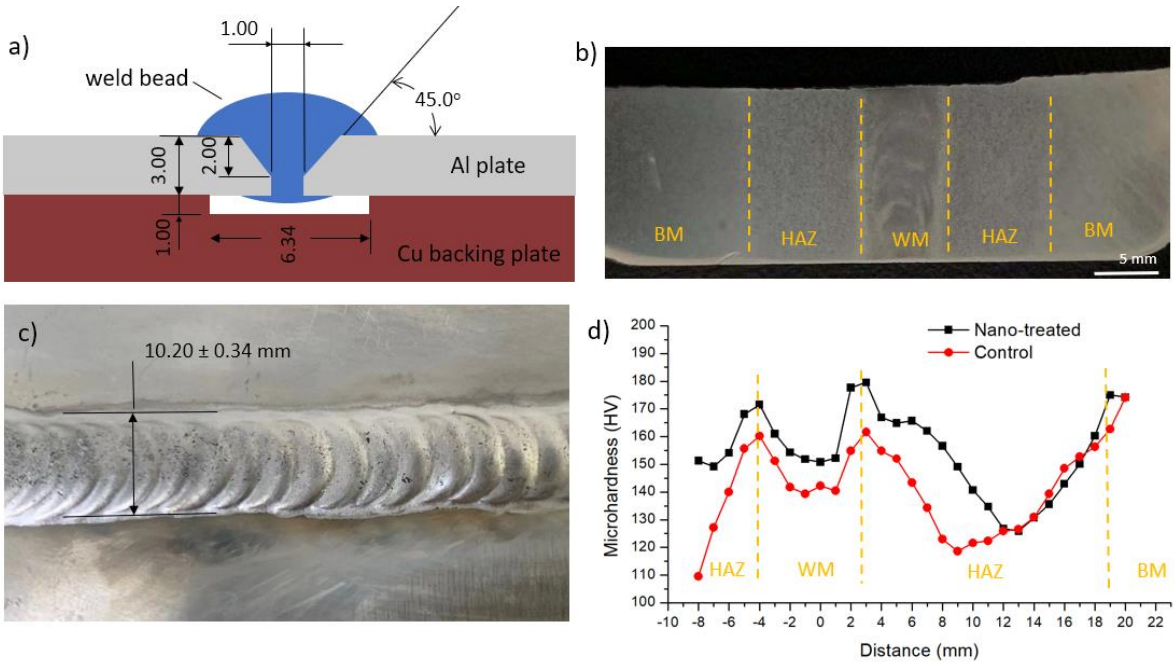

Figure 6-10. a) Illustration of the welding set up; b) image of the welded sample by nano-treated filler after grounding and etching; c) image of the weld bead before grounding and etching; d) microhardness of different regions of the welded samples naturally aged for 40 days

Table 6-2. Welding parameters

Type of current	Constant current
Current	180 A
Output frequency	180 Hz
Balance	85%
Argon flow rate	18 cc/min
Start delay	1.5 s
Electrode gap	2 mm

Table 6-3. Composition of the welding zone

	Al	Zn(wt.%)	Mg(wt.%)	Cu(wt.%)	Ti (wt.%)	TiC (vol.%)
Nano-treated	Bal.	5.64 ± 0.13	2.82 ± 0.08	0.79 ± 0.01	1.04 ± 0.04	0.76 ± 0.00
Control	Bal.	5.92 ± 0.13	2.67 ± 0.09	0.72 ± 0.01	0.00 ± 0.00	0.00 ± 0.00

`

The microstructure of the WM was characterized by optical images and SEM. The images are shown in Figure 6-11. As shown by the optical images in Figure 6-11a, b, dendritic arms appear in the control sample in the WM while these grains are small and equiaxed in the nano-treated one. Furthermore, in the SEM images in Figure 6-11c, d, there are much more solidified secondary phases in the control sample, and these secondary phases are detrimental to mechanical properties. The nanoparticles could change the volume fraction of secondary phases after casting, as discussed in Chapters 4.3 and 5.4, and a gradual heat transfer to the base material allows a longer time for "solution treatment" during cooling. In addition, the extra dissolved solutes allow a higher supersaturated solid solution in the nano-treated sample, which is beneficial to precipitation.

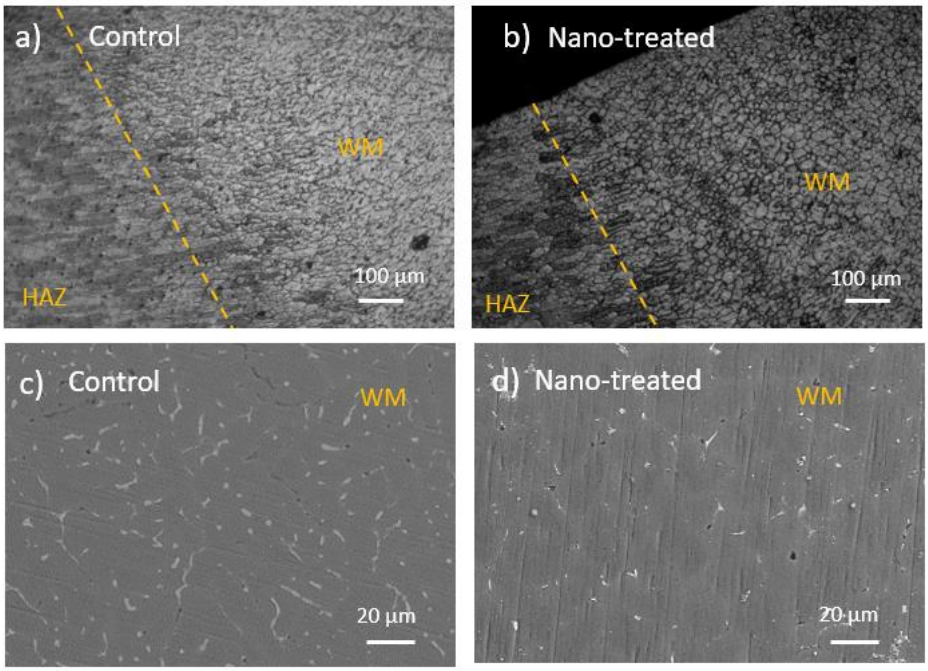

Figure 6-11. Optical images of the weld bead boundary of a) the control sample and b) the nano-treated sample; SEM images of the welding zone in the c) control sample, and d) nano-treated sample

`

Tensile bars were cut to test the mechanical properties of the weld. The welded plates were natural aged for 40 days before testing. Two tensile testing directions were chosen. One is perpendicular to the welding direction, and the other is longitudinal along the welding direction. The tensile test results and the tensile bar dimension are shown in Figure 6-12. For the test perpendicular to the welding zone, the tensile bar gage length is 30 mm, while the width of HAZ from microhardness testing is around 16 mm, and the width of WM is about 7 mm. This means the gage is within the HAZ, as shown in Figure 7-14a, and the weakest part in the tensile bar is in HAZ. After testing, the tensile bars of the nano-treated samples broke in the HAZ, but the control samples' tensile bars broke either in the WM or in the HAZ. Even though the microhardness of the WM is higher than in HAZ in the control sample, solidification shrinkage porosity in the welding zone made the region very weak. Similar failure is not observed in the nano-treated sample as nano-treating eliminates the solidification defects as discussed in the previous chapters. The stress-strain curves are presented in Figure 6-12a. The nano-treated welding sample shows greatly improved UTS, YS, and ductility. Its tensile strength is 428.8 ± 15.07 MPa which is approximately 77% of the base material strength. The total elongation is 2.03 ± 0.15%.

Testing results along the welding zone are shown in Figure 6-12b. The nano-treated sample has a tensile strength of 441.9 ± 21.0 MPa, yield strength of 350.2 ± 13.9 MPa, and a ductility of 1.67 ± 0.12%. All these properties outperform the control sample. The nano-teated sample recovered 80% of the strength of the base material after arc welding. However, the ductility of the weld is limited because some bubbles are generated during welding, possibly due to non-ideal welding conditions.

The tensile properties of the nano-treated sample (perpendicular to WM) after natural aging are compared with other welded high-strength aluminum alloys, as shown in Figure 6-13. The

`

nano-treated sample after natural aging has the second-highest tensile properties only behind the nano-treated sample after T6 heat treatment[7]. Thus, the nano-treating filler wire has shown great potential for welding AA7075 for field welding and large parts without post-weld heat treatment.

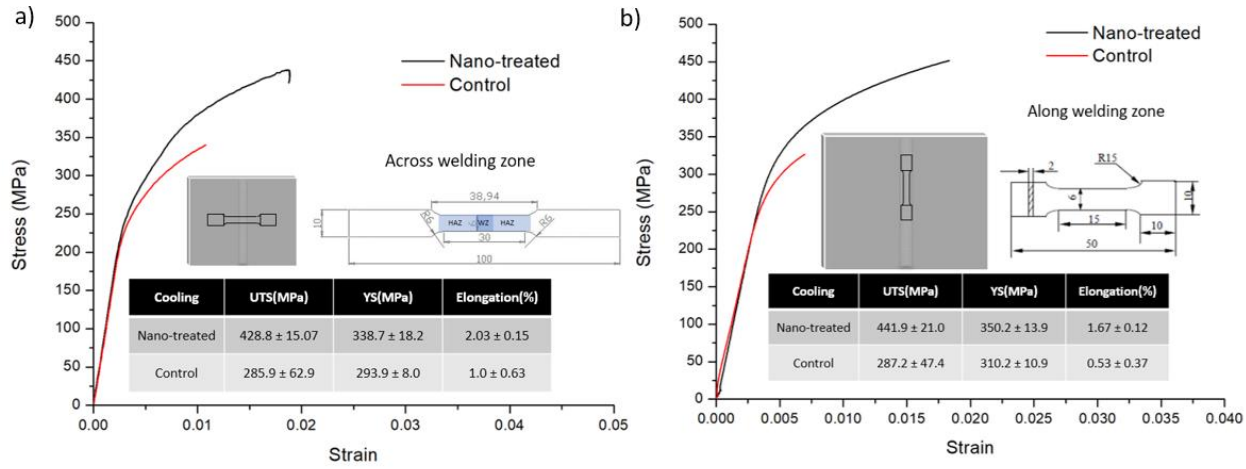

Figure 6-12. Figure x. Tensile testing of the samples aged for 40 days after welding. The inserted table contains tensile data. a) Testing direction perpendicular to welding zone; b) Testing along welding zone. The dimension of the cut tensile bar is above the table, and both welding zone and heat affected zones are marked

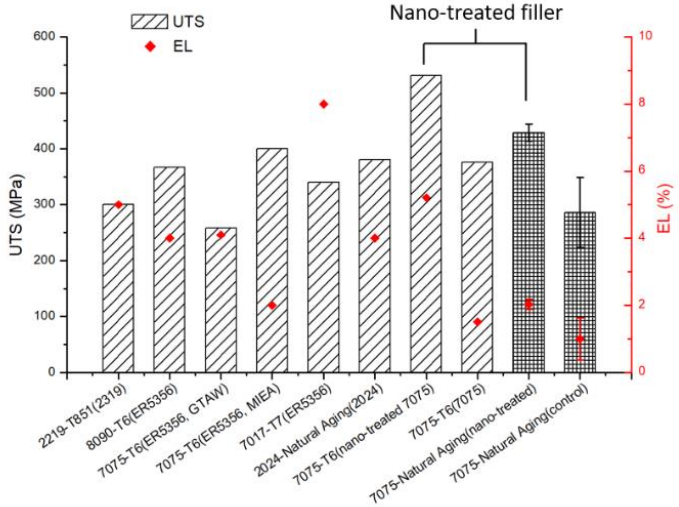

Figure 6-13. Mechanical strength of the welded high strength aluminum alloys: 2219 welded by 2319 filler wire, T85[186], 8090 welded by ER5356 filler wire, T6[187], 7075 welded by ER5356 filler wire and GTAW, T6[184], 7075 welded by ER5356 filler wire, and MIEA, T6[184], 7017 by ER5356 filler wire, T7[187], 2024 welded by 2024 filler wire, natural aging[188], 7075 welded by nano-treated 7075, T6[7], 7075 welded by 7075 filler wire, T6[7] and our welding results perpendicular to the welding direction after natural aging

`

6.5 Summary

Nano-treated Al-6.0Zn-2.6Mg-xCu samples containing different Cu contents have been fabricated and studied. The nano-treated samples have a refined microstructure, and the growth of the dendritic arms was inhibited. After the samples were natural aged for 44 days, the results suggest that nano-treating facilitated natural aging on these samples. Microhardness evolution curves and DSC analysis validated that the formation of GPII zones was faster in the nano-treated samples than the control ones.

Arc welding of commercial AA7075 aluminum plates was performed with both the nano-treated filler (B-0.5Cu-NP) wire and the control wire (B-0.5Cu). The nano-treated wire resulted in less secondary phase and refined grain in WM after welding. The microhardness in WM was higher than the one in the HAZ. The tensile testing shows that the nano-treated wire provides much better strength, yield, and ductility in both directions in the welded samples. The tensile strength perpendicular to the welding direction is 428.8 ± 15.07 MPa, approximately 77% of the base material strength, yield strength is 338.7 ± 18.2 MPa, and elongation is 2.03 ± 0.15%. after natural aging of 44 days. Compared to other arc-welded high-strength aluminum, the nano-treated filler provides the highest strength without PWHT and the second-highest strength only behind the welded sample with T6 after welding with nano-treated filler wire.

`

Chapter 7 Nano-Treating Enabled High Strength Al-Cu-Mg Alloy

AA2024 alloy (mainly 3.8 - 4.9%Cu, 1.2 -1.8%Mg, 0.3 -0.9%Mn) is one of the strongest 2000 series aluminum alloys widely used in the automotive and aerospace industries. Its tensile strength reaches 470 MPa at room temperature after heat treatment because it contains a relatively high amount of alloying elements for precipitation. Despite its good strength, this alloy is prone to hot cracking, shrinkage porosity, and macrosegregation during its final stage of solidification[160]. AA2024 is thus categorized as a wrought aluminum alloy for sheets, plates, and tubes, etc. Its cast form has limited mechanical properties due to the above-mentioned solidification defects. It would be significant if this alloy can be cast into complex shapes with high performance for industrial applications. As discussed earlier, nano-treating can modify the solidification behavior of alloys, such as reducing hot cracking susceptibility by grain refinement and postponed GCP. Thus, nano-treating could potentially make these conventional wrought alloys applicable into shape cast forms. Moreover, the alloy strength can hardly be increased by extra alloying content because of the limited solubility of Cu and Mg during solutionizing. Nano-treating is kinetically beneficial to secondary dissolution phases during solution treatment, but it was considered not possible to break the solubility limit of elements in solid solution.

Here in this chapter, nano-treated Al-4.6Cu-xMg-0.3Mn (x = 1.5, 2.0, 3.0, and 4.0) alloys were fabricated, and the mechanical properties of the cast tensile bars were tested. The alloys are designed to have compositions similar to standard AA2024, but a higher content of Mg was used to study how nano-treating would affect solubility limit of Cu and Mg in the alloys.

`

7.1 Fabrication of nano-treated Al-4.6Cu-xMg-0.3Mn alloys

Preparation of the Al-4.6Cu-xMg-0.3Mn alloys was similar to previous experiments but at a larger scale. Briefly, 10kg pure aluminum was melted in a large graphite crucible at 820^{o}C before 5kg of Al master nanocomposite with about 3.5 vol.% of TiC nanoparticles was added later. A certain amount of pure Cu, Mg, and Mn were added afterward. The designed volume fraction of the nanoparticles is to be 1.0 vol.%. Mechanical stirring at 60 RPM was applied for 10 mins for homogenization. Next, degassing with argon was applied for 20 mins, and the melt was left still for 10 mins after degassing. The fabricated alloy was then cast in a standard tensile bar mold with a dimension shown in Figure 7-1. The mold was designed according to the ASTM B108 standard and the detailed geometry of the tensile bar is shown in Figure 7-1b. The region marked in blue was cut for characterization. Control samples without nanoparticles were fabricated as well.

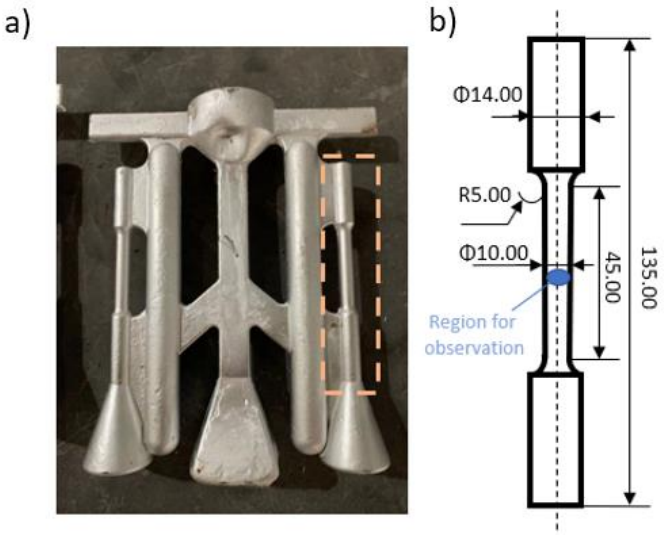

Figure 7-1. a) Image of a casted sample. b) Illustration of the tensile bar geometry

`

Optical observation and SEM were used for the microstructure study. The composition of the alloys was determined by a Spark CCD. DSC measured the latent heat release during heating. The chemical compositions of the samples are shown in Table 7-1. The compositions of the samples denoted as control samples (A-1.5Mg, B-2Mg, C-3Mg, and D-4Mg) and nano-treated ones (A-1.5Mg-NP, B-2Mg-NP, C-3Mg-NP, and D-4Mg-NP) are shown in the table. The Cu and Mn weight percentages are similar in these samples. However, the volume fraction of nanoparticles is less than designed because some nanoparticles were removed during fluxing and degassing.

Table 7-1. Compositions of the samples

samples	Al(wt.%)	Cu(wt.%)	Mg(wt.%)	Mn(wt.%)	Ti(wt.%)	Si(wt.%)	Fe(wt.%)	TiC vol.%
A-1.5Mg	Bal.	4.47 ± 0.01	1.49 ± 0.01	0.32 ± 0.00	0.00 ± 0.00	0.04 ± 0.00	0.72 ± 0.00	0.00 ± 0.00
A-1.5Mg-NP	Bal.	4.70 ± 0.10	1.58 ± 0.01	0.38 ± 0.00	0.97 ± 0.08	0.08 ± 0.01	0.29 ± 0.05	0.71 ± 0.05
B-2Mg	Bal.	4.79 ± 0.63	2.17 ± 0.32	0.31 ± 0.00	0.00 ± 0.00	0.07 ± 0.01	0.09 ± 0.01	0.00 ± 0.00
B-2Mg-NP	Bal.	4.67 ± 0.05	2.10 ± 0.07	0.35 ± 0.01	0.84 ± 0.02	0.07 ± 0.00	0.12 ± 0.01	0.62 ± 0.01
C-3Mg	Bal.	4.64 ± 0.12	3.03 ± 0.03	0.32 ± 0.00	0.00 ± 0.00	0.06 ± 0.00	0.09 ± 0.00	0.00 ± 0.00
C-3Mg-NP	Bal.	4.80 ± 0.16	2.95 ± 0.09	0.40 ± 0.01	1.21 ± 0.03	0.11 ± 0.01	0.27 ± 0.01	0.89 ± 0.02
D-4Mg	Bal.	4.66 ± 0.11	3.82 ± 0.05	0.34 ± 0.00	0.00 ± 0.00	0.05 ± 0.00	0.07 ± 0.00	0.00 ± 0.00
D-4Mg-NP	Bal.	4.76 ± 0.08	3.92 ± 0.06	0.37 ± 0.04	0.85 ± 0.04	0.07 ± 0.00	0.17 ± 0.01	0.62 ± 0.03

7.2 Microstructure analysis

The cast tensile bars were cut in the middle for characterization, as shown in Figure 7-1. The optical images of the samples are shown in Figure 7-2. The shrinkage porosities existed in control samples, as shown in Figure 7-2b. Due to chemical etching, the porosity is not very clear in the optical images. Thus, an inserted SEM image was provided to show the shrinkage porosities. The casting defects are typical for AA2024 because of inadequate inter-dendritic feeding of molten metal during the final stage of the solidification in the mushy zone[160]. As shown in Figure 7-2a-d,

`

dendritic arms grew to tens of microns during solidification, and shrinkage porosities were formed in the tips of the dendritic arms. However, there are few porosities in the nano-treated samples and the A-1.5Mg sample. The nano-treated samples have much smaller grains. For example, the average grain size of the B-2Mg sample is 418.8 ± 164.5 μm but reduces to 65.8 ± 4.5 μm by nano-treating in the B-2Mg-NP sample. As discussed in Chapter 4.12, nano-treating can refine the grain size and reduce the GCP of the alloy, thus enhancing the liquid feeding in the final stage of the solidification and preventing hot cracking and shrinkage porosity.

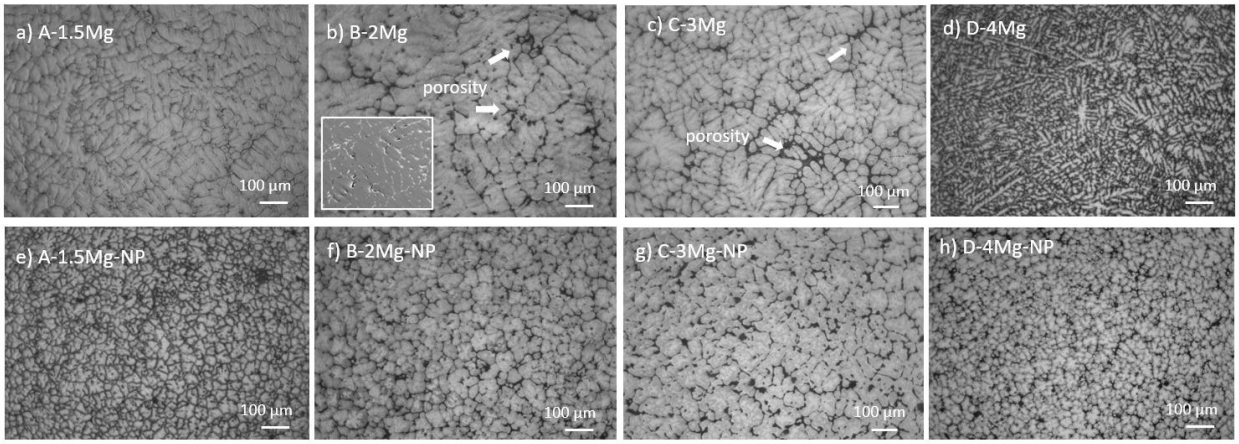

Figure 7-2 optical images of the as-cast samples: a) A-1.5Mg, b) B-2Mg, c) C-3Mg, d) D-4Mg, e) A-1.5Mg-NP, f) B-2Mg-NP, g) C-3Mg-NP, h) D-4Mg-NP The inserted image is an SEM image showing the shrinkage porosity

The SEM images are shown in Figure 7-3. The gray secondary phases in the SEM images are the S phase (Al_2CuMg). Nano-treated samples show refined equiaxed grains, while the control samples have long dendritic arms. Nanoparticles are mainly located at the grain boundaries and within the eutectic region, as shown in Figure 7-4.

`

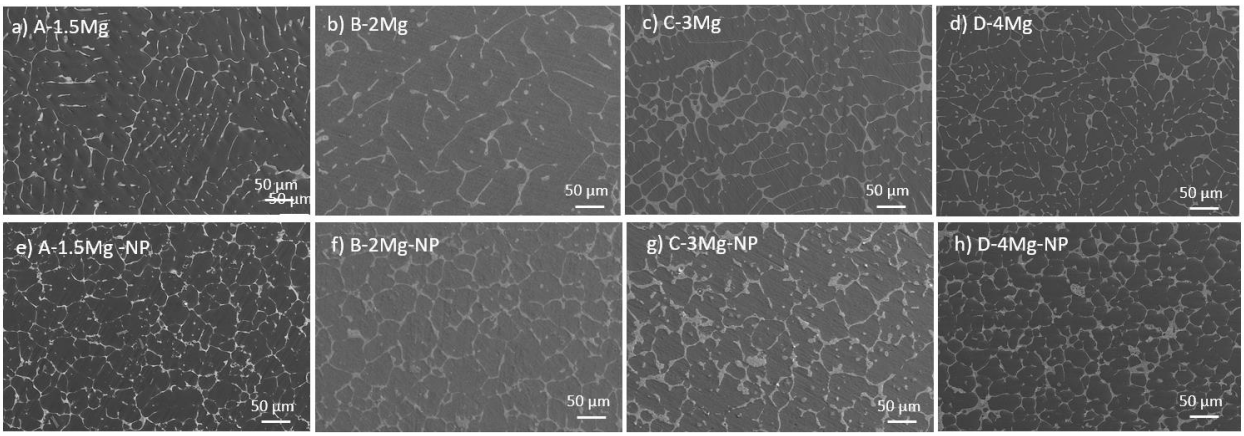

Figure 7-3. SEM images of the as-cast samples: a) A-1.5Mg, b) B-2Mg, c) C-3Mg, d) D-4Mg, e) A-1.5Mg-NP, f) B-2Mg-NP, g) C-3Mg-NP, h) D-4Mg-NP

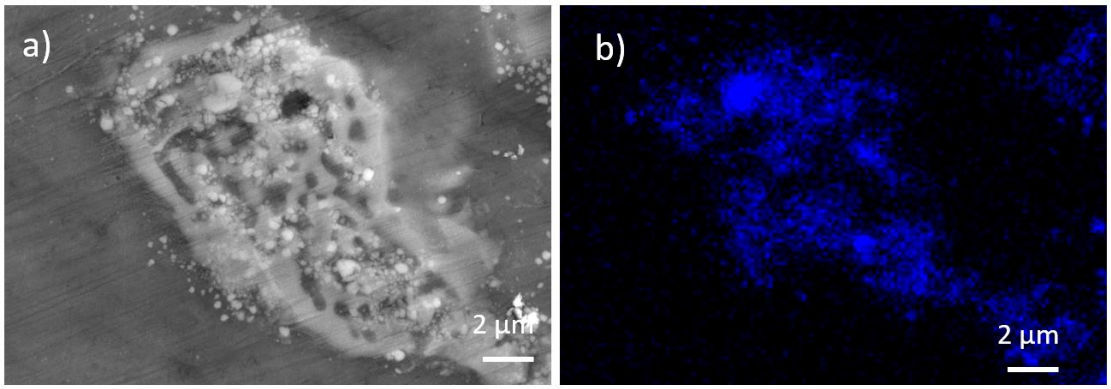

Figure 7-4. a) Typical eutectic phase in B-3Mg-NP sample with nanoparticles, b) EDS mapping of Ti corresponding to a)

The composition of the A-1.5Mg sample is designed to represent the standard AA2024. Therefore solution temperature of A-1.5Mg and A-1.5Mg-NP is similar to AA2024($495 \pm 3^{o}C$[189]). To determine suitable solutionizing temperatures for other non-standard alloys, DSC analysis was conducted. Approximately 15 mg of sample was heated to $550^{o}C$ at a heating rate of 10 K/min. The results are shown in Figure 7-5.

`

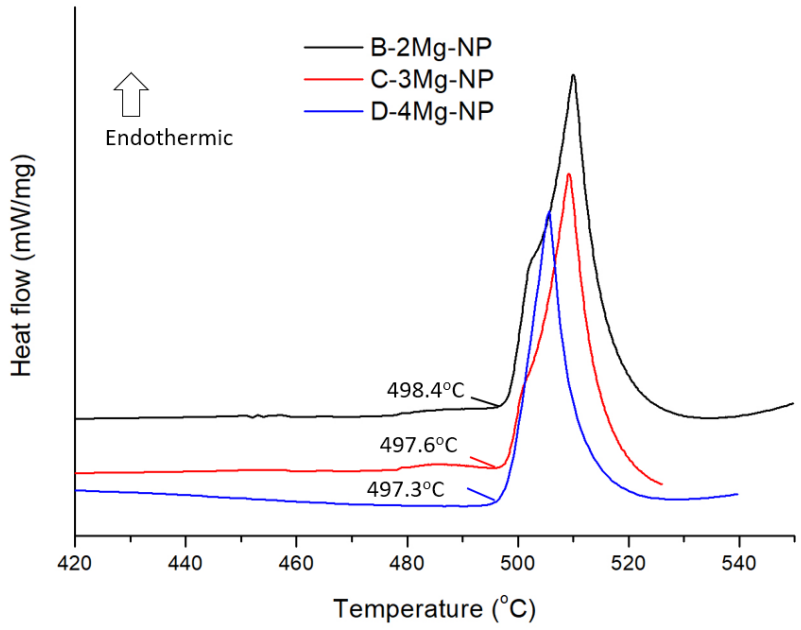

Figure 7-5. DSC analysis of the Al-Cu-xMg alloys during heating up

The peaks indicate the melting of the eutectic phase in the alloy. The start of the melting of all samples is about 498°C. It seems that the extra Mg did not reduce the solidus point much. To ensure a better dissolution of the secondary phase (S phase), all samples were first solutionized at 488°C for 24h and then 494°C for 6h. However, due to the extra amount of Mg above 1.8%, the solubility of S phase was greatly reduced[131]. The SEM images in different contrasts for the C-3Mg and C-3Mg-NP samples after solution treatment are shown in Figure 7-6a. The images are used to calculate the area fraction of the remaining secondary phases of each sample. The initial area fractions of the secondary phases in the C-3Mg sample and C-3Mg-NP sample are 9.14% and 12.72%, respectively, and the area fractions dropped to 6.07 % and 5.70%. Therefore, the secondary phase dissolution is 33.6% without nanoparticles while 55.2% with nanoparticles. Since approximately 1 vol.% of nanoparticles were added, the actual reduction of the secondary phase area is approximately 65.6% (from 10.7% to 3.7%) because every one volume percent of

`

nanoparticles takes approximately two percent of the area fraction. This promoted dissolution was discovered in all samples, as shown in Figure 7-6b. The nano-treated samples have a much higher area reduction comparing to the control samples. However, with a higher Mg content, the area reduction lowers in both samples.

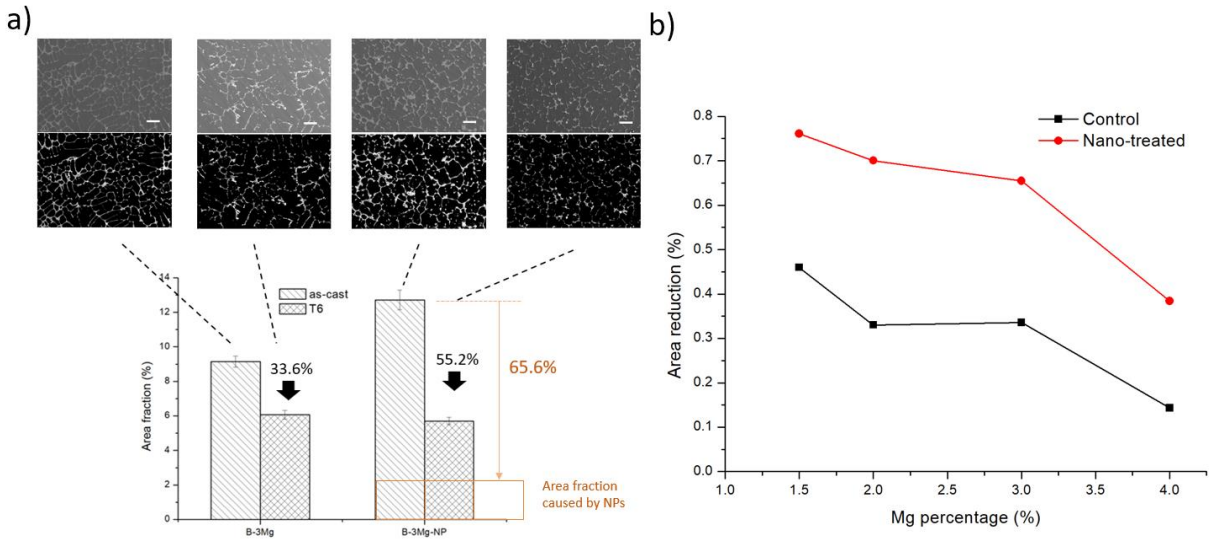

Figure 7-6. a) Calculated area fraction of the secondary phases of C-3Mg and C-3Mg-NP samples before and after solution treatment. The corresponding SEM images and converted black and white images are on the top. The scale bar is 50 µm. The brown bars indicate the area fraction occupied by nanoparticles. b) Area reduction of secondary phase in all samples

EDS mapping was applied to determine the undissolved secondary phases and solute concentration in the matrix. As shown in Figure 7-7, the C-3Mg sample has a considerable amount of secondary phases left after solution treatment, and the remaining phases are determined to be Al_2Cu and S phases. On the contrary, the remaining secondary phases in the C-3Mg-NP sample are the S phase and $Al_{18}Mn_3Ti_2$[190], and the remaining S phase is in much smaller sizes. The $Al_{18}Mn_3Ti_2$ is likely from Al_3Ti in the Al-3.5TiC master alloy. The nanoparticles are located mainly along the grain boundaries and within the S phase. Due to a better dissolution, the Al_2Cu phase was not observed in the nano-treated sample. The concentration of the solute atoms in the

`

matrix was measured by EDS mapping in the region marked by yellow squares in Figure 7-7a, d, and the weight percentages of Cu and Mg in the matrix are also shown.

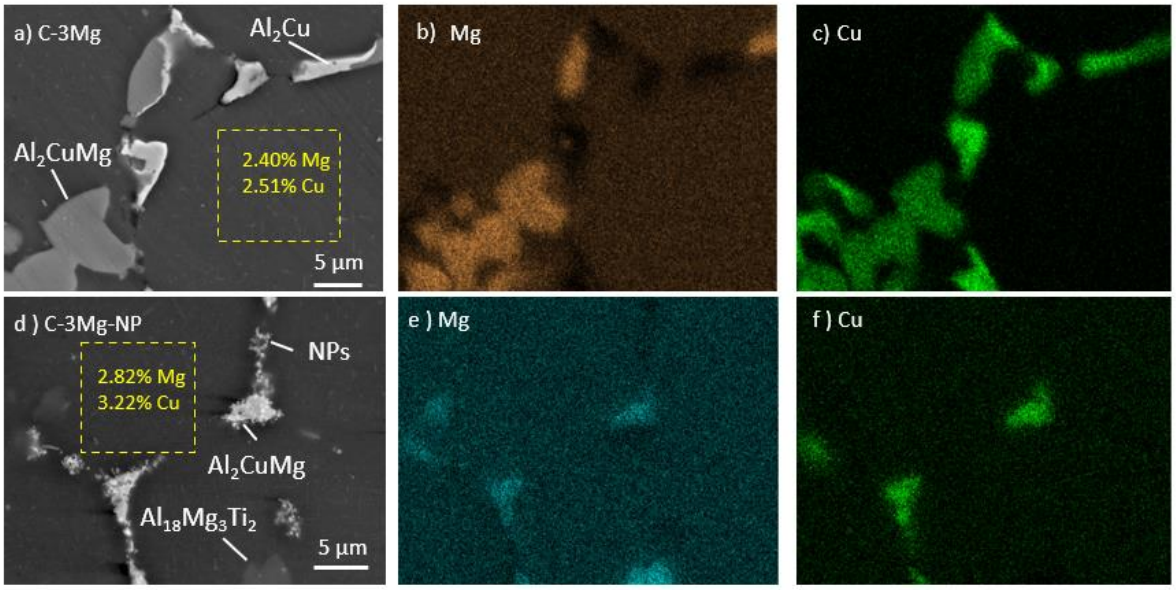

Figure 7-7. a) SEM image of C-3Mg after solution treatment; b, c) EDS mapping of Mg and Cu in a); d) SEM image of C-3Mg-NP; e, f) EDS mapping of Mg and Cu in d); EDS mapping applied to the region in the yellow squares in a, d) to determine the Mg and Cu composition in the matrix. In addition, weight percentages of the two elements are provided

In Figure 7-8, solute concentrations in all samples are summarized. All four nano-treated samples confirm higher Mg and Cu contents in the matrix than the control ones. When more Mg was added, the dissolution of Cu is significantly suppressed in the control sample. On the other hand, the dissolution suppression in the nano-treated sample was relieved when Mg was no more than 3%. In the earlier section 4.3, it was discovered that nanoparticles could promote the dissolution of secondary phases. However, a different mechanism may exist for the Al-Cu-xMg alloy in this case. Mg content normally limits the solubility of Cu because it can form an intermetallic S phase. As shown in Figure 2-23, the solubility of Cu at 775K is less than 3% when 3% of Mg is added to the solution. Therefore, the dissolution of Cu in the C-3Mg-NP sample not only surpasses the control sample but also broke the thermodynamic limit. Similarly, the A-1.5Mg-

`

NP and B-2Mg-NP samples are also above the solubility limit at the solution treatment temperature of 494°C. However, with 4% Mg added, both nano-treated and control samples fell below the solubility limit again.

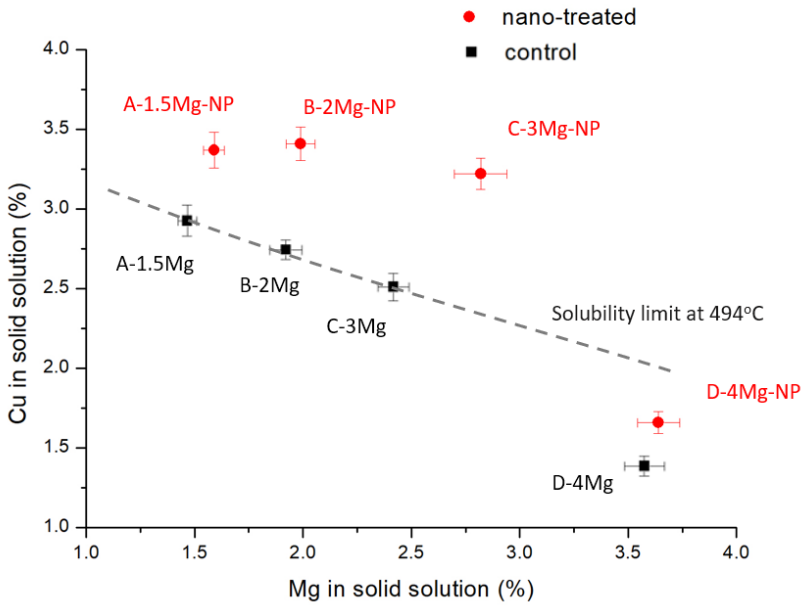

Figure 7-8. Summarized Mg and Cu composition in the solid solution after solution treatment. The dashed line is the solubility limit at 494°C according to the phase diagram from literature[131]

To further understand the dissolution thermodynamics of the nano-treated alloys, the Gibbs free energy was analyzed. As shown in Figure 7-9, in a simple binary phase system with A and B as the two elements (Figure 7-9a), their phases are α and β, as shown in Figure 7-9b, c with some nanoparticles inside the β phase. After a partial dissolution of the β phase, some nanoparticles now reside inside the α phase. During this process, the overall interfacial energy change can be described by Equation (7-1):

$$dG_\gamma = \left(\gamma_{NP-\alpha} - \gamma_{NP-\beta}\right)dA \tag{7-1}$$

`

Here $\gamma_{NP-\alpha}$ is the interfacial energy between nanoparticles and α phase; $\gamma_{NP-\beta}$ is the interfacial energy between nanoparticles and β phase; dA is the replaced area.

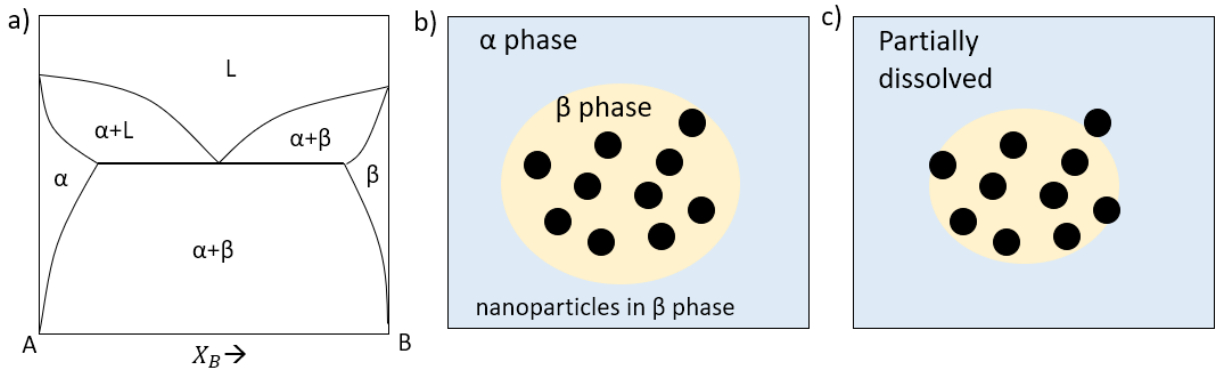

Figure 7-9. a) Simple binary eutectic phase diagram. b, c) Illustration of the dissolution process in a binary α-β system. Nanoparticles are within the β phase. After partial melting, some nanoparticles become in the α phase

To calculate the solubility of B during solution treatment, partial Gibbs free energy is written in Equation (7-2):

$$dG = dG^{\alpha} + dG^{\beta} = \left(\mu_A^{\alpha} - \mu_A^{\beta}\right)dn_A^{\alpha} + \left(\mu_B^{\alpha} - \mu_B^{\beta}\right)dn_B^{\alpha} + \left(\gamma_{NP-\alpha} - \gamma_{NP-\beta}\right)dA \quad (7\text{-}2)$$

Where dG^{α} and dG^{β} are Gibbs energy change in α and β phases, respectively; μ_A^{α} and μ_A^{β} are chemical potential of A in α and β phases, respectively; μ_B^{α} and μ_B^{β} are chemical potential of B in α and β phases respectively; dn_A^{α} and dn_B^{α} are partial molar of A and B in the α phase.

When β is an intermetallic phase that the solubility of A in β is zero, dn_A^{α} is zero. Also, dA depends on dn_B^{α}:

$$dA = Cdn_B^{\alpha} \quad (7\text{-}3)$$

Here C is the total area of nanoparticles in one mole β phase, and it is a constant.

`

When there are no nanoparticles, the chemical potentials of B in α and β phases are the same:

$$\mu_B^{\alpha*} = \mu_B^{\beta*} = \mu^{\alpha} + RTlnX_B^{\alpha*} \quad (7\text{-}4)$$

Here $\mu_B^{\alpha*}$ and $\mu_B^{\beta*}$ are the chemical potentials of B in α and β phases without nanoparticles; μ^{α} is $\mu^{\alpha}$the mole Gibbs free energy of pure β; $X_B^{\alpha*}$ is the solubility of B in α at temperature T without nanoparticles. R is the ideal gas constant.

Combining the above equations, the solubility can be calculated as:

$$X_B^{\alpha} = X_B^{\alpha*}\exp\left(\frac{(\gamma_{NP-\beta}-\gamma_{NP-\alpha})C}{RT}\right) \quad (7\text{-}5)$$

Theoretically, the solubility X_B^{α} can be increased when $\gamma_{NP-\beta} - \gamma_{NP-\alpha} > 0$. The above equation could be applied to the Al-Cu-Mg-TiC system. To determine the solubility of Cu, the dissolution of Mg is assumed to be complete. The solution temperature was 494°C, and 1 vol.% of nanoparticles were added to the alloy. Another assumption made here is that all TiC nanoparticles are within S phases after casting, and they are all spherical particles with a diameter of 100 nm so that constant C, the total area of nanoparticles in one mole S phase, can be acquired. C is 2.4×10^4 m^2/mol in this case.

As there is no available data for γ_{TiC-Al_2CuMg} in this system, the theoretical solubility increases vs. (γ_{TiC-Al_2CuMg} - γ_{TiC-Al}) curve is shown in Figure 7-10. With 0.2 J/m^{-2} interfacial energy difference, the solubility of Cu in Al could be doubled indicating that nanoparticle has a great potential to increase the solubility of the Cu in aluminum. The interfacial energy between TiC and aluminum, γ_{TiC-Al} was studied by density functional theory[191]. Due to the polar covalent

`

interaction between Al and C and their similar crystal structures and parameters, the work of adhesion is about 2.63 J/m^2 between $[001]_{Al}$ and $[001]_{Ti}$[191]. Thus, the interfacial energy is -0.05 J/m^2. While there is no available data for the interfacial energy between Al_2CuMg and TiC, the interfacial energy could be estimated by interface coherency. The coherent interface between two solids is smaller than 200 mJ/m^{2,} and the energy is between 200 mJ/m^2 to 500 mJ/m^2 when the interface is semi-coherent. The interfacial energy will be above 500 mJ/m^2 when it is incoherent[192]. TiC has an FCC structure and its lattice parameter a is 4.33 Å. The S phase has an orthorhombic lattice with three lattice parameters: a = 4.03 Å, b = 9.34 Å, c = 7.13 Å[193]. Due to the huge difference in lattice structure and lattice mismatch, no matter which TiC facet is parallel to $[001]_s$, there will always be 2/3 incoherent surfaces. Thus, the estimated γ_{TiC-Al_2CuMg} would be larger than (0.5 + 0.5 +0.2)*2/3 = 0.4 J/m^2. Even though this estimation is coarse, it illustrates a large enough difference in average interfacial energy between γ_{TiC-Al_2CuMg} and γ_{TiC-Al} to greatly improve the solubility of Cu in Al. The calculated solubility promotion is greater than acquired data in Figure 7-8 because the assumption that all nanoparticles are within the S phase is not accurate. As shown in Figure 7-4, many nanoparticles are partially in contact with the S phases and thus the total area of nanoparticles in one mole S phase is lower and the interfacial energy reduction is less.

`

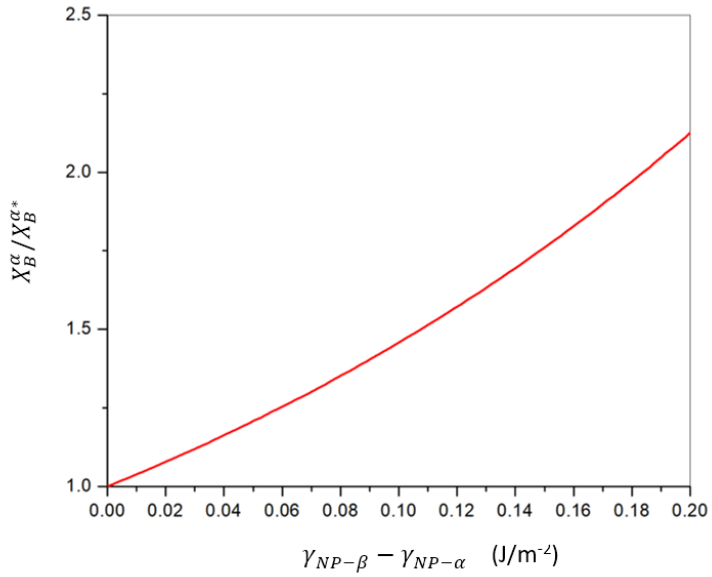

Figure 7-10. Calculated. $X_B^\alpha / X_B^{\alpha*}$ vs $\gamma_{NP-\beta} - \gamma_{NP-\alpha}$ in the Al-Cu-Mg-TiC system

However, this calculation is only valid when nanoparticles always stay with the S phase to increase overall free energy. In reality, supersaturated Cu would easily precipitate in regions away from nanoparticles to keep the Cu chemical potential in different phases at equilibrium. Here in this Al-Cu-Mg system, T phase precipitation will continuously consume Cu until all Mn is used.

The S phase dissolution is illustrated in Figure 7-11. The SEM image of the B-3Mg-NP sample after solution treatment at 488^{o}C for 4 hours is shown in Figure 7-11a. The S phases are partially dissolved at this time. Some nanoparticles located inside the S phase are now located outside the matrix but close to the S phase, possibly due to S phase partial dissolution. During this time, the rod shape T phase ($Al_{20}Cu_2Mn_3$) precipitates are observed in the matrix in Figure 7-11b. The dissolution of the S phase and the precipitation of the T phase occur at the same time. Figure 7-11c illustrates the dissolution process. Cu dissolves into the matrix and precipitates into the T phase during solutionization. After solutionization, the overall nanoparticle/S phase interface area

`

would be less. Figure 7-11d, e, f show how the dissolution of the S phase occurs from Figure 7-11a. The dissolution is faster in the nanoparticle-rich region like the bottom side of the S phase, while the dissolution process is slow on the up-right corner of this S phase because of fewer nanoparticles.

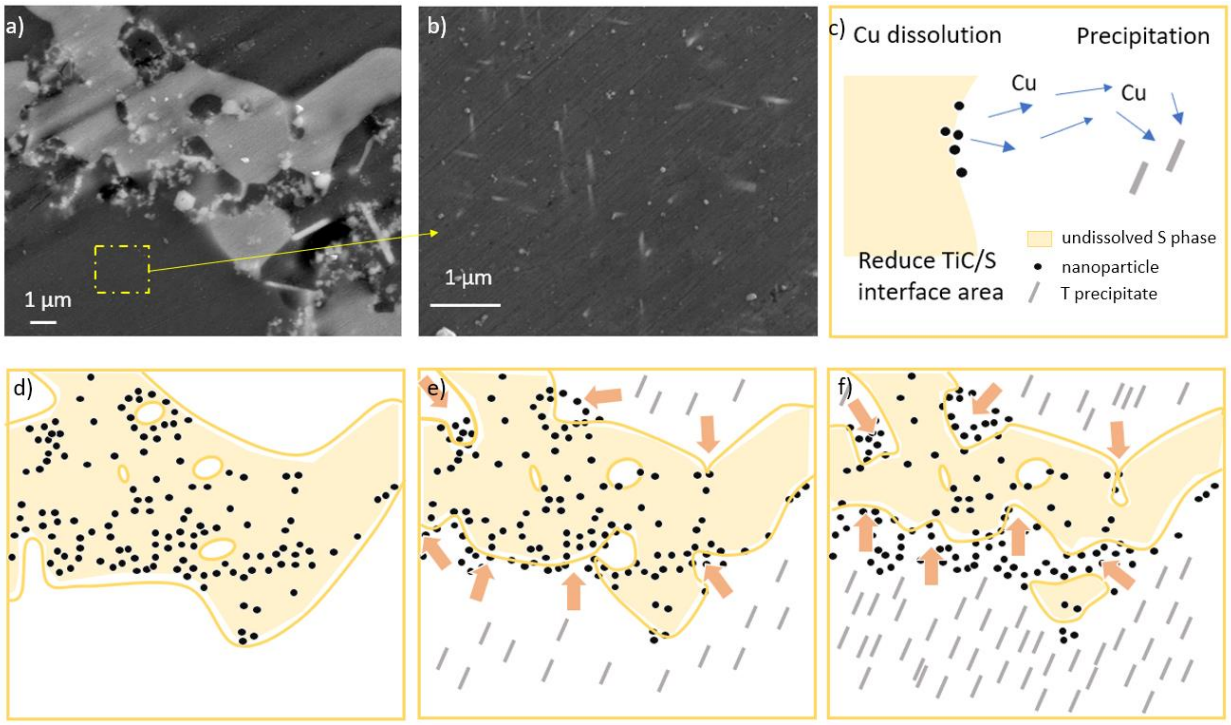

Figure 7-11. a) SEM image of the B-3Mg-NP sample solution treated at 488°C for 4 hours showing a partially dissolved S phase with nanoparticles. b) SEM image of the rod T phase precipitates observed in the yellow square in a). c) Illustration of the dissolution process. T phase precipitates when the S phase dissolves. Nanoparticles originally in the S phase are in the aluminum matrix during the dissolution of the S phase. d, e, f) Illustration of dissolution process that dissolution is fast in nanoparticle rich region. Figure f is a cartoon illustration of Figure a)

7.4 Promoted precipitation

The precipitation was studied by HAADF-STEM. The samples were first grounded to 100 µm thick and then electro-polished at 15 V by a twinjet unit (Struers TenuPol) with an electrolyte of 20% nitric acid in methanol at -20 °C. The samples were then examined by an FEI Talos F200X STEM equipped with a quad-detector EDS system at an accelerating voltage of 200kV.

`

The HAADF-STEM images of the control C-3Mg sample are shown in Figure 7-12. The observation direction is $[112]_{Al}$ as shown in the bottom-right corner of Figure 7-12a with an inserted SAED pattern on top-right. Two different types of precipitates can be seen in Figure 7-12a, b. The rod shape precipitate is the T phase ($Al_{20}Cu_2Mn_3$)[194]. The rod axis elongation direction of these T phases is along $<100>_{Al}$ in Figure 7-12 a,b, which was reported by others[195]. The EDS line scanning and mapping results in Figure 7-12c-f show the Mn and Cu peaks in these precipitates. The other precipitate is the S' phase. The S' precipitates are small lath, and its orientation is determined as $[\bar{1}00]_{Al}//[100]_{S'}$, $[02\bar{1}]_{Al}//[010]_{S'}$, $[012]_{Al}//[001]_{S}$ [196]. It has a habit plane of $\{120\}_{Al}$ and elongates along direction $<100>_{Al}$ [196]. The S' elongation direction is along $<100>_{Al}$ as described in the literature. However, these precipitates are not randomly located in the matrix but form precipitates-bands close to T phase precipitates. The band shape is very similar to dislocations especially screw dislocations marked by the white dash line in Figure 7-12a. This is possible because the T phase formed during solution treatment and dislocations are generated close to T phase precipitates during water quenching[168,195]. These dislocations become nucleations sites for S' phase precipitation. The STEM image (Figure 7-13) of C-3Mg sample after solution treatment and water quenching confirms that the distribution of dislocations is very similar to these precipitates-bands.

`

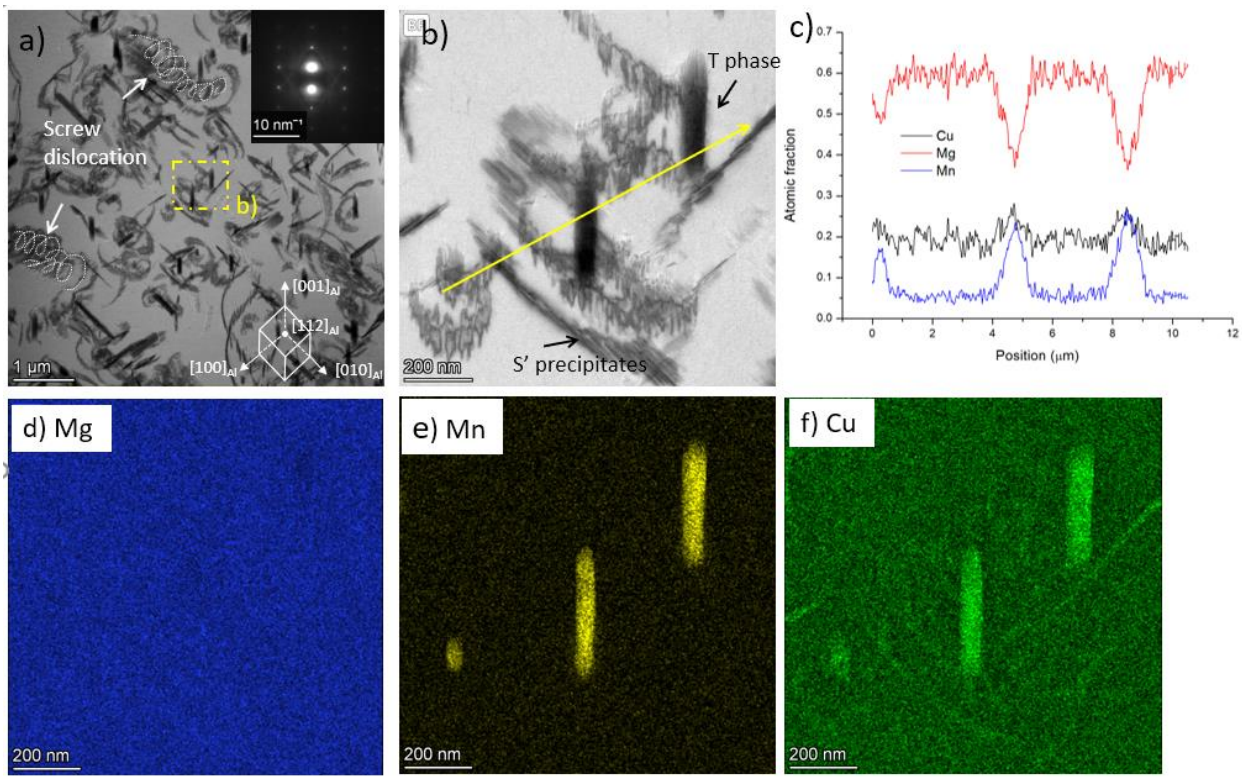

Figure 7-12. a) HAADF-STEM image of the C-3Mg sample after T6 showing different precipitates. The top-right inserted image is the diffraction pattern. The bottom-right illustration is the crystal orientation of the observed region. Screw-dislocation-like precipitate-bands are marked by white dash lines. b) Bright-field image of a region in the yellow square in a). The long arrow is the line scanning of Cu, Mg, Mn elements. c) Line scanning results. d, e, f) elemental mapping of Mg, Mn, and Cu of image b)

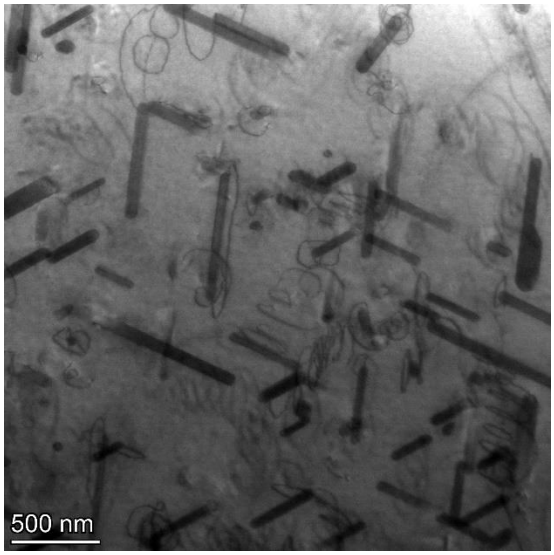

Figure 7-13. HAADF-STEM image of the C-3Mg image after solution treatment and quenching. Dislocations observed around T phases

The HAADF-STEM images of the nano-treated C-3Mg-NP sample are shown in Figure 7-14. The observation direction is $[112]_{Al}$, but the [100] direction is different, as shown by the SAED pattern on the top-right corner and the illustration of the crystal orientation in the bottom-right corner of Figure 7-13a. A grain boundary was marked by a red dash line. Compared to the control sample, much denser and finer S' precipitates appear in Figure 7-14b. Moreover, the S' precipitates are more uniformly distributed in the matrix. A similar S' precipitate band exists near edge dislocations marked by a white dash line in Figure 7-14b. Generally, the uniformly distributed S' precipitates have a larger size (about 500 nm in length), while the S' precipitates along dislocations are smaller (about 200 nm in length). TiC nanoparticles are observed along the grain boundary in Figure 7-14c, and corresponding EDS mapping is shown in Figure 7-14 d-f. The bottom-right corner has a stronger Mn and Cu signal because the sample is thicker in that region. As the viewing of dislocation-related S' precipitates and T phase is blocked by the dense S' precipitates in this direction, an image with a tilted angle was presented in Figure 7-15, showing a better contrast for the dislocation-related S' precipitate bands and T phase precipitates. The difference between the nano-treated and the control samples is mainly the density of the small S' precipitates in the matrix.

`

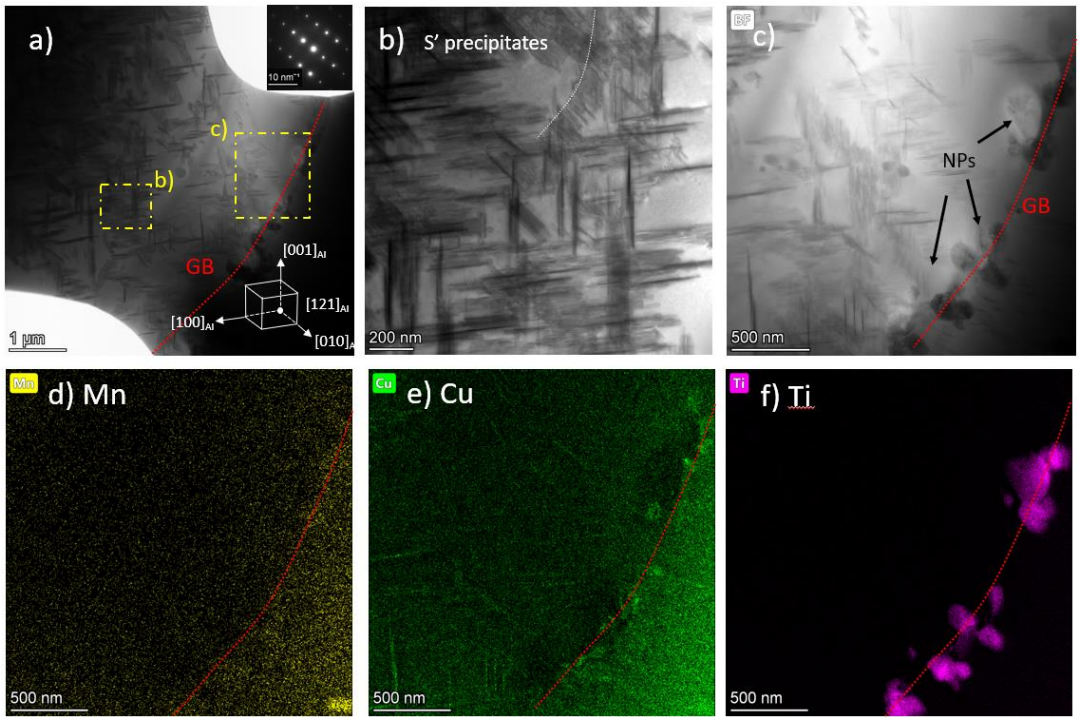

Figure 7-14. a) HAADF-STEM image of the C-3Mg-NP sample after T6 showing different precipitates. The top-right inserted image is the diffraction pattern. The bottom-right illustration is the crystal orientation of the observed region. The red dash curve is a grain boundary. b, c) Bright-field images of the regions in the yellow square in a) showing dense S' precipitates and NPs along the grain boundary. A white dash curve marks one edge dislocation. d, e, f) Elemental mapping of Mn, Cu, and Ti of image c)

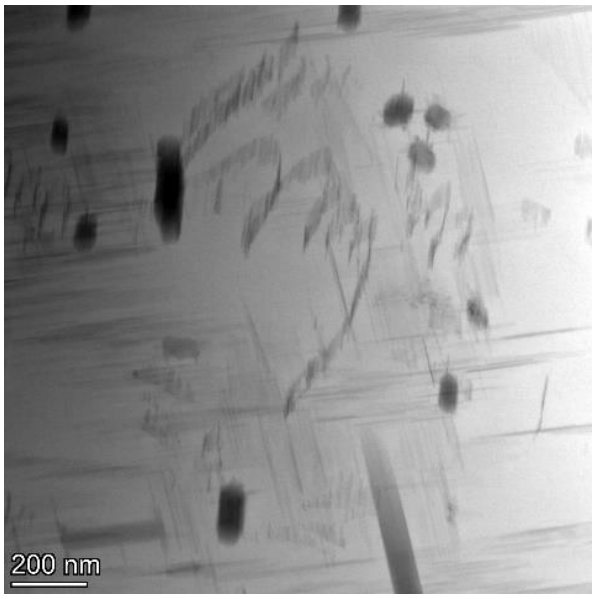

Figure 7-15. HAADF-STEM image of the B-3Mg-NP sample after T6 showing different precipitates and dislocations

`

7.5 Mechanical properties

The mechanical properties of the samples after T6 heat treatment were tested and presented in Figure 7-16. In the control samples, a higher Mg content from 1.5 wt.% to 2 wt.% increases the microhardness from 142.1 ± 5.4 HV to 146.1 ± 3.8 HV. However, when Mg content increases to 3 and 4 wt.%, the hardness dropped to 133.2 ± 4.6 HV and 131.1 ± 4.5 HV. In the nano-treated samples, the highest microhardness of 163.9 ± 10.2 HV was found in the C-3Mg-NP sample, but the hardness decreased quickly to 135.7 ± 6.4 HV when Mg is 4 wt.%. The tensile testing results also showed a similar trend, as shown in Figure 7-16b, c. The cast C-3Mg-NP sample after T6 has the best properties among nano-treated ones with a UTS of 451.3 ± 1.1MPa, a YS of 356.4 ± 5.9 MPa, and ductility of 4.11 ± 0.28%. The B-2Mg sample has the best mechanical properties among all control samples. Generally, all nano-treated samples have better UTS, YS, and elongation than their control samples. These results match well with the solubility enhancement in Figure 7-8. More dissolved solute elements result in better mechanical properties. The promotion of dissolution is attributed to denser S' precipitates and fewer remaining coarse secondary phases.

`

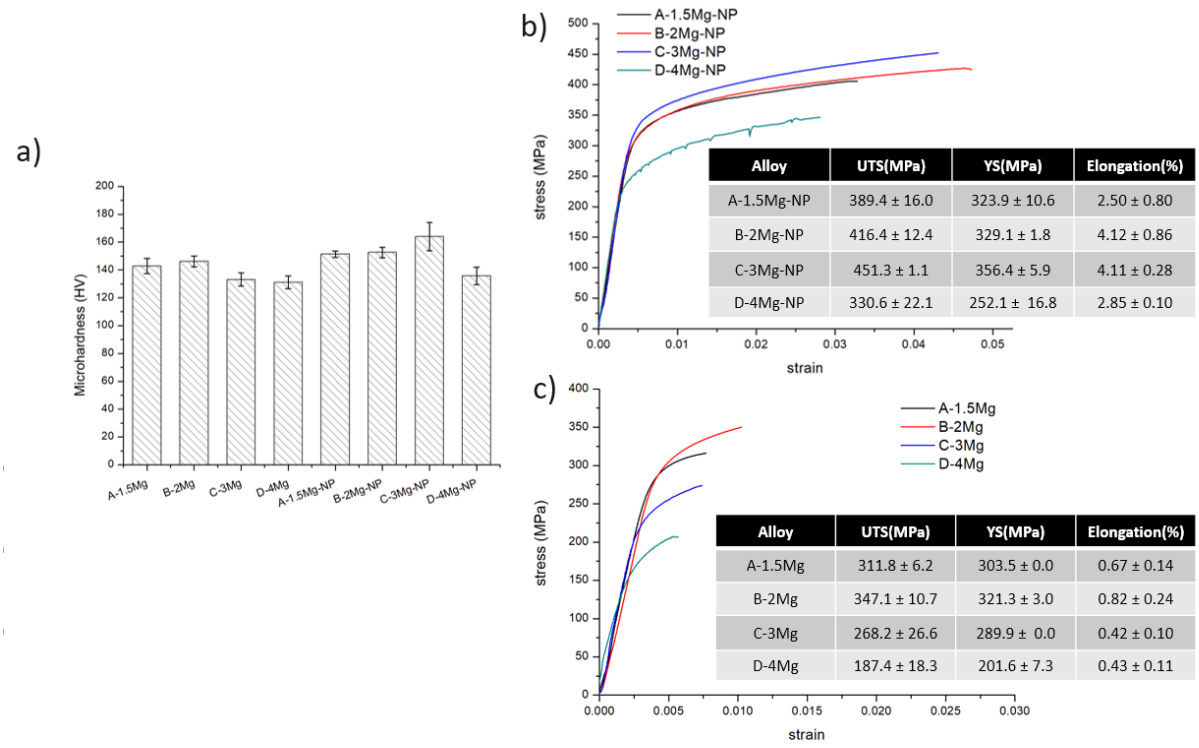

Alloy	UTS(MPa)	YS(MPa)	Elongation(%)
A-1.5Mg-NP	389.4 ± 16.0	323.9 ± 10.6	2.50 ± 0.80
B-2Mg-NP	416.4 ± 12.4	329.1 ± 1.8	4.12 ± 0.86
C-3Mg-NP	451.3 ± 1.1	356.4 ± 5.9	4.11 ± 0.28
D-4Mg-NP	330.6 ± 22.1	252.1 ± 16.8	2.85 ± 0.10

Alloy	UTS(MPa)	YS(MPa)	Elongation(%)
A-1.5Mg	311.8 ± 6.2	303.5 ± 0.0	0.67 ± 0.14
B-2Mg	347.1 ± 10.7	321.3 ± 3.0	0.82 ± 0.24
C-3Mg	268.2 ± 26.6	289.9 ± 0.0	0.42 ± 0.10
D-4Mg	187.4 ± 18.3	201.6 ± 7.3	0.43 ± 0.11

Figure 7-16. a) Microhardness of the samples after T6 heat treatment; b) Stress-strain curves of the nano-treated samples after T6. C) Stress-strain curves of the control samples after T. Inserted table contains tensile testing data

The fracture surface of the C-3Mg and C-3Mg-NP samples were also studied. The SEM images are presented in Figure 7-17. Porosities and microcracks are observed in the fracture surface of the C-3Mg sample, as shown in Figure 7-17a. Large pieces of undissolved S phases are everywhere, as shown in Figure 7-17c. However, there is little porosity in the fracture surface of the C-3Mg-NP sample, and the remaining undissolved S phase is much smaller. There is one microcrack found in the nano-treated sample, as shown in Figure 7-17b. Even though the dimple is not uniform in the nano-treated sample, the dimples in the nanoparticle-rich region are smaller than the nanoparticle-scarce region. As shown in Figure 7-17d, the nano-treated sample without plastic deformation shows a ductile fracture behavior and provides reasonably good ductility.

`

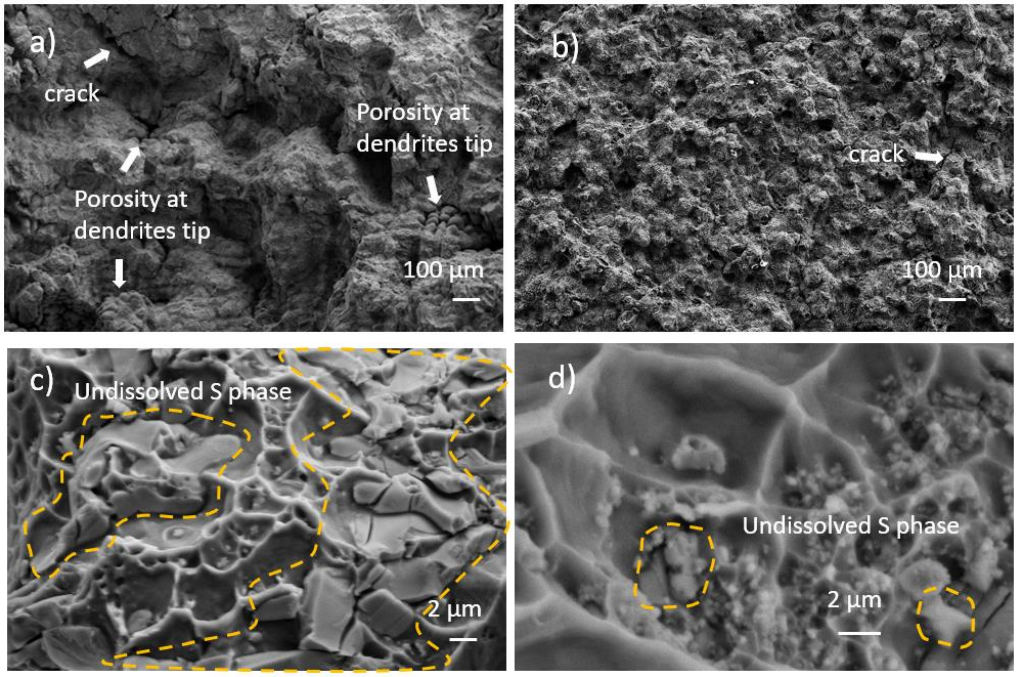

Figure 7-17. SEM images of the fracture surface, a, c) C-3Mg after T6 and b, d) C-3Mg-NP after T6. Shrinkage porosity, cracks, and undissolved S phases are marked

7.6 Summary

Nano-treated Al-4.6Cu-xMg-0.3Mn alloys were cast without hot cracking and shrinkage porosity. While a higher Mg content reduced the solubility of S phase in the control samples, nano-treating improved the dissolution of S phases during solution treatment and even broke the solubility limit until the Mg content is more than 3%. The promoted dissolution was possibly caused by reducing overall interfacial energy between nanoparticles and the S phase during solutionization.

Moreover, the density of S' precipitates was significantly increased by nano-treating when compared to control samples since a higher supersaturation was achieved in the nano-treated samples. The S' precipitates in the C-3Mg sample mostly nucleated along the dislocations to form

`

precipitation bands. In the nano-treated C-3Mg-NP sample, a higher supersaturation allows S' phase to precipitate along the dislocations as well as in the matrix, leading to a more uniform distribution of precipitates.

The mechanical properties were significantly improved by nano-treating at higher Mg content. In the control sample, when the Mg content was above 2 wt.%, its microhardness and tensile properties were reduced due to a limited dissolution of the S phase. In contrast, in the nano-treated samples, the extra Mg content provided extra strength. For example, the C-3Mg-NP sample offers a UTS of 451.3 ± 1.1MPa, a YS of 356.4 ± 5.9 MPa, and a ductility of 4.11 ± 0.28%. However, the UTS and YS decreased when the Mg weight percentage was 4 %

`

Chapter 8 Conclusions

This dissertation is motivated to study and apply nano-treating effects to further improve the properties of high-strength aluminum alloys by cost-effective manufacturing methods.

A new in-situ method was first developed to successfully synthesize TiB_2, TiC, ZrB_2, WC particles with smaller size and narrow size distribution in aluminum alloys. In addition, the parameters that influence the size of the synthesized nanoparticles were studied. While both concentration and reaction time did not significantly affect the particle size in a diluted liquid solution, the particle size increases rapidly with a higher reaction temperature. An interface-controlled reaction mechanism is proposed to understand this phenomenon. The new in-situ nanoparticle synthesis method establishes a solid foundation to allow nano-treating applicable for mass production.

A systematic study of the nano-treating effects on solidification and heat treatment was conducted. The solidification curves and microstructures of the aluminum alloys nano-treated by TiC nanoparticles confirm promoted nucleation and effective grain growth restriction. During the last stage of solidification, the grain coherent point was postponed by nanoparticles, thus allowing sufficient time for liquid feeding to prevent solidification shrinkage and hot tearing. These effects can significantly improve castability and ingot mechanical properties of traditionally difficult-to-cast alloys. After solidification, the volume fraction of the secondary phases is modified because the permeability of the liquid's coherent solid network and viscosity seemed altered by nano-treating. Furthermore, a promoted diffusion seemed to be assisted by interface and dislocation mediated diffusion. As the volume fraction, size of the secondary phases, and diffusivity are directly related to the dissolution speed of the secondary phases during solution treatment, nano-

`

treating becomes very effective in promoting solution treatment. The nano-treating method enables mass manufacturing of high-strength aluminum alloys such as AA7034 by traditional casting at a slow cooling rate. A better dissolution of the secondary phases results in a higher level of supersaturation of the solute atoms, and dislocations can serve as heterogeneous nucleation sites for precipitates. The precipitation process, aging, is facilitated as well. The promoted aging allows natural aging to produce adequate strengths at a shorter time. In general, nano-treating offers two powerful effects: “antibody effect” to enhance manufacturing capability and “vitamin effect” improves microstructure and properties of the alloy. Three application case studies were conducted to demonstrate the nano-treating effects.

The first application was to enable the manufacturing of high-strength Al-Zn-Mg-Cu alloy (AA7034). The nano-treated AA7034 was successfully cast by down-hill casting at a low cooling rate of 0.25 K/s. The as-cast AA7034 sample containing 2 vol.% TiC nanoparticles offer a UTS of 769.1 ± 68.3 MPa, a YS of 754.4 ± 27.9 MPa, and a 2.0 ± 0.9% ductility. The improved mechanical properties were due to the complete dissolution of secondary phases that were difficult to dissolve in pure AA 7034. The nano-treated samples show ductile fracture behavior, while the pure AA7034 sample was very brittle. The nano-treated cast samples have less segregation and carry fewer and smaller secondary phases than pure AA7034. A modified local solute redistribution equation (LSRE) was applied to calculate the volume of the eutectic phase. It shows that nanoparticles could change the volume fraction of the eutectic phase by influencing the permeability of the coherent solid network in the final stage of solidification and the viscosity of the molten melt. Furthermore, the dissolution of the secondary phases in 7034-1NP and 7034-2NP samples was promoted due to a refined microstructure and an accelerated diffusion.

`

The second application case study provided a solution to eliminating post-welding heat treatment after arc welding of AA7075 alloy. The nano-treated Al-6.0Zn-2.6Mg-xCu samples and their control samples containing different Cu percentages were fabricated and studied. The nano-treated samples have a refined microstructure with little dendritic arms. The nano-treated samples also show a facilitated aging behavior after natural aging for 44 days. The formation of GPII zones in the nano-treated samples is faster than the control samples after a detailed study on microhardness evolution curves, DSC analysis. Arc welding of commercial AA7075 aluminum plates was performed with both nano-treated filler wire and the control wire. The nano-treated wire resulted in less secondary phase and refined grains after welding. The tensile testing shows the nano-treated wire provides a good strength (428.8 ± 15.07 MPa), yield (338.7 ± 18.2 MPa), and ductility (2.03 ± 0.15%). Compared to other arc-welded high-strength aluminum, the nano-treated filler provides the highest strength without post-welding heat treatment.

The third application case study was to develop and cast new high-strength Al-Cu-Mg alloys. The standard AA2024 typically contains 4.5% Cu and a max of 1.8% Mg. In this study, nano-treated Al-4.6Cu-xMg-0.3Mn alloys contain 1.5% to 4.0% Mg were fabricated without shrinkage porosity. In the control samples, higher Mg reduced the solubility of the S phase, while nano-treating broke the solubility limit and significantly improve the dissolution of S phases during solution treatment. The promoted dissolution is believed to be induced by the reduction of overall interfacial energy between nanoparticles and the S phase. After artificial aging, the density of S' precipitates is greatly increased because nano-treating induced higher supersaturation when compared to control samples. Moreover, S' precipitates in the C-3Mg sample mostly nucleate along the dislocations and form precipitation bands. In the nano-treated C-3Mg-NP sample, the higher supersaturation allows S' phase to precipitate with the dislocations and more in the matrix,

`

leading to a more uniform distribution of finer precipitates. In the control sample, increasing the Mg weight percentage reduces its microhardness and tensile properties due to a limited dissolution of the S phase. In contrast, in the nano-treated samples, the extra Mg can provide extra strength. The cast C-3Mg-NP sample after T6 delivers a UTS of 451.3 ± 1.1MPa, a YS of 356.4 ± 5.9 MPa, and a ductility of 4.11 ± 0.28%. However, when Mg reaches the level of 4 wt.%, the properties of the nano-treated samples became worse due to the greatly reduced solubility of Cu.

In summary, this dissertation first discussed a new interface-controlled reaction for in-situ synthesis of ceramic nanoparticles before utilizing these nanoparticles for nano-treating of molten metals. Then the nano-treating effects on solidification and heat treatment were systematically studied. Two critical effects from nano-treating were summarized: “antibody effect” to enable scalable manufacturing of traditionally difficult-to-manufacture alloys without cracking and shrinkage porosities and “vitamin effect” to improve microstructure and properties of alloys. These effects were successfully demonstrated in developing and manufacturing high-performance aluminum alloys, partiuclarly manufacturing high-strength Al-Zn-Mg-Cu alloys, natural aging to AA7075 welds with nano-treated welding wires, and casting of new high-strength Al-Cu-Mg alloys. Nano-treating successfully promoted the solution treatment of high-strength Al-Zn-Mg-Cu by modifying secondary phases and enhancing diffusion. With a new nano-treated welding filler, AA7075 was arc welded and recovered 77% material strength of the base metal after natural aging. In addition, Nano-treating breaks the solubility limit of Mg and Cu in the new Al-Cu-Mg alloy possibly by interfacial energy reduction during solution treatment to offer significantly improved performance.

`

Chapter 9 Recommendations for Future Work

The scientific understanding of nano-treating effects on high-strength aluminum alloys in this dissertation demonstrates great potential to develop and manufacture new alloys that were traditionally deemed impossible. While some understanding of nanoparticle effects on solidification, solution treatment, aging, plastic deformation, and other metallurgy processes of aluminum alloys has been developed, reliable physics models still lack. A more systematic study on these effects is needed for aluminum alloys and all other materials systems. Little study has been conducted to fully understand how nano-treating would affect stress corrosion cracking, fatigue, and fracture toughness for practical applications. Following research directions are recommended:

9.1 Fabrication of new in-situ ceramic nanoparticles

In-situ ceramic nanoparticles are essential for making nano-treating applicable to industry. Ceramic nanoparticles like silicon carbide, boron carbide, titanium nitride, etc., are commonly added into different alloys systems. Still, these nanoparticles are not readily fabricated by the low-cost in-situ method. The flux-assisted in-situ synthesis can make nano-sized particles if suitable salts and reactants are used. For example, silicon carbide might be fabricated using potassium hexafluorosilicate (K_2SiF_6) and carbon in a fluoride salt pool. Activated carbon and KBF_4 can be used to fabricated B_4C.

Different nanoparticles would have different dispersion capabilities in different alloys. Therefore, new particles could provide more possibilities for suitable nanoparticles-treated alloys.

`

9.2 Physics models for nano-treating

Successful physics models can be used to develop new alloys and predict the alloy properties after nano-treating. For example, the following models might be beneficial for nano-treating.

1. Nanoparticle modified diffusion of alloy elements.

   While nanoparticles can facilitate solution treatment effectively, it is not clear how the overall diffusivity of the elements was impacted. As nanoparticles usually reside with the secondary phases at grain boundaries, they could block the matrix diffusion when nanoparticles enclose secondary phases. On the other hand, the nanoparticle-matrix interface and dislocations can speed up the diffusion of alloying elements. Therefore, the overall trend due to the competitive nature of nanoparticle effects needs more study in various alloy systems, and a better physics model is needed to shed more insights into nanoparticle's effect on diffusion.

2. Nanoparticle modified aging

   If the nanoparticle-influenced diffusivity is fully understood, the nanoparticle-modified aging can be better modeled too. Since the clustering of alloying elements is related to vacancy concentration in the matrix, the nanoparticle-modified vacancy concentration should also be studied. Nanoparticles would increase the overall defects (dislocations, grain boundaries, and nanoparticle-matrix interfaces), which could act as vacancy sinks to reduce the density of vacancies nearby. Even though one literature has stated that nanoparticles reduced the vacancy depletion close to the grain boundary[8], but no physical modeling has been built.

3. Nanoparticle dispersion in alloy

`

Nanoparticle dispersion in pure metal has been well studied. Still, in the alloys, other elements can alter the interfacial energy between nanoparticles and the melt and the system Hamaker constant for the nanoparticle dispersion in molten alloys. Thus, the dispersion model would need more careful development.

9.3 Other properties modified by nano-treating.

Nano-treating could alter the creep resistance, fatigue, fracture toughness, corrosion resistance, wear resistance, oxidation, and stress corrosion resistance of alloys. Therefore, all these aspects should be studied.

`

References

(1) Kaufman, J. G.; Rooy, E. L. *Aluminum Alloy Castings: Properties, Processes, and Applications*; ASM International: Materials Park, OH, 2004.

(2) Kaufman, J. G. *Introduction to Aluminum Alloys and Tempers*; ASM International: Materials Park, OH, 2000.

(3) Xu, D.; Li, Z.; Wang, G.; Li, X.; Lv, X.; Zhang, Y.; Fan, Y.; Xiong, B. Phase Transformation and Microstructure Evolution of an Ultra-High Strength Al-Zn-Mg-Cu Alloy during Homogenization. *Mater. Charact.* **2017**, *131*, 285–297. https://doi.org/10.1016/j.matchar.2017.07.011.

(4) Ferguson, J. B.; Schultz, B. F.; Mantas, J. C.; Shokouhi, H.; Rohatgi, P. K. Effect of Cu, Zn, and Mg Concentration on Heat Treating Behavior of Squeeze Cast Al-(10 to 12)Zn-(3.0 to 3.4)Mg-(0.8 to 1)Cu. *Metals* **2014**, *4* (3), 314–321. https://doi.org/10.3390/met4030314.

(5) Chen, L.-Y.; Xu, J.-Q.; Choi, H.; Konishi, H.; Jin, S.; Li, X.-C. Rapid Control of Phase Growth by Nanoparticles. *Nat. Commun.* **2014**, *5*, 3879. https://doi.org/10.1038/ncomms4879.

(6) Choi, H.; Cho, W.; Konishi, H.; Kou, S.; Li, X. Nanoparticle-Induced Superior Hot Tearing Resistance of A206 Alloy. *Metall. Mater. Trans. A* **2013**, *44* (4), 1897–1907. https://doi.org/10.1007/s11661-012-1531-8.

(7) Sokoluk, M.; Cao, C.; Pan, S.; Li, X. Nanoparticle-Enabled Phase Control for Arc Welding of Unweldable Aluminum Alloy 7075. *Nat. Commun.* **2019**, *10* (1), 98. https://doi.org/10.1038/s41467-018-07989-y.

`

(8) Li, X.; Cai, Q.; Zhao, B.; Liu, B.; Li, W. Precipitation Behaviors and Properties of Solution-Aging Al-Zn-Mg-Cu Alloy Refined with TiN Nanoparticles. *J. Alloys Compd.* **2018**, *746*, 462–470. https://doi.org/10.1016/j.jallcom.2018.02.271.

(9) Wang, M.; Wang, Y.; Liu, J.; Chen, Z.; Chen, H.; Wu, Y.; Zhang, F.; Wang, H. Effects of Zn Content on Microstructures and Mechanical Properties of In-Situ TiB2/Al-Zn-Mg-Cu Composites Subjected to Hot Extrusion. *Mater. Sci. Eng. A* **2019**, *742*, 364–372. https://doi.org/10.1016/j.msea.2018.11.030.

(10) Yuan, J.; Zuo, M.; Sokoluk, M.; Yao, G.; Pan, S.; Li, X. Nanotreating High-Zinc Al–Zn–Mg–Cu Alloy by TiC Nanoparticles. In *Light Metals 2020*; Tomsett, A., Ed.; The Minerals, Metals & Materials Series; Springer International Publishing: Cham, 2020; pp 318–323. https://doi.org/10.1007/978-3-030-36408-3_46.

(11) Ajayan, P. M.; Schadler, L. S.; Braun, P. V. Nanocomposite Science and Technology. 236.

(12) Casati, R.; Vedani, M. Metal Matrix Composites Reinforced by Nano-Particles—A Review. *Metals* **2014**, *4* (1), 65–83. https://doi.org/10.3390/met4010065.

(13) Shen, Y.; Li, X.; Hong, T.; Geng, J.; Wang, H. Effects of TiB2 Particles on Microstructure and Mechanical Properties of an In-Situ TiB2-Al-Cu-Li Matrix Composite. *Mater. Sci. Eng. A* **2016**, *655*. https://doi.org/10.1016/j.msea.2015.12.104.

(14) Guo, E.; Shuai, S.; Kazantsev, D.; Karagadde, S.; Phillion, A. B.; Jing, T.; Li, W.; Lee, P. D. The Influence of Nanoparticles on Dendritic Grain Growth in Mg Alloys. *Acta Mater.* **2018**, *152*, 127–137. https://doi.org/10.1016/j.actamat.2018.04.023.

(15) Wang, K.; Jiang, H. Y.; Jia, Y. W.; Zhou, H.; Wang, Q. D.; Ye, B.; Ding, W. J. Nanoparticle-Inhibited Growth of Primary Aluminum in Al–10Si Alloys. *Acta Mater.* **2016**, *103*, 252–263. https://doi.org/10.1016/j.actamat.2015.10.005.

`

(16) Cherepanov, A.; Cherepanova, V.; Manolov, V. Heterogeneous Nucleation and Growth of a Solid in a Nanomodified Alloy. *J. Cryst. Growth* **2019**, *527*, 125251. https://doi.org/10.1016/j.jcrysgro.2019.125251.

(17) Molleman, B.; Hiemstra, T. Size and Shape Dependency of the Surface Energy of Metallic Nanoparticles: Unifying the Atomic and Thermodynamic Approaches. *Phys. Chem. Chem. Phys.* **2018**, *20* (31), 20575–20587. https://doi.org/10.1039/C8CP02346H.

(18) Ju, X.; Zhang, F.; Chen, Z.; Ji, G.; Wang, M.; Wu, Y.; Zhong, S.; Wang, H.; Ju, X.; Zhang, F.; Chen, Z.; Ji, G.; Wang, M.; Wu, Y.; Zhong, S.; Wang, H. Microstructure of Multi-Pass Friction-Stir-Processed Al-Zn-Mg-Cu Alloys Reinforced by Nano-Sized TiB2 Particles and the Effect of T6 Heat Treatment. *Metals* **2017**, *7* (12), 530. https://doi.org/10.3390/met7120530.

(19) Wang, K.; Jiang, H. Y.; Wang, Q. D.; Ye, B.; Ding, W. J. Nanoparticle-Induced Nucleation of Eutectic Silicon in Hypoeutectic Al-Si Alloy. *Mater. Charact.* **2016**, *117*, 41–46. https://doi.org/10.1016/j.matchar.2016.04.016.

(20) Cao, C.; Chen, L.; Xu, J.; Zhao, J.; Pozuelo, M.; Li, X. Phase Control in Immiscible Zn-Bi Alloy by Tungsten Nanoparticles. *Mater. Lett.* **2016**, *174*, 213–216. https://doi.org/10.1016/j.matlet.2016.03.105.

(21) Katsarou, L.; Mounib, M.; Lefebvre, W.; Vorozhtsov, S.; Pavese, M.; Badini, C.; Molina-Aldareguia, J. M.; Jimenez, C. C.; Pérez Prado, M. T.; Dieringa, H. Microstructure, Mechanical Properties and Creep of Magnesium Alloy Elektron21 Reinforced with AlN Nanoparticles by Ultrasound-Assisted Stirring. *Mater. Sci. Eng. A* **2016**, *659*, 84–92. https://doi.org/10.1016/j.msea.2016.02.042.

`

(22) Saboori, A.; Padovano, E.; Pavese, M.; Dieringa, H.; Badini, C. Effect of Solution Treatment on Precipitation Behaviors, Age Hardening Response and Creep Properties of Elektron21 Alloy Reinforced by AlN Nanoparticles. *Materials* **2017**, *10* (12). https://doi.org/10.3390/ma10121380.

(23) Zhou, D.; Qiu, F.; Jiang, Q. The Nano-Sized TiC Particle Reinforced Al–Cu Matrix Composite with Superior Tensile Ductility. *Mater. Sci. Eng. A* **2015**, *622*, 189–193. https://doi.org/10.1016/j.msea.2014.11.006.

(24) Cao, C.; Yao, G.; Jiang, L.; Sokoluk, M.; Wang, X.; Ciston, J.; Javadi, A.; Guan, Z.; Rosa, I. D.; Xie, W.; Lavernia, E. J.; Schoenung, J. M.; Li, X. Bulk Ultrafine Grained/Nanocrystalline Metals via Slow Cooling. *Sci. Adv.* **2019**, *5* (8), eaaw2398. https://doi.org/10.1126/sciadv.aaw2398.

(25) Tamirisakandala, S.; Bhat, R. B.; Tiley, J. S.; Miracle, D. B. Grain Refinement of Cast Titanium Alloys via Trace Boron Addition. *Scr. Mater.* **2005**, *53* (12), 1421–1426. https://doi.org/10.1016/j.scriptamat.2005.08.020.

(26) *Mechanical Metallurgy*; 1986.

(27) Zhu, M.; Keller, T. S.; Spengler, D. M. Effects of Specimen Load-Bearing and Free Surface Layers on the Compressive Mechanical Properties of Cellular Materials. *J. Biomech.* **1994**, *27* (1), 57–66. https://doi.org/10.1016/0021-9290(94)90032-9.

(28) Matvienko, O.; Daneyko, O.; Kovalevskaya, T.; Khrustalyov, A.; Zhukov, I.; Vorozhtsov, A. Investigation of Stresses Induced Due to the Mismatch of the Coefficients of Thermal Expansion of the Matrix and the Strengthening Particle in Aluminum-Based Composites. *Metals* **2021**, *11* (2), 279. https://doi.org/10.3390/met11020279.

`

(29) Zhang, X.; Hu, T.; Rufner, J. F.; LaGrange, T. B.; Campbell, G. H.; Lavernia, E. J.; Schoenung, J. M.; van Benthem, K. Metal/Ceramic Interface Structures and Segregation Behavior in Aluminum-Based Composites. *Acta Mater.* **2015**, *95*, 254–263. https://doi.org/10.1016/j.actamat.2015.05.021.

(30) Dorward, R. C. Precipitate Coarsening during Overaging of Al–Zn–Mg–Cu Alloy. *Mater. Sci. Technol.* **1999**, *15* (10), 1133–1138. https://doi.org/10.1179/026708399101505176.

(31) Liu, Y.; Zhu, X.; Li, M.; O'Hayre, R. P.; Yang, W. Nanoparticles at Grain Boundaries Inhibit the Phase Transformation of Perovskite Membrane. *Nano Lett.* **2015**, *15* (11), 7678–7683. https://doi.org/10.1021/acs.nanolett.5b03668.

(32) Chen, L.-Y.; Xu, J.-Q.; Choi, H.; Pozuelo, M.; Ma, X.; Bhowmick, S.; Yang, J.-M.; Mathaudhu, S.; Li, X.-C. Processing and Properties of Magnesium Containing a Dense Uniform Dispersion of Nanoparticles. *Nature* **2015**, *528* (7583), 539–543. https://doi.org/10.1038/nature16445.

(33) Javadi, A.; Pan, S.; Li, X. Scalable Manufacturing of Ultra-Strong Magnesium Nanocomposites. *Manuf. Lett.* **2018**, *16*, 23–26. https://doi.org/10.1016/j.mfglet.2018.03.001.

(34) Tjong, S. C.; Ma, Z. Y. Microstructural and Mechanical Characteristics of in Situ Metal Matrix Composites. *Mater. Sci. Eng. R Rep.* **2000**, *29* (3), 49–113. https://doi.org/10.1016/S0927-796X(00)00024-3.

(35) Tee, K. L.; Lu, L.; Lai, M. O. Synthesis of in Situ Al–TiB2 Composites Using Stir Cast Route. *Compos. Struct.* **1999**, *47* (1), 589–593. https://doi.org/10.1016/S0263-8223(00)00030-1.

(36) Emamy, M.; Mahta, M.; Rasizadeh, J. Formation of TiB2 Particles during Dissolution of TiAl3 in Al–TiB2 Metal Matrix Composite Using an in Situ Technique. *Compos. Sci. Technol.* **2006**, *66* (7), 1063–1066. https://doi.org/10.1016/j.compscitech.2005.04.016.

`

(37) Rai, R. N.; Saha, S. C.; Datta, G. L.; Chakraborty, M. Studies on Synthesis of In-Situ Al-TiC Metal Matrix Composites. *IOP Conf. Ser. Mater. Sci. Eng.* **2016**, *117*, 012042. https://doi.org/10.1088/1757-899X/117/1/012042.

(38) Birol, Y. Grain Refining Efficiency of Al–Ti–C Alloys. *J. Alloys Compd.* **2006**, *422* (1), 128–131. https://doi.org/10.1016/j.jallcom.2005.11.059.

(39) Banerji, A.; Reif, W. Development of Al-Ti-C Grain Refiners Containing TiC. *Metall. Trans. A* **1986**, *17* (12), 2127–2137. https://doi.org/10.1007/BF02645911.

(40) Tong, X. C.; Fang, H. S. Al-TiC Composites In Situ Processed by Ingot Metallurgy and Rapid Solidification Technology: Part I. Microstructural Evolution. *Metall. Mater. Trans. A* **1998**, *29* (3), 875–891. https://doi.org/10.1007/s11661-998-0278-8.

(41) Birol, Y. In Situ Processing of TiCp-Al Composites by Reacting Graphite with AI-Ti Melts. *J. Mater. Sci.* **1999**, *34* (7), 1653–1657. https://doi.org/10.1023/A:1004541002939.

(42) Liu, Z.; Fredriksson, H. On the Precipitation of TiC in Liquid Iron by Reactions between Different Phases. *Metall. Mater. Trans. A* **1997**, *28* (2), 471–483. https://doi.org/10.1007/s11661-997-0148-9.

(43) Nakata, H.; Choh, T.; Kanetake, N. Fabrication and Mechanical Properties of in Situ Formed Carbide Particulate Reinforced Aluminium Composite. *J. Mater. Sci.* **1995**, *30* (7), 1719–1727. https://doi.org/10.1007/BF00351601.

(44) Chrysanthou, A.; Erbaccio, G. Production of Copper-Matrix Composites by in Situ Processing. *J. Mater. Sci.* **1995**, *30* (24), 6339–6344. https://doi.org/10.1007/BF00369685.

(45) Zhang, E.; Zeng, S.; Li, Q.; Bo, Y.; Ma, M. A Study on the Kinetic Process of Reaction Synthesis of TiC: Part I. Experimental Research and Theoretical Model. *Metall. Mater. Trans. A* **1999**, *30* (4), 1147–1151. https://doi.org/10.1007/s11661-999-0166-x.

`

(46) Niu, L.; Hojamberdiev, M.; Xu, Y. Preparation of in Situ-Formed WC/Fe Composite on Gray Cast Iron Substrate by a Centrifugal Casting Process. *J. Mater. Process. Technol.* **2010**, *210* (14), 1986–1990. https://doi.org/10.1016/j.jmatprotec.2010.07.013.

(47) Zhong, L.; Yan, Y.; Ovcharenko, V. E.; Cai, X.; Zhang, X.; Xu, Y. Microstructural and Mechanical Properties of In Situ WC-Fe/Fe Composites. *J. Mater. Eng. Perform.* **2015**, *24* (11), 4561–4568. https://doi.org/10.1007/s11665-015-1742-4.

(48) Zhong, L.; Zhang, X.; Chen, S.; Xu, Y.; Wu, H.; Wang, J. Fe–W–C Thermodynamics and in Situ Preparation of Tungsten Carbide-Reinforced Iron-Based Surface Composites by Solid-Phase Diffusion. *Int. J. Refract. Met. Hard Mater.* **2016**, *57*, 42–49. https://doi.org/10.1016/j.ijrmhm.2016.02.001.

(49) Liu, X.; Liu, Y.; Huang, D.; Han, Q.; Wang, X. Tailoring In-Situ TiB2 Particulates in Aluminum Matrix Composites. *Mater. Sci. Eng. A* **2017**, *705*, 55–61. https://doi.org/10.1016/j.msea.2017.08.047.

(50) Mohanavel, V.; Rajan, K.; Senthil Kumar, K. R. Study on Mechanical Properties of AA6351 Alloy Reinforced with Titanium Di-Boride (TiB2) Composite by In Situ Casting Method https://www.scientific.net/AMM.787.583 (accessed 2019 -04 -30). https://doi.org/10.4028/www.scientific.net/AMM.787.583.

(51) Tang, Y.; Chen, Z.; Borbély, A.; Ji, G.; Zhong, S. Y.; Schryvers, D.; Ji, V.; Wang, H. W. Quantitative Study of Particle Size Distribution in an In-Situ Grown Al–TiB2 Composite by Synchrotron X-Ray Diffraction and Electron Microscopy. *Mater. Charact.* **2015**, *102*, 131–136. https://doi.org/10.1016/j.matchar.2015.03.003.

`

(52) Fjellstedt, J.; Jarfors, A. E. W. On the Precipitation of TiB2 in Aluminum Melts from the Reaction with KBF4 and K2TiF6. *Mater. Sci. Eng. A* **2005**, *413–414*, 527–532. https://doi.org/10.1016/j.msea.2005.09.054.

(53) Li, Z.; Chen, D.; Wang, H.; Lavernia, E. J.; Shan, A. Nano-TiB2 Reinforced Ultrafine-Grained Pure Al Produced by Flux-Assisted Synthesis and Asymmetrical Rolling. *J. Mater. Res. Warrendale* **2014**, *29* (21), 2514–2524. http://dx.doi.org/10.1557/jmr.2014.280.

(54) Feng, C. F.; Froyen, L. Microstructures of in Situ Al/TiB2 MMCs Prepared by a Casting Route. *J. Mater. Sci.* **2000**, *35* (4), 837–850. https://doi.org/10.1023/A:1004729920354.

(55) Han, G.; Zhang, W.; Zhang, G.; Feng, Z.; Wang, Y. High-Temperature Mechanical Properties and Fracture Mechanisms of Al–Si Piston Alloy Reinforced with in Situ TiB2 Particles. *Mater. Sci. Eng. A* **2015**, *633*, 161–168. https://doi.org/10.1016/j.msea.2015.03.021.

(56) Chen, D.; Chen, Z.; Zhang, P.; Zhang, Y. J.; Ma, H.; Wang, H. W. Bending Properties of AA7055 Aluminum Alloy Reinforced with In Situ TiB2 Particles https://www.scientific.net/AMR.535-537.1005 (accessed 2018 -11 -16). https://doi.org/10.4028/www.scientific.net/AMR.535-537.1005.

(57) Lu, L.; Lai, M. O.; Chen, F. L. Al-4 Wt% Cu Composite Reinforced with in-Situ TiB2 Particles. *Acta Mater.* **1997**, *45* (10), 4297–4309. https://doi.org/10.1016/S1359-6454(97)00075-X.

(58) Wang, M.; Chen, D.; Chen, Z.; Wu, Y.; Wang, F.; Ma, N.; Wang, H. Mechanical Properties of In-Situ TiB2/A356 Composites. *Mater. Sci. Eng. A* **2014**, *590*, 246–254. https://doi.org/10.1016/j.msea.2013.10.021.

`

(59) Wood, J. V.; Davies, P.; Kellie, J. L. F. Properties of Reactively Cast Aluminium–TiB2 Alloys. *Mater. Sci. Technol.* **1993**, *9* (10), 833–840. https://doi.org/10.1179/mst.1993.9.10.833.

(60) Lakshmi, S.; Lu, L.; Gupta, M. In Situ Preparation of TiB2 Reinforced Al Based Composites. *J. Mater. Process. Technol.* **1998**, *73* (1), 160–166. https://doi.org/10.1016/S0924-0136(97)00225-2.

(61) Xue, J.; Wang, J.; Han, Y.; Chen, C.; Sun, B. Behavior of CeO2 Additive in In-Situ TiB2 Particles Reinforced 2014 Al Alloy Composite. *Trans. Nonferrous Met. Soc. China* **2012**, *22* (5), 1012–1017. https://doi.org/10.1016/S1003-6326(11)61277-6.

(62) Chen, Y.; Chung, D. D. L. In Situ Al-TiB Composite Obtained by Stir Casting. *J. Mater. Sci.* **1996**, *31* (2), 311–315. https://doi.org/10.1007/BF01139145.

(63) Sivaprasad, K.; Babu, S. P. K.; Natarajan, S.; Narayanasamy, R.; Kumar, B. A.; Dinesh, G. Study on Abrasive and Erosive Wear Behaviour of Al 6063/TiB2 in Situ Composites. *Mater. Sci. Eng. A* **2008**, *498* (1), 495–500. https://doi.org/10.1016/j.msea.2008.09.003.

(64) Han, Y.; Liu, X.; Bian, X. In Situ TiB2 Particulate Reinforced near Eutectic Al–Si Alloy Composites. *Compos. Part Appl. Sci. Manuf.* **2002**, *33* (3), 439–444. https://doi.org/10.1016/S1359-835X(01)00124-5.

(65) Birol, Y. In Situ Synthesis of Al–TiCp Composites by Reacting K2TiF6 and Particulate Graphite in Molten Aluminium. *J. Alloys Compd.* **2008**, *454* (1), 110–117. https://doi.org/10.1016/j.jallcom.2006.12.016.

(66) Vinod Kumar, G. S.; Murty, B. S.; Chakraborty, M. Development of Al–Ti–C Grain Refiners and Study of Their Grain Refining Efficiency on Al and Al–7Si Alloy. *J. Alloys Compd.* **2005**, *396* (1), 143–150. https://doi.org/10.1016/j.jallcom.2004.12.039.

`

(67) Sheibani, S.; Najafabadi, M. Fazel. In Situ Fabrication of Al–TiC Metal Matrix Composites by Reactive Slag Process. *Mater. Des.* **2007**, *28* (8), 2373–2378. https://doi.org/10.1016/j.matdes.2006.08.004.

(68) Zhang, S.; Zhao, Y.; Chen, G.; Cheng, X. Microstructures and Dry Sliding Wear Properties of in Situ (Al3Zr+ZrB2)/Al Composites. *J. Mater. Process. Technol.* **2007**, *184* (1), 201–208. https://doi.org/10.1016/j.jmatprotec.2006.11.023.

(69) Dinaharan, I.; Murugan, N.; Parameswaran, S. Influence of in Situ Formed ZrB2 Particles on Microstructure and Mechanical Properties of AA6061 Metal Matrix Composites. *Mater. Sci. Eng. A* **2011**, *528* (18), 5733–5740. https://doi.org/10.1016/j.msea.2011.04.033.

(70) Fan, Q.; Chai, H.; Jin, Z. Mechanism of Combustion Synthesis of TiC–Fe Cermet. *J. Mater. Sci.* **1999**, *34* (1), 115–122. https://doi.org/10.1023/A:1004430028260.

(71) Zhang, X.; Lü, W.; Zhang, D.; Wu, R.; Bian, Y.; Fang, P. In Situ Technique for Synthesizing (TiB+TiC)/Ti Composites. *Scr. Mater.* **1999**, *41* (1), 39–46. https://doi.org/10.1016/S1359-6462(99)00087-1.

(72) Mishra (Pathak), S. K.; Das, S. K.; Ramachandrarao, P.; Yu Belov, D.; Mamyan, S. Synthesis of Zirconium Diboride-Alumina Composite by the Self-Propagating, High-Temperature Synthesis Process. *Metall. Mater. Trans. A* **2003**, *34* (9), 1979–1983. https://doi.org/10.1007/s11661-003-0162-5.

(73) Kuruvilla, A. K.; Prasad, K. S.; Bhanuprasad, V. V.; Mahajan, Y. R. Microstructure-Property Correlation in AlTiB2 (XD) Composites. *Scr. Metall. Mater.* **1990**, *24* (5), 873–878. https://doi.org/10.1016/0956-716X(90)90128-4.

`

(74) Ma, Z. Y.; Bi, J.; Lu, Y. X.; Shen, H. W.; Gao, Y. X. Microstructure and Interface of the in Situ Forming TiB2-Reinforced Aluminum Composite. *Compos. Interfaces* **1993**, *1* (4), 287–291. https://doi.org/10.1163/156855493X00121.

(75) Ma, Z. Y.; Li, J. H.; Li, S. X.; Ning, X. G.; Lu, Y. X.; Bi, J. Property-Microstructure Correlation in in Situ Formed Al2O3, TiB2 and Al3Ti Mixture-Reinforced Aluminium Composites. *J. Mater. Sci.* **1996**, *31* (3), 741–747. https://doi.org/10.1007/BF00367894.

(76) Taheri-Nassaj, E.; Kobashi, M.; Choh, T. Fabrication and Analysis of in Situ Formed Boride/Al Composites by Reactive Spontaneous Infiltration. *Scr. Mater.* **1997**, *37* (5), 605–614. https://doi.org/10.1016/S1359-6462(97)00140-1.

(77) Popov, V. A.; Shelekhov, E. V.; Prosviryakov, A. S.; Presniakov, M. Y.; Senatulin, B. R.; Kotov, A. D.; Khomutov, M. G. Particulate Metal Matrix Composites Development on the Basis of in Situ Synthesis of TiC Reinforcing Nanoparticles during Mechanical Alloying. *J. Alloys Compd.* **2017**, *707*, 365–370. https://doi.org/10.1016/j.jallcom.2016.10.051.

(78) Biselli, C.; Morris, D. G.; Randall, N. Mechanical Alloying of High-Strength Copper Alloys Containing TiB2 and Al2O3 Dispersoid Particles. *Scr. Metall. Mater.* **1994**, *30* (10), 1327–1332. https://doi.org/10.1016/0956-716X(94)90267-4.

(79) Lu, L.; Lai, M. O.; Niu, X. P.; Ho, H. N. In-Situ Formation of TiB2 Reinforced Aluminium via Mechanical Alloying. *Z. Fuer Met. Res. Adv. Tech.* **1998**, *89* (8), 567–572.

(80) Huang, L. J.; Geng, L.; Xu, H. Y.; Peng, H. X. In Situ TiC Particles Reinforced Ti6Al4V Matrix Composite with a Network Reinforcement Architecture. *Mater. Sci. Eng. A* **2011**, *528* (6), 2859–2862. https://doi.org/10.1016/j.msea.2010.12.046.

`

(81) Sahoo, P.; Koczak, M. J. Analysis of in Situ Formation of Titanium Carbide in Aluminum Alloys. *Mater. Sci. Eng. A* **1991**, *144* (1), 37–44. https://doi.org/10.1016/0921-5093(91)90207-4.

(82) Sahoo, P.; Koczak, M. J. Microstructure-Property Relationships of in Situ Reacted TiC/Al Cu Metal Matrix Composites. *Mater. Sci. Eng. A* **1991**, *131* (1), 69–76. https://doi.org/10.1016/0921-5093(91)90345-N.

(83) Premkumar, M. K.; Chu, M. G. Synthesis of TiC Particulates and Their Segregation during Solidification InIn Situ Processed AI-TiC Composites. *Metall. Trans. A* **1993**, *24* (10), 2358–2362. https://doi.org/10.1007/BF02648608.

(84) Premkumar, M. K.; Chu, M. G. Al TiC Particulate Composite Produced by a Liquid State in Situ Process. *Mater. Sci. Eng. A* **1995**, *202* (1), 172–178. https://doi.org/10.1016/0921-5093(95)09787-2.

(85) Lu, L.; Fuh, J. Y. H.; Chen, Z. D.; Leong, C. C.; Wong, Y. S. In Situ Formation of TiC Composite Using Selective Laser Melting. *Mater. Res. Bull.* **2000**, *35* (9), 1555–1561. https://doi.org/10.1016/S0025-5408(00)00339-1.

(86) Berns, H.; Wewers, B. Development of an Abrasion Resistant Steel Composite with in Situ TiC Particles. *Wear* **2001**, *251* (1), 1386–1395. https://doi.org/10.1016/S0043-1648(01)00790-6.

(87) Man, H. C.; Yang, Y. Q.; Lee, W. B. Laser Induced Reaction Synthesis of TiC+WC Reinforced Metal Matrix Composites Coatings on Al 6061. *Surf. Coat. Technol.* **2004**, *185* (1), 74–80. https://doi.org/10.1016/j.surfcoat.2003.10.132.

(88) Zhang, Z.; Chen, Y.; Zhang, Y.; Gao, K.; Zuo, L.; Qi, Y.; Wei, Y. Tribology Characteristics of Ex-Situ and in-Situ Tungsten Carbide Particles Reinforced Iron Matrix Composites

`

Produced by Spark Plasma Sintering. *J. Alloys Compd.* **2017**, *704*, 260–268. https://doi.org/10.1016/j.jallcom.2017.02.003.

(89) Shu, D.; Li, Z.; Zhang, K.; Yao, C.; Li, D.; Dai, Z. In Situ Synthesized High Volume Fraction WC Reinforced Ni-Based Coating by Laser Cladding. *Mater. Lett.* **2017**, *195*, 178–181. https://doi.org/10.1016/j.matlet.2017.02.076.

(90) Yuan, Y.; Li, Z. Growth Mechanism of In-Situ WC Grain in Fe-Ni-W-C Alloys System. *J. Alloys Compd.* **2018**, *738*, 379–393. https://doi.org/10.1016/j.jallcom.2017.11.382.

(91) Yuan, Y.; Li, Z. Microstructure and Tribology Behaviors of In-Situ WC/Fe Carbide Coating Fabricated by Plasma Transferred Arc Metallurgic Reaction. *Appl. Surf. Sci.* **2017**, *423*, 13–24. https://doi.org/10.1016/j.apsusc.2017.06.080.

(92) Zhang, Q.; Chen, D. L. A Model for Predicting the Particle Size Dependence of the Low Cycle Fatigue Life in Discontinuously Reinforced MMCs. *Scr. Mater.* **2004**, *51* (9), 863–867. https://doi.org/10.1016/j.scriptamat.2004.07.006.

(93) Chen, Z. Z.; Tokaji, K. Effects of Particle Size on Fatigue Crack Initiation and Small Crack Growth in SiC Particulate-Reinforced Aluminium Alloy Composites. *Mater. Lett.* **2004**, *58* (17), 2314–2321. https://doi.org/10.1016/j.matlet.2004.02.034.

(94) Cao, C.; Liu, W.; Javadi, A.; Ling, H.; Li, X. Scalable Manufacturing of 10 Nm TiC Nanoparticles through Molten Salt Reaction. *Procedia Manuf.* **2017**, *10* (Supplement C), 634–640. https://doi.org/10.1016/j.promfg.2017.07.066.

(95) Javadi, A.; Pan, S.; Cao, C.; Yao, G.; Li, X. Facile Synthesis of 10 nm Surface Clean TiB2 Nanoparticles. *Mater. Lett.* **2018**, *229*, 107–110. https://doi.org/10.1016/j.matlet.2018.06.054.

`

(96) Thanh, N. T. K.; Maclean, N.; Mahiddine, S. Mechanisms of Nucleation and Growth of Nanoparticles in Solution. *Chem. Rev.* **2014**, *114* (15), 7610–7630. https://doi.org/10.1021/cr400544s.

(97) Guo, M. X.; Wang, M. P.; Shen, K.; Cao, L. F.; Li, Z.; Zhang, Z. Synthesis of Nano TiB2 Particles in Copper Matrix by in Situ Reaction of Double-Beam Melts. *J. Alloys Compd.* **2008**, *460* (1), 585–589. https://doi.org/10.1016/j.jallcom.2007.06.026.

(98) Estruga, M.; Chen, L.; Choi, H.; Li, X.; Jin, S. Ultrasonic-Assisted Synthesis of Surface-Clean TiB2 Nanoparticles and Their Improved Dispersion and Capture in Al-Matrix Nanocomposites. *ACS Appl. Mater. Interfaces* **2013**, *5* (17), 8813–8819. https://doi.org/10.1021/am402719p.

(99) Worldwide aluminum consumption forecast 2029 https://www.statista.com/statistics/863681/global-aluminum-consumption/ (accessed 2021 -09 -07).

(100) Boeing: 787 By Design https://www.boeing.com/commercial/787/by-design/#/featured (accessed 2018 -11 -17).

(101) Rambabu, P.; Eswara Prasad, N.; Kutumbarao, V. V.; Wanhill, R. J. H. Aluminium Alloys for Aerospace Applications. In *Aerospace Materials and Material Technologies : Volume 1: Aerospace Materials*; Prasad, N. E., Wanhill, R. J. H., Eds.; Indian Institute of Metals Series; Springer Singapore: Singapore, 2017; pp 29–52. https://doi.org/10.1007/978-981-10-2134-3_2.

(102) Gao, T.; Zhang, Y.; Liu, X. Influence of Trace Ti on the Microstructure, Age Hardening Behavior and Mechanical Properties of an Al–Zn–Mg–Cu–Zr Alloy. *Mater. Sci. Eng. A* **2014**, *598*, 293–298. https://doi.org/10.1016/j.msea.2014.01.062.

`

(103) *Friction Stir Welding of High Strength 7XXX Aluminum Alloys*; Elsevier, 2016. https://doi.org/10.1016/C2014-0-01708-X.

(104) X.-M, L.; Starink, M. J. Effect of Compositional Variations on Characteristics of Coarse Intermetallic Particles in Overaged 7000 Aluminium Alloys. *Mater. Sci. Technol.* **2001**, *17* (11), 1324–1328. https://doi.org/10.1179/026708301101509449.

(105) Kai, W.; Baiqing, X.; Yongan, Z.; Guojun, W.; Xiwu, L.; Zhihui, L.; Shuhui, H.; Hongwei, L. Microstructure Evolution of a High Zinc Containing Al-Zn-Mg-Cu Alloy during Homogenization. *Rare Met. Mater. Eng.* **2017**, *46* (4), 928–934. https://doi.org/10.1016/S1875-5372(17)30124-8.

(106) Lim, S. T.; Lee, Y. Y.; Eun, I. S. Microstructural Evolution during Ingot Preheat in 7xxx Aluminium Alloys for Thick Semiproduct Applications https://www.scientific.net/MSF.519-521.549 (accessed 2018 -11 -20). https://doi.org/10.4028/www.scientific.net/MSF.519-521.549.

(107) Li, N.; Cui, J. Microstructural Evolution of High Strength 7B04 Ingot during Homogenization Treatment. *Trans. Nonferrous Met. Soc. China* **2008**, *18* (4), 769–773. https://doi.org/10.1016/S1003-6326(08)60132-6.

(108) Xu, D. K.; Rometsch, P. A.; Birbilis, N. Improved Solution Treatment for an As-Rolled Al–Zn–Mg–Cu Alloy. Part I. Characterisation of Constituent Particles and Overheating. *Mater. Sci. Eng. A* **2012**, *534*, 234–243. https://doi.org/10.1016/j.msea.2011.11.065.

(109) Takahashi, A.; Kobayashi, T.; Toda, H. In-Situ SEM Study on Effect of Inclusion Particles on Fracture Behavior in Al-Li System Alloy. *KeikinzokuJournal Jpn. Inst. Light Met.* **1999**, *49* (4), 166–171. https://doi.org/10.2464/jilm.49.166.

`

(110) Xu, D. K.; Rometsch, P. A.; Birbilis, N. Improved Solution Treatment for an As-Rolled Al–Zn–Mg–Cu Alloy. Part II. Microstructure and Mechanical Properties. *Mater. Sci. Eng. A* **2012**, *534*, 244–252. https://doi.org/10.1016/j.msea.2011.11.073.

(111) Weiland, H.; Rollett, A.; Cassada, W. *13th International Conference on Aluminum Alloys (ICAA 13): Conference Proceedings*; Springer, 2017.

(112) Wen, K.; Fan, Y.; Wang, G.; Jin, L.; Li, X.; Li, Z.; Zhang, Y.; Xiong, B. Aging Behavior and Precipitate Characterization of a High Zn-Containing Al-Zn-Mg-Cu Alloy with Various Tempers. *Mater. Des.* **2016**, *101*, 16–23. https://doi.org/10.1016/j.matdes.2016.03.150.

(113) Dupasquier, A.; Ferragut, R.; Iglesias, M. M.; Massazza, M.; Riontino, G.; Mengucci, P.; Barucca, G.; Macchi, C. E.; Somoza, A. Hardening Nanostructures in an AlZnMg Alloy. *Philos. Mag.* **2007**, *87* (22), 3297–3323. https://doi.org/10.1080/14786430701271959.

(114) Stiller, K.; Warren, P. J.; Hansen, V.; Angenete, J.; Gjønnes, J. Investigation of Precipitation in an Al–Zn–Mg Alloy after Two-Step Ageing Treatment at 100° and 150°C. *Mater. Sci. Eng. A* **1999**, *270* (1), 55–63. https://doi.org/10.1016/S0921-5093(99)00231-2.

(115) Li, H.; Cao, F.; Guo, S.; Jia, Y.; Zhang, D.; Liu, Z.; Wang, P.; Scudino, S.; Sun, J. Effects of Mg and Cu on Microstructures and Properties of Spray-Deposited Al-Zn-Mg-Cu Alloys. *J. Alloys Compd.* **2017**, *719*, 89–96. https://doi.org/10.1016/j.jallcom.2017.05.101.

(116) Chen, Z.; Mo, Y.; Nie, Z. Effect of Zn Content on the Microstructure and Properties of Super-High Strength Al-Zn-Mg-Cu Alloys. *Metall. Mater. Trans. A* **2013**, *44* (8), 3910–3920. https://doi.org/10.1007/s11661-013-1731-x.

(117) Marlaud, T.; Deschamps, A.; Bley, F.; Lefebvre, W.; Baroux, B. Influence of Alloy Composition and Heat Treatment on Precipitate Composition in Al–Zn–Mg–Cu Alloys. *Acta Mater.* **2010**, *58* (1), 248–260. https://doi.org/10.1016/j.actamat.2009.09.003.

`

(118) Liu, J.; Zhang, Y.; Li, X.; Li, Z.; Xiong, B.; Zhang, J. Thermodynamic Calculation of High Zinc-Containing Al-Zn-Mg-Cu Alloy. *Trans. Nonferrous Met. Soc. China* **2014**, *24* (5), 1481–1487. https://doi.org/10.1016/S1003-6326(14)63216-7.

(119) Liu, Y.; Jiang, D.; Li, B.; Ying, T.; Hu, J. Heating Aging Behavior of Al–8.35Zn–2.5Mg–2.25Cu Alloy. *Mater. Des.* **2014**, *60*, 116–124. https://doi.org/10.1016/j.matdes.2014.03.060.

(120) Wen, K.; Fan, Y.; Wang, G.; Jin, L.; Li, X.; Li, Z.; Zhang, Y.; Xiong, B. Aging Behavior and Fatigue Crack Propagation of High Zn-Containing Al-Zn-Mg-Cu Alloys with Zinc Variation. *Prog. Nat. Sci. Mater. Int.* **2017**, *27* (2), 217–227. https://doi.org/10.1016/j.pnsc.2017.02.002.

(121) Wen, K.; Xiong, B.; Zhang, Y.; Li, Z.; Li, X.; Huang, S.; Yan, L.; Yan, H.; Liu, H. Single-Stage Aging Behaviour and Precipitate Evolution in a High Zn-Containing Al–9.78Zn–2.02Mg–1.76Cu Alloy. *Mater. Sci. Technol.* **2018**, *34* (6), 718–724. https://doi.org/10.1080/02670836.2017.1410951.

(122) Dong, J.; Cui, J. Z.; Yu, F. X.; Zhao, Z. H.; Zhuo, Y. B. A New Way to Cast High-Alloyed Al–Zn–Mg–Cu–Zr for Super-High Strength and Toughness. *J. Mater. Process. Technol.* **2006**, *171* (3), 399–404. https://doi.org/10.1016/j.jmatprotec.2005.07.010.

(123) Seyed Ebrahimi, S. H.; Aghazadeh, J.; Dehghani, K.; Emamy, M.; Zangeneh, Sh. The Effect of Al−5Ti−1B on the Microstructure, Hardness and Tensile Properties of a New Zn Rich Aluminium Alloy. *Mater. Sci. Eng. A* **2015**, *636*, 421–429. https://doi.org/10.1016/j.msea.2015.03.015.

(124) Wen, K.; Xiong, B.-Q.; Fan, Y.-Q.; Zhang, Y.-A.; Li, Z.-H.; Li, X.-W.; Wang, F.; Liu, H.-W. Transformation and Dissolution of Second Phases during Solution Treatment of an Al–

`

Zn–Mg–Cu Alloy Containing High Zinc. *Rare Met.* **2018**, *37* (5), 376–380. https://doi.org/10.1007/s12598-016-0768-6.

(125) Starink, M. J.; Gao, N.; Furukawa, M.; Horita, Z.; Xu, C.; Langdon, T. G. MICROSTRUCTURAL DEVELOPMENTS IN A SPRAY-CAST Al-7034 ALLOY PROCESSED BY EQUAL-CHANNEL ANGULAR PRESSING. 12.

(126) Wang, F.; Xiong, B.; Zhang, Y.; Zhu, B.; Liu, H.; He, X. Effect of Heat Treatment on the Microstructure and Mechanical Properties of the Spray-Deposited Al–10.8Zn–2.8Mg–1.9Cu Alloy. *Mater. Sci. Eng. A* **2008**, *486* (1), 648–652. https://doi.org/10.1016/j.msea.2007.09.049.

(127) Ma, Y.; Chen, Z.; Wang, M.; Chen, D.; Ma, N.; Wang, H. High Cycle Fatigue Behavior of the In-Situ TiB2/7050 Composite. *Mater. Sci. Eng. A* **2015**, *640*, 350–356. https://doi.org/10.1016/j.msea.2015.06.023.

(128) Wang, J.; Geng, J.; Li, Y.; Cai, L.; Wang, M.; Chen, D.; Ma, N.; Wang, H. Stress Corrosion Cracking Behavior of In-Situ TiB 2 /7050 Composite. *Mater. Res. Express* **2018**, *5* (12), 126501. https://doi.org/10.1088/2053-1591/aadfa1.

(129) Campbell, F. C. Chapter 2 - Aluminum. In *Manufacturing Technology for Aerospace Structural Materials*; Campbell, F. C., Ed.; Elsevier Science: Oxford, 2006; pp 15–92. https://doi.org/10.1016/B978-185617495-4/50002-0.

(130) Angers, R.; Krishnadev, M. R.; Tremblay, R.; Corriveau, J.-F.; Dubé, D. Characterization of SiCp/2024 Aluminum Alloy Composites Prepared by Mechanical Processing in a Low Energy Ball Mill. *Mater. Sci. Eng. A* **1999**, *262* (1), 9–15. https://doi.org/10.1016/S0921-5093(98)01030-2.

(131) Mondolfo, L. F. *Aluminum Alloys: Structure and Properties*; Butterworths: London, 1979.

`

(132) Sha, G.; Marceau, R. K. W.; Gao, X.; Muddle, B. C.; Ringer, S. P. Nanostructure of Aluminium Alloy 2024: Segregation, Clustering and Precipitation Processes. *Acta Mater.* **2011**, *59* (4), 1659–1670. https://doi.org/10.1016/j.actamat.2010.11.033.

(133) Estruga, M.; Chen, L.; Choi, H.; Li, X.; Jin, S. Ultrasonic-Assisted Synthesis of Surface-Clean TiB2 Nanoparticles and Their Improved Dispersion and Capture in Al-Matrix Nanocomposites. *ACS Appl. Mater. Interfaces* **2013**, *5* (17), 8813–8819. https://doi.org/10.1021/am402719p.

(134) Kumar, N.; Gautam, R. K.; Mohan, S. In-Situ Development of ZrB2 Particles and Their Effect on Microstructure and Mechanical Properties of AA5052 Metal-Matrix Composites. *Mater. Des.* **2015**, *80*, 129–136. https://doi.org/10.1016/j.matdes.2015.05.020.

(135) Shang, H.; Lu, Y.; Zhao, F.; Chao, C.; Zhang, B.; Zhang, H. Preparing High Surface Area Porous Carbon from Biomass by Carbonization in a Molten Salt Medium. *RSC Adv.* **2015**, *5* (92), 75728–75734. https://doi.org/10.1039/C5RA12406A.

(136) Yang, B.; Wang, F.; Zhang, J. S. Microstructural Characterization of in Situ TiC/Al and TiC/Al–20Si–5Fe–3Cu–1Mg Composites Prepared by Spray Deposition. *Acta Mater.* **2003**, *51* (17), 4977–4989. https://doi.org/10.1016/S1359-6454(03)00292-1.

(137) Tong, X. C.; Shen, N. F.; Liu, B. C. The Structure of a Rapidly Solidified Al-Fe-Ti-C Alloy. *J. Mater. Sci.* **1995**, *30* (14), 3680–3689. https://doi.org/10.1007/BF00351885.

(138) Tong, X. C. Fabrication of in Situ TiC Reinforced Aluminum Matrix Composites Part I: Microstructural Characterization. *J. Mater. Sci.* **1998**, *33* (22), 5365–5374. https://doi.org/10.1023/A:1004494116119.

`

(139) Tong, X. C.; Ghosh, A. K. Fabrication of in Situ TiC Reinforced Aluminum Matrix Composites. *J. Mater. Sci.* **2001**, *36* (16), 4059–4069. https://doi.org/10.1023/A:1017946927566.

(140) Gotman, I.; Koczak, M. J.; Shtessel, E. Fabrication of Al Matrix in Situ Composites via Self-Propagating Synthesis. *Mater. Sci. Eng. A* **1994**, *187* (2), 189–199. https://doi.org/10.1016/0921-5093(94)90347-6.

(141) Wang, H. Y.; Jiang, Q. C.; Li, X. L.; Wang, J. G. In Situ Synthesis of TiC/Mg Composites in Molten Magnesium. *Scr. Mater.* **2003**, *48* (9), 1349–1354. https://doi.org/10.1016/S1359-6462(03)00014-9.

(142) Herbert, M. A.; Sarkar, C.; Mitra, R.; Chakraborty, M. Microstructural Evolution, Hardness, and Alligatoring in the Mushy State Rolled Cast Al-4.5Cu Alloy and In-Situ Al4.5Cu-5TiB2 Composite. *Metall. Mater. Trans. A* **2007**, *38* (9), 2110–2126. https://doi.org/10.1007/s11661-007-9264-9.

(143) Mandal, A.; Maiti, R.; Chakraborty, M.; Murty, B. Effect of TiB2 Particles on Aging Response of Al–4Cu Alloy. *Mater. Sci. Eng. A* **2004**, *386* (1–2), 296–300. https://doi.org/10.1016/S0921-5093(04)00938-4.

(144) Mandal, M.; Mitra, R. Effect of Pre-Cold Rolling on the Evolution of Microstructure, Microtexture, and Mechanical Properties of the Mushy State Rolled in-Situ Al-4.5Cu-5TiB2 Composite. *Mater. Charact.* **2018**, *146*, 267–278. https://doi.org/10.1016/j.matchar.2018.10.010.

(145) Tu, J. P.; Wang, N. Y.; Yang, Y. Z.; Qi, W. X.; Liu, F.; Zhang, X. B.; Lu, H. M.; Liu, M. S. Preparation and Properties of TiB2 Nanoparticle Reinforced Copper Matrix Composites

`

by in Situ Processing. *Mater. Lett.* **2002**, *52* (6), 448–452. https://doi.org/10.1016/S0167-577X(01)00442-6.

(146) El-Mahallawy, N.; Taha, M. A.; Jarfors, A. E. W.; Fredriksson, H. On the Reaction between Aluminium, K2TiF6 and KBF4. *J. Alloys Compd.* **1999**, *292* (1–2), 221–229. https://doi.org/10.1016/S0925-8388(99)00294-7.

(147) Liang, Y.; Zhou, J.; Dong, S.; Yang, T. Thermodynamic Analysis of the Formation of In-Situ Reinforced Phases in Cast Al-4.5Cu Alloy. *J. Wuhan Univ. Technol.-Mater Sci Ed* **2008**, *23* (3), 342. https://doi.org/10.1007/s11595-007-3342-0.

(148) Anestiev, L.; Froyen, L.; van Vugt, L. On the Kinetics of Diffusion Controlled Precipitation under Microgravity. *J. Appl. Phys.* **2000**, *88* (4), 2130–2137. https://doi.org/10.1063/1.1303849.

(149) Nielsen, A. E. DIFFUSION CONTROLLED GROWTH OF A MOVING SPHERE. THE KINETICS OF CRYSTAL GROWTH IN POTASSIUM PERCHLORATE PRECIPITATION. *J. Phys. Chem.* **1961**, *65* (1), 46–49. https://doi.org/10.1021/j100819a014.

(150) Wang, L. Atomistics of Self-Diffusion in Liquid Metals. *EPJ Web Conf.* **2017**, *151*, 02004. https://doi.org/10.1051/epjconf/201715102004.

(151) Wang, T.; Zhang, F.; Yang, L.; Fang, X. W.; Zhou, S. H.; Kramer, M. J.; Wang, C. Z.; Ho, K. M.; Napolitano, R. E. A Computational Study of Diffusion in a Glass-Forming Metallic Liquid. *Sci. Rep.* **2015**, *5*, 1–9. https://doi.org/10.1038/srep10956.

(152) Wang, X.; Song, J.; Vian, W.; Ma, H.; Han, Q. The Interface of TiB2 and Al3Ti in Molten Aluminum. *Metall. Mater. Trans. B* **2016**, *47* (6), 3285–3290. https://doi.org/10.1007/s11663-015-0570-0.

`

(153) Li, Q.; Jun, Y.-S. The Apparent Activation Energy and Pre-Exponential Kinetic Factor for Heterogeneous Calcium Carbonate Nucleation on Quartz. *Commun. Chem.* **2018**, *1* (1), 1–9. https://doi.org/10.1038/s42004-018-0056-5.

(154) Pan, S.; Guan, Z.; Yao, G.; Yuan, J.; Li, X. Mo-Enhanced Chemical Stability of TiC Nanoparticles in Molten Al. *J. Alloys Compd.* **2021**, *856*, 158169. https://doi.org/10.1016/j.jallcom.2020.158169.

(155) Pourgharibshahi, M.; Divandari, M.; Saghafian, H.; Timelli, G. Eutectic Nucleation in 7xxx Series Aluminum Alloys from a Non-Classical Viewpoint. *Metall. Mater. Trans. A* **2020**, *51* (9), 4572–4583. https://doi.org/10.1007/s11661-020-05876-0.

(156) Dehnavi, M.; Kuhestani, F.; Haddad-Sabzevar, M. Cooling Curve Analysis in Binary Al-Cu Alloys: Part I- Effect of Cooling Rate and Copper Content on the Eutectic Formation. *Metall. Mater. Eng.* **2015**, *21* (3), 195–206. https://doi.org/10.30544/80.

(157) Dehnavi, M.; Haddad-Sabzevar, M.; Avazkonnadeh-Gharavol, M. H. Cooling Curve Analysis in Binary Al-Cu Alloys: Part II- Effect of Cooling Rate and Grain Refinement on The Thermal and Thermodynamic Characteristics. *Metall. Mater. Eng.* **2015**, *21* (3), 207–222. https://doi.org/10.30544/81.

(158) Gibbs, J. W.; Mendez, P. F. Solid Fraction Measurement Using Equation-Based Cooling Curve Analysis. *Scr. Mater.* **2008**, *58* (8), 699–702. https://doi.org/10.1016/j.scriptamat.2007.12.022.

(159) Ghoncheh, M. H.; Shabestari, S. G.; Asgari, A.; Karimzadeh, M. Nonmechanical Criteria Proposed for Prediction of Hot Tearing Sensitivity in 2024 Aluminum Alloy. *Trans. Nonferrous Met. Soc. China* **2018**, *28* (5), 848–857. https://doi.org/10.1016/S1003-6326(18)64718-1.

`

(160) Shabestari, S. G.; Ghoncheh, M. H. Investigation on the Effect of Cooling Rate on Hot Tearing Susceptibility of Al2024 Alloy Using Thermal Analysis. *Metall. Mater. Trans. B* **2015**, *46* (6), 2438–2448. https://doi.org/10.1007/s11663-015-0450-7.

(161) Mahjoub, R.; Laws, K. J.; Stanford, N.; Ferry, M. General Trends between Solute Segregation Tendency and Grain Boundary Character in Aluminum - an Ab Inito Study. *Acta Mater.* **2018**. https://doi.org/10.1016/j.actamat.2018.07.069.

(162) Wu, C.; Ma, K.; Zhang, D.; Wu, J.; Xiong, S.; Luo, G.; Zhang, J.; Chen, F.; Shen, Q.; Zhang, L.; Lavernia, E. J. Precipitation Phenomena in Al-Zn-Mg Alloy Matrix Composites Reinforced with B 4 C Particles. *Sci. Rep.* **2017**, *7* (1), 9589. https://doi.org/10.1038/s41598-017-10291-4.

(163) Kumar, A.; Barda, H.; Klinger, L.; Finnis, M. W.; Lordi, V.; Rabkin, E.; Srolovitz, D. J. Anomalous Diffusion along Metal/Ceramic Interfaces. *Nat. Commun.* **2018**, *9* (1), 5251. https://doi.org/10.1038/s41467-018-07724-7.

(164) Ferragut, R.; Somoza, A.; Tolley, A.; Torriani, I. Precipitation Kinetics in Al–Zn–Mg Commercial Alloys. *J. Mater. Process. Technol.* **2003**, *141*, 35–40. https://doi.org/10.1016/S0924-0136(02)01044-0.

(165) Puiggali, M.; Zielinski, A.; Olive, J. M.; Renauld, E.; Desjardins, D.; Cid, M. Effect of Microstructure on Stress Corrosion Cracking of an Al-Zn-Mg-Cu Alloy. *Corros. Sci.* **1998**, *40* (4), 805–819. https://doi.org/10.1016/S0010-938X(98)00002-X.

(166) Sha, G.; Cerezo, A. Early-Stage Precipitation in Al–Zn–Mg–Cu Alloy (7050). *Acta Mater.* **2004**, *52* (15), 4503–4516. https://doi.org/10.1016/j.actamat.2004.06.025.

`

(167) Liu, W.; Cao, C.; Xu, J.; Wang, X.; Li, X. Molten Salt Assisted Solidification Nanoprocessing of Al-TiC Nanocomposites. *Mater. Lett.* **2016**, *185*, 392–395. https://doi.org/10.1016/j.matlet.2016.09.023.

(168) Wang, Z.; Chen, M.; Jiang, H.; Li, H.; Li, S. Effect of Artificial Ageing on Strength and Ductility of an Al-Cu-Mg-Mn Alloy Subjected to Solutionizing and Room-Temperature Rolling. *Mater. Charact.* **2020**, *165*, 110383. https://doi.org/10.1016/j.matchar.2020.110383.

(169) Yang, S.; Xing, Q.; Yu, H.; Wang, Y.; Dai, S. Al-Zn-Mg-Cu Alloys with Strength of 800MPa. *J. Mater. Eng.* **2018**, *46* (4), 82–90. https://doi.org/10.11868/j.issn.1001-4381.2017.000277.

(170) Zuo, M.; Sokoluk, M.; Cao, C.; Yuan, J.; Zheng, S.; Li, X. Microstructure Control and Performance Evolution of Aluminum Alloy 7075 by Nano-Treating. *Sci. Rep.* **2019**, *9* (1), 1–11. https://doi.org/10.1038/s41598-019-47182-9.

(171) Martin, J. H.; Yahata, B. D.; Hundley, J. M.; Mayer, J. A.; Schaedler, T. A.; Pollock, T. M. 3D Printing of High-Strength Aluminium Alloys. *Nature* **2017**, *549* (7672), 365–369. https://doi.org/10.1038/nature23894.

(172) Xu, J. Q.; Chen, L. Y.; Choi, H.; Li, X. C. Theoretical Study and Pathways for Nanoparticle Capture during Solidification of Metal Melt. *J. Phys. Condens. Matter* **2012**, *24* (25), 255304. https://doi.org/10.1088/0953-8984/24/25/255304.

(173) Kai, W.; Baiqing, X.; Yongan, Z.; Guojun, W.; Xiwu, L.; Zhihui, L.; Shuhui, H.; Hongwei, L. Microstructure Evolution of a High Zinc Containing Al-Zn-Mg-Cu Alloy during Homogenization. *Rare Met. Mater. Eng.* **2017**, *46* (4), 928–934. https://doi.org/10.1016/S1875-5372(17)30124-8.

`

(174) Liu, G.; Geng, J.; Li, Y.; Cai, L.; Chen, D.; Wang, M.; Ma, N.; Wang, H. Microstructures Evolution of Nano TiB2/7050Al Composite during Homogenization. *Mater. Charact.* **2020**, *159*, 110019. https://doi.org/10.1016/j.matchar.2019.110019.

(175) *Casting*, [10. ed.], 4. print.; ASM International, Stefanescu, D. M., ASM International, Eds.; ASM handbook; ASM International: Materials Park, Ohio, 1998.

(176) Mehrabian, R.; Keane, M.; Flemings, M. C. Interdendritic Fluid Flow and Macrosegregation; Influence of Gravity. *Metall. Mater. Trans. B* **1970**, *1* (5), 1209–1220. https://doi.org/10.1007/BF02900233.

(177) Petrov, D.; Watson, A.; Gröbner, J.; Rogl, P.; Tedenac, J.-C.; Bulanova, M.; Turkevich, V. Aluminium – Magnesium – Zinc. 19.

(178) Nielsen, Ø.; Arnberg, S. L.; Mo, A.; Thevik, H. Experimental Determination of Mushy Zone Permeability in Aluminum-Copper Alloys with Equiaxed Microstructures. *Metall. Mater. Trans. A* **1999**, *30* (9), 2455–2462. https://doi.org/10.1007/s11661-999-0254-y.

(179) Bashirnezhad, K.; Bazri, S.; Safaei, M. R.; Goodarzi, M.; Dahari, M.; Mahian, O.; Dalkılıça, A. S.; Wongwises, S. Viscosity of Nanofluids: A Review of Recent Experimental Studies. *Int. Commun. Heat Mass Transf.* **2016**, *73*, 114–123. https://doi.org/10.1016/j.icheatmasstransfer.2016.02.005.

(180) Corcione, M. Empirical Correlating Equations for Predicting the Effective Thermal Conductivity and Dynamic Viscosity of Nanofluids. *Energy Convers. Manag.* **2011**, *52* (1), 789–793. https://doi.org/10.1016/j.enconman.2010.06.072.

(181) Sigworth, G. K.; Howell, J.; Rios, O.; Kaufman, M. J. Heat Treatment of Natural Aging Aluminum Casting Alloys. *Int. J. Cast Met. Res.* **2006**, *19* (2), 123–129. https://doi.org/10.1179/136404605225023198.

`

(182) Metallurgy of Heat Treatable Aluminum Alloys. In *Heat Treating of Nonferrous Alloys*; Totten, G. E., Ed.; ASM International, 2016; pp 65–113. https://doi.org/10.31399/asm.hb.v04e.a0006287.

(183) Lee, S.-H. Precipitation Strengthening in Naturally Aged Al–Zn–Mg–Cu Alloy. *Mater. Sci.* **2021**, 8.

(184) Alatorre, N.; Ambriz, R. R.; Noureddine, B.; Amrouche, A.; Talha, A.; Jaramillo, D. Tensile Properties and Fusion Zone Hardening for GMAW and MIEA Welds of a 7075-T651 Aluminum Alloy. *Acta Metall. Sin. Engl. Lett.* **2014**, *27* (4), 694–704. https://doi.org/10.1007/s40195-014-0103-x.

(185) Ma, C.; Zhao, J.; Cao, C.; Lin, T.-C.; Li, X. Fundamental Study on Laser Interactions With Nanoparticles-Reinforced Metals—Part I: Effect of Nanoparticles on Optical Reflectivity, Specific Heat, and Thermal Conductivity. *J. Manuf. Sci. Eng.* **2016**, *138* (12), 121001–121001. https://doi.org/10.1115/1.4033392.

(186) Wolfe, T. D. 2519-T87 ALUMINUM ARMOR ALLOYS • FOR USE IN ARMY VEHICLE SYSTEMS. 27.

(187) Edwards, M. R.; Stoneham, V. E. THE FUSION WELDING OF Al-Li-Cu-Mg (8090) ALLOY. **1987**. https://doi.org/10.1051/jphyscol:1987333.

(188) Pickin, C. G. Arc Welding of High Strength Aluminium Alloys for Armour System Applications, Cranfield University, School of Applied Sciences, 2011.

(189) Shih, H.-C.; Ho, N.-J.; Huang, J. C. Precipitation Behaviors in Al-Cu-Mg and 2024 Aluminum Alloys. *Metall. Mater. Trans. A* **1996**, *27* (9), 2479–2494. https://doi.org/10.1007/BF02652342.

`

(190) Lee, S.-H.; Kayani, S. H.; Jung, J.-G.; Baik, S.-I.; Kim, M.-S.; Lee, Y.-K.; Euh, K. Crystallographic Characterization of Al18Mg3Ti2 Intermetallic Phase in Al–Zn–Mg–Cu–Zr–Ti Alloy. *J. Alloys Compd.* **2020**, *844*, 156173. https://doi.org/10.1016/j.jallcom.2020.156173.

(191) Liu, L. M.; Wang, S. Q.; Ye, H. Q. Adhesion and Bonding of the Al/TiC Interface. *Surf. Sci.* **2004**, *550* (1–3), 46–56. https://doi.org/10.1016/j.susc.2003.12.031.

(192) Porter, D. A.; Easterling, K. E.; Easterling, K. E. *Phase Transformations in Metals and Alloys (Revised Reprint)*, 3rd ed.; CRC Press: Boca Raton, 2009. https://doi.org/10.1201/9781439883570.

(193) Pang, X.; Yang, W.; Yang, J.; Pang, M.; Zhan, Y. Atomic Structure, Stability and Electronic Properties of S(Al2CuMg)/Al Interface: A First-Principles Study. *Intermetallics* **2018**, *93*, 329–337. https://doi.org/10.1016/j.intermet.2017.10.014.

(194) Cheng, S.; Zhao, Y. H.; Zhu, Y. T.; Ma, E. Optimizing the Strength and Ductility of Fine Structured 2024 Al Alloy by Nano-Precipitation. *Acta Mater.* **2007**, *55* (17), 5822–5832. https://doi.org/10.1016/j.actamat.2007.06.043.

(195) Chen, Y. Q.; Pan, S. P.; Liu, W. H.; Liu, X.; Tang, C. P. Morphologies, Orientation Relationships, and Evolution of the T-Phase in an Al-Cu-Mg-Mn Alloy during Homogenisation. *J. Alloys Compd.* **2017**, *709*, 213–226. https://doi.org/10.1016/j.jallcom.2017.03.161.

(196) Wang, S. C.; Starink, M. J. Two Types of S Phase Precipitates in Al–Cu–Mg Alloys. *Acta Mater.* **2007**, *55* (3), 933–941. https://doi.org/10.1016/j.actamat.2006.09.015.

`